U.PORTO

FEUP FACULDADE DE ENGENHARIA
UNIVERSIDADE DO PORTO

Effect of Viscoelastic Damping of Polymer-based Composite Materials in the Mitigation of Footbridge Vibrations

Vitor Dacol

Thesis submitted to the Faculty of Engineering of the University of Porto – FEUP in partial fulfillment of the requirements for the degree of Doctor of Philosophy in Civil Engineering

Supervisors
Associate Professor Dra. Elsa de Sá Caetano (Advisor)
Full Professor Dr. João Pedro Ramôa Ribeiro Correia (Co-advisor)

Programa Doutoral em Engenharia Civil (PRODEC)
Departamento de Engenharia Civil (DEC)
Faculdade de Engenharia (FEUP)
Universidade do Porto (UP)

Porto, 2021

BMV,

…amo-te à ti…

ABSTRACT

The construction of structures with progressively longer spans and current aesthetic trends advocating very slender and lightweight solutions has resulted in an increased sensitivity of walkways to dynamic actions, which may require the implementation of measures to mitigate vibrations and meet human comfort criteria. For this purpose, it is imperative to have a good understanding of the effects of loads on this type of structure. In this context, the actions caused by pedestrians involve, in most cases, the control of comfort issues and not of structural stability.

To ensure acceptable levels of comfort, some strategies can be implemented which aim to mitigate vibrations in footbridges. One of the possible forms of action is to move away from the resonance frequencies (natural) of the footbridge from the typical frequencies of pedestrian actions, which can be achieved by increasing the stiffness of the structure or just the deck. However, the mass increase generally associated with the stiffness increase negatively affects the aesthetics of the footbridge. On the other hand, the increase in structural damping is currently the most frequent and effective measure in the attenuation of vibrations associated with pedestrian actions.

In this sense, the structural use of fibre-reinforced polymer composite materials, based on a polymeric matrix, is a feasible strategy to mitigate, or even control, excessive vibrations that may generate discomfort to users because it combines the structural versatility of polymer-based composites (stiffness, lightness and durability) with its high damping capacity. These materials present a dynamic behaviour that can be described by the viscoelasticity theory, according to which polymeric materials, when subjected to harmonic load cycles, present harmonic deformation cycles, with the same frequency, but with a phase delay about the corresponding load cycles, which characterises the material damping.

In this thesis, the viscoelastic damping capacity of polymer-based composites was investigated and its applicability to the composition of a footbridge was assessed, taking advantage of the characteristics and benefits that can result in the dynamic behaviour of these structures.

The thesis is composed of five papers that have been published or submitted for publication. The first three papers focus on viscoelasticity and the behaviour of polymeric materials (and their composites), namely the creep and relaxation functions and their relationship with the dynamic storage and loss modulus. Based on the Exponential-Power Law, two new methods of data fitting in viscoelasticity were presented. In the last two papers, an experimental campaign was conducted to investigate the dynamic behaviour of glass fibre reinforced polymer (GFRP) based composites. Initially, through laboratory experiments of beams with free support, and applying modal identification methods, the aim was to identify and quantify the difference in damping of steel and a GFRP composite, demonstrating that the damping of the latter is higher than that of steel. Finally, based on ambient vibration tests and impact tests, a campaign of modal identification tests of the São Silvestre footbridge, located in the city of Ovar, Portugal, produced with GFRP profiles and steel fibre reinforced self-compacting concrete (SFRSCC) deck, was performed. Through the measured data and with a numerical and analytical analysis, it was possible to demonstrate that the GFRP structure of the pedestrian bridge has damping characteristics capable of attenuating the vibrations of the structure.

Keywords: Viscoelasticity, Composites, GFRP, Natural Frequency, Damping, Dynamic Behaviour, Dynamic Mechanical Analysis, Footbridges.

RESUMO

A construção de estruturas com vãos progressivamente mais longos e as tendências estéticas actuais, advogando soluções muito esbeltas e leves, resultou num aumento da sensibilidade das passarelas a acções dinâmicas, o que pode exigir a implementação de medidas para mitigar as vibrações e, assim, satisfazer os critérios de conforto humano. Para este efeito, é imperativo ter uma boa compreensão dos efeitos das cargas sobre este tipo de estruturas. Neste contexto, as acções causadas por peões envolvem, na maioria dos casos, o controlo de questões de conforto e não de estabilidade estrutural.

De forma a garantir níveis aceitáveis de conforto, podem ser implementadas algumas estratégias as quais visam mitigar as vibrações em passarelas. Uma das formas possíveis de actuação é afastar as frequências de ressonância (naturais) das frequências típicas das acções pedestres, o que pode ser conseguido através de um aumento da rigidez da estrutura ou apenas do tabuleiro. No entanto, o aumento de massa tipicamente associado ao aumento de rigidez depara-se com questões estéticas. Por seu lado, o aumento do amortecimento estrutural é actualmente a medida mais frequente e mais eficaz na atenuação das vibrações associadas às acções pedestres.

Neste sentido, a utilização estrutural de materiais compósitos reforçados com fibras, baseados numa matriz polimérica, é uma estratégia exequível para mitigar, ou mesmo controlar, as vibrações excessivas que podem gerar desconforto aos utilizadores, pois combina a versatilidade estrutural dos compósitos à base de polímeros (rigidez, leveza e durabilidade) com a sua elevada capacidade de amortecimento. Estes materiais apresentam um comportamento dinâmico que pode ser descrito pela teoria da viscoelasticidade, segundo a qual os materiais poliméricos (e os seus compósitos), quando sujeitos a ciclos de carga harmónicos, apresentam ciclos de deformação harmónicos, com a mesma frequência, mas com um atraso de fase relativamente aos ciclos de carga correspondentes, o que caracteriza o amortecimento material.

Nesta tese, foi investigada a capacidade de amortecimento viscoelástico dos compósitos à base de polímeros e a sua aplicabilidade à composição de uma ponte pedonal, aproveitando as características e benefícios que podem resultar no comportamento dinâmico destas estruturas.

A tese é composta por cinco artigos que foram publicados ou submetidos. Os três primeiros artigos centram-se na viscoelasticidade e no comportamento de materiais poliméricos ou compósitos de matriz polimérica, nomeadamente nas funções de fluência e relaxação e a sua relação com o módulo de armazenamento dinâmico e perda. Com base na Lei Exponential-Potência, foram apresentados dois novos métodos de ajustamento de dados em viscoelasticidade. Nos últimos artigos, foi conduzida uma campanha experimental para investigar o comportamento dinâmico dos compósitos à base de polímeros reforçados com fibras de vidro (GFRP, do inglês, glass fibre reinfroced polymer). Inicialmente, através de experiências de laboratório de vigas com suporte livre, e aplicando métodos de identificação modal, o objectivo foi identificar e quantificar a diferença entre o amortecimento do aço e de um compósito de GFRP, demonstrando que o amortecimento deste último é maior do que o do aço. Finalmente, com base em ensaios de vibração ambiental e testes de impacto, foi realizada uma campanha de identificação modal da passarela São Silvestre, localizada na cidade de Ovar, Portugal, produzida com perfis de GFRP e tabuleiro em concreto auto-compactável reforçado com fibras de aço (SFRSCC, do inglês, steel fibre reinforced self-compacting concrete). Através dos dados medidos e com uma análise numérica e analítica, foi possível demonstrar que a estrutura de GFRP da ponte pedonal tem características amortecedoras capazes de atenuar as vibrações da estrutura.

Palavras-chave: Viscoelasticidade, Compósitos, GFRP, Frequência Natural, Amortecimento, Comportamento Dinâmico, Análise Mecânica Dinâmica, Pontes pedonais.

ACKNOWLEDGEMENTS

To all those who have been involved in this work in any way, or who have only crossed this path, I express my fraternal gratitude and my desire for our lives to progress towards prosperity and peace.

Gratitude is an aspect of human life that gives, he who has it, eternal aptitude to serve. The noblest sense of gratitude is its attachment to voluntary respect.

Dear Dra. Elsa Caetano, my gratitude is mirrored in my respect, I am sure that all your dedication, all your great and infallible patience, and your wise knowledge, are nourishment for my curiosity and restlessness.

Dr. João Ramôa Correia, I dedicate to the noble teacher, my deep gratitude for his voluntariness in directing my confused ideas and, gently, putting them in the plumb line.

To Professor Guibert Ulric Crevecoeur (Federal Public Service Economy - Department of Energy - Brussels, Belgium), my special thanks for his useful remarks have led to a significant improvement of the present contribution.

I wish to express my utmost thanks to Dr. José A. Gonilha for his useful remarks and all the information and material kindly provided about the São Silvestre footbridge.

I would like to thank Dr. Carlos Moutinho for kindly helping me in the acquisition of materials that were used in the experimental phase of this research.

For my mother and father, with whom I talk every day, take care of you.

For my sister, you may listen to “Sail away sweet sister”.

For my dear Neide Dacol, If I knew where you were, I would have found you sooner.

List of Appended Papers

I Dacol, V.; Caetano, E. ***Modelling the three-stage of creep.*** *Proceedings of the 3rd RILEM Spring Convention and Conference (RSCC2020). Volume 3: Service Life Extension of Existing Structures, Guimarães, Portugal, 2020.* https://doi.org/10.1007/978-3-030-76465-4.

II Dacol, V.; Caetano, E.; Correia, J.R. ***A Combined Exponential-Power-Law Method for Interconversion between Viscoelastic Functions of Polymers and Polymer-Based Materials.*** *Polymers 2020, 12, 3001.* https://doi.org/10.3390/polym12123001. *Published: 16 December 2020. Impact Factor: 4.493 (2020).*

III Dacol, V.; Caetano, E.; Correia, J.R. ***A New Viscoelasticity Dynamic Fitting Method Applied for Polymeric and Polymer-Based Composite Materials.*** *Materials 2020, 13, 5213.* https://doi.org/10.3390/ma13225213. *Published: 18 November 2020. Impact Factor: 3.920 (2020).*

IV Dacol, V.; Caetano, E.; Correia, J.R. ***Comparative Study of Damping on Pultruded GFRP and Steel Beams.*** *Polymers 2021, 13, 2201.* https://doi.org/10.3390/polym13132201. *Published: 2 July 2021. Impact Factor: 4.493 (2020).*

V Dacol, V.; Caetano, E.; Correia, J.R. ***Modal Identification and Damping Analysis of a Full-Scale GFRP-SFRSCC Hybrid Footbridge.*** *Submitted to Engineering Structures in January 2022. Impact Factor: 4,471 (2021).*

Contents

Abstract **v**

Acknowledgements **ix**

List of Append Papers **xi**

1. Introduction **1.1**

1.1. Motivation 1.1
1.2. Research Objectives and Methodology 1.2
1.3. Thesis Structure 1.3
1.4. References 1.4

2. Rheology of Polymers and Viscoelasticity **2.1**

2.1 Justification 2.1
2.2 Introduction 2.1
2.3 Principles of Viscoelasticity 2.1
2.4 Linear Viscoelasticity 2.4
2.5 Discrete Viscoelastic Models 2.7
2.6 Representation of the Creep Compliance 2.11
2.7 Final Considerations 2.12
2.8 References 2.13

3. Dynamic Behaviour of Polymer-Based Materials: The Viscoelastic Damping **3.1**

3.1. Justification 3.1
3.2. Introduction 3.1
3.3. Hysteresis Cycle 3.2
3.4. The Complex Modulus 3.3
3.5. Damping Mechanisms 3.5
3.6. A Brief Note on Hysterical Damping 3.8
3.7. Effects of Temperature and Frequency on The Complex Modulus and Loss Factor 3.11
3.8. Final Considerations 3.16
3.9. References 3.17

4. Vibrations in Footbridges **4.1**

4.1. Justification 4.1
4.2. Initial Considerations 4.1
4.3. Characterization of Dynamic Actions 4.1
4.4. Load Functions 4.6
4.5. Comfort Criteria and Verification Procedures 4.11

4.6. Final Considerations 4.13
4.7. References 4.15

5. Summary of Appended Papers 5.1

5.1. Paper 1 5.2
5.2. Paper 2 5.2
5.3. Paper 3 5.3
5.4. Paper 4 5.3
5.5. Paper 5 5.4

6. Conclusions and Future Work 6.1

6.1. Conclusions from the research 6.1
The Viscoelasticity Approach 6.2
The Dynamic Evaluation 6.2
6.2. Looking to the future 6.3

Paper 1 A
Paper 2 B
Paper 3 C
Paper 4 D
Paper 5 E

List of Figures

Figure 2.1. Stress-strain graph of viscoelastic material (adapted from Barra [3]) 2.2
Figure 2.2. Illustrative scheme (adapted from Barra [3]) 2.2
Figure 2.3. Shear in a viscous material 2.3
Figure 2.4. Creep of an ideal viscoelastic material (adapted from Nandini et al. [6]) 2.4
Figure 2.5. The three stages of creep 2.5
Figure 2.6. Creep and recovery with full recovery 2.5
Figure 2.7. Creep Relaxation under Constant Deformation 2.6
Figure 2.8. The ideal cycle of hysteresis 2.6
Figure 2.9. Representation of elastic spring and viscous damper 2.8
Figure 2.10. Maxwell's linear viscoelastic model. 2.8
Figure 2.11. Voigt-Kelvin Linear Viscoelasticity Model 2.9
Figure 2.12. Maxwell's generalized model 2.10
Figure 2.13. Generalized Kelvin model 2.10
Figure 3.1. Oscillatory stress and strain and phase delay (adapted from Findley et al. [4]) 3.2
Figure 3.2. Phasor diagram of complex stress 3.4
Figure 3.4. Phasor diagram of the complex modulus 3.4
Figure 3.4. PVC-NBR/graphite hysteresis loop 3.6
Figure 3.5. Regions of Viscoelastic Behaviour of an Epoxy 3.12
Figure 3.6. Dynamic-mechanical properties of epoxy resin and epoxy/fiber composites with different fiber orientations (adapted from Lorandi et al. [7]) 3.13
Figure 3.7. Thermodynamic analysis DGEBA/TEPA and DGEBA/D230 (adapted from Junior et al. [30]) 3.14
Figure 3.8. Dynamic-Mechanical Analysis of ABS+PC blend (adapted from Souza et al. [1]) 3.15
Figure 3.9. Internal temperature in a polymer (adapted from Cazenove et al. [35]). 3.15
Figure 4.1. Variation of step speed according to age and gender (adapted from Ingólfsson et al. [1]) 4.2
Figure 4.2. Walking load function in three directions (adapted from Bachmann et al. [4]). 4.3
Figure 4.3. Frequency distribution of standard walking steps (adapted from Matsumoto et al. [8]) 4.4
Figure 4.4. Relationships among step frequency, speed and length (adapted from Bachmann et al. [4]) 4.4
Figure 4.5. Evolution of step force-to-weight ratio for fast walking (adapted from Queiroz [11]) 4.5
Figure 4.6. Vertical step force-to-weight ratio of both feet (adapted from Bachmann et al. [4]) 4.5
Figure 4.7. Contact time, amplification factor, and step frequency (adapted from Bachmann et al. [4]) 4.6
Figure 4.8. Fourier coefficients for running (adapted from Bachmann et al. [4]) 4.10
Figure 4.9. Dynamic analysis 4.11
Figure 4.10. Dynamic analysis organization chart (adapted from Hivoss [2]) 4.12

List of Tables

Table 2.1. Correlation among step frequency, speed and length 2.4
Table 2.2. Vertical DLF for a pedestrian walk 2.7
Table 2.3. Parameters for walking load models 2.8
Table 2.4. Parameters for load models for running 2.10
Table 2.5. DLF for vandalism action 2.11
Table 2.6. Frequency range with risk of resonance 2.12
Table 2.7. Maximum accelerations recommended 2.12
Table 2.8. Comfort classes and maximum accelerations 2.13
Table 3.1. Glass transition temperature (Tg) and melting temperature (Tm) of polymers 3.13
Table 4.1. Correlation among step frequency, speed and length (Wheeler [10]). 4.4
Table 4.2. Vertical DLF for a pedestrian walk (adapted from Krus [16]) 4.7
Table 4.3. Parameters for walking load models (adapted from Hivoss [17]). 4.8
Table 4.4. Parameters for load models for running (adapted from Hivoss [17]). 4.10
Table 4.5. DLF for vandalism action (adapted from Agu et al. [15]). 4.11
Table 4.6. Frequency range with risk of resonance 4.12
Table 4.7. Maximum recommended accelerations (adapted from Alves [19]) 4.12
Table 4.8. Comfort classes and maximum accelerations (adapted from Hivoss [2]). 4.13

1. Introduction

1.1. Motivation

Reinforced concrete, steel and wood are the structural materials more traditionally used in the construction of footbridges, being often used in combination (Murphy [1]). However, the costs of maintaining these structures have led to the demand for more durable materials that enable longer construction-deconstruction cycles. In this context, according to Potyrała [2], until 2011, about 201 bridges were built around the world using fibre-reinforced polymer (FRP) composites and, of these, 80 were executed exclusively with this material. In the last decade, the number of FRP bridges has grown remarkably.

The construction of structures with progressively longer spans and the current aesthetic trends, advocating very slender and lightweight solutions, has resulted in an increased sensitivity of footbridges to dynamic actions, which may require the implementation of measures to mitigate vibrations and the fulfilment of human comfort criteria. In this respect, mention should be made to the Millenium Bridge in London, where excessive horizontal vibrations, induced by the passage of thousands of people during its inauguration (2000), have caused intolerable levels of vibration (Norberto [3]).

In the context of the fulfilment of human comfort criteria, some strategies have been implemented to mitigate vibrations in pedestrian bridges. One of the possible forms of action is the removal of structural frequencies from the typical frequencies of pedestrian actions, achieved by increasing the structure´s stiffness. However, the effectiveness of such a measure is limited, considering the consequent aesthetic cost and the inevitable increase in the associated mass (Caetano *et al.* [4]).

The increase in structural damping through the installation of vibration control systems is currently the most frequent and most effective measure for the mitigation of vibrations associated with pedestrian actions. This measure was used in the Pedro e Inês bridge, in Coimbra, where the possibility of *lock-in* was foreseen (Sanches [5]), consisting of the installation of a set of tuned mass damping absorbers. These devices are particularly suited to structures subjected to periodic actions and with a dynamic response dominated by the contribution of a particular vibration mode (Moutinho *et al.* [6]).

In the meantime, and by analogy with applications in the field of aeronautical engineering, the question arises of achieving adequate levels of damping for footbridges through the material that constitutes their structure. In this context, the use of FRP composites which, besides their lightness and durability, have a viscoelastic behaviour capable of giving them high levels of damping, is potentially attractive (Ferry [7]).

In this sense, Treviso *et al.* [8] state that polymer-based materials have much higher damping levels than traditional engineering materials. For example, it is possible to mention steel, which has a damping factor in the order of 0.1% to 0.8%, while polyethene LD-400 has a damping factor of up to 10% (Masotti [9]), *i.e.*, 100 times higher.

The ability to simultaneously store and dissipate energy when subjected to mechanical stress makes polymers and polymeric composites unique materials when it is necessary to balance dynamic responses with comfort criteria in pedestrian structures.

The use of these materials in civil engineering structures, although infrequent, is not new. The Aberfeldy footbridge in the United Kingdom is perhaps the first well-documented application of FRP composites in footbridges. However, most of the bridges already built were designed to serve as a proof of concept in terms of ensuring strength and deformability, or sustainability, and most of them were also based on typical shapes of steel structures (Burgoyne [10]). Therefore, there is a challenge

to explicitly use composite materials in civil engineering structures, namely in footbridges, to mitigate vibrations.

1.2. Research Objectives and Methodology

Based on already sedimented concepts of dynamics of footbridges and mechanics of polymer-based composite materials, the main objective of this PhD thesis was to study the dynamic behaviour of polymer-based composite materials and to assess the technical feasibility and advantages of using their viscoelastic damping in the design of footbridges, particularly regarding their capacity to mitigate vibrations.

To achieve the general objective stated above, this research was developed in 2 main stages:

1. The viscoelastic investigation

This stage comprised a study of the viscoelasticity of polymeric and polymer-based composite materials, namely of their creep and relaxation functions and their relationship with the dynamic storage and loss modulus; in fact, the investigation of the creep response engineering materials should integrate the design of structures and their behaviour for a long time of operation;

2. The damping investigation

This stage included an investigation of the dynamic behaviour of free-free supported beams, to assess their natural frequencies and to compare their damping capacity and obtain parameters that indicate a basis for a viable comparison between structures made of steel and pultruded glass-FRP (GFRP). The modal characterisation of a full-scale GFRP-SFRSCC (steel fibre reinforced self-compacting concrete) hybrid footbridge enabled the transition to full-scale analysis. This was accompanied by the analysis of structure response to dynamic loads and assessment of the corresponding capacity to dissipate energy, which was subsequently compared to the performance of models designed with conventional materials, namely, steel.

Considering the first part of this thesis objective above outlined, an analytical evaluation and refinement of concepts of time-dependent mechanical behaviour of polymers was carried out, whose main result was the development of methods for the analytical adjustment of polymer behaviour under static and quasi-static actions. In this scenario, a new model of interconversion between creep and relaxation was proposed, which presented excellent accuracy in adjusting experimental data. Following the same mathematical methodology, a new method has been proposed for the desirable interconnection between polymeric and polymer-composite materials' quasi-static and dynamic behaviour. The approximate interconversion scheme was derived to obtain the complex moduli to convert the measured creep compliance to relaxation modulus.

Regarding the second outlined objective, the following studies were developed:

(i) applied set laboratory experiments were conducted on samples of GFRP and steel plates to compare their intrinsic damping. The tests were conducted under free boundary conditions to reduce possible localised damping at the supports.

(ii) A modal characterisation of the São Silvestre footbridge, a GFRP footbridge with a free-span of 10 m located in Ovar, Portugal, was carried out, enabling to experimentally extract its natural frequencies, damping ratio and vibration modes. Additional tests performed under the crossing by pedestrians enabled the characterisation of the response, which was used to calibrate a numerical model.

(iii) A numerical study of the GFRP-based and an equivalent steel-based footbridge solution was carried out using finite element models to evaluate their performance under dynamic loads and to allow a comparison between both solutions.

1.3. Thesis Structure

This PhD thesis is presented as a collection of papers published and submitted to peer-review international journals, preceded by five introductory chapters with the following content:

I. Chapter 1: provides the context of the thesis, describes the general objectives and overall methodology and presents the document's structure.
II. Chapter 2: deals with aspects of polymer rheology, the basis for the understanding of viscoelasticity and, consequently, the damping that these materials provide. It focuses on the description of linear and non-linear viscoelastic models. The relations of creep, relaxation and hysteresis are presented to highlight the behaviour of polymeric materials.
III. Chapter 3: describes the behaviour of composites in the face of thermal and dynamic disturbances and discusses how these materials can introduce damping to the structure through the complex modulus concept.
IV. Chapter 4: describes the dynamic behaviour of footbridges by characterising the actions that give rise to such behaviour, their particularities and the aspects that involve the characterisation of the users' comfort.
V. Chapter 5: presents a summary of the papers that constitute this doctoral thesis.
VI. Chapter 6: presents the conclusions and the topics that are worth being mentioned and investigated in future studies.
VII. Chapter 7: presents the publications that resulted from the conducted research.

1.4. References

[1] N. Murphy, "Feasibility analysis of a fibre reinforced polymer bridge," Master Thesis, KTH Royal Institute of Technology, 2013.

[2] P. B. Potyrała, "Use of Fibre Reinforced Polymer Composites in Bridge Construction. State of the Art in Hybrid and All-Composite Structures," Master Thesis - Universitat Politécnica de Catalunya, 2011.

[3] J. P. C. Norberto, "Caracterização do comportamento dinâmico do passadiço pedonal do Campus da FCT - UNL," Master Thesis, Universidade Nova de Lisboa, 2014.

[4] E. de S. Caetano and Á. A. M. F. Cunha, "Implementation of a passive control system in a lively footbridge," in *IABSE Report*, 2013, no. MAY 2013, doi: 10.2749/222137813806479025.

[5] J. P. F. Sanches, "Controlo de Vibrações em Pontes Pedonais Sujeitas a Acções de Multidões," Master Thesis, Universidade Nova de Lisboa, 2012.

[6] C. Moutinho, Á. Cunha, and E. Caetano, "Análise experimental da eficiência de TMDs para a atenuação da resposta sísmica de estruturas de edifícios," *6º Congr. Nac. Sismol. e Eng. Sísmica*, pp. 621–630, 2004.

[7] J. D. Ferry, *Viscoelastic Properties of Polymers*, Third Edit., vol. 63. Wiconsin: John Wiley & Sons, Inc., 1980.

[8] A. Treviso, B. Van Genechten, D. Mundo, and M. Tournour, "Damping in composite materials: Properties and models," *Compos. Part B Eng.*, vol. 78, pp. 144–152, 2015, doi: 10.1016/j.compositesb.2015.03.081.

[9] D. Masotti, "Comparação de métodos de determinação de amortecimento estrutural através de técnicas de ajuste de curvas de funções resposta emfFrequência," Master Thesis, Universidade Federal de Santa Catarina, 2013.

[10] C. J. Burgoyne, "Advanced composites in civil engineering in europe," *Struct. Eng. Int. J. Int. Assoc. Bridg. Struct. Eng.*, vol. 9, no. 4, pp. 267–273, 1999, doi: 10.2749/101686699780481682.

2. Rheology of Polymers and Viscoelasticity

2.1 Justification

This chapter describes the rheological aspects of polymers as an introduction and foundation for the presentation of the viscoelastic theory of polymeric and polymer-based materials. Due to their molecular peculiarities, polymers show mechanical behaviour that ranges from that shown by essentially elastic materials and that presented by viscous materials. Such behaviour, called viscoelastic, is the basis for studying how polymers attenuate vibrations in structures, particularly those where dynamic factors are preponderant, such as footbridges.

2.2 Introduction

Viscoelastic polymers are materials whose behaviour results from the combination of a reversible shear and elastic deformation, caused by the angular deformation of the molecules, and which also depends on time to recover from such deformation. Such materials do not have a proportional character or a constant proportionality between deformation and stress, like the modulus of elasticity. The mechanical responses of polymers to stresses are sensitive and extremely dependent on structural and external factors, such as load, temperature, humidity and time [1]. These materials are characterized by presenting an intermediate behaviour between elastic solids and viscous fluids, having direct dependence on the temperature and the time scale of action.

This capacity to store and dissipate energy simultaneously, inserts, in the scope of structural analysis, a variable whose relevance needs to be measured. In structural applications, it is necessary to consider the time-dependent behaviour and its implication in the mechanical response of the material.

The temporal dependence on mechanical properties is the result of the combination of effects of elastic and liquid-solid materials, which define the viscoelastic behaviour. In this context, the mechanical properties of polymeric materials, when obtained from conventional tensile, compression or shear tests, and presented in the form of stress-strain graphs, express the behaviour of the material for a short period of time and are not suitable for estimating this long-term behaviour (Pagliosa [2]).

2.3 Principles of Viscoelasticity

As mentioned, the response of a viscoelastic material results from the combination of the mechanical behaviour of elastic and viscous materials. Fundamentally, the elastic portion is responsible for energy storage, whereas the viscous portion is responsible for energy dissipation.

Viscoelastic behaviour can manifest itself in several ways, which can include [1]:

a. Creep under constant loading;
b. Stress relaxation under constant deformation;
c. Time-dependent deformation recovery after complete load removal;
d. Time-dependent creep rupture; and
e. Fatigue resistance depending on the excitation frequency.

Figure 2.1 illustrates the typical stress-strain relationship of a viscoelastic material, in which, when unloading, the response of the material returns differently from when loading and, after a certain time, the original configuration is restored. For a better understanding of viscoelasticity and its dependence on time, Figure 2.2 illustrates a polymeric plate, simply-supported and supporting a given mass.

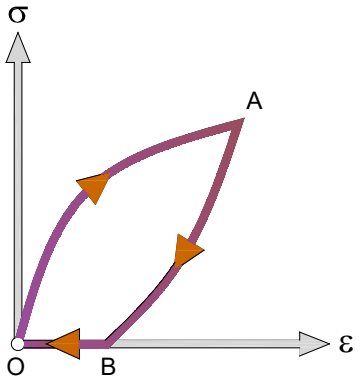


Figure 2.1. Stress-strain graph of viscoelastic material (adapted from Barra [3])

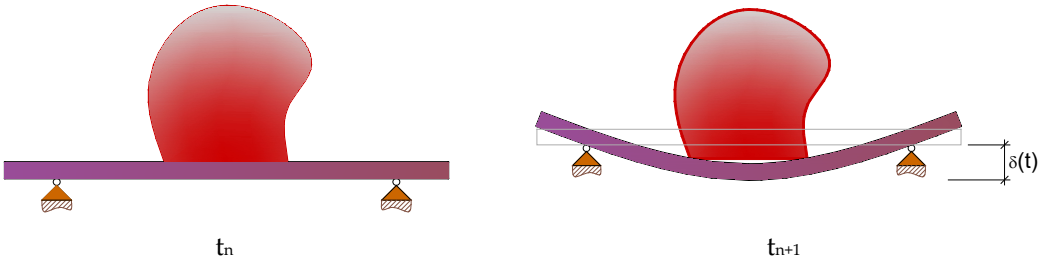


Figure 2.2. Illustrative scheme (adapted from Barra [3])

Keeping the temperature constant, the surface will tend to deform over time due to the action of the mass weight. Removing the load, the surface will not return immediately to its initial (undeformed) position. Partial or total recovery will depend on time.

According to Barra [3], at the molecular level, this process can be described as follows:

> *"... the polymeric mass can be seen in its undeformed state, as having curled or tangled chains (Randon Coil). When this entangled structure is subjected to constant tension, the molecules exert a retractive response to this tension to maintain their more stable (folded) shape. Under the continuous influence of the tension applied over time, the chains slide about each other. Therefore, the entangled structure is deformed, passing to an elongated conformation ... "*

With the removal of the applied stress, the molecules tend to return to their stable state, *i.e.*, the folded conformation and, thus, the material tends to return to its original shape.

A simple problem of viscoelasticity can be represented by an expression that relates the dependence of mechanical behaviour with time plus the combination of an elastic solid and viscous fluid, in which, the stress $\boldsymbol{\sigma}$ is a generic function of strain and time, $\boldsymbol{F}$, as follow

Elastic Solid		**Viscous Fluid**		**Viscoelastic Solid**
$\boldsymbol{\sigma = E\varepsilon}$	+	$\boldsymbol{\sigma = \eta \frac{\partial \varepsilon}{\partial t}}$	=	$\boldsymbol{\sigma = F(\dot{\varepsilon}, t)}$

Mathematically, viscosity, as shown above, describes the behaviour of ideal viscous fluids, where the stress is proportional to the strain rate and the proportionality constant is the fluid viscosity. Expression (2.1) illustrates the shear stress dependence

$$\boldsymbol{\tau = \eta \frac{\partial v}{\partial \mu} = \eta \gamma} \tag{2.1}$$

where:

$\boldsymbol{\tau}$ is shear stress;

$\boldsymbol{v}$ is speed;
$\boldsymbol{\mu}$ is the direction of the speed gradient;
$\boldsymbol{\eta}$ is the viscosity of the fluid.

Expression (3.1**)** derives from the experiment carried out by Newton [3], where a fluid is sheared between two plates; one is static and the other is movable (Figure 2.3).

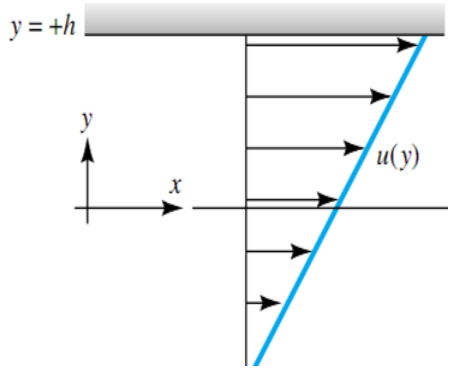


Figure 2.3. Shear in a viscous material

The proportionality described by Newton is restricted to a certain number of fluids because there are materials that, under shear-directed flow, present different behaviour from that predicted by Newton [3]. For those, the viscosity depends on the applied shear or, even, on the period of exposure. In this way, viscosity is no longer a constant, becoming a property that depends on the conditions under which the material is deformed.

Conceptually, fluids can be classified according to their flow behaviour, being split into Newtonian and non-Newtonian fluids.

Newtonian fluids

Newtonian fluids are those in which viscosity is affected by temperature and pressure, but does not change with an increasing rate of shear stress or with time. A fluid that shows Newtonian behaviour will be characterized by the constitutive expression (2.1) and, under normal and stable conditions of temperature and pressure, its viscosity is easily measurable [4], and is called **absolute viscosity**. All gases and most liquids that have the simple molecular conformation and low molecular weight are considered Newtonian, such as water, honey, glycerin and benzene.

Non-Newtonian Fluids

Non-Newtonian fluids are those in which the viscosity varies with the increase or decrease of the stress applied to it or of the history of deformation. Unlike Newtonian fluids, non-Newtonian fluids have a non-linear relationship between stress and shear rate, in addition to having elasticity or viscosity limits depending on the time and on deformation history, concomitantly or not. Non-Newtonian phenomena are divided into 3 (three) large families [3], namely:

i. Time-independent;
ii. Time-dependent; and
iii. Viscoelastic.

As previously described, polymers are materials whose properties depend on time and which, in addition to this dependence, present a behaviour different from other non-Newtonian fluids, simultaneously presenting behaviour of elastic solids and viscous fluids, which is why they are classified as viscoelastic.

Depending on the degree of deformation (magnitude and time) that the polymer undergoes, the study of viscoelasticity can be observed in linear and non-linear regimes.

In summary, the rheological behaviour of a polymeric material in the linear viscoelasticity regime corresponds to deformations and low shear rates, where the morphology of the polymeric material is not affected. The rheological response of polymeric material in the non-linear

viscoelasticity regime, on the other hand, corresponds to deformations and shear rates or extensions for which the morphology is modified (adapted from Martin [5]).

Although linear viscoelastic principles help describe long-term properties, they are inadequate in cases where applied stresses reach values where non-linear behaviour can be observed.

2.4 Linear Viscoelasticity

Linear viscoelasticity is a theory that describes the behaviour of materials by linear expressions, to whole or fractional derivatives. The most general theory of linear viscoelasticity was formulated by Boltzmann, in 1894, which is based on the principle of superposition of deformations:

> *"Creep is a function of the complete loading history; each loading step makes an independent contribution to total loading history; the final and total deformation is the sum of each contribution".*

The statement above is called the **Boltzmann Superposition Principle** and describes that the deformation at time t is determined by the superposition of responses to the complete set of stress increments at moments t', before t.

Such principle can also be formulated as follows [6]:

a. Creep in a sample is a function of the entire loading history;
b. Each load increase makes an independent and additive contribution to the total deformation.

This implies that, for each additional load increase, the material deforms as if a single load increase had been applied equally to the sum of the n increments up to that moment. It also admits that, once the load is removed, the recovery of the material will follow the same course of time and will be identical to the initial creep response.

Besides, the principle expresses that the contribution of each stress or deformation effect is independent, the final response resulting from the sum of all effects. The mathematical formulation of viscoelastic behaviour based on the Boltzmann principle is illustrated in Figure 2.4.

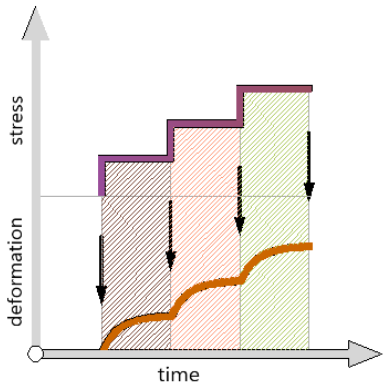


Figure 2.4. Creep of an ideal viscoelastic material (adapted from Nandini *et al.* [6])

In this way, the total deformation at the moment t can be given by a convolution integral and, for a uniaxial case, it can be defined by the following generalized expression

$$\sigma(t) = \int_{-\infty}^{t} J\,(t - \tau_n)\, d\varepsilon(\tau_n) \tag{2.2}$$

where J is the creep modulus of the polymer (Diacenco [8]), expressed by

$$J(t) = \frac{1}{\eta} t \tag{2.3}$$

In linear theory, the response of a viscoelastic material can be divided into two functions which, in turn, describe the behaviour of the material over time: creep and relaxation. Rheologically, both are manifestations of the same molecular mechanism. In particular, the relaxation response moves to its equilibrium value more quickly than the creep response.

Creep

As a result of their viscoelastic behaviour, polymeric materials show an increase in their deformation overtime under the action of a constant load and this occurs at any temperature. This effect is known as **creep** and occurs due to the molecular rearrangement in the polymer induced by the stress (Kühl [9]).

Unlike elastic materials, in viscoelastic materials, an initial immediate elastic deformation occurs, followed by a time-dependent deformation. There may also be a permanent viscous flow, especially under very high loads or when loads are applied for a long time [2].

According to Findley *et al.* [10], creep can be divided into three stages:

a. Stage I: a primary creep - the material undergoes rapid deformation, with a pronounced rate, until it reaches relatively constant values, reaching a certain balance;
b. Stage II: a secondary creep - at this stage, the deformation rate is constant;
c. Stage III: tertiary creep - the deformation rate increases exponentially here, leading to material failure.

Figure 2.5 illustrates creep behaviour in polymers under constant stress, including the three stages mentioned above.

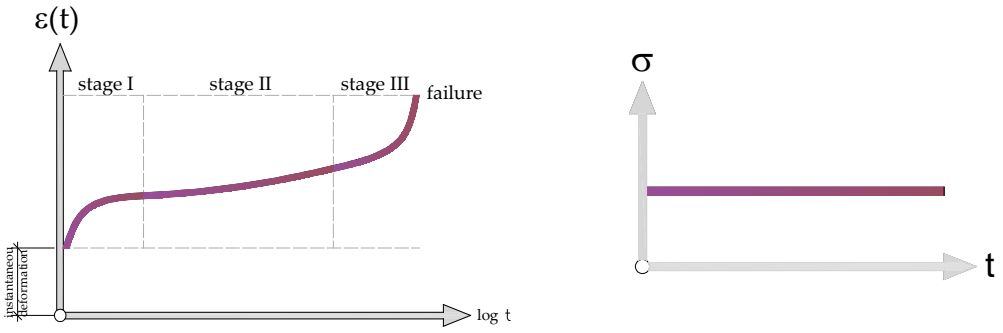


Figure 2.5. The three stages of creep.

However, if the applied stress is removed before the creep rupture, there is an immediate elastic recovery, equal to the initial elastic deformation, followed by a recovery period. Depending on the level of the applied excitation, the material may not recover to its original shape and a permanent deformation is installed. The magnitude of this permanent deformation will depend on the duration and magnitude of applied stress, in addition to the temperature [10].

Figure 2.6 illustrates the creep function with recovery due to the removal of the load, as the expression (2.3**)** can be rewritten as (2.4) for the creep case.

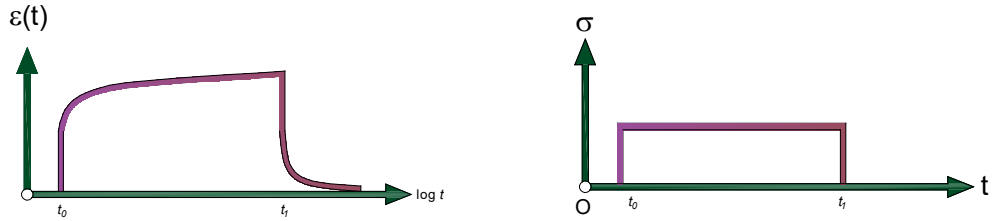


Figure 2.6. Creep and recovery with full recovery.

$$J(t) = \frac{\varepsilon(t)}{\sigma_0} \tag{2.4}$$

Relaxation

Similar to the creep process, as a result of the viscoelastic molecular mechanism of the polymer, these materials, when subjected to a constant deformation over time, present **stress relaxation** throughout deformation application. Under such conditions, the material exhibits an instant increase in stress, which gradually decreases over time, until it reaches a constant value, as illustrated in Figure 2.7.

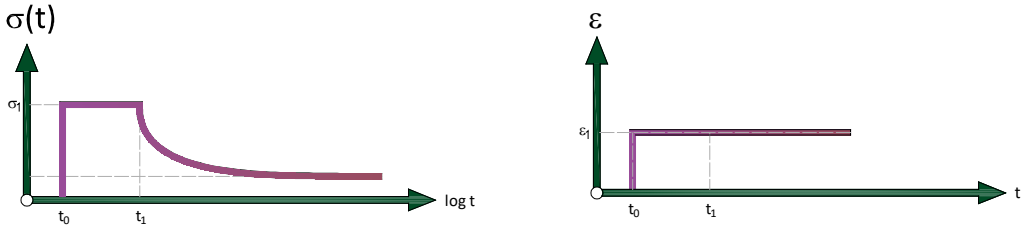


Figure 2.7. Creep Relaxation under Constant Deformation

The expression (2.5) describes the function of the Relaxation Modulus – ***G(t)*** as a function of time, under constant deformation.

$$\boldsymbol{G(t) = \frac{\sigma(t)}{\varepsilon_1}} \tag{2.5}$$

Hysteresis

The viscoelastic theory is based on the fact that this type of material, when subjected to harmonic stress cycles, will present harmonic deformation cycles, at the same frequency, but with phase delay with the stress. Within certain limits, the stress versus deformation graph will have the shape of an ellipse and will tend to maintain this shape as amplitudes increase, as depicted in Figure 2.8.

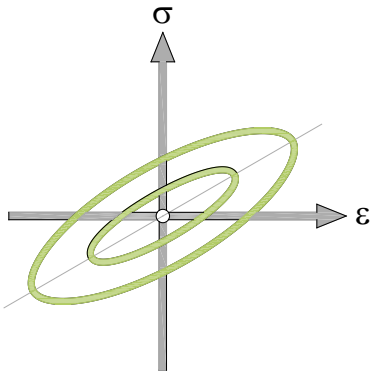


Figure 2.8. The ideal cycle of hysteresis.

The angle formed between the major axis of the hysteresis ellipse and the axis of the abscissa is proportional to the stiffness of the polymer and the ratio between the minor and major axes may indicate the material's damping capacity. The study of this hysteresis cycle is the basis for studying the behaviour of viscoelastic materials as a function of temperature, excitation frequency or deformation. The hysteresis cycle illustrated above can be characterized analytically by the expression (2.6), which describes the deformation of a hypothetical polymer in the time domain

$$\boldsymbol{\tau(t) = G\gamma(t) \pm G\eta\sqrt{\gamma_0^2 - \gamma(t)^2}} \tag{2.6}$$

where:

- $\boldsymbol{\tau(t)}$ shear stress in the time domain;
- $\boldsymbol{\gamma(t)}$ shear deformation at time **t**;

$\boldsymbol{\gamma_0}$ maximum shear deformation during the hysteresis cycle;
$\boldsymbol{G}$ proportionality constant (modulus of cutting elasticity);
$\boldsymbol{\eta}$ loss factor.

The expression (2.6) can be used to estimate the complex modulus of viscoelastic materials. If the stress varies harmonically, the deformation $\boldsymbol{\gamma(t)}$ will also do so and, therefore

$$\boldsymbol{\gamma(t) = \gamma_0 \cdot sin(\omega t)} \tag{2.7}$$

where:

$\boldsymbol{\omega}$ angular frequency, expressed in radians per second

By introducing (2.7) in (2.6) and proceeding with the appropriate algebraic sequences, it can be written that stress, in the time domain, will be

$$\boldsymbol{\tau(t) = G\gamma(t) + \frac{G\eta}{|\omega|} \cdot \frac{d\gamma(t)}{dt}} \tag{2.8}$$

Likewise, the following expression results, which relates axial deformations with axial stresses

$$\boldsymbol{\sigma(t) = E\varepsilon(t) + \frac{E\eta}{|\omega|} \cdot \frac{d\varepsilon(t)}{dt}} \tag{2.9}$$

2.5 Discrete Viscoelastic Models

The viscoelastic behaviour of a material can be represented by discrete mechanical models, which involve the sum (i) of the elastic behaviour of springs and (ii) of the viscous behaviour of shock absorbers or dampers.

The springs represent the reversible character of the deformation of ideal elastic solids, where the deformation response is instantaneous and there is no permanent or irrecoverable deformation and all the energy used to deform the spring is stored and fully reversible [3].

On the other hand, the dampers represent the irreversible character of the viscous deformation, in which the stress is proportional to the deformation rate and the energy is dissipated during the deformation process.

Through the expressions presented early, it is possible to illustrate the different behaviours of elastic solid and viscous fluid, as shown in Figure 2.9. The spring or damper elements are not sufficient to represent the viscoelastic behaviour of the materials in isolation. In this sense, more complex models have been proposed, combining the actions of springs and dampers in an appropriate way for each type of material [11]. In the following, some of the main models adopted in the study of the viscoelasticity of polymeric materials are presented.

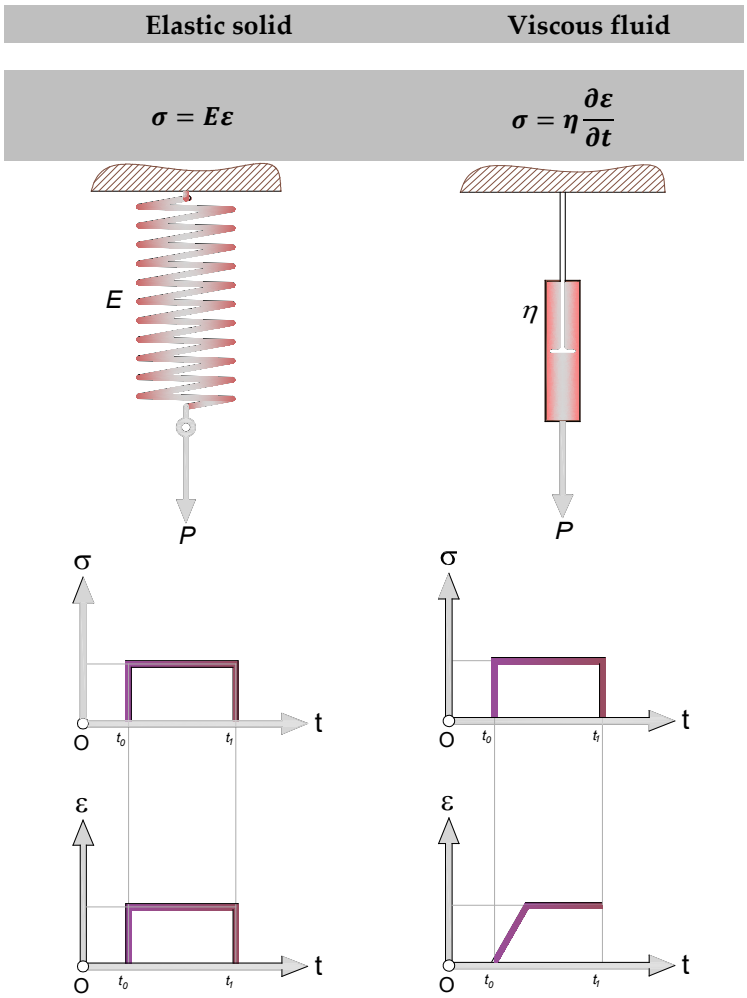


Figure 2.9. Representation of elastic spring and viscous damper

Maxwell Model

The model proposed by Maxwell (1831-1879) consists of a system where an elastic spring and a viscous damper, both linear, are combined in series. In this system, both elements experience the same stress, but different deformations. Figure 2.10 illustrates the model.

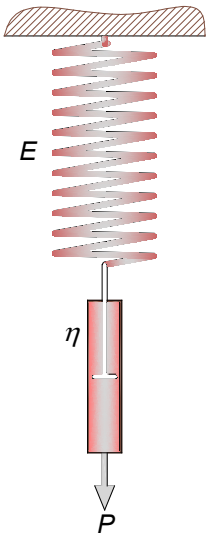


Figure 2.10. Maxwell's linear viscoelastic model.

The stress in each element of the Maxwell model can be given by the expressions of viscosity early defined and being the elements connected in series, the total deformation will be the sum of the deformations of each element, as follows

$$\boldsymbol{\varepsilon_t = \varepsilon_m + \varepsilon_a} \tag{2.10}$$

where:

$\boldsymbol{\varepsilon_t}$ is the total deformation of the system;
$\boldsymbol{\varepsilon_m}$ is the deformation of the spring element;
$\boldsymbol{\varepsilon_a}$ is the deformation of the damping element.

To obtain the variation rate of the system deformation, the expression (2.10) is derived in relation to time $\boldsymbol{t}$, and the following differential expression of deformation of the Maxwell model is obtained

$$\boldsymbol{\dot{\varepsilon}_t(t) = \dot{\varepsilon}_m(t) + \dot{\varepsilon}_a(t)} \tag{2.11}$$

where:

$\boldsymbol{\dot{\varepsilon}_t}$ is the total deformation rate of the system;
$\boldsymbol{\dot{\varepsilon}_m}$ is the deformation rate of the spring element;
$\boldsymbol{\dot{\varepsilon}_a}$ is the deformation rate of the damping element.

Expression (2.11) can be rewritten according to the stresses observed in the system [12], yielding

$$\boldsymbol{\dot{\varepsilon}_t(t) = \frac{\dot{\sigma}(t)}{E} + \frac{\sigma(t)}{\eta}} \tag{2.12}$$

Voigt-Kelvin Model

In the Voigt-Kelvin model, the spring and damper elements are arranged in parallel and both are subject to the same deformation, but under different stresses, as illustrated in Figure 2.11.

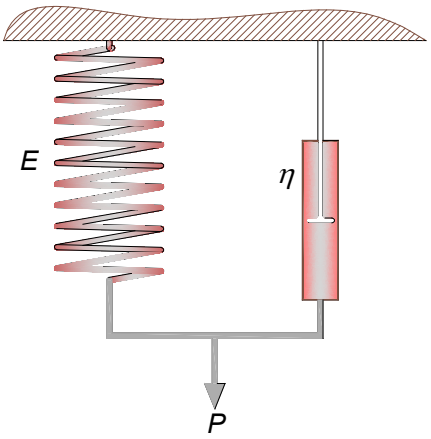


Figure 2.11. Voigt-Kelvin Linear Viscoelasticity Model.

According to this model, the equilibrium expression is given by

$$\boldsymbol{\sigma(t) = \sigma_m(t) + \sigma_a(t)} \tag{2.13}$$

where:

$\boldsymbol{\sigma_m}$ is the stress in the spring element;
$\boldsymbol{\sigma_a}$ is the stress in the damping element.

The compatibility of deformation is expressed as

$$\boldsymbol{\varepsilon_t(t) = \varepsilon_m(t) = \varepsilon_a(t)} \tag{2.14}$$

From (2.13) and (2.14), the constitutive expressions of the system are

$$\boldsymbol{\sigma_m(t) = E \cdot \varepsilon_m(t)} \tag{2.15}$$

$$\boldsymbol{\sigma_a(t) = \eta \cdot \dot{\varepsilon}_a(t)} \tag{2.16}$$

And the differential expression of the Voigt-Kelvin model is given by

$$\boldsymbol{\dot{\varepsilon}_a(t) + \frac{E}{\eta} \cdot \varepsilon(t) = \frac{\sigma(t)}{\eta}} \tag{2.17}$$

Complex Models

The models presented so far may still be too simplified to represent the behaviour of real materials. To create a reasonably complex model, in terms of the ability to describe the actual material behaviour, one can launch innumerable combinations, both in terms of several components, and in types of connections [13].

However, when models with numerous combined elements are represented, although the precision is increased, the mathematical complexity becomes problematic. Thus, the use of a finite but substantial number of elements, typically between 4 (four) and 10 (ten), leads to good results, as cited by Jones [14].

Despite presenting multiple relaxation times, most real materials can be represented by generalized models based on Maxwell or Voigt-Kelvin parameters. In this sense, the generalized Maxwell model shows a system formed by $\boldsymbol{n}$ Maxwell elements connected in parallel, as shown in (2.12).

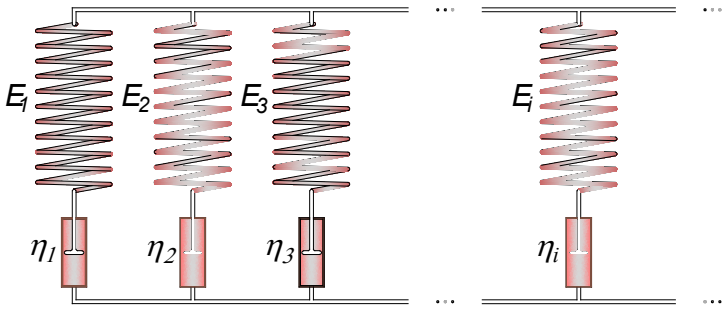


Figure 2.12. Maxwell's generalized model.

The differential expression that governs the system is given by the following expression

$$\boldsymbol{\dot{\varepsilon} = \dot{\sigma} \sum_{i=1}^{n} \frac{1}{E_i} + \sigma \sum_{i=1}^{n} \frac{1}{\eta_i}} \tag{2.18}$$

In the same way, the generalized Kelvin model consists of $\boldsymbol{n}$ Kelvin elements connected in series. Figure 2.13 shows the model and the differential expression that governs the system is given by expression (2.19).

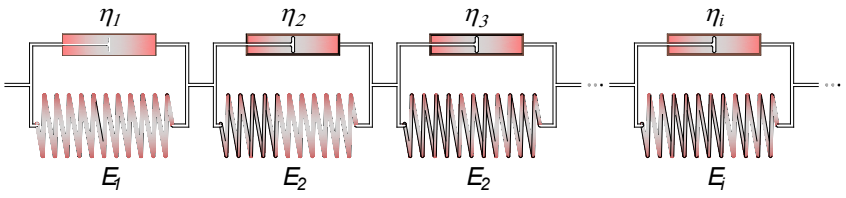


Figure 2.13. Generalized Kelvin model.

$$\dot{\varepsilon} = \dot{\sigma} \sum_{i=1}^{n} \frac{1}{E_i} + \sigma \sum_{i=1}^{n} \frac{1}{\eta_i} \tag{2.19}$$

2.6 Representation of the Creep Compliance

For the viscoelasticity models described by springs and dampers, the creep curve given by the expression (3.2), for the time $t = 0$, has a finite derivative [13]. However, polymeric materials show rapid deformation variations early in the application of stress, which suggests some inaccuracy, as already mentioned, for models with few elements.

To avoid models composed of numerous elements, but still maintaining a certain level of precision, some empirical approaches are presented.

Findley's Power Law

Considering that the creep curves for many polymers are similar to those of some metals, some authors have proposed several empirical mathematical models to represent the creep data. A widely used model for the study of creep is that of Findley, whose expression describes the creep behaviour of many polymers with good precision and over a wide time scale. To obtain it, it is assumed that [15]

$$\varepsilon_c = m \cdot \left(\frac{t}{t_0}\right)^{n_f} \tag{2.20}$$

where:

- ε_c is the time-dependent deformation component at time **t**;
- m is a non-dimensional parameter of the material;
- n_f is a material parameter independent of the deformation;
- t is the elapsed time in hours;
- t_0 1 (one) hour.

With few exceptions, it is possible to measure the creep of viscoelastic materials by the constitutive expression

$$\varepsilon_t = \varepsilon_0 + \varepsilon_c \tag{2.21}$$

where:

- ε_t is the total deformation at time **t**;
- ε_0 is the instantaneous deformation;
- ε_c is the deformation dependent on time **t** (creep).

With expression (2.21), the expression (2.20) is rewritten, which is the expression proposed by Findley [10]

$$\varepsilon_t = \varepsilon_0 + m \cdot t^{n_f} \tag{2.22}$$

The expression (2.22) has been used to describe the creep behaviour of polymeric composites, as described in Yang *et al*. [16], Garrido *et al*. [17] and Sá *et al*. [18].

2.7 Final Considerations

Polymers are materials characterized by their dynamic behaviour where there is a phase delay between the application of a disturbance (tension or deformation) and its response. This characteristic, called viscoelasticity, implies that under constant stress or deformation over time, the material will undergo, internally, molecular interactions, which will lead to its continuous, but limited, physical accommodation, through creep or relaxation.

In this chapter, a hysteresis cycle was also presented which, in viscoelasticity, illustrates how a polymer responds to excitations. In general, this cycle has been mathematically defined. Linear viscoelastic concepts have also been described, with the characterization of some discrete models, and the main theories describing both concepts have been presented.

2.8 References

[1] L. C. Farina, "Caracterização viscoelástica por meio de ensaios de fluência e ruptura por fluência de compósitos poliméricos de matriz de resina epoxídica e fibra de carbono," Master Thesis, Instituto de Pesquisas Energéticas e Nucleares, 2009.

[2] C. Pagliosa, "Determinação experimental de propriedades viscoelásticas de material polimérico," Master Thesis, Universidade Federal de Santa Catarina, 2004.

[3] G. Barra, "Fundamentos de reologia de materiais poliméricos." Folhas de Apoio, Universidade Federal de Santa Catarina, 2010.

[4] H. H. M. E. Ferreira, "Escoamento de fluidos newtonianos e viscoelásticos em torno de um cilindro: estudo numérico de efeitos tridimensionais," Master Thesis, Faculdade de Engenharia da Universidade do Porto, 2006.

[5] G. P. Martin, "Estudo da Viscoelasticidade Linear e Não Linear de PP-PA-6 Compatibilizadas ou Não," PhD Thesis, Universidade de São Paulo, 2006.

[6] V. V. Nandini, K. V. Venkatesh, and K. C. Nair, "Basic elasticity and viscoelasticity," Princeton University Press, 2008. doi: 10.4103/0972-0707.43416.

[7] A. J. A. Gomez, "Comportamento viscoelástico de enrijecedores à flexão," Master Thesis, Universidade Federal do Rio de Janeiro, 2009.

[8] A. A. Diacenco, "Modelagem por elementos finitos de materiais compósitos estruturais incorporando material viscoelástico para o controle passivo de vibração e ruído," Master Thesis, Universidade Federal de Itajubá, 2010.

[9] A. Kühl, "Uma formulação viscoelastoplástica não linear aplicada ao polietileno de alta densidade (pead)," Master Thesis, Universidade do Estado de Santa Catarina, 2014.

[10] W. N. Findley, J. S. Lai, and K. Onaram, *Creep and Relaxation of Nonlinear Viscoelastic Materials - With an Introduction to Linear Viscoelasticity*. New York: Dover Publications Inc., 1976.

[11] F. Costi, "Metodologia numérica aplicada a viscoelasticidade em polímeros," Master Thesis, Pontífica Universidade Católica do Paraná, 2006.

[12] I. Romero, "Modelos Constitutivos - Viscoelasticidade Linear." Folhas de Apoio, Universidade Federal de Alagoas, p. 5, 2005.

[13] R. J. M. Guedes, "Previsão da Vida Útil de Materiais Compósitos de Matriz Polimérica," PhD Thesis, Faculdade de Engenharia da Universidade do Porto, Porto, 1997.

[14] D. I. G. Jones, *Handbook of Viscoelastic Vibration Damping*. Arizona, USA: Wiley & Sons Ltd., 2001.

[15] J. S. Horvath, "Mathematical modeling of the stress-strain-time behavior of geosynthetics using the findley equation: general theory and application to eps-block geofoam," New York, 1998.

[16] J. L. Yang, Z. Zhang, A. K. Schlarb, and K. Friedrich, "On the characterization of tensile creep resistance of polyamide 66 nanocomposites. Part II: Modeling and prediction of long-term performance," *Polymer (Guildf).*, vol. 47, no. 19, pp. 6745–6758, 2006, doi: 10.1016/j.polymer.2006.07.060.

[17] M. Garrido, J. R. Correia, P. Barbosa, S. Cabral-fonseca, and F. Branco, "Fluência em corte de núcleos em espuma de poliuretano utilizados em painéis sanduíche compósitos: efeito da temperatura," 2014.

[18] M. F. Sá, A. M. Gomes, J. R. Correia, and N. P. Silvestre, "Comportamento à fluência em flexão de elementos pultrudidos de gfrp – parte II - estudo analítico," in *Encontro Nacional de Materiais e Estruturas Compósitas*, 2010, p. 8.

3. Dynamic Behaviour of Polymer-Based Materials: The Viscoelastic Damping

3.1. Justification

This chapter aims at describing the dynamic-mechanical behaviour of polymers and, then, at conceptualizing the particularities of viscoelastic damping, which is characteristic of these materials. Within this scope, it is worth referring that polymers and polymer-based composites present peculiar aspects under the combined effect of temperature and frequency.

From the study of the dynamic behaviour of polymers, there is a need for a detailed understanding of how these materials attenuate dynamic disturbances in slender structures. It is necessary, at first, to describe the damping mechanisms to direct the work towards the type of damping inherent to the structure, *i.e.*, that is due exclusively to the material that composes it, and particularly the viscoelastic damping.

In this context, the concepts herein presented will serve as a basis for the study of polymer-based composites that may provide the attenuation of vibrations in the structure of footbridges.

3.2. Introduction

Polymers, in general, show viscoelastic behaviour, which is associated with the ability of these materials to simultaneously store and dissipate energy under mechanical stress. Thus, the coupled system (elasticity and viscosity) tends to have its damping rate increased, providing a reduction in vibrations [1]. Souza *et al.* [1] refer that when these materials deform, part of the dissipated energy will not result in deformation, since this fraction is spent to overcome the internal friction of the material. The effects of energy dissipation are generated, mainly, due to the inhomogeneity of the material.

The behaviour of the polymer, as described, is influenced by the way its long molecular chains respond to actions and, due to the interaction between them, such behaviour will depend on the applied stress levels, the amplitude of the deformations, the material temperature and the frequency at which the disturbances are caused [2].

In this context, understanding the response of polymeric composites to dynamic excitations, natural or not, relies on understanding the cycles through which deformations and recoveries occur, in addition to the physical factors that interfere in these cycles.

As will be shown ahead, one of the relevant mechanical characteristics of a polymer is the existence of a complex modulus composed by the simultaneous action of two dynamic components: one in-phase and the other out of phase with excitation, which can be translated into its damping capacity through the dissipation of energy.

The damping capacity or even the dynamic behaviour of the composite will depend, additionally, on the micromechanical characteristics of its conformation, such as the amount and direction of the reinforcements. At the constituent level, energy dissipation in fibre-reinforced composites is induced by different processes, such as the viscoelastic behaviour of the matrix, the damping at the fibre-matrix interface, the damping due to damage, among other aspects [3].

In summary, the dynamic characterization of polymeric composites must necessarily take into account the dependence of these materials on the stress, strain, temperature and frequency amplitudes, simultaneously or not.

3.3. Hysteresis Cycle

As described earlier in this work, the viscoelastic theory is based on the fact that the polymeric material, when subjected to harmonic stress cycles, shows harmonic deformation cycles, at the same frequency, but with a phase delay about the corresponding stress cycles. Within certain limits, the stress versus strain graph will have the shape of an ellipse and this format tends to be maintained as the stress and strain amplitudes increase, as shown in Figure 2.8, in Chapter 2, page 2.6.

The study of this hysteresis cycle will be the initial basis for studying the behaviour of a viscoelastic material as a function of temperature, excitation frequency or deformation.

The cycle illustrated in Figure 2.8 can be characterized analytically if it is assumed that the response to a harmonic excitation will be harmonically similar.

Consider a mechanical deformation of the type of

$$\boldsymbol{\varepsilon(t) = \varepsilon_0 \cdot sin(\omega t)} \tag{3.1}$$

where:

$\boldsymbol{\varepsilon(t)}$	is the deformation applied in the time domain;
$\boldsymbol{\varepsilon_0}$	is the amplitude of deformation during the hysteresis cycle;
$\boldsymbol{\omega}$	is the angular frequency, expressed in radians per second.

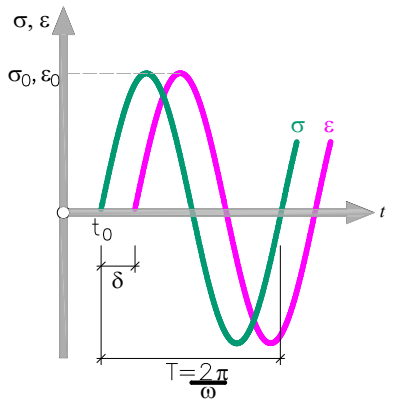
In response, the stress $\boldsymbol{\sigma(t)}$ will be harmonic, but with a phase delay $\boldsymbol{\delta}$; in this way, we have

$$\boldsymbol{\sigma(t) = \sigma_0 \cdot sin(\omega t + \delta)} \tag{3.2}$$

where:

$\boldsymbol{\sigma_0}$	is the stress amplitude during the hysteresis cycle;
$\boldsymbol{\omega}$	is the angular frequency, expressed in radians per second;
$\boldsymbol{\delta}$	is the lag angle between excitation and response.

Figure 3.1 illustrates the excitation and response given by the expressions (3.1) and (3.2).



Purely elastic response $\boldsymbol{\delta = 90°}$

Purely viscous response $\boldsymbol{\delta = 0°}$

Viscoelastic response $\boldsymbol{0° < \delta < 90°}$

Figure 3.1. Oscillatory stress and strain and phase delay (adapted from Findley *et al.* [4]).

The expression (3.2) can be rewritten as follows

$$\boldsymbol{\sigma(t) = \sigma_0 \cdot sin(\omega t) cos\delta + \sigma_0 \cdot sin(\delta) cos(\omega t)} \tag{3.3}$$

The deformation rate can be obtained by deriving (3.1) as a function of time

$$\boldsymbol{\frac{d\varepsilon(t)}{dt} = \dot{\varepsilon} = \varepsilon_0 \cdot \omega \cdot cos(\omega t)} \tag{3.4}$$

Through appropriate algebraic operations, equation (3.3) can be rewritten and take the following form

$$\boldsymbol{\sigma(t) = \frac{\sigma_0}{\varepsilon_0} \cdot cos(\delta) \cdot \varepsilon(t) + \frac{\sigma_0}{\varepsilon_0} \cdot \frac{1}{\omega} \cdot \dot{\varepsilon} \cdot sin(\delta)} \tag{3.5}$$

The second term of (3.5) involves the deformation flow over time and represents the damping or dissipation energy characteristic of the material under harmonic excitation. It is important to note that the expression (3.5) differs from the corresponding viscous damping equation in that the deformation flow, $\dot{\varepsilon} = d\varepsilon/dt$, is not constant, like in the case of viscosity, but **inversely proportional to the excitation frequency** [5].

3.4. The Complex Modulus

Equation (3.5) describes the hysteresis cycle in the time domain and can be used to determine the viscoelastic properties of polymers. The viscous behaviour of polymers is evident under dynamic load where the viscous damping property reduces the range of free vibrations [6].

One can generalize the harmonic response; thus, for a disturbance arising from an oscillatory deformation of the type

$$\boldsymbol{\varepsilon(t) = \varepsilon_0 \cdot cos(\omega t)} \tag{3.6}$$

the response of the system can be defined as follows

$$\boldsymbol{\sigma(t) = \sigma_0 \cdot cos(\omega t + \delta)} \tag{3.7}$$

Through Euler's relations, $\boldsymbol{e^{i\omega t} = cos(\omega t) + i \cdot sen(\omega t)}$, and from the relationship

$$\boldsymbol{\sigma(t) = \sigma_0 \cdot e^{i(wt+\delta)}} \tag{3.8}$$

the equation (3.7) assumes the following form

$$\boldsymbol{\sigma(t) = \sigma_0 \cdot cos(\omega t + \delta) + i \cdot \sigma_0 \cdot sin(\omega t + \delta)} \tag{3.9}$$

in which (3.7) is the real part of (3.9), and it is possible to express the complex part of the system expressed in (3.9) when carrying out certain algebraic operations, namely

$$\boldsymbol{\sigma(t) = \sigma_0 \cdot e^{i(\omega t+\delta)} = (\sigma_0 \cdot e^{i\delta}) \cdot e^{i\omega t}} \tag{3.10}$$

The first term of the right expression (3.10) is the **complex stress amplitude**, $\boldsymbol{\sigma^*}$

$$\boldsymbol{\sigma^* = \sigma_0 \cdot e^{i\delta} = \sigma_0 \cdot cos(\delta) + i \cdot \sigma_0 \cdot sin(\delta) = \sigma_0' + i \cdot \sigma_0''} \tag{3.11}$$

The terms $\boldsymbol{\sigma_0'}$ and $\boldsymbol{\sigma_0''}$ are the real and imaginary parts of $\boldsymbol{\sigma^*}$, respectively. The equality in (3.11) can be illustrated by Figure 3.2, in which $\boldsymbol{Im}$ and $\boldsymbol{Re}$ are the imaginary and real planes, respectively.

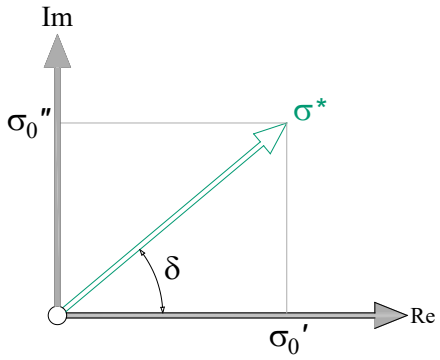


Figure 3.2. Phasor diagram of complex stress.

From the phasor diagram, the following relations may be collected.

$$\boldsymbol{\sigma_0}' = \boldsymbol{\sigma_0} \cdot \boldsymbol{cos(\delta)} \tag{3.12}$$

$$\boldsymbol{\sigma_0}'' = \boldsymbol{\sigma_0} \cdot \boldsymbol{sin(\delta)} \tag{3.13}$$

The response of the material is given by

$$\boldsymbol{\sigma(t)} = \boldsymbol{\sigma^*} \cdot \boldsymbol{e^{i\omega t}} \tag{3.14}$$

It is convenient to write the stress function (3.14) as a complex quantity, $\boldsymbol{\sigma^*(t)}$, whose real part is in phase with the deformation and the imaginary part is 90° out of phase; thereby

$$\boldsymbol{\sigma^*(t)} = \boldsymbol{\sigma_0}' \cdot \boldsymbol{cos(\omega t)} + \boldsymbol{i} \cdot \boldsymbol{\sigma_0}'' \cdot \boldsymbol{sin(\omega t)} \tag{3.15}$$

The existence of complex stress indicates that there will be, concomitantly with this, a **complex stiffness**, which will have real and imaginary components, reasonably called **dynamic moduli**, both being the ratio between the complex stress and the deformation, but with significant differences.

The **complex modulus**, $\boldsymbol{E^*}$, given by equation (3.16), will have a real part, called the **storage modulus**, $\boldsymbol{E' = Re(E^*)}$, which represents the (elastic) energy storage capacity during the material deformation process, being a reversible measure and corresponding to the elastic response, added to an imaginary part, called the **loss modulus**, $\boldsymbol{E'' = Im(E^*)}$, which represents the capacity of the viscoelastic material to dissipate energy, characterizing the viscous response.

$$\boldsymbol{E^*} = \frac{\boldsymbol{\sigma^*}}{\boldsymbol{\varepsilon_0}} = \frac{\boldsymbol{\sigma_0}}{\boldsymbol{\varepsilon_0}} \cdot \boldsymbol{e^{i\delta}} = \frac{\boldsymbol{\sigma_0}}{\boldsymbol{\varepsilon_0}} \cdot \boldsymbol{cos(\delta)} + \boldsymbol{i} \cdot \frac{\boldsymbol{\sigma_0}}{\boldsymbol{\varepsilon_0}} \cdot \boldsymbol{sin(\delta)} = \boldsymbol{E'} + \boldsymbol{i} \cdot \boldsymbol{E''} \tag{3.16}$$

Figure 3.4 illustrates the vector components of the complex modulus.

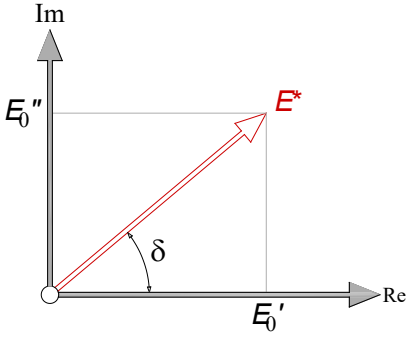


Figure 3.3. Phasor diagram of the complex modulus.

Intuitively, it is possible to verify the existence of a correlation between the loss modulus and the storage modulus:

$$\boldsymbol{tan(\delta)} = \boldsymbol{\eta} = \frac{\boldsymbol{E''}}{\boldsymbol{E'}} \tag{3.17}$$

The ratio presented in (3.17), known as **"*tan delta*"** or loss tangent, is related to the dynamic damping of the material, being, in some publications, called the **hysteretic damping factor**, $\boldsymbol{\eta}$, or also the **loss factor**.

Its definition allows us to evaluate the difference between elastic and viscous behaviour. Lorandi *et al.* [7] refer that the higher value of $\boldsymbol{tan\,\delta}$, the greater the difference between elastic and viscous behaviours, signalling a material in which the viscous response predominates over the elastic response.

The $\boldsymbol{tan\,\delta}$ is also used to determine the value of the glass transition temperature, $\boldsymbol{T_g}$, of the polymer, since, with the increase in temperature, that parameter shows a peak.

It should be noted that all types of internal damping, and particularly those inherent to the movement of polymer chains, are related to hysteresis cycles. In this sense, De Silva *et al.* [8] state that the term "hysterical damping" may be inappropriate. Certainly, any material or system that cyclically dissipates energy presents however small cycles of hysteresis when subjected to oscillatory disturbances. This means that inelasticity can manifest itself in different ways, which leads to the dissipation of energy [9].

As seen, in viscoelastic materials, the relationship between hysteresis and damping is fundamental for determining their capacity to dissipate energy.

3.5. Damping Mechanisms

Damping is how the mechanical energy of a dynamic system is dissipated, usually by converting kinetic energy into internal thermal energy, either by macro and microscopic internal conditions or by external conditions. Every form of energy dissipation in a structure introduces some damping in its vibration and, of course, the type of energy that mechanical energy is transformed in will depend on the system and the physical mechanism that causes such dissipation (Adhikari [10]).

Understanding the energy dissipation mechanisms in structures and materials is essential for the correct quantification of the effects of damping [11]. In this sense, De Silva *et al.* [8] mention that the knowledge of the magnitude of damping in a dynamic system is paramount for the analysis and use of the system. Particularly, where acceptance of the structure in service requires specific levels of comfort, knowledge of the damping system becomes essential in the analysis of the project.

In a dynamic system, there are some forms of energy dissipation and, for the same system, several types of damping may be present. De Silva *et al.* [8] highlight three primary damping mechanisms in a dynamic system:

a. Structural or external damping (in joints, interfaces and support devices);
b. Internal (or material) damping;
c. Fluidic damping (or the interaction between the structure and a viscous fluid).

It is important to note that fluidic damping characterizes a type of external energy dissipation and, when necessary, will be treated accordingly.

External Mechanisms of Damping

The external damping mechanisms are those inherent to the boundary conditions, *i.e.*, to the environment surrounding the system, and not to the material that composes it. It means that the energy dissipation will be given by the interaction of the structure with the environment, or between parts of the same structure, and the form of this interaction will define the intensity of the damping [11].

The damping due to friction from relative displacement or friction between the components of the system, called Coulomb friction or dry friction, is one of the most important type since it is present in all everyday situations and is relatively effective. The physical characteristics of the materials and the normal forces of interaction will determine the efficiency and intensity of this type of damping.

Other models of external damping can be mentioned: acoustic radiation, dissipation by pumping [12] and impact. Silva *et al.* [8] highlight that structural type damping is estimated through local measurements, which, however, can generate measurement errors since the values obtained represent the total damping of the mechanical system.

Kareem *et al*. [13] present four models of external damping applied to structures, as follows:

a. Passive damping
   It can be summed up as a device that dissipates energy through some kind of movement and does not need any external source of energy. It can also be divided into two types: direct and indirect energy dissipation. The former acts with traditional dissipation mechanisms, such as elastomers shearing and friction dampers; those with indirect dissipation act to alter the natural frequency of the structure, such as the tuned mass dampers (TMD) and impact dampers.
b. Active damping
   They need an external source of energy and act through hydraulic or electromagnetic systems that can adapt to changes in the environment or variations in loading.
c. Semi-active damping
   They combine the characteristics of the active and passive models and have the ability to adjust the active damping, in addition to not requiring great external energy for their operation.
d. Hybrid damping
   In hybrid damping systems, active dampers are combined with passive systems; the active system kicks in when the dynamic loads exceed the capacity of the passive system.

Internal Damping Mechanisms: Viscoelastic Damping

The internal or material damping is associated with several factors, such as microstructural defects, thermoelastic effects and, particularly in polymers, with internal mechanisms of intramolecular interaction of the material, translated into movements of the molecular chains.

Consider the hysteresis cycle of a generic viscoelastic polymer represented in Figure 3.4.

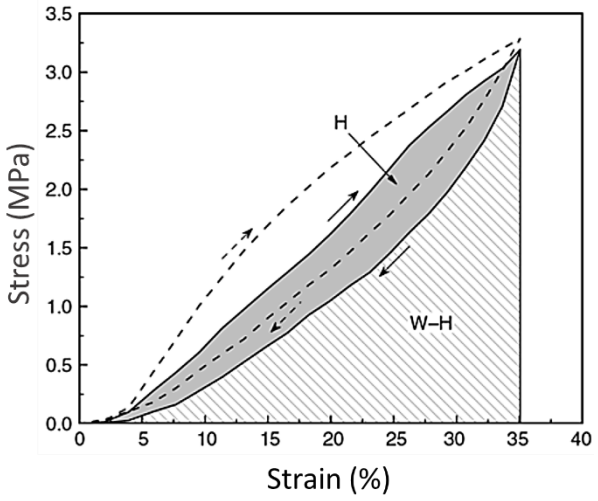


Figure 3.4. PVC-NBR/graphite hysteresis loop.

In the hysteresis cycle illustrated by Figure 3.4, the disturbance was generated by an oscillatory deformation of the type described in expression (3.6), which, by definition, will have a response of the type described in expression (3.7). The stress response can be written in terms of the complex modulus, and, therefore, written as a function of the deformation - expression (3.18).

$$\boldsymbol{\sigma(\omega, t) = E^{*}(\omega) \cdot \varepsilon(t)} \tag{3.18}$$

Decomposing expression (3.18) and properly rearranging its terms, yields

$$\boldsymbol{\sigma(\omega,t) = E'(\omega)\cdot\varepsilon(t) + \frac{E''(\omega)}{\omega}\cdot i\omega\varepsilon(t) = E'(\omega)\cdot\varepsilon(t) + \frac{E''(\omega)}{\omega}\cdot\dot{\varepsilon}(t)} \tag{3.19}$$

The solid hatched area within the hysteresis cycle (Figure 3.4, indication "H") represents the energy dissipated, per volume unit, during the deformation cycle [14]. Such energy can be described as being proportional to the loss modulus of the material through the relationships between work and energy. The work, given per unit of volume, performed on a material under stress is defined as

$$\boldsymbol{W = \int \sigma\, d\varepsilon = \int_0^t \sigma\,\dot{\varepsilon} dt} \tag{3.20}$$

For a single complete loading and unloading cycle, the energy stored in the elastic deformation and the dissipated energy, for a complete cycle (0 to $2\pi/\omega$), will be given as

$$\boldsymbol{U = \oint \sigma d\varepsilon = \frac{1}{2} E'\varepsilon_0{}^2} \tag{3.21}$$

$$\boldsymbol{H = \oint \sigma d\varepsilon = \int_0^{2\pi/\omega} \sigma\,\dot{\varepsilon} dt} \tag{3.22}$$

Thus, the energy dissipated in the cycle, $\boldsymbol{H}$, will be calculated by applying the term to the right of the expression (3.19) in expression (3.22)

$$\boldsymbol{H = \int_0^{2\pi/\omega} \left[E'(\omega)\cdot\varepsilon(t) + \frac{E''(\omega)}{\omega}\cdot\dot{\varepsilon}(t)\right]\dot{\varepsilon} dt = \varepsilon_0^2\cdot\omega\cdot\pi\cdot E''} \tag{3.23}$$

As it is possible to denote, in a material with viscoelastic damping, the stress and the internal damping depend on the frequency of variation of the imposed excitation and, consequently, on the frequency of the oscillatory movement [8].

Evaluating the expressions shown above, one may define the damping or loss factor in terms of the energy involved in the system illustrated in Figure 3.4.

$$\boldsymbol{\eta = \frac{1}{2\pi}\cdot\frac{H}{U}} \tag{3.24}$$

According to Beards [15], for most real structures, it is not usually possible to separate the structural stiffness from its hysteretic damping. Thus, in mathematical models, such quantities are considered coupled.

Carfagni *et al.* [16] state that the loss factor is the measurement index that best generalizes the damping since it can be used successfully in non-linear systems, because the damping rates, such as the **critical damping ratio**, $\boldsymbol{\xi}$, have definitions based on a viscous single degree of freedom (SDOF) models.

The loss factor is usually related to the damping ratio by the following expression

$$\boldsymbol{\eta = 2\xi} \tag{3.25}$$

The accuracy of this relationship is restricted to small amounts of damping [9]. In this sense, Liu [17] describes that for expression (3.25) to have a minimum precision of 5%, the damping values must be contained in the range of $\boldsymbol{0 \le \eta \le 0,3}$. In [18], the authors point to a more precise relationship between the two indices, as shown in the expression (3.26).

$$\eta = 2\xi\sqrt{1-\xi^2} \tag{3.26}$$

3.6. A Brief Note on Hysterical Damping

In a dynamic system, different forms of energy dissipation can be present. These are: *(i)* the structural or external damping (in joints, interfaces and support devices); *(ii)* internal (or material) damping; and *(iii)* the fluidic damping (or the interaction between the structure and a viscous fluid).

For materials whose behaviour is predominantly viscoelastic, structural damping is relevant and cannot be neglected. The frequency-dependent behaviour of the stiffness of a viscoelastic material directly affects the system's modal frequencies and damping, which results in complex vibration modes and differences in the relative phase of vibration [19].

In this regard, the influence of the viscoelastic damping of the structure on the natural frequencies of a dynamic system is presented as follows.

In a viscously damped single-degree-of-freedom structure, the fundamental equation of motion for free vibrations has the following form

$$m\ddot{u} + c\dot{u} + ku = 0 \tag{3.27}$$

where

- $\boldsymbol{m}$ is the mass;
- $\boldsymbol{c}$ is the viscous damping;
- $\boldsymbol{k}$ is the stiffness.

For a full-polymer composite system, the viscous damping may be set to zero. Then, equation (3.27) reduces to

$$m\ddot{u} + ku = 0 \tag{3.28}$$

The stiffness characteristic of the viscoelastic material is frequency- and temperature-dependent, which implies the need to re-calculate the stiffness at each frequency and/or temperature value. The stiffness is expressed as a complex quantity and is given by

$$k^*(\omega) = k'(\omega) + ik''(\omega) \tag{3.29}$$

where

- $\boldsymbol{k^*}$ is the complex stiffness of viscoelastic material;
- $\boldsymbol{k'}$ is the storage modulus of viscoelastic material;
- $\boldsymbol{k''}$ is the loss modulus of viscoelastic material;
- $\boldsymbol{i}$ is the imaginary unit given by $\sqrt{-1}$;
- $\boldsymbol{\omega}$ is the frequency.

Substituting equation (3.29) in equation (3.28), yields

$$m\ddot{u} + k'(1 + i\eta)u = 0 \tag{3.30}$$

where:

- $\boldsymbol{\eta}$ is the loss factor (or the hysteretic damping ratio).

The second term of equation (3.30) is *the stiffness and hysteretic damping* combined into one complex expression [20], the so-called *complex stiffness*.

As observed in Neumark [20], the free vibration response of a system with hysteretic damping in equation (3.30) is more complex than that of a system under forced oscillations, and no satisfactory solution has been given. Earlier, Bishop [21] explained that the main difficulty stems from the fact

that hysteretic damping has not been defined for motion other than *harmonic* oscillation and the free vibration is not harmonic.

Since the use of a harmonic solution to solve the differential equation would make it impossible to guarantee a zero response when the system has zero initial displacement and velocity, the hysteretic damping has a non-casual behaviour. In Crandall [22], the author has stated that this model violates the principle of causality, which means that if a system is at rest before some action takes place on it, then the response given by the model has to be zero for any time before that action. This non-causality was also confirmed by Gaul *et al.* [23], who verified the existence of a non-zero response associated with the structural damping model, which leads to a precursor response and causes small deviations from the introduced initial conditions.

To avoid this non-causality problem, a different mathematical representation of the initial conditions has been proposed in Ribeiro *et al.* ([24] and [25]), in which these initial conditions are established in a complex form, setting the initial displacement and velocity as complex values.

The equation (3.30) is the homogeneous equation and its solution is given by

$$u = Ce^{\lambda t} \tag{3.31}$$

where:

$\boldsymbol{C}$ is a constant (and complex in general);

$\boldsymbol{\lambda}$ is the eigenvalue.

Substituting equation (3.31) into equation (3.30) leads to the algebraic equation

$$\lambda^2 m + k'(1 + i\eta) = 0 \tag{3.32}$$

Note that the term $\boldsymbol{k'(1 + i\eta)}$ in equation (3.32) is given as a complex, whose real part represents the stiffness itself, while the imaginary part represents the energy dissipation.

The solution of equation (3.32) leads to an eigenvalue determination problem where

$$\lambda^2 = -\frac{k'}{m}(1 + i\eta) \tag{3.33}$$

Setting $\boldsymbol{\omega_n = \sqrt{k'/m}}$, in which $\boldsymbol{\omega_n}$ is the undamped-natural frequency of the system, one may rewrite equation (3.33) as

$$\lambda^2 = -{\omega_n}^2(1 + i\eta) \tag{3.34}$$

Equation (3.34) provides the relationship between the undamped-natural frequency, $\boldsymbol{\omega_n}$, and the complex eigenvalue, $\boldsymbol{\lambda}$. Furthermore, from equation (3.34), the solution of equation (3.32) is

$$\lambda = \pm\omega_n\sqrt{1 + i\eta} \tag{3.35}$$

Taking into account the real positive quantities $\boldsymbol{\alpha}$ and $\boldsymbol{\beta}$ given by

$$\alpha = \sqrt{\frac{-1+\sqrt{1+\eta^2}}{2}} \; and \; \beta = \sqrt{\frac{1+\sqrt{1+\eta^2}}{2}} \tag{3.36}$$

equation (3.35) can be rewritten as

$$\lambda = \pm\omega_n(\alpha - i\beta) \tag{3.37}$$

From the relations (3.35), the solution $x(t)$ can then be expressed in the form of

$$x(t) = C_1 e^{\lambda t} + C_2 e^{-\lambda t} \tag{3.38}$$

Since $\boldsymbol{\alpha}$ is a real positive quantity, equation (3.38) has no physical meaning as it would imply a growing response along the time for the first member of right-hand, $\boldsymbol{C_1 e^{\lambda t}}$. Thus, one has to impose that $\boldsymbol{C_1 = 0}$ and equation (3.38) becomes

$$x(t) = C e^{-\alpha \omega_n t} e^{i\beta\omega_n t} \tag{3.39}$$

Since $\boldsymbol{C}$ is a complex constant, it can be written as

$$C = g + ih \tag{3.40}$$

where $\boldsymbol{g}$ and $\boldsymbol{h}$ **are constants.**

The evaluation of $\boldsymbol{C}$ is possible by imposing initial conditions of displacement and velocity. However, when imposing the usual initial conditions as

$$\begin{aligned} x(0) &= x_0 \\ \dot{x}(0) &= v_0 \end{aligned} \tag{3.41}$$

the results are

$$\begin{aligned} x_0 &= g + ih \\ v_0 &= -\omega_n(\alpha - i\beta)x_0 \end{aligned} \tag{3.42}$$

When $\boldsymbol{x_0 = v_0 = 0}$, this implies that $\boldsymbol{g = h = 0}$.

To obtain a solution beyond the trivial one, Ribeiro *et al.* [24] proposed the following initial conditions

$$\begin{aligned} x(0) &= x_0 + i\mathcal{I}m(x(0)) \\ \dot{x}(0) &= v_0 + i\mathcal{I}m(\dot{x}(0)) \end{aligned} \tag{3.43}$$

In equation (3.43), $\boldsymbol{x_0}$ and $\boldsymbol{v_0}$ are the measured and real parts of $\boldsymbol{x(0)}$ and $\boldsymbol{\dot{x}(0)}$, respectively. In effect, from equation (3.43), we have

$$\begin{aligned} x_0 + i\mathcal{I}m\big(x(0)\big) &= g + ih \quad (= C) \\ v_0 + i\mathcal{I}m(\dot{x}(0)) &= -\omega_n(\alpha - i\beta)(g + ih) \end{aligned} \tag{3.44}$$

From equation (3.44), the following form is obtained to express the initial displacement and velocity for a system with hysteretic damping

$$\begin{aligned} x(0) &= x_0 - i\left[\frac{v_0 + \omega_n \alpha x_0}{\omega_n \beta}\right] \\ \dot{x}(0) &= v_0 + i\left[\omega_n \frac{\sqrt{1+\eta^2}}{\beta} x_0 + \frac{\alpha}{\beta} v_0\right] \end{aligned} \tag{3.45}$$

And the response is given by

$$x(t) = \left[x_0 - i\left(\frac{v_0 + \omega_n \alpha x_0}{\omega_n \beta}\right)\right] e^{-\alpha\omega_n t} e^{i\beta\omega_n t} \tag{3.46}$$

The real and imaginary parts of equation (4.46) are given, respectively, by

$$\Re e[x(t)] = \left[x_0 \cos(\omega_n \beta t) + \left(\frac{v_0 + \omega_n \alpha x_0}{\omega_n \beta}\right) \sin(\omega_n \beta t)\right] e^{-\alpha\omega_n t} \tag{3.47}$$

and

$$\mathcal{I}m[x(t)] = i\left[x_0 \sin(\omega_n \beta t) - \left(\frac{v_0 + \omega_n \alpha x_0}{\omega_n \beta}\right)\cos(\omega_n \beta t)\right] e^{-\alpha \omega_n t} \tag{3.48}$$

From the response of the system given by equations (3.47) and (3.48), the hysteretic-damped natural frequency is given by

$$\omega_h = \omega_n \beta = \omega_n \sqrt{\frac{1+\sqrt{1+\eta^2}}{2}} \tag{3.49}$$

At this point, it is important to note that the natural frequencies of a system with hysteretical damping will always be higher than those of the corresponding undamped system, by contrast to the equation of the viscous-damped natural frequency

$$\omega_v = \omega_n \sqrt{1-\xi^2} \tag{3.50}$$

in which the natural damped frequency will always be lower than the frequency of an undamped system.

It must be pointed out that the hysteretic-damped natural frequency in equation (3.49) is stiffness proportional and, for a viscoelastic material, the stiffness has a frequency- and temperature dependency. This implies that the natural frequencies of a polymer-based system vary according to the frequency and temperature variations, *i.e.*

$$\omega_h(\omega, T) = \omega_n(\omega, T)\beta(\omega, T) = \omega_n(\omega, T) \sqrt{\frac{1+\sqrt{1+\eta^2(\omega, T)}}{2}} \tag{3.51}$$

Finally, the effective stiffness, $\boldsymbol{k_e}$, and the effective natural frequency, $\boldsymbol{\omega_e}$, of a viscoelastic system are, respectively [26]

$$k_e = k'\sqrt{1+\eta^2} \tag{3.52}$$

and

$$\omega_e = \sqrt{\frac{k'}{2m}}\left[\frac{1+\sqrt{1+\eta^2}}{2}\right]^{\frac{1}{2}} \tag{3.53}$$

3.7. Effects of Temperature and Frequency on the Complex Modulus and Loss Factor

The mechanical properties of most viscoelastic materials are particularly sensitive to temperature. The understanding of the effects of temperature on the mechanical behaviour of these materials becomes paramount for their structural applications. In parallel, the excitation frequency also influences the mechanical response of polymers, but with less sensitive variational effects.

Effects of Temperature

The morphological characteristic of polymers makes them especially sensitive to temperature variations. Small variations will not drastically affect the properties of the polymer; it is paramount to know to which temperature ranges the structure will be submitted and, within this range, to investigate the behaviour of the composite.

Polymers, in general, have five regions of viscoelastic behaviour, identified as:

I. Glassy region;
II. Transition region;
III. Rubbery plateau;
IV. Rubbery flow region;
V. Viscous flow region.

Thermoplastic polymers show the five regions of behaviour, whereas thermosets show only the first three regions. In fact, under high temperatures, thermosetting polymers degrade and do not melt, *i.e.*, they do not have a rubbery and viscous flow region [14]. In prolonged periods under high temperatures, thermosets degrade and may appear to be in a flow region, besides presenting darkening of their colour.

Figure 3.5 shows the five regions of viscoelastic behaviour of an epoxy and the variation in the storage modulus as a function of temperature. It should be noted that epoxy, a thermosetting polymer, does not have a melting temperature; after the glass transition, the rubbery plateau is followed up to the limit of stability of the material, from which its thermal degradation (decomposition) begins.

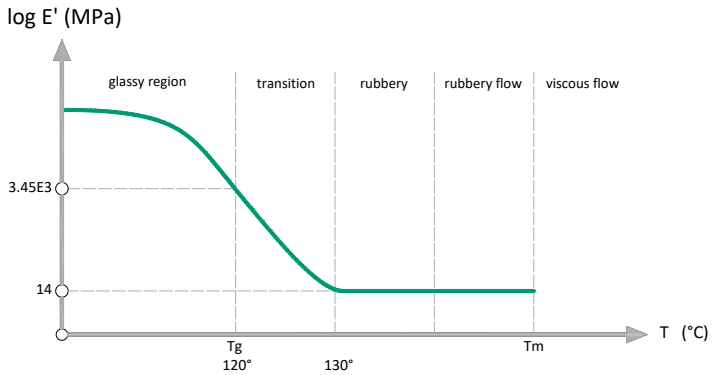


Figure 3.5. Regions of Viscoelastic Behaviour of an Epoxy.

In the **glassy region**, the storage modulus, $\boldsymbol{E'}$, of the polymer is maximum and its loss factor, $\boldsymbol{\eta}$, is reduced. In this region, the polymer has a vitreous behaviour, with high rigidity and can sometimes have a fragile behaviour.

As the temperature rises and approaches the **glass transition temperature**, $\boldsymbol{T_g}$, the storage modulus decreases remarkably. In contrast, the loss modulus, $\boldsymbol{E''}$, and the loss factor, $\boldsymbol{\eta}$, increase, and reach peak values within the **transition region** (generally, these two peaks occur for non-coincident temperature values). At the glass transition point (more precisely, across a temperature range), the primary transition occurs, with a significant change in the elasticity modulus. This region is associated with large-scale movements of polymer chains [27].

In the **rubbery region** or **rubber plateau**, both the storage modulus and the loss factor have reduced values and vary little with increasing temperature.

The two **flow regions**, rubbery and viscous, are characterized by the decrease of both moduli (storage and loss) and the loss factor. The material becomes sticky and spreads with applied pressure. As the material is heated to the viscous flow region, its viscosity decreases steadily.

There are, in fact, discrete transitions, called secondary transitions or secondary relaxations, where small changes in the moduli occur, attributed to small molecular movements of the material.

According to Barra [28], secondary transitions, $\boldsymbol{\gamma}$, and $\boldsymbol{\beta}$, are related to the amorphous part and refer to the movement of side groups of the polymeric chain, or part of them when the main chain does not show movement. The primary transition, $\boldsymbol{\alpha}$, also related to the amorphous part of the polymer, represents the molecular movement of a chain segment, as a whole, and points to the glass transition temperature, $\boldsymbol{T_g}$.

After the region of the primary transition related to the amorphous part, $\boldsymbol{\alpha}$, other transitions occur, now associated with the crystalline part of the material and they are related to movements that are part of the crystal. The first one, just after the $\boldsymbol{\alpha}$, transition, is said to be secondary transition and represents the movement of crystal chains that constitute metastable phases. Subsequently, recrystallization and definitive melting occur in the case of thermoplastics, which is related to the melting temperature, $\boldsymbol{T_m}$, a so-called primary transition.

Figure 4.6 illustrates the variation in the mechanical properties of an epoxy resin and two composites conformed with the same resin and reinforced by glass fibres in perpendicular directions, for the same frequency of disturbance.

The damping capacity and stiffness of a viscoelastic material are related to its transition temperature from the glassy state to the amorphous one, and it is the temperature at which the material reaches its maximum damping value. The efficiency of the system, in terms of vibration control, will depend on the relationship between the operating temperature of the structure and the transition temperature of the material [2].

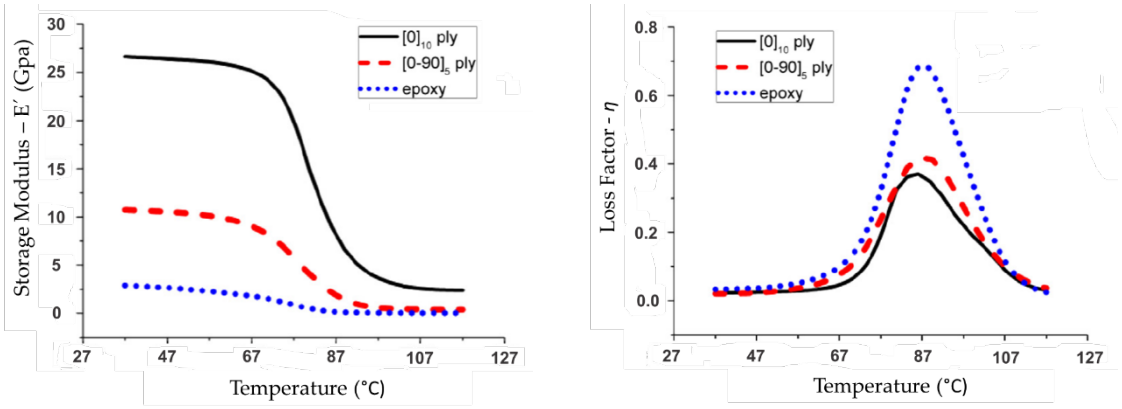


Figure 3.6. Dynamic-mechanical properties of epoxy resin and epoxy/fibre composites with different fibre orientations (adapted from Lorandi *et al.* [7]).

Table 3.1 presents some glass transition and melting temperatures of some polymers, values that will vary and will depend on the composition, manufacturing conditions and curing of the polymer.

Table 3.1. Approximate Glass transition temperature ($\mathbf{T_g}$) and melting temperature ($\mathbf{T_m}$) of some polymers.

Material	T_g (°C)	T_m (°C)
Polytetrafluoroethylene (Teflon)	-97	327
High density polyethylene (HDPE)	-90	137
Polypropylene (PP)	-18	175
Polyethylene terephthalate (PET)	69	265
Polyvinyl chloride (PVC)	87	212
Polystyrene (PS)	100	240
Epoxy	75	-

Certain factors can influence the establishment of the glass transition temperature of polymers, among which the following are mentioned [29]:

Flexibility

The more flexible the polymer chain, the lower the temperature that will allow rotations around the C-C connections and the lower the $\boldsymbol{T_g}$. The presence of aromatic rings (*e.g.*, benzene) in the main chain makes the material less flexible, raising the $\boldsymbol{T_g}$. The presence of oxygen atoms makes the molecules more flexible and, consequently, $\boldsymbol{T_g}$ will be lower.

Geometry

The larger the substituting groups (CH_3) present in the polymer chain, the greater the interference with the main chain, thus hindering their movements and, consequently, the greater the $\boldsymbol{T_g}$.

Plasticizer

Normally small molecules lodge among the polymer chains, moving them apart from one another, making it difficult for the chains to interact, providing a decrease in $\boldsymbol{T_g}$.

Careful analysis of the thermodynamic properties of a composite can allow the identification of dynamic moduli and the loss factor for a range of temperatures of interest, in particular, those to which the structure will be exposed. Figure 3.7 shows the result of a thermodynamic test of two epoxy systems based on DGEBA (Diglycidyl Ether Bisphenol A) originated from aliphatic amines TEPA (Tetraethylenepentamine) and D230 (*Jefamine*), in which it is possible to observe the reductions of the storage modulus, and the peaks of the damping factor near the glass transition temperature.

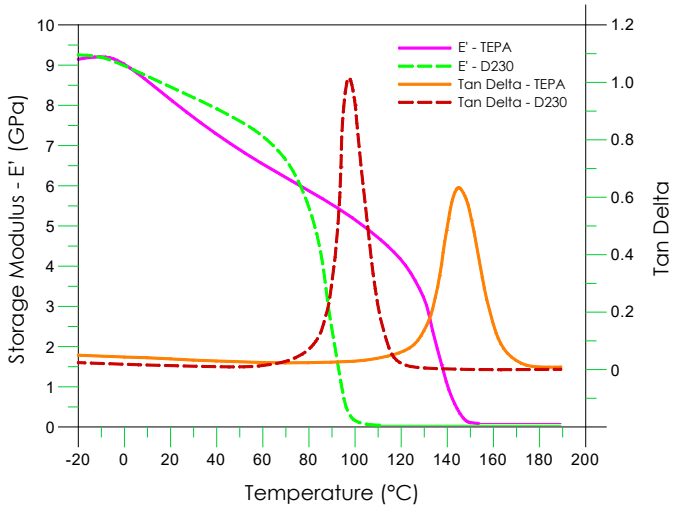


Figure 3.7. Thermodynamic analysis DGEBA/TEPA and DGEBA/D230 (adapted from Junior *et al.* [30]).

Effects Of Frequency

Upon being deformed, the long molecular chains of a viscoelastic material are disturbed from their equilibrium position and interact with each other in reaction to the imposed deformation. Then, there is a movement of rearrangement in the molecular chains, restoring balance.

Since the disturbance is imposed in the form of harmonic cyclic deformation, the molecular chains, in response, reach the state of dynamic equilibrium responding in line with the excitation [2]. In this way, the rigidity of the viscoelastic material is amplified with the increase in the frequency of harmonic excitation. Conversely, as the frequency of harmonic disturbance decreases, the rigidity of the viscoelastic material decreases.

At low frequencies, the long polymeric chains have time to move with each other, resulting in a low modulus. Under high excitation frequencies, the chains have no time to move and, therefore, the material has a high modulus [31].

The storage modulus, $\boldsymbol{E'}$, increases as the frequency increases, with a slight variation rate within the glassy and amorphous region (regions III, IV and V) and a marked gradient within the transition region. The loss factor, $\boldsymbol{\eta}$, increases as the frequency grows and reaches its maximum value within the transition region and decreases again as the frequency continues to increase.

Figure 3.8 illustrates these features, by presenting the variation of the Complex Modulus, $\boldsymbol{E^*}$, and the Loss Factor, $\boldsymbol{\eta}$, of a polymer blend **ABS+PC** (Acrylonitrile-Butadiene-Styrene / Polycarbonate) tested by Souza *et al*. [1] at an average temperature of 19°C using the ASTM-756-05 method [32].

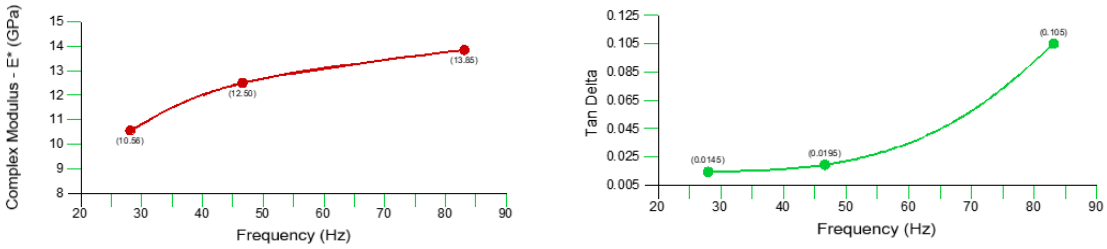


Figure 3.8. Dynamic-Mechanical Analysis of ABS+PC blend (adapted from Souza *et al.* [1]).

In the analysis of a polymer, the determination of transitions is done, in general, by monitoring the temperature variation. However, the frequency of the excitation at which the temperature is scanned affects the transition temperature [33].

It is at low frequencies that viscoelastic behaviour predominates; the polymer can be moved through a transition region by changing the disturbance frequency [33].

It should be noted that viscoelastic materials, when subjected to cyclic loading, dissipate part of their energy in the form of heat within the material's volume [34]. Usually, this phenomenon, called **internal self-heating**, is not taken into account in mechanical designs that incorporate this type of material.

Figure 3.9 illustrates the influence of self-heating on the internal temperature of an acrylic resin adhesive.

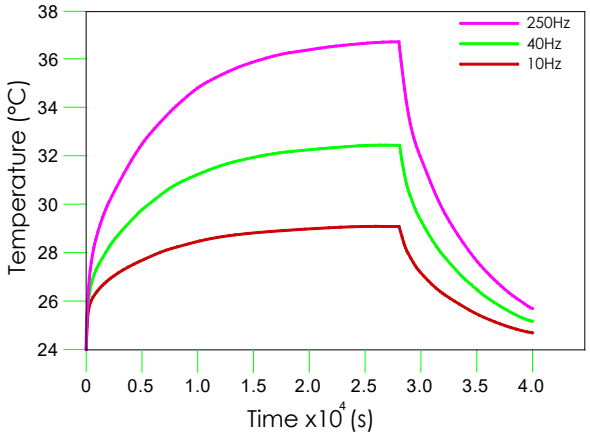


Figure 3.9. The internal temperature in a polymer (adapted from Cazenove *et al.* [35]).

Gopalakrishna and Lai [36] cite, as an example, the fact that viscoelastic damping devices in buildings, when they are subjected to severe storms, deform cyclically, converting kinetic energy into heat. As a consequence, there is an increase in the internal temperature in the polymeric material, thus changing its rigidity and damping level.

Katunin *et al*. [37] describe that the phenomenon of internal self-heating, under certain loading conditions, can dominate the fatigue process of the material and mention that the degradation frequently occurs when the temperature exceeds the glass transition temperature. Briefly, they describe that, during cyclic loading, the mechanical energy resulting from out-of-phase oscillations between stress and deformation, is dissipated in the form of heat and, considering the low thermal conductivity of most industrial polymers used for manufacturing of composites, the heat generated is stored in the damping structure itself, causing self-heating. They also mention that this increase is known, in some sources, as **hysteretic heating temperature**.

In addition to the frequency amplitude, the amplitude of the loading at constant frequency also imposes changes in the internal temperature of the polymer.

3.8. Final Considerations

Due to their molecular structure, in general, polymers show an intermediate mechanical behaviour between an elastic phase and a viscous phase, which is reflected by their intrinsic ability to dissipate kinetic energy, namely by their viscoelastic damping. In fact, during a complete loading and unloading cycle, the deformation of the polymeric material follows a phase delay with the disturbance.

As demonstrated, the best way to represent this behaviour is through a phasor diagram, where it is possible to decompose the rigidity of the material in a real and complex phase. The hysteresis cycle, then, can be used to define the energy dissipation parameter, called loss factor and which represents the damping capacity of the polymeric material.

However, because the damping presented by polymers originates from its molecular structure, it is sensitive to changes in temperature and, to a lesser extent, to the frequency of oscillation of the disturbance. In this context, concepts have been presented to suggest ways of manipulating the properties of polymers to meet certain structural needs and which motivated the beginning of this work.

3.9. References

[1] J. C. Souza and J. J. Lima Jr, "Determinação dos Módulos de Armazenagem e de Perda de Materiais Viscoelásticos - Padrão ASTM," *Nono Simpósio de Mecânica Computacional*. Associação Brasileira de Métodos Computacionais em Engenharia, São João Del-Rei – MG, 2010.

[2] R. S. Moreira and J. D. Rodrigues, "Caracterização dinâmica do módulo complexo de materiais viscoelásticos," *Métodos Computacionais em Engenharia -*. Lisboa, p. 15, 2004.

[3] J.-M. Berthelot, M. Assarar, Y. Sefrani, and A. El Mahi, "Damping analysis of composite materials and structures," *Compos. Struct.*, vol. 85, no. 3, pp. 189–204, 2008, doi: 10.1016/j.compstruct.2007.10.024.

[4] W. N. Findley, J. S. Lai, and K. Onaram, *Creep and Relaxation of Nonlinear Viscoelastic Materials - With an Introduction to Linear Viscoelasticity*. New York: Dover Publications Inc., 1976.

[5] D. I. G. Jones, *Handbook of Viscoelastic Vibration Damping*. Arizona, USA: Wiley & Sons Ltd., 2001.

[6] J. C. Gerdeen, PhD, PE, and R. A. L. Rorrer, *Engineering Design with Polymers and Composites*, Second. CRC Press, 2011.

[7] N. P. Lorandi, M. O. H. Cioffi, and H. O. Jr, "Análise dinâmico-mecânica de materiais compósitos poliméricos," *Sci. cum Ind.*, vol. 4, no. 13, pp. 48–60, 2016, doi: 10.18226/23185279.v4iss1p48.

[8] C. W. De Silva, A. Borbely, J. F. Kreider, and L. R. Davis, *Vibration Damping, Control, and Design*. Vancouver, Canada: Taylor & Francis Group, LLC, 2007.

[9] D. Masotti, "Comparação de métodos de determinação de amortecimento estrutural através de técnicas de ajuste de curvas de funções resposta em frequência," Master Thesis, Universidade Federal de Santa Catarina, 2013.

[10] S. Adhikari, "Damping Models for Structural Vibration," PhD Thesis, Cambridge University, 2000.

[11] E. H. Aseka, "Projeto, construção e determinação de propriedades de amortecedor viscoelástico para uso em estruturas," Master Thesis, Universidade Federal do Rio Grande do Sul, 2002.

[12] A. de Oliveira, "Adição de amortecimento estrutural usando materiais viscoelásticos," Master Thesis, Universidade Federal de Santa Catarina, 2004.

[13] A. Kareem, T. Kijewski, and Y. Tamura, "Mitigation of motion of tall buildings with specific examples of recent applications," *Wind Struct.*, vol. 2, no. 3, pp. 201–251, 2007, doi: 10.12989/was.1999.2.3.201.

[14] H. F. Brinson and L. C. Brinson, *Polymer Engineering Science and Viscoelasticity: An introduction*, 2ª Edition. New York: Springer, 2015.

[15] C. F. Beards, *Structural Vibration: Analysis and Damping*, First Edit. Londres: Butterworth-Heinemann, 1996.

[16] M. Carfagni, E. Lenzi, and M. Pierini, "The loss factor as a measure of mechanical damping," in *SPIE proceedings series*, 1998, pp. 580–584.

[17] W. Liu, "Experimental and Analytical Estimation of Damping in Beams and Plates with Damping Treatments," PhD Thesis, University of Kansas, 2008.

[18] E. J. Graesser and C. R. Wong, "The relationship of traditional damping measures for materials with high damping capacity: a review," in *M3D: Mechanics and Mechanisms of Material Damping, Edição 1169*, Philadelphia, 1992, pp. 316–343.

[19] Y. Wang and D. J. Inman, "Finite element analysis and experimental study on dynamic properties of a composite beam with viscoelastic damping," *J. Sound Vib.*, vol. 332, no. 23, pp. 6177–6191, 2013, doi: 10.1016/j.jsv.2013.06.016.

[20] S. Neumark, "Concept of Complex Stiffness Applied to Problems of Oscillations with Viscous and Hysteretic Damping," *Aeronaut. Res. Counc.*, 1962.

[21] R. E. D. Bishop, "The Treatment of Damping Forces in Vibration Theory," *J. R. Aeronaut. Soc.*,

vol. 59, no. 539, pp. 738–742, 1955, doi: 10.1017/s0368393100117122.

[22] S. H. Crandall, "The role of damping in vibration theory," *J. Sound Vib.*, vol. 11, no. 1, pp. 3–18, 1970, doi: 10.1016/S0022-460X(70)80105-5.

[23] L. Gaul, S. Bohlen, and S. Kempfle, "Transient and forced oscillations of systems with constant hysteretic damping," *Mech. Res. Commun.*, vol. 12, no. 4, pp. 187–201, 1985.

[24] A. M. R. Ribeiro, J. M. M. Silva, L. Reis, and M. J. Freitas, "Free Vibration Response Using the Constant Hysteretic Damping Model," in *XIth International Conference on Vibration Engineering*, 2005, no. September, doi: 10.13140/2.1.1970.9443.

[25] A. M. R. Ribeiro, N. M. M. Maia, and J. M. M. Silva, "Free and forced vibrations with viscous and hysteretic damping - a different perspective," in *5th International Conference on Mechanics and Materials in Design*, 2006, no. January, doi: 10.13140/2.1.3019.5207.

[26] T. J. Reid, "Free Vibration and Hysteretic Damping," *Aeronaut. J.*, vol. 60, no. 544, p. 283, 1956.

[27] J. Feng and Z. Guo, "Temperature-frequency-dependent mechanical properties model of epoxy resin and its composites," *Compos. Part B Eng.*, vol. 85, pp. 161–169, 2016, doi: 10.1016/j.compositesb.2015.09.040.

[28] G. M. O. Barra, "Viscoelasticidade e DMTA." Folhas de Apoio, Universidade Federal de Santa Catarina, 2005.

[29] M. C. Paiva, "Estrutura e propriedades de polímeros." Folhas de Apoio, Universidade do Minho, Guimarães, p. 45, 2006.

[30] B. Junior, L. P. Amaral, and C. R. Rodríguez, "Propriedades mecânicas e aspectos da microestrutura de sistemas epoxídicos dgeba," in *II Confresso Fluminense de Iniciação Científica e Tecnologia*, 2010, pp. 3–6.

[31] J. M. Biggerstaff, "Vibrational Damping of Composite Materials," PhD Thesis. University of California San Diego, 2006.

[32] ASTM International, "Standard Test Method for Measuring Vibration-Damping Properties of Materials," in *Annual Book of ASTM Standards*, 2005, p. 14.

[33] K. P. Menard, *Dynamic Mechanical Analysis - A Practical Introdution*, Second. New York: Taylor & Francis Group, LLC, 2008.

[34] V. G. Karnaukhov and L. P. Goncharov, "Self-heating of viscoelastic materials under cyclic loads," *Strength Mater.*, vol. 7, no. 2, pp. 164–168, 1975, doi: 10.1007/BF01522140.

[35] J. De Cazenove, D. A. Rade, A. M. G. De Lima, and C. A. Araújo, "A numerical and experimental investigation on self-heating effects in viscoelastic dampers," *Mech. Syst. Signal Process.*, vol. 27, no. 1, pp. 433–445, 2012, doi: 10.1016/j.ymssp.2011.05.004.

[36] H. S. Gopalakrishna and M. L. Lai, "Finite element heat transfer analysis of viscoelastic damper for wind applications," *J. Wind Eng. Ind. Aerodyn.*, vol. 77–78, pp. 283–295, 1998, doi: 10.1016/S0167-6105(98)00150-0.

[37] A. Katunin, A. Wronkowicz, M. Bilewicz, and D. Wachla, "Criticality of self-heating in degradation processes of polymeric composites subjected to cyclic loading: a multiphysical approach," *Arch. Civ. Mech. Eng.*, vol. 17, no. 4, pp. 806–815, 2017, doi: 10.1016/j.acme.2017.03.003.

4. Vibrations in Footbridges

4.1. Justification

The dynamic behaviour of footbridges, as well as the aspects that define it, are part of the double support of this work, here referred to as the **active** phase, complemented by the phase referred to as **reactive**, which is formed by the viscoelastic response of the material used in the footbridge.

In this sense, it becomes necessary to identify and characterize the actions associated with different human activities, the analysis of the structural behaviour of footbridges and the characterization of the comfort level of their users in terms of normative limits, bearing in mind the calculated response and the type of expected use.

Therefore, the objective of this chapter is to outline the details that involve the service conditions of footbridges.

4.2. Initial Considerations

Footbridge structures are prone to vibrations in one or more natural frequencies within the range of typical human activity, such as walking, running, or jumping [1]. In general, disturbances induced by pedestrians involve comfort issues and safety or resistance problems.

According to the document Hivoss [2], when designing footbridges the analysis of vibrations induced by the action of pedestrians must be considered in the project to ensure that:

a. Vibrations due to pedestrian traffic are acceptable to users;
b. The synchronization phenomenon (*lock-in*[1]) does not take place;
c. The stability of the pedestrian structure is guaranteed when subject to intentional disturbance.

Among the main strategies to mitigate excessive vibrations in walkways, the increase of stiffness is one of the possible solutions, but it generally affects the aesthetics of the footbridge. On the other hand, the increase in structural damping through vibration control systems is currently the most frequent and most effective measure in mitigating vibrations associated with pedestrian actions. Such systems are, in general, formed by materials with mechanical viscoelastic characteristics, such as Tuned Mass Damper (TMD) systems, consisting of a mass connected to the structure through a spring and a viscous damper [3].

4.3. Characterisation of Dynamic Actions

In general, most civil engineering loads can be classified as dynamic, as they vary over time. According to Bachmann *et al.* [4], what differentiates dynamic and static loads is the presence of forces of inertia, due to acceleration, and damping. However, in practice, loads with slight or modest variation are treated as quasi-static and their dynamic effects are neglected.

The magnitude of these forces and their function over time depending on how they oscillate externally and on the structure's response to such disturbances. Thus, according to their variation in time, dynamic actions can be characterized as harmonic and periodic; they may also have a transitory character and assume an impulsive nature.

---

[1] *The lock-in phenomenon will be described later in this chapter*

Most of the excitations induced by pedestrians can be treated as periodic, as they are characterized by a variation in the time that is repeated in periods or regular intervals.

Although the function that governs the action takes an arbitrary form within these periods, its repetitiveness allows it to be decomposed into a series of harmonic loads through the Fourier Transform. Bachmann *et al.* [4] claim that periodic excitations are long enough to allow responses (vibrations) to be considered stationary.

The actions that the pedestrian movement can induce to pedestrian bridges are, naturally, derived from their physical activity and translated by the various forms of movement, where the most relevant are:

a. walk;
b. run;
c. jump (vandalism).

The dynamic character of this type of action comes from its variation over time, both in relation to its intensity and in relation to its position.

The ways in which such actions are characterized can be summarized by quantifying certain aspects, among which, the following are essential:

a. Frequency of steps and/ or jumps;
b. Step speed;
c. Step length;
d. Foot-to-floor contact time;
e. Pedestrian density.

All the parameters mentioned will vary according to the characteristics of each person and are sensitive to gender and age, as shown in Figure 4.1.

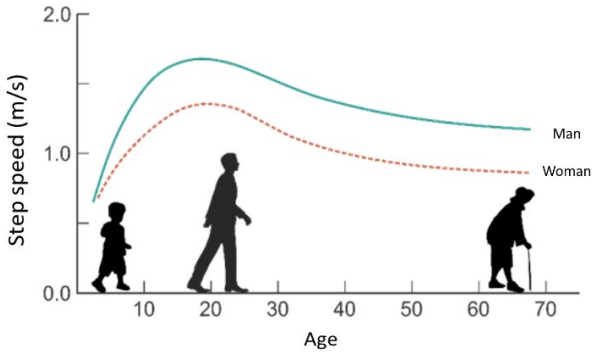


Figure 4.1. Variation of step speed according to age and gender (adapted from Ingólfsson *et al.* [1])

Pedestrian actions can be decomposed into three vector components, one vertical and two horizontal, the latter acting laterally and longitudinally to the plane of the bridge deck. However, the magnitudes of horizontal loads are much smaller than vertical ones. Figure 4.2 illustrates walking forces, represented by load functions, developed during a single cycle [5].

Regarding the quantification of loads, Dos Santos [6] describes that the deterministic characterization of human actions is inconsistent due to the variable character of human behaviour, as previously described, and to factors that affect group behaviour. However, despite the significant stochastic data analysis research, the deterministic model has been predominantly used and will also be used in this chapter, based on the premise that the feet of a pedestrian produce the same force which is periodic [5].

It should also be noted that the aspects that can characterize the actions of a pedestrian are a function of the frequency of steps, the increase of which leads to a decrease in the time of foot-pavement contact and an increase in the length and speed of steps.

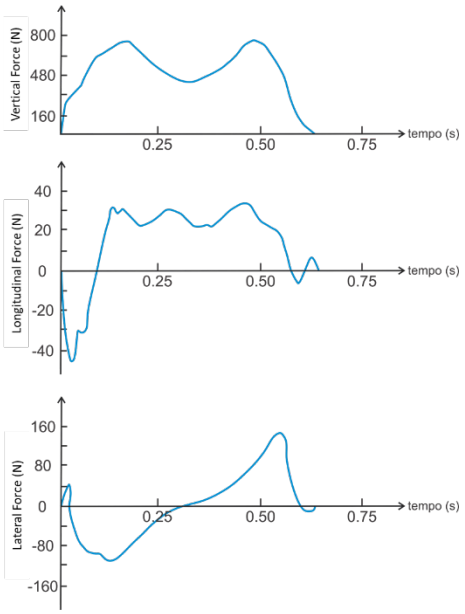


Figure 4.2. Walking load function in three directions (adapted from Bachmann *et al.* [4]).

4.3.1 Walking and Running

The most common pedestrian actions are those due to walking movement, which can be at slow, normal or fast speed. According to Sétra [7], what differs the activity of walking from that of running is that, in the first, there is a continuous contact of the pedestrian with the pavement, whereas in running, such contact is discontinuous.

Frequency

Defined as the number of steps taken by a pedestrian per unit of time, the **frequency of steps**, f_p, can be considered the parameter with the most significant influence in the characterisation of pedestrian walking or running on bridges [4], because, as already described, its variation directly affects other parameters of the description of the pedestrian action.

It is easy to understand that the step frequency, as well as all the parameters that characterize pedestrian action, cannot be reduced to a standard set of values. However, numerous studies and tests have been conducted over the years and, for a deterministic approach, it is necessary to take such results into account. In this context, Bachmann *et al.* [4] quote the work of Matsumoto *et al.* [8], who present the results of the investigation of a normal walk for a sample of 505 pedestrians, illustrated in Figure 4.3.

Speed and Length

The step speed, s_s, is directly related to the **step frequency** and **length**, s_l, through the relationship (4.1)

$$s_s = s_f \cdot s_l \tag{4.1}$$

The particular characteristics of each lead to different values of step frequency and length, but they can generate the same speed. In this sense, Kobayashi [9] refers that the parameters of step length, frequency, or speed have stochastic variations depending on each individual. Wheeler [10] presents a polynomial approximation, the result of experiments, where he lists the three variables involved, summarized in Table 4.1 and illustrated by Figure 4.4.

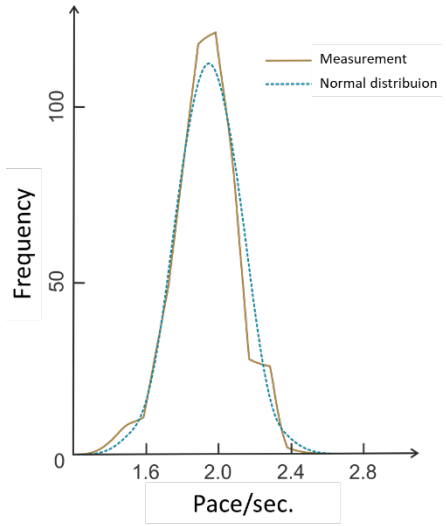


Figure 4.3. Frequency distribution of standard walking steps (adapted from Matsumoto *et al.* [8])

Table 4.1. Correlation among step frequency, speed and length (Wheeler [10]).

Pace	Frequency (Hz)	Speed (m/s)	Length (m)
Slow walking pace	≈ 1.70	1.10	0.60
Normal walking pace	≈ 2.00	1.50	0.75
Fast walking pace	≈ 2.30	2.20	1.00
Slow run	≈ 2.50	3.30	1.30
Fast run	> 3.20	5.50	1.75

It is also important to highlight the variations in vertical force induced by the steps over time; in this respect, it is possible to verify the existence of two peaks of maximum load, the first being related to the impact of the heel on the floor and the second to the impact of the tip of the foot (Figure 4.5).

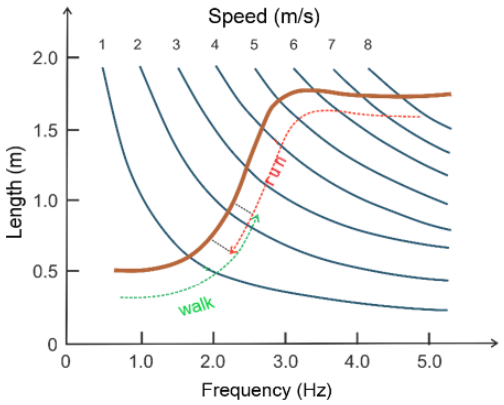


Figure 4.4. Relationships among step frequency, speed and length (adapted from Bachmann *et al.* [4])

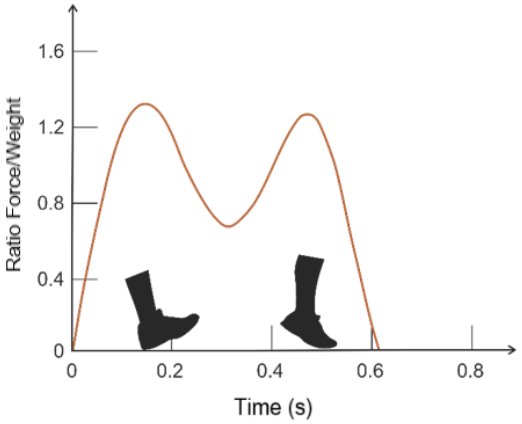


Figure 4.5. Evolution of step force-to-weight ratio for fast walking (adapted from Queiroz [11])

Contact Time

Another characteristic to be described refers to the time during which the pedestrian's foot is in contact with the floor, namely, the **contact time**, $\boldsymbol{t_p}$. This corresponds to the time interval in which one of the pedestrian's feet comes into contact with the pavement until the moment when such contact ceases to exist. In fact, *e.g.*, during a walk, the function of loading concerning the contact time of each foot will be superimposed (Figure 4.6).

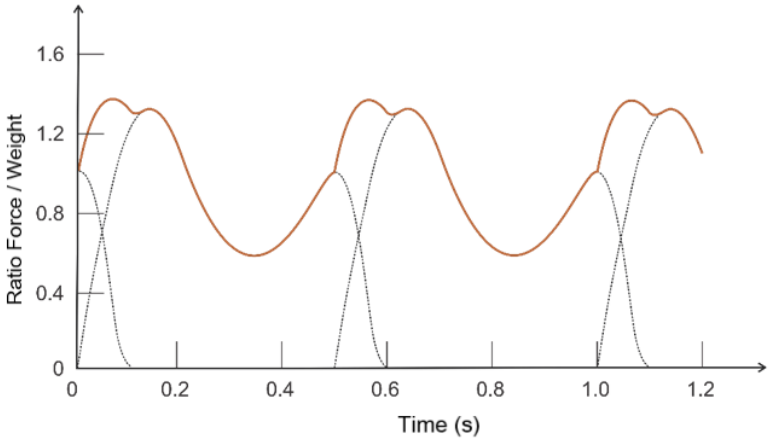


Figure 4.6. Vertical step force-to-weight ratio of both feet (adapted from Bachmann *et al.* [4])

The construction of the load function is based on the assumption that both feet produce the same force [12]. Similarly, the functions for side loads will have the same overlap principle. Bachmann *et al.* [4] present a formulation to describe the load functions for walking and running, *i.e.*, for continuous and discontinuous contact with the pavement. Such models are described and commented hereinafter (sections 4.4.1 and 4.4.2).

Wheeler [10] proposed a relation between the foot-pavement contact time with the step frequency and the dynamic load coefficient; in that work, it is described that the contact time is inversely proportional to the frequency and amplification factor, with shorter durations resulting in more energetic actions on the pavement (Figure 4.7).

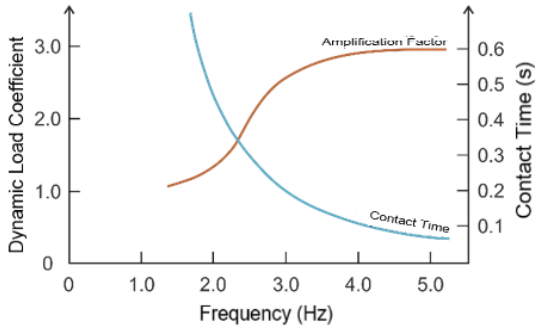


Figure 4.7. Contact time, amplification factor, and step frequency (adapted from Bachmann *et al.* [4])

4.3.2 Jumping (Vandalism)

Vandalism can be defined as an intentional and synchronized movement of a pedestrian or group of pedestrians to excite a structure excessively [13]. Note that the randomness of this type of loading makes it challenging to predict and estimate it.

The resonance achieved by vandalism actions can take different forms, depending on the characteristics of the induced vibration: lateral, vertical, or torsional flexion. In this respect, Caetano *et al.* [14] mention that the easiest way to cause vertical excitation in a structure is to jump over the same point on the floor. They describe, however, that vertical excitations from groups of pedestrians occur, to a greater degree, due to a type of movement called "swinging", where the feet of individuals are in permanent contact with the floor and their knees induce flexion.

Bachmann *et al.* [4] suggest that the mathematical modelling of the pedestrian action of repeatedly jumping can be represented as a localised harmonic load produced by a group of pedestrians, in which the time of foot contact with the ground, $\boldsymbol{t_p}$, will be part of the complete jump cycle. Briefly, this model describes load by vandalism as a sequence of semi-sinusoidal pulses proportional to the weight of the vandals and an impact factor.

According to Kobayashi [9], this model does not consider, however, the variations that may exist within the contact range, since the change in the number of pedestrians participating in the action leads to a variation in the dynamic load factor (DLF), in the series of Fourier, within the time domain. In this sense, Agu *et al.* [15] presented a proposal where the number of pedestrians is inserted in the mathematical model to describe the effect of vandalism.

4.4. Load Functions

As already described, there are two models of analysis that can describe the structural response to dynamic loads: (i) a deterministic model and (ii) a stochastic one. The load functions modelled in this research will start from expressions that describe the law of variation of action over time, for each type of step, making use precisely of a deterministic model.

4.4.1 Walking

The load function for the walking movement, where there is continuous contact with the floor, can be considered a periodic function that represents the sum of a static portion, defined as the weight of the pedestrian, and a dynamic part, which characterizes the steps. The total force produced by a pedestrian can also be broken down into three components, a vertical one, and two horizontal ones; these, in turn, only have the dynamic portion.

Such a periodic function can be written by a Fourier series, which will represent the total sum of the effect generated by walking. The Expressions (4.2), (4.3), and (4.4) define the load values of the vertical, lateral, and longitudinal components, respectively,

$$F_{vertical}(t) = G\left[1 + \sum_{i=1}^{n} \alpha_i \cdot sin(2\pi \cdot i \cdot f_p \cdot t - \varphi_i)\right] \quad (4.2)$$

$$F_{lateral}(t) = G\left[\sum_{i=\frac{1}{2}}^{n} \alpha_i \cdot sin(\pi \cdot i \cdot f_p \cdot t - \varphi_i)\right] \quad (4.3)$$

$$F_{longitudinal}(t) = G\left[\sum_{i=\frac{1}{2}}^{n} \alpha_i \cdot sin(2\pi \cdot i \cdot f_p \cdot t - \varphi_i)\right] \quad (4.4)$$

where:

G is the weight of the pedestrian;
α_i is the Fourier coefficient associated with the i-nth harmonic;
f_p is the step frequency;
φ_i is the phase angle between the i-nth harmonic and the first.

Several studies have been carried out to determine the values of the dynamic load coefficients (DLF), and their main results are shown in Table 4.2.

Table 4.2. Vertical DLF for a pedestrian walk (adapted from Krus [16])

Author	Frequency (Hz)	α_1	α_2	α_3	α_4
Bachmann	2.0	0.4	0.1	0.1	-
	2.4	0.5	-	-	-
Young	-	$0.37(f_p - 0.95)$	$0.54 + 0.0044f_p$	$0.026 + 0.0050f_p$	$0.01 + 0.0051f_p$
Schulze	-	0.37	0.1	0.12	0.04

Bachmann *et al.* [4] state that most cases of pedestrian-induced vibrations are governed only by the first harmonic, but propose the values for the phase angles as $\varphi_1 = 0$, and $\varphi_2 = \varphi_3 = \varphi_4 = \pi/2$.

When a group or a flow of pedestrians are present, adding individual loads, assuming resonance and in-phase amongst all pedestrians, would be too conservative. Different authors have therefore investigated the loads applied by the pedestrians when moving in a crowd.

Model by Matsumoto et al. [8]

Matsumoto *et al.* [8] presented a proposal to estimate the effect of random action by several pedestrians, having suggested a probabilistic distribution of the possibility of synchronizing movements among pedestrians; they assumed a Poisson distribution, depending on only one parameter, λ, interpreted as the average pedestrian arrival rate, given in pedestrians per second per pavement width. In this process, the dynamic response for a point in the structure is estimated by multiplying the amplitude of the vibration caused by just one pedestrian by an **amplification factor** m_n, given by

$$m_n = \sqrt{\lambda \cdot T_o} \quad (4.5)$$

where:

λ average pedestrian rate per period of time;
T_o is the time needed to cross the pavement;
$T_o = L/v_p$, where **L** is the length of the pavement;
$\lambda \cdot T_o$ is the simultaneous number of pedestrians on the bridge.

The root $\sqrt{\boldsymbol{\lambda \cdot T_o}}$ can be translated as the number of synchronized pedestrians circulating along the pavement, which, in theory, can be considered a limitation of the proposal, as it considers that all pedestrians are in the same movement frequency. Furthermore, the fact that it does not consider the damping provided by the structure makes this model too simplified.

Models of Sétra [7] and HIVOSS [2]

This model consists of determining an equivalent number of pedestrians, $\boldsymbol{N_{eq}}$, which, in phase and tune with the natural frequency of the structure, produce the same response as the real number of pedestrians, $\boldsymbol{N}$, in random circulation. In this model, the critical damping ratio, $\boldsymbol{\xi}$, represents the contribution portion of the structure to the model.

Based on experimental results, the manual provides two functions for estimating $\boldsymbol{N_{eq}}$.

$$\textbf{For } \boldsymbol{d_p < 1,0 \frac{pedestrian}{m^2}} \rightarrow \boldsymbol{N_{eq} = 10,8 \cdot \sqrt{N \cdot \xi}} \tag{4.6}$$

$$\textbf{For } \boldsymbol{d_p \geq 1,0 \frac{pedestrian}{m^2}} \rightarrow \boldsymbol{N_{eq} = 1,85 \cdot \sqrt{N}} \tag{4.7}$$

The action of an isolated pedestrian is directly enhanced by the application of the index $\boldsymbol{N_{eq}}$.

Using the same concept of the equivalent number of pedestrians, the guide HIVOSS [17] proposes a load model that includes a probabilistic reduction coefficient, ψ, to take into account the step frequency approximation to the critical range of natural frequencies of the structure.

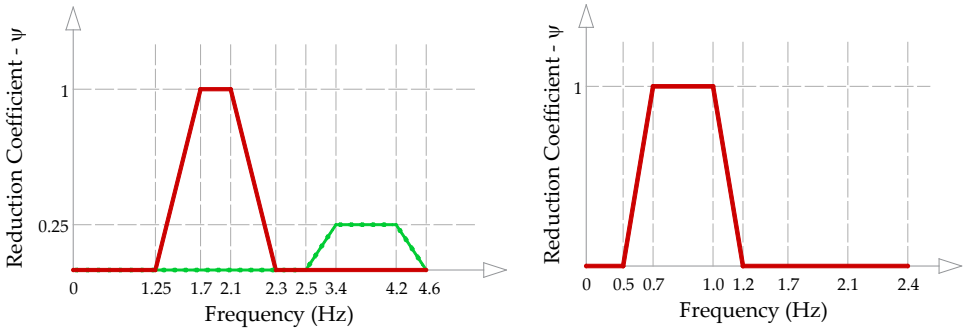
$$\boldsymbol{F(t) = G \cdot cos(2\pi \cdot i \cdot f_p \cdot t) \cdot n' \cdot \psi} \tag{4.8}$$

where:

- $\boldsymbol{G}$ is the weight of the pedestrian;
- $\boldsymbol{f_p}$ is the step frequency, assumed to be equal to the natural frequency of the bridge;
- $\boldsymbol{n'}$ is the equivalent number of pedestrians on the loaded surface S;
- $\boldsymbol{\psi}$ is the reduction coefficient.

The amplitude of action $\boldsymbol{G}$, the equivalent number of pedestrians $\boldsymbol{n'}$ and the reduction coefficient $\boldsymbol{\psi}$ are shown in Table 4.3.

Table 4.3. Parameters for walking load models (adapted from Hivoss [17]).

Parameter	Vertical	Longitudinal	Lateral
(N)	280	14	35
ψ			
n′	*See expressions (4.7) e (4.8)*		

Density

The description of the pedestrian action is best expressed when the effect of more than one pedestrian is combined, translated in terms of pedestrian density, $\boldsymbol{d_p}$, which can be described as the overlapping of the vibrations induced by the $\boldsymbol{n}$ pedestrians that walk through the structure. At certain times, such overlap can increase or decrease the amplitude of the resulting vibration, depending on the frequency and phase of the action.

In this sense, some aspects must be considered, namely the following [4]:

a) The density calculation is determined by the feasibility of walking or running, which corresponds to the upper limit of 1.6 to 1.8 pedestrians/m², which will induce a static load of 1100 to 1400 N/m²; Matsumoto *et al.* [8] suggest the limit value of 1.0 pedestrian/m²;
b) Pedestrians tend to adjust their steps to any floor vibration, which makes any formulation hypothesis very difficult.

Indeed, the step speed tends to decrease with increasing pedestrian density and, thus, an individual will adjust his walk to the movement of the crowd. According to FIB [18], from 0.60 pedestrian/m², the steps enter the first stage of restriction; as the density increases to 1.0 pedestrian/m², the freedom of movement is gradually inhibited and pedestrians need to adjust their movements to one another's. At 1.5 pedestrians/m², displacement columns are formed with reduced speed. On the other hand, a density in the order of 2.0 pedestrians/m² corresponds to a very crowded flow, characterized by a sliding movement, where only small steps are possible; at this stage, the pedestrians cannot move on their own.

4.4.2. Running

The load function for the running movement of one pedestrian is characterized by a single maximum load, taken at the moment when one of the feet touches the pavement, being expressed by a sequence of semi-sinusoidal pulses (4.9)

$$\boldsymbol{F_p(t)} = \begin{cases} \boldsymbol{k_p \cdot G \cdot sin(\pi \cdot t/t_p)} & \boldsymbol{for\ t \le t_p} \\ \boldsymbol{0} & \boldsymbol{for\ t_p \le t \le T_p} \end{cases} \tag{4.9}$$

where:

$\boldsymbol{k_p}$ is defined as a dynamic impact factor: $\boldsymbol{F_{p,max}/G}$;
$\boldsymbol{F_{p,max}}$ is the maximum value of the applied force;
$\boldsymbol{G}$ is the weight of the pedestrian;
$\boldsymbol{t_p}$ is the time of foot-pavement contact;
$\boldsymbol{T_p}$ is the duration of the step: $\boldsymbol{T_p = 1/f_p}$.

The time of contact, $\boldsymbol{t_p}$, may be defined by the use of the graph shown in Figure 4.7 or approximated by the following expression

$$\boldsymbol{t_p = \frac{2}{f_p^{2.13}}} \tag{4.10}$$

The running model can be described by the addition of the static weight of the pedestrian to the harmonic load components, that is, by the development of a Fourier series

$$\boldsymbol{F_p(t) = G\left[1 + \sum_{i=1}^{n} \alpha_i \cdot cos(2\pi \cdot i \cdot f_p \cdot \left(t - \frac{t_p}{2 \cdot i}\right))\right]} \tag{4.11}$$

Bachmann *et al.* [4] present an abacus for determining the $\boldsymbol{\alpha_i}$ coefficients of the Fourier series for running. The authors state that the vibration caused by running is dominated by the first harmonic.

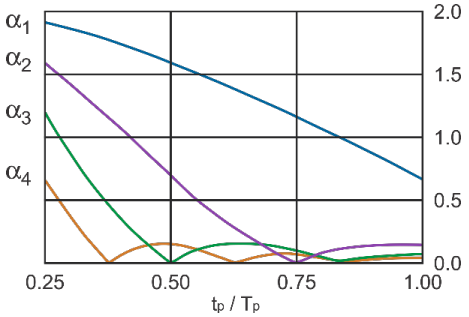


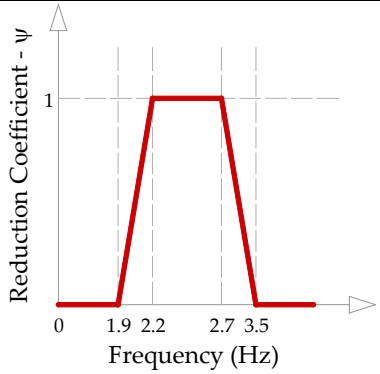
Figure 4.8. Fourier coefficients for running (adapted from Bachmann *et al.* [4]).

Regarding the horizontal load components for running, Setra [7] states that the transversal portion has a reduced relative amplitude in comparison with the vertical component, whereas the longitudinal fraction will be slightly more significant. Hivoss [2] adds, for the load function for the running model, a reduction factor, $\boldsymbol{\psi}$, similar to that used for walking, resulting in the following expression

$$\boldsymbol{F(t) = G \cdot cos(2\pi \cdot i \cdot f_p \cdot t) \cdot n' \cdot \psi} \tag{4.12}$$

Table 4.4 shows the values recommended in that document for the amplitude of action $\boldsymbol{G}$, the equivalent number of pedestrians $\boldsymbol{n'}$ and the reduction coefficient $\boldsymbol{\psi}$.

Table 4.4. Parameters for load models for running (adapted from Hivoss [17]).

Parameter	**Vertical**
G (N)	1250
$\boldsymbol{\psi}$	
$\boldsymbol{n'}$	$\boldsymbol{= n}$

4.4.3 Vandalism

Agu *et al.* [15] describe a function for vandalism actions that take into account the number of pedestrians participating in the act, which imposes an amplification factor in the load function used for describing a walking action

$$\boldsymbol{F_p(t) = N \cdot G\left[\sum_{i=1}^{n} c_i \cdot sin(2\pi \cdot i \cdot f_p \cdot t + \varphi_i)\right]} \tag{4.13}$$

where:

- $\boldsymbol{N}$ is the number of pedestrians;
- $\boldsymbol{G}$ is the weight of the pedestrian;
- $\boldsymbol{c_i}$ is the Fourier coefficient or DLF associated with the i-nth harmonic;
- $\boldsymbol{f_p}$ is the frequency of the steps;
- $\boldsymbol{\varphi_i}$ is the phase angle between the i-nth harmonic and the first.

Table 4.5 shows the values of DLF for (4.13).

Table 4.5. DLF for vandalism action (adapted from Agu *et al.* [15]).

Step frequency	DLF
$1.5 \leq f_p \leq 3.0$	1.5
$3.0 < f_p \leq 6.0$	0.6
$6.0 < f_p \leq 90$	0.1

4.5. Comfort Criteria and Verification Procedures

The characterization of the level of comfort of a structure is the balance between its mechanical properties and the actions imposed on it. To determine the structural response, a dynamic analysis of the structure under pedestrian actions is necessary, in which the fundamental equation of the movement is divided into its structural portion and the active portion (loads), as illustrated in Figure 4.9, in which, m, c and k are the mass, viscous damping and stiffness of the system, respectively, while $F(t)$ is the acting load.

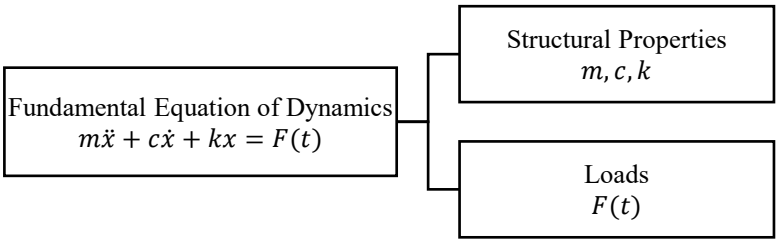


Figure 4.9. Dynamic analysis.

The comparison between structural properties and actions must be carried out based on established criteria, which refer to the critical frequencies and maximum accepted accelerations. The design of a footbridge should ensure that reduced vibration levels are achieved during its lifetime.

In this way, comfort can be achieved in two ways: by limiting the maximum vertical and horizontal accelerations to the values tolerable by pedestrians or by designing structures where their fundamental frequencies are far from the critical frequencies, which must be translated by the frequencies that characterize the pedestrian movement. The procedure for analyzing a pedestrian bridge can be summarized by the organization chart illustrated in Figure 4.10.

4.5.1 Bands of Resonance Risk

The definition of the critical range of natural frequencies and their comparison with those calculated for the pedestrian bridge is the first step in assessing the degree of comfort of the pedestrian structure. It is suggested that, whenever one or more natural frequencies of the structure are within the resonance risk band, a dynamic analysis of the structure is carried out. Table 4.6 summarizes the frequency ranges where there is a risk of resonance.

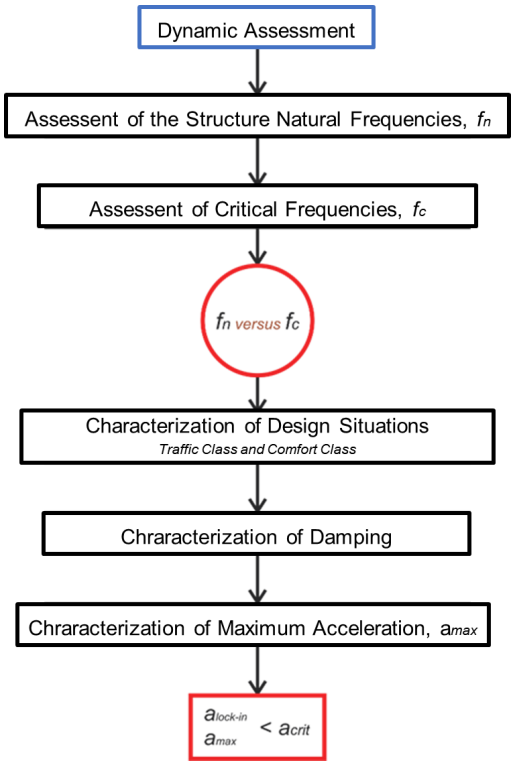


Figure 4.10. Dynamic analysis organization chart (adapted from Hivoss [2])

Table 4.6. Frequency range with risk of resonance

Document	Frequency (Hz)	
	Vertical	Horizontal
BS 5400 [1]	$f_p < 5.0$ [1]	$f_p < 1.5$ [2]
Bachmann [3]	$1.6 < f_p < 2.4$	
Sétra [4]	$1.0 < f_p < 5.0$	$0.3 < f_p < 2.5$
Hivoss [5]	$1.25 < f_p < 4.6$	$0.5 < f_p < 1.2$
EN 1990 – Annex A2	$1.25 < f_p < 2.3$	$0.5 < f_p < 1.2$

Notes

[1] *Verification made from the calculation of the natural frequency of the first vertical mode with the bridge unloaded*

[2] *Check done with the effect of the pedestrian mass*

[3] *To consider a statistical distribution of the step frequency; for pedestrian structures with reduced stiffness and reduced damping, the range is limited to 3.5 and 4.5 Hz*

[4] *Frequency bands defined from four risk levels*

[5] *It mentions that the vertical excitation through the second harmonic can take place*

4.5.2. Comfort Class Characterization

According to Hivoss [2], human comfort criteria are, in general, defined by a limit acceleration for the pedestrian structure. Regarding the limitation of accelerations, the various technical documents do not present consistent proposals. Table 4.7 shows the recommendations of different documents.

Table 4.7. Maximum recommended accelerations (adapted from Alves [19])

Document	Acceleration (m/s²)	
	Vertical	Horizontal
BS 5400-2	$\leq 0.5 \cdot \sqrt{f_n}$	–
Canadian Norm	$\leq 0.25 \cdot f_n^{0.78}$	–
EC 1990 - Annex A1	≤ 0.70	≤ 0.20

In the context of this research, the criterion proposed in Hivoss [2] will be used, which consists of the definition of four comfort classes, each of which limits the values of accelerations (Table 4.8).

Table 4.8. Comfort classes and maximum accelerations (adapted from Hivoss [2]).

Comfort class	Degree of comfort	Limit Accelerations (m/s²)	
		Vertical	Lateral
CL 1	Maximum	< 0.5	< 0.1
CL 2	Medium	$0.5 \leq a_{max} \leq 1.0$	$0.1 \leq a_{max} \leq 0.3$
CL 3	Minimum	$1.0 < a_{max} \leq 2.5$	$0.3 < a_{max} \leq 0.8$
CL 4	Unacceptable Discomfort	$a_{max} > 2.5$	$a_{max} > 0.8$

4.5.3. Lateral Lock-in

Also called *feedback* [20], the *lock-in* effect is the phenomenon in which a group of pedestrians, in progress with random step rates and phase angles, gradually synchronize their step frequency with the frequency of oscillation of the structure until it enters in phase with the movement of the pedestrian bridge [21]. In effect, there is an amplification of the structure's response to the action of the pedestrian and this occurs both in the vertical and horizontal directions.

Because of their joints, vertical vibrations are attenuated by the pedestrian's body and, thus, will be less susceptible to perception. In the horizontal direction, human sensitivity is much higher and causes the pedestrian to compensate for the displacement of its centre of gravity, moving the feet apart during the walk and adjusting its frequency with that of the structure.

With the gradual synchronization, the lateral displacements are amplified and pedestrians' discomfort increases, and more and more individuals start to walk synchronously with the displacement of the structure.

Caetano *et al.* [20] have validated the expression (4.14) which one was deduced to describe the behaviour of London's Millennium Bridge, initially proposed by Dallard *et al.* [22], to estimate the number of pedestrians, $\boldsymbol{N_L}$, from which the synchronization effect is initiated.

$$\boldsymbol{N_L = \frac{8\pi\xi M}{k}} \tag{4.14}$$

where:

- $\boldsymbol{\xi}$ is the critical damping ratio;
- $\boldsymbol{M}$ is the modal mass;
- $\boldsymbol{k}$ is a constant.

The expression (4.14) is valid for a uniform distribution of pedestrians on the deck, with sinusoidal vibration mode and constant $\boldsymbol{k}$ defined with the value of $\mathbf{300\ N \cdot s/m}$ for a frequency range of $\mathbf{0,5}$ to $\mathbf{1,0\ Hz}$.

In the context of the possibility of lateral synchronization, the manual Hivoss [2] defines a range of accelerations that can initiate the phenomenon, as follows

$$\boldsymbol{a_{lock-in} = 0.1\ to\ 0.15\ \frac{m}{s^2}} \tag{4.15}$$

4.6. Final Considerations

Footbridges are characterized by structural slenderness, low weight and high susceptibility to vibrations, especially those induced by pedestrians. The diversity of actions that can be produced by human action makes the study of the responses to pedestrian structures a realm that makes it possible to address different criteria and requirements and to consider equally different definitions and assumptions.

As shown, the actions that produce the most relevant dynamic effects on footbridges are those arising from the movement of pedestrians on the walkway. In this sense, each pedestrian step is characterized with an impulse, directed vertically and horizontally, which induces the structure to vibrational movement, which can lead to discomfort in the use of the structure.

Critical limits were shown in terms of frequencies and accelerations defined by the various guidelines to guarantee human comfort in footbridges. In this context, in the present investigation, we will try to explore the concept of viscoelastic damping to counteract the vibrational tendency of pedestrian structures, through the use of polymeric composites.

4.7. References

[1] E. T. Ingólfsson, C. T. Georgakis, and J. Jönsson, "Pedestrian-induced lateral vibrations of footbridges: a literature review," *Eng. Struct.*, vol. 45, pp. 21–52, 2012, doi: 10.1016/j.engstruct.2012.05.038.

[2] Research Fund for Coal and Steel, "Hivoss - Human induced Vibrations of Steel Structures - Design of Footbridges - Background Document," 2007.

[3] C. Moutinho, Á. Cunha, and E. Caetano, "Análise experimental da eficiência de TMDs para a atenuação da resposta sísmica de estruturas de edifícios," *6º Congr. Nac. Sismol. e Eng. Sísmica*, pp. 621–630, 2004.

[4] H. Bachmann and W. Ammann, *Vibrations in Structures - Induced by Man and Machines*. Zurich: IABSE - AIPC - IVBH, 1987.

[5] S. Živanović, A. Pavic, and P. Reynolds, "Vibration serviceability of footbridges under human-induced excitation: A literature review," *J. Sound Vib.*, vol. 279, no. 1–2, pp. 1–74, 2005, doi: 10.1016/j.jsv.2004.01.019.

[6] C. M. dos Santos, "Avaliação do comportamento dinâmico de uma passarela submetida a carregamentos induzidos por pedestres," Master Thesis, Universidade Federal do Rio de Janeiro, 2011.

[7] Setra, "Guide méthodologique passerelles piétonnes (Technical guide Footbridges: Assessment of vibrational behaviour of footbridges under pedestrian loading)," Service d'études techniques des routes et autoroutes, Paris - France, 2006.

[8] Y. Matsumoto, H. Shiojiri, and T. Nishioka, "Dynamic design of footbridges," *IABSE Proc.*, pp. 17–78, 1978.

[9] M. Kobayashi, *Prediction and Control of Pedestrian Induced Vibration on an Interior Footbridge*, no. February. Lyngby, Denmark: Department of Civil Engineering, Technical University of Denmark, 2011.

[10] J. E. Wheeler, "Prediction and control of pedestrian-induced vibration in footbridges," *J. Struct. Div.*, pp. 2045–2065, 1982.

[11] M. de M. Queiroz, "Técnicas de análise dinâmica de passarelas," Master Thesis, Universidade Federal do Rio de Janeiro, 2014.

[12] J. P. F. Sanches, "Controlo de Vibrações em Pontes Pedonais Sujeitas a Acções de Multidões," Master Thesis, Universidade Nova de Lisboa, 2012.

[13] V. Sána, M. Polák, T. Plachy, and E. Fanfulová, "Comparison of current models for excitation of footbridges due to walking Pedestrians and Vandalism With Experiment," in *9th International Conference on Structural Dynamics*, 2014, no. July, pp. 983–990.

[14] E. Caetano, Á. Cunha, and C. Moutinho, "Vandal loads and induced vibrations on a footbridge," *J. Bridg. Eng.*, vol. 16, no. 3, pp. 375–382, 2011, doi: 10.1061/(ASCE)BE.1943-5592.0000154.

[15] E. Agu and M. Kaspersky, "A random load model for loads induced by coordinated movements of crowds," in *6th European Conference on Structural Dynamics*, 2005, pp. 4751–4754, doi: 10.1109/ICETCE.2011.5776407.

[16] T. de C. A. P. Krus, "Análise dinâmica e controlo passivo de vibrações de uma ponte pedonal," Master Thesis, Universidade Nova de Lisboa, 2012.

[17] Research Fund for Coal and Steel, "Hivoss - Human Induced Vibrations of Steel Structures - Design of Footbridges - Footbridge Guidelines," 2008.

[18] FIB, *Guidelines for the Design of Footbridges*, Bulletin 3. Lausanne, Switzerland: fédération internationale du béton (fib), 2005.

[19] R. A. F. Alves, "Comportamento dinâmico de pontes sob a acção pedonal," Master Thesis, Faculdade de Engenharia da Universidade do Porto, 2008.

[20] E. Caetano, Á. Cunha, A. da Fonseca, R. Bastos, and A. da F. Junior, "Assessment and control of human induced vibrations in the new Coimbra footbridge," in *Footbridge 2005 - Second International Conference*, 2005, no. Figure 1.

[21] M. C. A. Junior, "Avaliação experimental da sincronização por densificação de grupos de

pedestres em passarelas," Master Thesis, Universidade Federal da Paraíba, 2008.

[22] P. Dallard, A. Flint, S. Le Bourva, A. Low, R. M. R. Smith, and M. Willford, "The London Millenium Footbridge," *Struct. Eng.*, vol. 79, no. 22, pp. 17–35, 2001, doi: 10.2749/101686699780481709.

5. Summary of Appended Papers

This chapter presents a summary of the papers that constitute this doctoral thesis.

The development of this research began with the study of rheological aspects involving polymer-based materials and their viscoelastic behaviour. As described in Chapter 2, due to their molecular peculiarities, polymers and polymer-based composites exhibit mechanical behaviour ranging from essentially elastic materials to viscous ones. Such behaviour is the basis for studying how polymers attenuate vibrations in structures, particularly those predominantly affected by dynamic behaviour, such as footbridges.

The basis of viscoelasticity theory and classical rheological creep models, as described in Chapter 2, have proven ineffective in predicting the structure's service life. The investigation of the creep response of selected engineering materials should integrate the design of structures subjected to mechanical loads over a long period of operation (self-weight, static loads).

In this sense, it became necessary to search for alternative procedures for the determination of the critical phases of deformation in the long term. Through the work developed by Professor Guibert Crevecoeur, formulations were proposed that link the creep and relaxation functions and the possibility of obtaining the dynamic moduli from the creep compliance and the relaxation modulus functions. The first two papers encompass this analysis and characterisation.

As stated in Chapter 3, the particular behaviour of polymer-based materials is reflected by their intrinsic ability to dissipate kinetic energy, namely by their viscoelastic damping. Therefore, the linear viscoelastic materials should be experimentally characterised under (i) constant static load and/or (ii) harmonic load. In the first load case, the viscoelastic behaviour is described through creep compliance or the relaxation modulus. The viscoelastic behaviour is characterised by the complex modulus and the loss factor in the second load case. In this context, Paper 3 presents the deduction of a function capable of effectively describing the dynamic behaviour of the polymer-based composite and correlating this behaviour with creep.

It becomes important to clarify that at the beginning of this research, the strategy outlined was to develop a composite material capable of providing high levels of damping, and then a new footbridge architecture would be developed, and the physical model would be built. Despite the extensive research and analytical development of functions that allow estimating the service life of polymer-based structures, as well as establishing reciprocity between creep and relaxation with the complex modulus, it was assessed that it would be of more value to the research to use an existing GFRP-based footbridge for the dynamic study since the development of a new model with unique architectural characteristics would require intensive research for comparative evaluation with structures made of conventional materials.

Thus, to assess the benefits of using a structure made of pultruded GFRP rather than a conventional material—steel, a comparative analysis between the dynamic characteristics of GFRP and steel beams is presented in Paper 4. Furthermore, to exclusively address the structural damping of GFRP and Steel materials, a test program was conducted based on samples of similar dimensions of the two materials tested in a free boundary condition. From these tests, it was possible to conclude that the damping factor of GFRP is approximately five times higher than that of steel. Finally, the results presented in this paper were used to perform an extensive modal characterisation and dynamic analysis of the São Silvestre pedestrian bridge, a GFRP reinforced concrete hybrid bridge.

Using the load models and comfort criteria described in Chapter 4, the structural response to pedestrian loads measured on the footbridge was used to calibrate the numerical model of the GFRP structure. These results are shown in Paper 5, together with the results of an equivalent numerical model made of steel. This paper shows that the load models defined in guidelines are not adequate to predict the structural response, both using steel or composite based materials, due to the high natural frequencies of the footbridge, which are typical of short spans. Nevertheless, high harmonic

effects are observed that may be responsible for high amplitudes of vibration. Moreover, when acceleration grows, it is visible that the composite-based material exhibits a much better performance than steel due to the higher capacity to attenuate vibrations.

5.1. Paper 1

Dacol, V.; Caetano, E. ***Modelling the three-stage of creep.*** *Proceedings of the 3rd RILEM Spring Convention and Conference (RSCC2020).Volume 3: Service Life Extension of Existing Structures, Guimarães, Portugal, 2020. https://doi.org/10.1007/978-3-030-76465-4.*

This paper presents a study conducted to estimate the 4 instants of time characterising the three stages of creep curve of polymeric and polymer-based materials presented in Chapter 2: (1) the first transition point, that is the transition point between transient and steady creep; (2) the secondary point, that is the inflexion point of the creep curve where the strain rate reaches its minimum; (3) the second transition point, that is the transition point between steady and accelerated creep; and (4) the instability point.

The creep curve used in this study was constructed using data resulting from a numerical simulation of an experiment of Liu et al. (2008), where a sample cut from a 24'' HDPE-Pipe was tested for five different stress levels.

A brief review of the fitting methodology was first presented concerning the creep behaviour and its three stages. This methodology was applied to the numerical description of the creep behaviour of high-density polyethene. The time-dependent and stress-dependent approach was easily applied to a viscoelastic material. The transition points were calculated, and a creep safety envelope was defined and a lifetime prediction could be made.

Although there was no comparative analysis of the useful life of the material based on standards, the creep curves obtained by the Crevecoeur adjustment methodology evidenced a good fitting to the data presented by Liu et al. (2008).

The paper follows the work published by Crevecoeur (1992) and is based on a combination of an exponential and a power-law approach for fitting the creep test data to predict the lifetime of the structural system and its creep safety envelope.

5.2. Paper 2

Dacol, V.; Caetano, E.; Correia, J.R. A Combined Exponential-Power-Law Method for Interconversion between Viscoelastic Functions of Polymers and Polymer-Based Materials. Polymers 2020, 12, 3001. https://doi.org/10.3390/polym12123001. Impact Factor: 4.493 (2020).

This paper first presents a brief review of some methods of interconversion between linear viscoelastic properties of polymeric composites in the time domain. Their theoretical background is presented and the relation between creep and relaxation and the constitutive integrals of linear viscoelasticity are summarised. It was shown that most of the classical methods of interconversion are based on the power-law and exponential methods of the fitting. Despite their ease of application, these methods are not efficient in representing the full-path curve of the creep behaviour of polymers and polymer-composites, namely their three creep stages.

In the second part of the paper, a new approximate interconversion scheme that uses a convenient Laplace transform and an approximated Gamma-function to convert the measured creep compliance to relaxation modulus is presented. Data available in the literature are used to assess the consistency of the viscoelastic functions via the new interconversions presented in this work. The Exponential Power Law (EPL) method of creep fitting is converted to the EPL relaxation modulus expression, and the creep data is successfully fitted. To validate the EPL interconversion, three spectrum data collected from the literature are used as a reference. The results obtained show that (i)

the EPL fitting method proposed herein is very simple to implement, due to the small number of coefficients that need to be determined, and is quick to apply. In addition, (ii) the method is stable and accurate, as attested by the achieved Pearson correlation coefficient, greater than 0,97 for all test data considered.

5.3. Paper 3

Dacol, V.; Caetano, E.; Correia, J.R. A New Viscoelasticity Dynamic Fitting Method Applied for Polymeric and Polymer-Based Composite Materials. Materials 2020, 13, 5213. https://doi.org/10.3390/ma13225213. Impact Factor: 3.920 (2020).

This paper presents a new approximate interconversion scheme to convert the measured dynamic moduli into creep compliance modulus and relaxation modulus. The proposed method uses a convenient Laplace and Carson transform and its relationship to the Fourier Domain, coupled with the application of the Moivre and Euler Theorem.

The Exponential Power Law (EPL) creep fitting method has been converted to the EPL dynamic modulus equation and the data available in the literature have been successfully fitted. In particular, the test data concerning three different polymeric or polymer-based composites were used to validate the numerical approach: a pure polymer thermoplastic resin specimen, an E-glass-epoxy composite laminate, and an elastic-viscoelastic sandwich beam.

The results obtained show the accuracy of the EPL Method in fitting the data from creep, relaxation, and dynamic tests. Moreover, the method can show the three stages of creep (long-time behaviour). In addition, it is shown that fitting based on the EPL method is easy to implement since only three terms need to be found in any data spectrum, and no pre-smoothing procedure is required to ensure a good fit. Furthermore, the stability of this method is demonstrated by the achieved Pearson correlation coefficients, which was higher than 0.96 for the different examples.

5.4. Paper 4

Dacol, V.; Caetano, E.; Correia, J.R. Comparative Study of Damping on Pultruded GFRP and Steel Beams. Polymers 2021, 13, 2201. https://doi.org/10.3390/polym13132201. Impact Factor: 4.493 (2020).

This paper aims to investigate the dynamic behaviour of GFRP free-supported beams to evaluate their modal characteristics (frequency, damping, and modal shape). To assess the benefits of using a structure made of pultruded GFRP rather than a conventional material—steel, a comparative analysis between the dynamic characteristics of GFRP and steel beams is performed. To specifically address material damping and to minimise the interference of the boundary conditions, the beams are tested in a free condition, resting on a low-density foam base. The results show that the damping capacity of GFRP is much higher than that of steel, as the measured damping factor of GFRP is five times higher than that of steel for the same boundary conditions and similar geometry. Furthermore, the fact that the frequencies of the tested specimens resemble the two different materials highlights the perceived damping qualities of the polymer-based composite material. Finally, an energy method for evaluating the influence of the scale factor on material damping is applied, which made it possible to infer that damping varies as a function of frequency but is not explicitly affected by the length of the specimens.

5.5. Paper 5

Dacol, V.; Caetano, E.; Correia, J.R. Modal Identification and Damping Analysis of a Full-Scale GFRP-SFRSCC Hybrid Footbridge. Submitted to Engineering Structures in January 2022. Impact Factor: 4.471 (2021).

This paper presents a study about the dynamic behaviour of an 11 m long GFRP-concrete hybrid footbridge, made of two I-shaped pultruded glass fibre reinforced polymer (GFRP) main girders and thin steel fibre reinforced self-compacting concrete (SFRSCC) deck, in operation since 2015 in the city of Ovar. The main goal was (i) to assess the benefits of using a structure made of pultruded GFRP instead of a conventional material (steel), and (ii) to improve the knowledge and understanding of the dynamic properties of composite footbridges. Based on experimental techniques of output-only and input-output identification, the resonant frequencies, damping ratios and mode shapes of the footbridge were identified using the Enhanced Frequency Domain Decomposition (EFDD) and the Operational PolyMAX methods. A finite element (FE) model of the footbridge was developed and, after calibration with test data, a study on the damping characteristics of the GFRP footbridge was conducted to compare its structural performance under human loads, especially its vibration mitigation capacity, with that of an equivalent structural system made of steel profiles. The identified modal components were also compared to experimental results collected from the literature for a conventional-based material footbridge. The impact of higher harmonics of the pedestrian load in the dynamic responses of short-span footbridges was also evaluated, and their important influence was demonstrated. Overall, the results obtained show that the structural use of polymer-based composite materials as footbridge components can contribute to limiting vibrations or even act as self-dampers.

6. Conclusions and Future Work

6.1. Conclusions from the research

The main objective of this PhD thesis was to prove the advantages of the use of polymer-based composite materials in the design of footbridges, particularly in the aspect of their dynamic behaviour and their ability to attenuate excessive pedestrian-induced vibrations. In addition, it was sought to produce consistent parameters that make it possible to develop numerical models capable of simulating the behaviour of footbridges designed with fibre-reinforced polymer-based composite materials with reasonable accuracy.

The purpose of this work was to find an answer to the following central question:

> *Could the viscoelastic damping characteristic of polymer-based composite materials improve the dynamic performance of footbridges, especially in terms of damping ratio and vibration attenuation?*

Understanding and modelling the viscoelastic behaviour of polymers and polymer-based materials for a wide range of quasi-static and high strain rates is of great interest to applications in which they are subjected to mechanical loads over a long time as the self-weight or other static loads. In this context, an incursion was made into the viscoelastic theory. Its manifestations and its relationship with viscoelastic damping, understood as a component of the polymer complex modulus was established.

This doctoral project's initial idea consisted of defining, producing, and testing a composite material that could provide damping levels within a pre-defined range, namely between 2% and 5%. Establishing a method to predict the lifetime of a composite footbridge, where the creep phases could provide a clear insight into the structure's durability, was another challenge at this phase. In parallel, evaluating and measuring the influence of creep on the damping of the polymer-based composite was an additional element that emerged during the development of the interconversion method between quasi-static and dynamic behaviour of polymeric and polymer-composite materials.

In this sense, the interconversion between the creep and relaxation functions was defined and, from these, the connection with the complex modulus was established.

After the analytical functions have been developed and tested, the next step would be to produce the composite and test it. Then, a new pedestrian architecture could be developed, and the physical model would be built. Despite the extensive research and analytical development of functions that allow estimating the service life of polymer-based structures, as well as establishing reciprocity between creep and relaxation with the complex modulus, a change of strategy was required, and it was decided to use an existing GFRP-based footbridge for the dynamic study. The PhD research developed by Dr José Gonilha and the construction of the São Silvestre footbridge provided better conditions for the comparative analysis between pedestrian structures of polymeric composite-based materials and conventional ones, such as steel. However, as the São Silvestre footbridge is not monitored concerning its deflection, it was not possible to use the functions developed to estimate the structure's service life.

Indeed, the "creep" component was not fundamental for the accurate understanding of the damping capacity of GFRP structures, even though creep is intrinsically linked to the energy dissipation of the material. However, having a numerical model that allows estimating the service life of this type of structure is an important issue for further studies.

In the following paragraphs, the evolution of this work is briefly described and the main achievements and findings.

The Viscoelasticity Approach

During the first phase of this research, the viscoelasticity theory was studied in-depth, and an extensive review of the concepts of creep and relaxation in polymers was undertaken. The knowledge of how creep sets specific limits on the use of polymer-based composites in structures was fundamental to validate the mechanical models used in the design of footbridges.

The research conducted by Professor Guibert Crevecoeur on exponential equations combined with power functions as the base of this phase. In fact, "creep modelling for structural analysis" aims to develop methods to simulate and analyse the time-dependent changes of stress and strain states in engineering structures up to the critical stage of creep rupture and including the service stage.

The first step was to develop a new approximate interconversion scheme using a convenient Laplace transform and an approximated Gamma function to convert the measured creep compliance to the relaxation modulus. In terms of the scientific motivation of this part of the work, two main aspects are highlighted: (i) existing methods are not able to represent satisfactorily the full-path of creep, namely its three stages; and (ii) a method of interconversion becomes an important tool as it allows for more efficient utilisation of resources in a rheology laboratory.

The second step refers to the dynamic behaviour of polymeric and polymer-based composite materials under service conditions and the need for their characterisation. A powerful and simple to implement technique was proposed for the processing and analysis of dynamic mechanical data in which the dynamic moduli expressions may be obtained from the Exponential-Power Law Method (EPL) of the creep compliance and the relaxation modulus functions. The advantages of the EPL method were shown, namely its simplicity and straightforwardness in performing the desirable interconversion between the quasi-static and dynamic behaviour of polymeric and polymer-based composite materials.

The Dynamic Evaluation

The second phase of this research focused on experimental campaigns for the modal identification of structures and for the assessment of the benefits of using a structure made of pultruded GFRP profiles rather than conventional material, like steel. For this purpose, a comparative analysis of the dynamic characteristics of GFRP and steel beams was performed. An experimental model with free supports was used to eliminate the influence of boundary conditions. These tests were performed to gather modal data from the specimens, namely, the vibration frequencies of the beams, by performing input-output testing based on the excitation of an impact hammer.

As expected, for a given frequency, the damping ratio of the polymer-based GFRP composite specimen was higher than that of the steel-based specimen. In addition, a relatively simple mathematical expression has been proposed to evaluate the trend of the damping ratio of the material as a function of the frequency variation. These tests provided a model that allows evaluating whether the damping levels of a footbridge built with polymer-based composite materials are higher compared to the same structure built from steel profiles.

Finally, the modal characterisation of a hybrid footbridge, made of GFRP profiles and an SFRSCC deck, installed in northern Portugal and operation since 2015, was presented. An experimental campaign of the São Silvestre footbridge was carried out, which comprised an extensive modal identification, and focused particularly on the damping performance of polymer-based materials, namely GFRP profiles, to dissipate energy and to mitigate the vibrations of slender structures, as footbridges.

Several numerical analyses were performed by varying the pedestrian's velocity and simulating one or more pedestrians crossing the footbridge. Furthermore, the tuned numerical model of the GFRP-SFRSCC hybrid footbridge was replicated and the GFRP profiles were replaced by commercial steel profiles. This second model was submitted to the same load scenario and the results were used for a comparison purpose. Despite its greater deformability than the steel-based hybrid system, the GFRP-based hybrid system showed a better response in maximum vertical acceleration, showing 24%

lower amplitude for a single pedestrian moving. Concerning the crowd simulations, the GFRP-based model presented an amplitude of vertical acceleration 48% lower than that of the steel-based model.

In addition, it was possible to show the high importance to improve the characterisation of actions and in considering high harmonics in modal analysis of structures with high frequencies, as short-span footbridges.

The results obtained show that the structural hybrid solution for pedestrian usage, characterised by its susceptibility to excessive vibrations due to its slenderness, can improve its dynamic performance with the use of polymer-based composites, especially in terms of damping ratio and vibration attenuation.

6.2. Looking to the future

This PhD work has dealt with some cross-cutting themes, some of which should be further developed in the future. In this context, the following questions/topics are worth being mentioned and investigated in future studies:

1. What influence can the ageing of the polymeric and polymer-based composite materials provide to the modal characteristics of the structure?

Damping in polymers is closely related to their viscoelastic behaviour and the chains and bonds between their molecules. Molecular ageing due to various environmental agents (acting in isolation or combined, e.g., moisture, temperature, UV radiation) can influence the polymer's ability to rearrange its bonds when subjected to static or dynamic stresses. In this perspective, it is expected that the material's ability to dissipate energy can be affected. How and how much would be the answer to be sought.

2. Does the creep behaviour presented by polymeric and polymer-based composite materials affect its damping capacity?

As mentioned above, damping in polymeric materials is linked to their viscoelastic behaviour. Creep compliance can be understood as a slow deformation that can be reversed within certain limits in the case of a polymer. Since polymeric bonds rearrange themselves when creep occurs, it would be expected that the damping of this type of material would undergo some change in this process. In this sense, evaluating the dynamic behaviour of polymers along the different creep stages could provide answers to this question.

3. How to insert the viscoelastic damping, namely the complex modulus, in a numerical model to estimate the behaviour of polymer-based composite structures?

The numerical implementation of the viscoelastic behaviour of composite materials in FEM should allow the dynamic analysis of laminated and pultruded structures, in which the material damping due to the inherent characteristics of polymeric resins and reinforcing fibres corresponds to a given complex modulus. Because of their mechanical properties, polymeric composites require numerical treatment in the frequency domain, which should concomitantly provide temporal analysis since time-dependent phenomena, such as creep and ageing, affect the complex modulus and, consequently, their viscoelasticity. In addition, the dependence of these materials on temperature variations constitutes another variable of the system. Thus, the numerical simulation of the structural behaviour through the incorporation of viscoelasticity should be able to describe the variation of this behaviour as a function of the temperature and frequency, in addition to the

transient aspects of the material (creep, relaxation, ageing). A viable numerical proposal would be the possibility of including the loss and dynamic modulus functions in the damping and stiffness matrices of the system. However, this nonlinearity may overload the analysis model, making it slow; moreover, it would require long-term experimental data on the durability of generic composite materials (i.e. depending on the type of fibres and resin, and other aspects, such as the type of processing), which presently is not available. The solution to this dichotomy is the core of this proposal.

Paper 1

Dacol, V.; Caetano, E.

Modelling the three-stage of creep.

Proceedings of the 3rd RILEM Spring Convention and Conference (RSCC2020). Volume 3: Service Life Extension of Existing Structures, Guimarães, Portugal, 2020. https://doi.org/10.1007/978-3-030-76465-4.

Modelling the Three-Stage of Creep



Vitor Dacol and Elsa Caetano

Abstract Over the last years, several studies have addressed the time-dependent mechanical behaviour of polymeric composites. When subjected to a constant stress, viscoelastic materials experience a time-dependent increase in strain. This phenomenon is known as viscoelastic creep and manifests as a tendency of a solid material to deform permanently under the influence of constant stress: tensile, compressive, shear or flexural. When applied to polymers, creep is the result of the inherent viscoelastic nature that causes time dependency of behavior. As well known, the initial strain in a material is roughly predicted by its stress-strain modulus. Then, the material will continue to deform slowly with time indefinitely or until rupture or yielding causes failure. A typical creep curve reveals a three-stage behavior, (1) the transient stage, where the deformation rate decreases with time, (2) the steady-state, characterized by a "relatively" uniform rate gradient and (3) the accelerated phase, where the strain rate increases until rupture. In polymers at low strains (nearly to 1%), creep is essentially recoverable after unloading. However, in certain cases, creep failure is the most important degradation mode of a structure (turbine blades, aircraft parts). Furthermore, in civil engineering works, this kind of deformations may be substantial throughout the required service life. The investigation of the creep response of selected engineering materials should integrate the design of structures subjected to mechanical loads over a long time of operation (self-weight, static loads). The aim of "creep modeling for structural analysis" is the development of methods to simulate and analyze the time-dependent changes of stress and strain states in engineering structures up to the critical stage of creep rupture, passing through service state. In particular, the key in identifying these three stages above described lies in the location of the transition points between stages. This work presents a study conducted to estimate the 4 instants of time of the creep curve: (1) the first transition point, that is the transition point between transient and steady creep; (2) the secondary point, that is the inflexion point of the creep curve where the strain rate reaches its minimum; (3) the second transition point, that is the transition point between steady and accelerated creep; and (4) the instability point. This research follows the work

V. Dacol (✉) · E. Caetano
Faculty of Engineering (FEUP), CONSTRUCT (ViBEST), Porto, Portugal
e-mail: vitor.dacol@fe.up.pt

© The Author(s), under exclusive license to Springer Nature Switzerland AG 2022

J. Sena-Cruz et al. (eds.), *Proceedings of the 3rd RILEM Spring Convention and Conference (RSCC 2020)*, RILEM Bookseries 34,
https://doi.org/10.1007/978-3-030-76465-4_7

publish by Crevecoeur [3] and is based on a combination of an exponential and a power law approach to the creep test data of HDPE pipe sample.

Keywords Viscoelasticity · Creep · Creep behaviour · Stages of creep · Polymer Ageing

1 Introduction

Creep is a slow, continuous deformation of a material under a constant stress and temperature. As a result of its inherent viscoelastic nature, polymers present a time-dependent deformation that occurs under any temperature. Creep of polymeric solids can be subdivided into several stages, where instantaneous creep takes place upon loading, followed by transient creep where the strain-rate reaches its minimum. It then increases and approaches an asymptotic limit and rupture occurs.

Therefore, the study on the process of creep is essential and significant for engineering applications concerning temperature and stress and has been a challenge in the design of structures subjected to loads for long periods of time. According to Monfared [14], predicting creep behaviour is of utmost importance on advanced reinforced or non-reinforced materials design, such as polymeric composite.

In fact, to define parameters to prevent unsafe and undesired events such as progressive deformations and local reduction of material strength, may be an important tool in development of more slender and durable structures. In this context, estimating of transition points between stages of creep may help in linear and non-linear analysis of the structure behaviour.

On the other hand, Crevecoeur [6] shows a non-linear kinetics in the ageing of biological systems, which is characterized by three successive stages such as observed in a creep curve of polymeric composite. Crevecoeur shows that a model useful for the follow-up of operating inert systems allows to find back typical curves and laws related to the ageing of biological systems.

Based on the work of Crevecoeur and through a combination of an exponential and a power law approach to the creep test data of FRP sample, this paper proposes a simple approach to modelling the three-stages of polymer creep.

2 Theoretical Background

The combination of mechanical behavior of elastic and viscous materials characterizes the response of a viscoelastic material.

According to Barra [1], due its molecular nature, the polymeric mass may be seen formed from a twisted or tangled chains in its undeformed state. Subjected to constant tension, molecules exert a retractive response to this tension in order to maintain their stable (folded) conformation. Under continuous tension, the chains

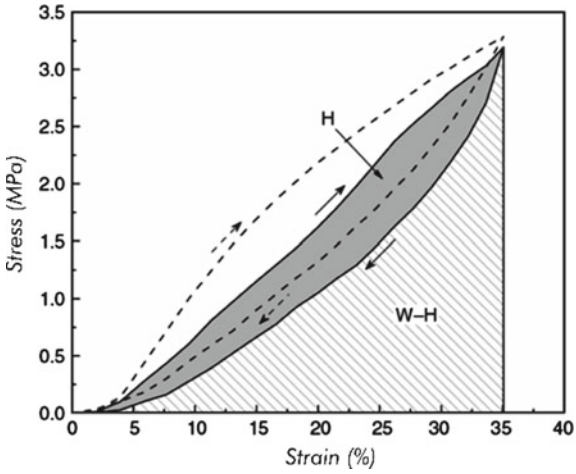


Fig. 1 Stress-strain relationship of viscoelastic materials

slide relatively to each other and the tangled structure is deformed into an extended conformation. When the applied load is released before the creep rupture occurs, an immediate elastic recovery equal to the elastic deformation, followed by a period of slow recovery is observed.

Within certain limits, the graphic tension versus deformation will take the shape of an ellipse. This format tends to be maintained to the extent that the amplitudes of tension and deformation grow (Fig. 1).

The viscoelastic behaviour manifests itself in several ways, which comprise: (a) creep under constant load; (b) relaxation of tension under constant deformation; (c) recovery of time dependent deformation after complete removal of load; (d) rupture due to time-dependent creep; (e) fatigue resistance dependent on the excitation frequency.

Basically, there are three principal ways to describe the viscoelastic behavior [19] in time domain. The first one is the Boltzmann superposition principle so-called the integral representation expressed by the convolution integral (1).

$$\varepsilon(t) = \int_{-\infty}^{t} J(t - \tau_n) d\sigma(\tau_n) \tag{1}$$

The second way, represented by a differential equation (2), uses assemblages of Hookean springs and Newtonian viscous elements (dashpots) as models through several forms of combinations. For a Maxwell rheological model, total strain yields:

$$\frac{\partial \varepsilon}{\partial t} = \eta \dot{\varepsilon} \tag{2}$$

The third method is based on assumptions about the molecules themselves which dynamic tests are more convenient to be used for. This last method will not be described in this paper.

2.1 Creep

Depending on the level of excitation applied, the material may not recover to its original shape, and then a permanent deformation becomes installed. The magnitude of this permanent deformation will depend on the duration and the amount of tension applied, as well as the temperature [8].

For a constant temperature, this creep description is illustrated by Fig. 2 and translated by expression (3).

$$J(t) = \in (t)/\sigma_0 \tag{3}$$

For most applications, composite structures may be designed using linear elastic analysis. However, due to the effects of environment, there are instances where time dependent phenomena such as creep may be important long-term design considerations.

In these cases, creep failure is the most important degradation mode of a structure (turbine blades, aircraft parts) and its behavior must be known until its failure. An example showing importance of the creep phenomenon is the creep behavior of epoxy-based structural adhesives. Compared to other joining methods, welding or bolting for example, epoxy-based structural adhesives provide advantages, such as its high strength-to-weight ratio [10].

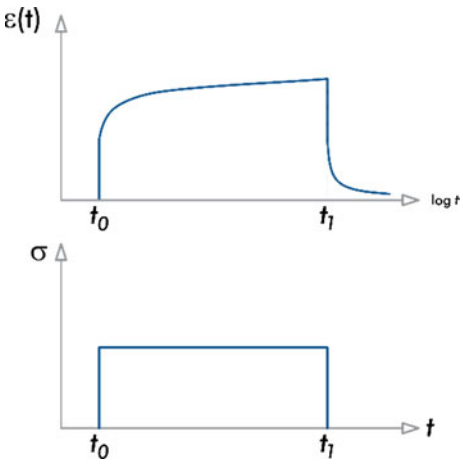


Fig. 2 Creep and recovery description

2.2 The Three-Stages of Creep

As known, viscoelastic material is a rheological material that exhibits time-temperature rate of loading dependence, with the response being a function of the current input and also of the current and past input history.

Under a sustained load over a long period of time, viscoelastic materials undergo three stages of strain evolution (Fig. 3).

The typical creep curve showed in Fig. 3 may be described as follow:

(a) First stage: so-called Primary or Transient creep, in which creep occurs at a decreasing rate;
(b) Second stage: so-called Second or Steady-state creep, in which strain rate reaches its minimum and shows a nearly constant value;
(c) Third stage: so-called Tertiary or Accelerated creep, where the strain rate increases quickly and its end the rupture occurs.

Figure 4 shows the strain rate of creep behavior and the total relationship of an ideal creep curve, the so-called creep bathtub. The bathtub curve usually gives the failure rate for an operating system.

According to Naumenko and Altenbach [15], the secondary creep is for many applications the most important creep model. The relative equilibrium, i.e., a uniform rate of strain gradient, enables the long-term behavior of the structure to be analyzed

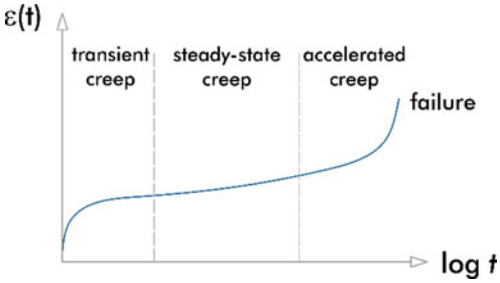


Fig. 3 Three-stages of creep

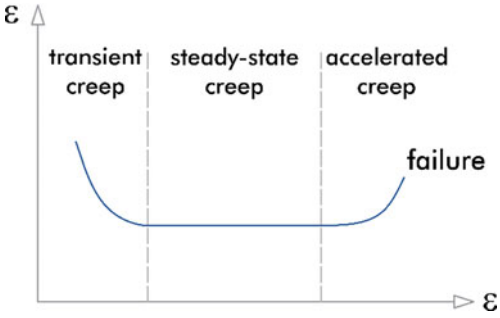


Fig. 4 Strain rate bathtub

assuming stationary creep processes. The extent of this stage depends on the combination of applied stress and system temperature. For relatively low stresses, the secondary stage may have a considerable extent before the onset of tertiary creep [2].

However, for components with a close fit, the primary creep needs to be taken into account. Bolts and copper canisters for the storage of spent nuclear fuel are an example of this [16].

On its turn, the tertiary creep leads to an unstable crack propagation and materials failure at end. The point where the accelerated creep starts is known as flow time and is defined as the time at which the shear deformation under constant volume starts, i.e., wherein the volume does not change. In an idealized curve of creep, tertiary stage only occurs at high stress or for ductile materials.

Furthermore, stress impacts significantly the strain rate where the increase of the stress by one order causes an increase of strain rate about four orders approximately [11].

Thus, to provide a better understanding of the structure behavior over time, these three-stages of creep should be known in order to avoid undesired behavior and even irreversible failure.

In particular, the key to determining these three-stages is in the fact that how to locate the transition points between stages along the creep curve. At last instance, it translates in the determination of secondary stage boundaries and in the predicting a creep safe envelope.

2.3 Biological Ageing Analogy

As defined in Luder [13], biological ageing is usually considered the continuous accumulation of damage or deterioration, at the level of the cells, tissues, organs or organism, which reduces vitality and ultimately leads to death.

Crevecoeur [6] shows that ageing could be seen as a multifactorial process. According to that, there is a widely observed non-linear kinetics in the ageing of biological systems, which is characterised by three successive stages, (1) firstly the ageing rate is high, but it decreases quickly to a minimum, from which (2) it remains nearly constant during the major part of the process until (3) it starts increasing again up to the final collapse of the system.

Concerning to this, taking ageing in the broad sense, as the whole process of going from birth to death, non-linearities appear. Those can be found in nature as reflecting successive periods in the life of biological systems, such as in the "survival, mortality or growth curves" (see Van Voorhies [20], Luder [13] and Fotsis et al. [9], respectively).

Selye [17] described the three stages of a system reaction, termed General Adaptative Syndrome (GAS) where "there is an integrated syndrome of closely interrelated adaptive reactions to non-specific stress itself". The first stage of GAS is the "Alarm Reaction", which can be corresponding to an elastic response of polymer under static

load; the second stage is called "Stage of Resistance", in which "a certain resistance is built up against the damaging stimulus" that could be translated in terms of steady creep rate; at last, the tertiary stage, called "Stage of Exhaustion", where the system loses its resistance and fails with several internal changes.

Thus, the parallel between biological ageing and polymeric creep behavior can be explained by assuming that a polymeric structure is composed of interconnected microstructures operating together under an input stress.

In this way, Crevecoeur [4] shows the similarity between creep behavior and mechanical system ageing, where the failure rate of mechanical repairable systems that deteriorate with time due to ageing can usually be visualized by a bathtub curve, as shown in the creep rate curve.

3 Modeling Approach

Crevecoeur [5] suggests a differential equation to synthesize the strain rate behavior of creep expressed by the bathtub curve:

$$\frac{\dot{\varepsilon}(t)}{\varepsilon_e(t)} = \alpha + \frac{\beta}{t_i} \tag{4}$$

where:

$\dot{\boldsymbol{\varepsilon}}(\boldsymbol{t})$ *is the strain rate*
$\boldsymbol{\varepsilon_e}(\boldsymbol{t})$ *is the measured strain from creep test*
$\boldsymbol{\alpha}, \boldsymbol{\beta}$ *are constants to be fitted, where* $\boldsymbol{\alpha} > \mathbf{0}$ *and* $\beta < \mathbf{1}$ *and* $\alpha \ll \boldsymbol{\beta}$.

Once (4) is integrated, it gives a combination of an exponential and a power law function (5).

$$\varepsilon_e(t) = k.e^{\alpha.t}.t^{\beta} \tag{5}$$

where:

$\boldsymbol{k}$ *is a constant for a given temperature and load.*

The three parameters $\boldsymbol{\alpha}$, $\boldsymbol{\beta}$ and $\boldsymbol{k}$ are constant as long as the physical constraints on the system remain constant, i.e., while the stress and temperature remain constant, these three parameters stay constant.

Crevecoeur [6] introduces a third system constraint which is called the internal "*organisation*" of the system. In the case of a polymer, this can be understood as the molecular arrange of the polymer and the micromechanical assemblage of the composite material.

According to Smith [18], the values of the parameter $\boldsymbol{\beta}$ will typically range between 0.15 and 0.65. However, this quantity can have values between 0 and 1 [3].

In (5) the quantity $(1/\boldsymbol{\alpha})$ gives the order of magnitude of the time scale for the creep process. Physically, this quantity corresponds to a time called "*instability time*", $\boldsymbol{t_i}$, [6], i.e.:

$$\frac{1}{\alpha} = \mathrm{t_i} \tag{6}$$

The *instability time* is one that from it there is a risk that the system starts to fail. At $\boldsymbol{t_i}$, if the load is not removed or operating conditions are not relaxed, the system will become impaired. It means that the system will usually continue after $\boldsymbol{t_i}$ but the process leading to the collapse is irreversibly started.

According to Crevecoeur [6], it is noticeable that the *instability time* occurs in tertiary creep and it is possible to divide the third stage into two parts, (1) before $\boldsymbol{t_i}$ (the predictable ageing) and (2) after $\boldsymbol{t_i}$ (the statistically predictable ageing).

The system failure takes place about 20–40% of life after $\boldsymbol{t_i}$.

Applying (6) into (5), yields (7).

$$\varepsilon_e(t) = k.e^{\left(\frac{t}{t_i}\right)}.t^{\beta} \tag{7}$$

where:

$\boldsymbol{\varepsilon_e(t)}$ *is the creep strain measured at* $\boldsymbol{t}$.

From Eq. (7), at some given time $\boldsymbol{t_n}$, it is expectable that:

$$t = t_i \ldots \text{that means} \ldots \varepsilon_e(t) = \varepsilon(t_i) \tag{8}$$

From the equality (8), Eq. (7) yields (8).

$$\varepsilon_i(t_i) = k.e^{1}.t_i^{\beta} \tag{9}$$

where:

$\boldsymbol{\varepsilon_i(t_i)}$ *is the strain at* $\boldsymbol{t_i}$.

The quotient between (7) and (9) yields (10):

$$\frac{\varepsilon_e(t)}{\varepsilon_i(t_i)} = \exp\left(\frac{t}{t_i} - 1\right).\left(\frac{t}{t_i}\right)^{\beta} \tag{10}$$

From data pairs $(\boldsymbol{\varepsilon_e}, \boldsymbol{t})$, it is expectable that $(\boldsymbol{\varepsilon_i}, \boldsymbol{t_i}, \boldsymbol{\beta})$ converge from a successive iteration of (10).

Moreover, according to Crevecoeur [7] the use of $\boldsymbol{\varepsilon_e(t)/\varepsilon_i(t_i)}$ and $\boldsymbol{t/t_i}$ allows to normalize the shape of the creep curve, independently of how long the process lasts. In fact, for a given $\boldsymbol{\beta}$ and making $\boldsymbol{\varepsilon_e(t) = \varepsilon_i(t_i)}$, the creep curve will look similar for a small $\boldsymbol{t_i}$ (tests at higher stress or temperature) as well as for a larger $\boldsymbol{t_i}$ (tests at lower stress or temperature).

To find the time of steady creep, Crevecoeur [6] suggests the following relation:

$$t_{2ary} = t_i.\left(\sqrt{\beta} - \beta\right) \tag{11}$$

Expression (11) gives the point where the strain rate reaches its minimum and corresponds to the point of inflexion on the creep curve.

From (11), the secondary strain point, $\boldsymbol{\varepsilon_{2ary}}$, is estimated using (7).

It must to be warned that the 2ary stage (the steady-state stage) has visually the aspect of a straight line but in fact it is an approximate linearization for practical applications and shows a quasi-straight linear zone.

The point $(\boldsymbol{\varepsilon_{2ary}}, \boldsymbol{t_{2ary}})$ is somewhere in the 2ary stage where the creep curve turns from concave (from below) to convex (from below) form.

Furthermore, it is possible to mark several periods of time on the creep curve. Comparing biological and inert systems, Crevecoeur [6] distinguishes some periods of time:

(1) the instability time—$\boldsymbol{t_i}$;
(2) the actual time of collapse—$\boldsymbol{t_r}$ (*the 'lifespan'*);
(3) the maximum possible lifetime—$\boldsymbol{t_m}$ (*the 'longevity'*); and
(4) the statistical average of lifetimes—$\boldsymbol{t_\mu}$, (*the 'life expectancy'*).

These periods of time are shown in Fig. 5

where:

$\boldsymbol{t_{1ary}}$ *is the transition point between transient and steady creep*
$\boldsymbol{t_{2ary}}$ *is the inflexion point of the creep curve*
$\boldsymbol{t_{3ary}}$ *is the second transition point (flow time)*

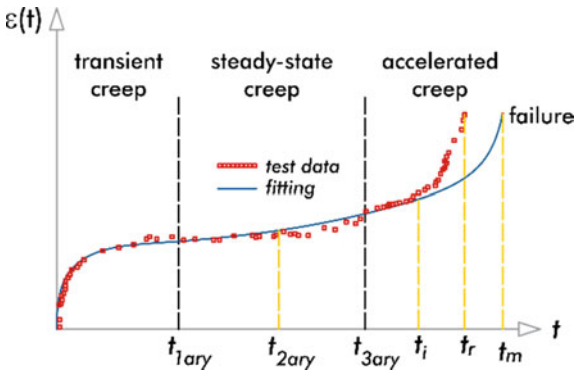


Fig. 5 Periods of time on a hypothetical creep curve

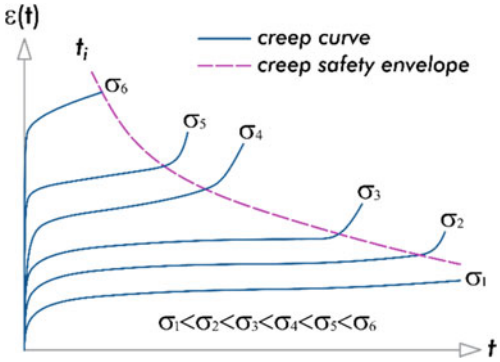


Fig. 6 Creep envelope for a given temperature

t_i *is the instability time*
t_r *is the actual time of failure*
t_m *is the maximum possible lifetime.*

Applying t_{2ary} to the derivative of (5) and comparing its straight line to creep data curve, it is expectable to determine t_{1ary} and t_{3ary} taking the difference between the straight line and creep data less than to **1%**.

3.1 Creep Safety Envelope

Once defined the critical points on the creep curve (for a given temperature and load), it is possible to determine different critical points for a spectral of different values of stress for a specific temperature or different levels of temperature for a range of stress values. Fig. 6 shows a creep safety envelope for an aleatory polymeric sample at a given temperature.

4 Material Testing

In order to simulate the above described fitting, sampled points from the creep curves identified by Liu et al. [12] are used as the actual experimental values to be matched.

4.1 Liu's Creep Data

The creep experimental data are obtained for creep testing of a sample extracted from HDPE (high-density polyethylene) pipes at 5 stress levels. From a Generalized

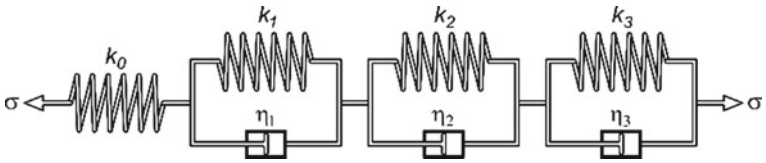


Fig. 7 Generalized kelvin model

Table 1 Fitted values from Eq. (12)

Stress (MPa)	$\mathbf{k}_0$ (MPa)	$\mathbf{k}_1$ (MPa)	$\mathbf{k}_2$ (MPa)	$\mathbf{k}_3$ (MPa)
2.97	650	797.3889	2320.3566	925.0882
5.97	580	913.5936	1212.2605	695.0461
7.71	520	1224.7911	1104.9922	385.8572
10.31	500	1034.2045	694.1084	226.4555
12.19	470	1128.4448	806.0972	140.6875

Adapted from Liu et al. [12]

Kelvin Model (Fig. 7), a Dirichlet Series with three terms were used to represent the resulting strain (12). The tests were conducted at room temperature of about 22 °C.

Table 1 shows the fitted values of experimental data from Eq. (12).

$$\varepsilon_D(t) = \frac{\sigma(t)}{k_0(\sigma)} + \sum_{i=1}^{3} \frac{\sigma(t)}{k_i(\sigma)}\left[1 - \exp\left(-\frac{t}{\tau_i}\right)\right] \tag{12}$$

where the respective relaxion times are:

$\boldsymbol{\tau}_1 = 500\,\boldsymbol{s}$
$\boldsymbol{\tau}_2 = 10000\,\boldsymbol{s}$
$\boldsymbol{\tau}_3 = 200000\,\boldsymbol{s}$

The sampled points from the creep curves identified in Table 1 are used to simulate the actual experimental values to be matched and the resulted strain-time curves are depicted in Fig. 8.

5 Application of Crevecoeur Fitting Methodology

From the data spectra generated by Eq. (12), Crevecoeur equation coefficients are fitted for each stress level and presented in Table 2.

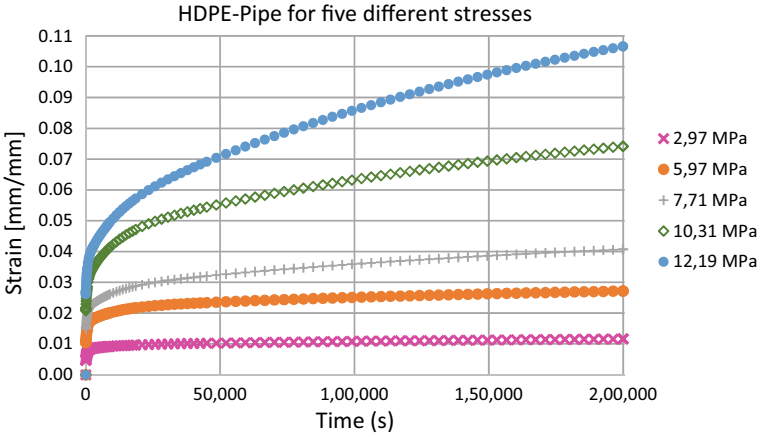


Fig. 8 Creep curves until end of measurements

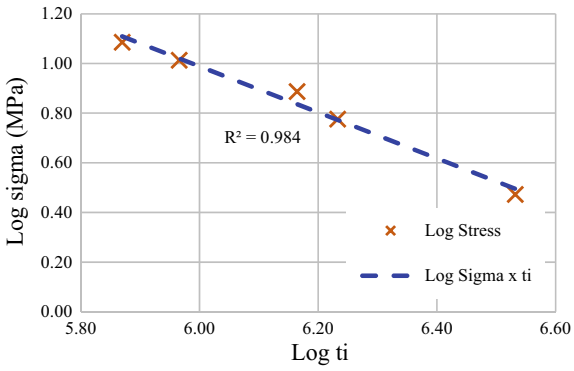
Table 2 Crevecoeur equation coefficients

Stress (MPa)	**k**	**β**	$\mathbf{t_i}$ (s)	**error** (%)	r-Person
2.97	0.00558	0.055	3.403.676	0.60	0.9763
5.97	0.00880	0.085	1.709.402	0.80	0.9901
7.71	0.00900	0.113	1.459.854	0.90	0.9990
10.31	0.01340	0.124	924.214	1.10	0.9982
12.19	0.01320	0.150	740.741	1.90	0.9975

5.1 Fitting Quality

In order evaluate the quality of the fitted values, the relationship diagram between $\boldsymbol{log\,\sigma}$ versus $\boldsymbol{log\,t_i}$ and $\boldsymbol{\epsilon(t_i)}$ versus $\boldsymbol{log\,t_i}$ is shown in Fig. 9.

Fig. 9 Evaluation diagram



The linear relation plotted is similar to a typical failure mode of HDPE Pipe, the so-called Mode–1, where the pipe fails mainly in a ductile manner under mechanical overload at higher stresses (see Xu et al. [21]), that indicates an acceptable correlation between data test and the approach.

6 Results and Comments

Figure 10 and Table 3. Strain Correlation show the relationship between the strain at t_i and t_{2ary}, $\varepsilon_i(t_i)$ and $\varepsilon_{2ary}(t_{2ary})$. This one reveals a constant ratio between the instability time and the time of steady creep, over the stress increment.

6.1 Transition Points

In order to exemplify the strain rate bathtub the strain rate for 12,19 MPa is depict in Fig. 11.

From derivative of (5) and applying the t_{2ary}, it is expectable to find the values of t_{1ary} and t_{3ary} where the difference between the strain rate line from (4) and the creep data curve is less than or equal to 1%. Tables 4 and 5. Pairs of Transition Points (2/2) shows the values of each pairs of fitted points.

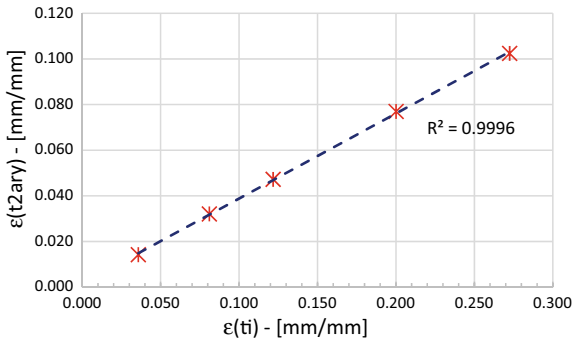


Fig. 10 Strain correlation

Table 3 Strain correlation

Stress (MPa)	$\varepsilon(t_i)$ (mm/mm)	$\varepsilon(t_{2ary})$ (mm/mm)	Strain ratio
2.97	0,036	0,014	0,398
5.97	0,081	0,032	0,396
7.71	0,122	0,047	0,388
10.31	0,200	0,077	0,385
12.19	0,272	0,102	0,376

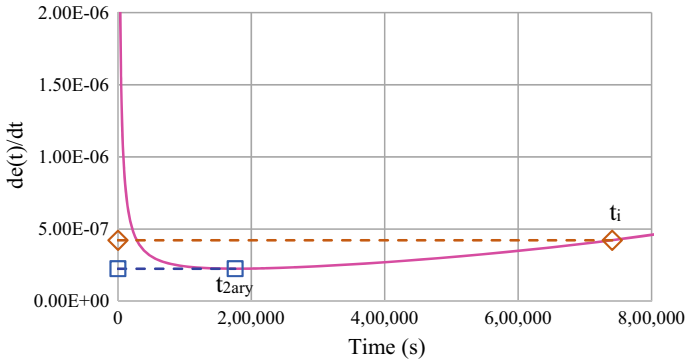


Fig. 11 Strain bathtub for 12,19 MPa.

Table 4 Pairs of transition points (1/2)

Stress (MPa)	$\varepsilon(t_{1ary})$ (mm/mm)	t_{1ary} (s)	$\varepsilon(t_{2ary})$ (mm/mm)	t_{2ary} (s)
2.97	0,011	77.400	0,014	611.031
5.97	0,026	142.200	0,032	353.073
7.71	0,044	260.000	0,047	325.773
10.31	0,059	77.400	0,077	210.847
12.19	0,087	109.800	0,102	175.777

Table 5 Pairs of transition points (2/2)

Stress (MPa)	$\varepsilon(t_{3ary})$ (mm/mm)	t_{3ary} (s)	$\varepsilon(t_i)$ (mm/mm)	t_i (s)	$\varepsilon(t_m)$ (mm/mm)	t_m (1s)
2.97	0,023	2.150.000	0,036	3.403.676	0,055	4.424.779
5.97	0,042	710.000	0,081	1.709.402	0,124	2.393.162
7.71	0,051	404.000	0,122	1.459.854	0,189	2.043.796
10.31	0,120	518.000	0,200	924.214	0,311	1.293.900
12.19	0,139	330.000	0,272	740.741	0,428	1.037.037

From expression (5) and the values from Tables 4 and 5. Pairs of Transition Points (2/2), the theoretical creep curves for each step of stress are depicted in Fig. 12

Once defined the critical points on the creep curve shown in Table 4, creep safety envelope is created and the shape of the curve is given in Fig. 13.

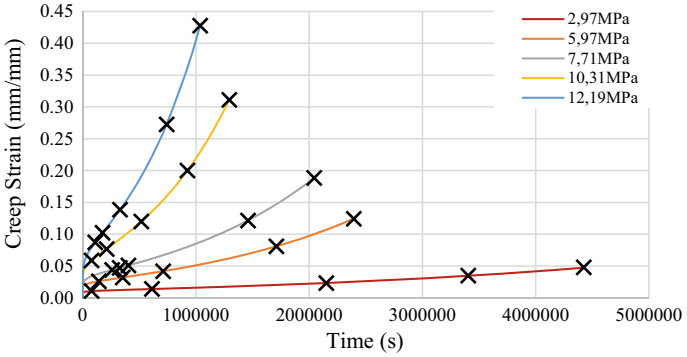


Fig. 12 Transition points

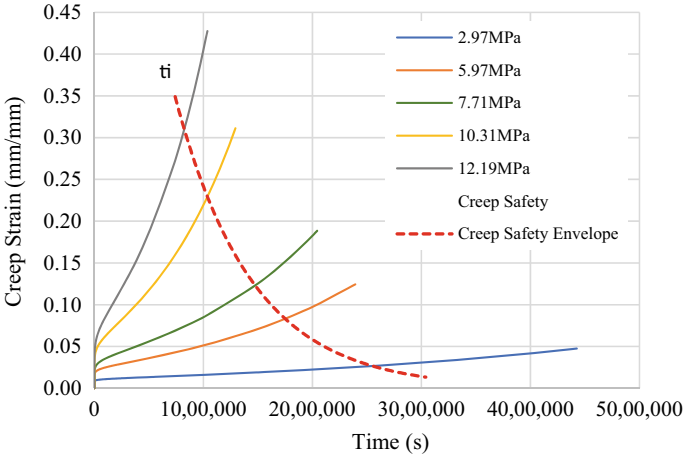


Fig. 13 Creep safety envelope

7 Conclusions

This paper presented a study conducted to estimate the 4 instants of time characterizing the creep curve: (1) the first transition point, that is the transition point between transient and steady creep; (2) the secondary point, that is the inflexion point of the creep curve where the strain rate reaches its minimum; (3) the second transition point, that is the transition point between steady and accelerated creep; and (4) the instability point.

The creep curve used in this study was constructed using data resulting from a numerical simulation of an experiment of Liu et al. [12], where a sample cut from a 24" HDPE-Pipe was tested for five different stress levels.

A brief review of the fitting methodology was first presented concerning the creep behavior and its three-stages. This methodology was applied then to the numerical description of the creep behavior of a PE. The time-dependent and stress-dependent approach was easily applied to a viscoelastic material. The transition points were calculated and a creep safety envelope was defined and a lifetime prediction could be made.

Although there was no comparative analysis of the useful life of the material based on standards, the creep curves obtained by the Crevecoeur adjustment methodology evidenced a good fitting.

Acknowledgements The authors wish to express their utmost thanks to Professor Guibert Ulric Crevecoeur (Federal Public Service Economy—Department of Energy—Brussels, Belgium) for his useful remarks having led to a significant improvement of the present contribution.

This work was financially supported by: Base Funding—UIDB/04708/2020 of the CONSTRUCT—Instituto de I&D em Estruturas e Construções—funded by national funds through the FCT/MCTES (PIDDAC).

References

1. Barra, G.: Fundamentos de reologia de materiais poliméricos. Florianópolis–SC (2010). http://emc5744.barra.prof.ufsc.br/Reologiaparte1.pdf
2. Cao, P., Short, M.P., Yip, S.: Understanding the mechanisms of amorphous creep through molecular simulation. Proc. Nat. Acad. Sci. U. S. A. **114**(52), 13631–13636 (2017). https://doi.org/10.1073/pnas.1708618114
3. Crevecoeur, G.U.: Quelques réflexions autour de la courbe de fluage—Une nouvelle perspective. Journal des Ingénieurs, bimestral (1992)
4. Crevecoeur, G.U.: A Model for the integrity assessment of ageing repairable systems. IEEE Trans. Reliab. **42**(1), 148–155 (1993). https://doi.org/10.1109/24.210287
5. Crevecoeur, G.U.: Reliability assessment of ageing operating systems. Eur. J. Mech. Environ. Eng. **39**(4), 219–228 (1994)
6. Crevecoeur, G.U.: A system approach modelling of the three-stage non-linear kinetics in biological ageing. Mech. Ageing Dev. **122**(3), 271–290 (2001). https://doi.org/10.1016/s0047-6374(00)00233-5
7. Dacol, V.: Prof. Guibert Ulric Crevecoeur interview, ResearchGate, 19 Oct 2019, Porto–Portugal (2019)
8. Findley, W.N., Lai, J.S., Onaram, K.: Creep and Relaxation of Nonlinear Viscoelastic Materials—With an Introduction to Linear Viscoelasticity. Dover Publications Inc., New York (1976)
9. Fotsis, T., et al.: The endogenous oestrogen metabolite 2-methoxyoestradiol inhibits angiogenesis and suppresses tumour growth. Nature **368**(6468), 237–239 (1994). https://doi.org/10.1038/368237a0
10. Guedes, R.M.: *Creep and Fatigue in Polymer Matrix Composites*, *Woodhead Publishing*. Woodhead Publishing Limited, Cornwall, UK (2011). https://doi.org/10.1007/s13398-014-0173-7.2
11. Iskakbayev, A., Teltayev, B., Rossi, C.O.: Steady-state creep of asphalt concrete. Appl. Sci. **7**(2) (2017). https://doi.org/10.3390/app7020142
12. Liu, H., Polak, M.A., Penlidis, A.: A practical approach to modeling time-dependent nonlinear creep behavior of polyethylene for structural applications. Polym. Eng. Sci. **48**, 9 (2008). https://doi.org/10.1002/pen

13. Luder, H.U.: Onset of human aging estimated from hazard functions associated with various causes of death. Mech. Ageing Dev. **67**(3), 247–259 (1993). https://doi.org/10.1016/0047-6374(93)90003-a
14. Monfared, V.: Review on creep analysis and solved problems. Intech **i**(10), 31 (2016). http://dx.doi.org/10.5772/57353
15. Naumenko, K., Altenbach, H.: Modeling of creep for structural analysis (2007). https://doi.org/10.1007/978-3-540-70839-1
16. Sandström, R.: Basic model for primary and secondary creep in copper. Acta Mater. **60**(1), 314–322 (2012). https://doi.org/10.1016/j.actamat.2011.09.052
17. Selye, H.: Stress and the general adaptation syndrome. Br. Med. J., 1383–1392 (1950). https://doi.org/10.1159/000227975
18. Smith, D.J.: Reliability and maintainability in perspective—practical, contractual, commercial and software aspects. J. Chem. Inform. Model. (1988). Third Edit. Edited by Macmillan. https://doi.org/10.1017/cbo9781107415324.004
19. Vincent, J.: Structural Biomaterials, Structural Biomaterials. Springer International Publishing Switzerland, London (1982)
20. Van Voorhies, W.A.: Production of sperm reduces nematode lifespan. Nature **359**, 710–713 (1992)
21. Xu, C., Xu, P., Shi, J.: Investigation on creep-rupture failure time of HDPE pipe under hydrostatic pressure. American Society of Mechanical Engineers, Pressure Vessels and Piping Division (Publication) PVP, 6(PARTS A AND B), pp. 913–918 (2011). https://doi.org/10.1115/pvp2011-57840

Paper 2

Dacol, V.; Caetano, E.; Correia, J.R.

A Combined Exponential-Power-Law Method for Interconversion between Viscoelastic Functions of Polymers and Polymer-Based Materials

Polymers 2020, 12, 3001. *https://doi.org/10.3390/polym12123001*

Published: 16 December 2020.

Impact Factor: 4.493 (2020).

polymers

MDPI

Article

A Combined Exponential-Power-Law Method for Interconversion between Viscoelastic Functions of Polymers and Polymer-Based Materials

Vitor Dacol [1,*], Elsa Caetano [1] and João R. Correia [2]

[1] CONSTRUCT (ViBEST), Faculty of Engineering (FEUP), University of Porto, 4200-465 Porto, Portugal; ecaetano@fe.up.pt

[2] CERIS, DECivil, IST, University of Lisbon, 1049-001 Lisbon, Portugal; joao.ramoa.correia@tecnico.ulisboa.pt

* Correspondence: vitor.dacol@fe.up.pt; Tel.: +351-913-098-842

Received: 27 November 2020; Accepted: 13 December 2020; Published: 16 December 2020



Abstract: Understanding and modeling the viscoelastic behavior of polymers and polymer-based materials for a wide range of quasistatic and high strain rates is of great interest for applications in which they are subjected to mechanical loads over a long time of operation, such as the self-weight or other static loads. The creep compliance and relaxation functions used in the characterization of the mechanical response of linear viscoelastic solids are traditionally determined by conducting two separate experiments—creep tests and relaxation tests. This paper first reviews the steps involved in conducting the interconversion between creep compliance and relaxation modulus in the time domain, illustrating that the relaxation modulus can be obtained from the creep compliance. This enables the determination of the relaxation modulus from the results of creep tests, which can be easily performed in pneumatic equipment or simple compression devices and are less costly than direct relaxation tests. Some existing methods of interconversion between the creep compliance and the relaxation modulus for linear viscoelastic materials are also presented. Then, a new approximate interconversion scheme is introduced using a convenient Laplace transform and an approximated Gamma function to convert the measured creep compliance to the relaxation modulus. To demonstrate the accuracy of the fittings obtained with the method proposed, as well as its ease of implementation and general applicability, different experimental data from the literature are used.

Keywords: viscoelasticity; creep and relaxation; interconversion; stages of creep; mechanical analysis; mechanical characterization; structure–property relationships

1. Introduction

The linear viscoelastic functions that describe the creep and relaxation behavior of polymers and polymer-based materials are mathematically equivalent, and each function contains essentially the same information on the creep and relaxation properties of those materials. Through an appropriate mathematical operation, a linear viscoelastic material function can be converted into another material function.

Polymers and polymer-based materials are extensively used as structural materials in the aerospace and automotive industries, civil engineering [1], and biomechanics. Due to this, a variety of methods applicable to the interconversion of static (creep) and dynamic (relaxation) functions (concerning appropriate experimental data of various polymeric and composite materials) have been investigated over the last few decades to provide a better characterization of those materials [2].

Despite the conceptual simplicity of the viscoelastic properties of polymeric materials, there are operational difficulties in obtaining them from experiments. In this context, interconversion procedures are especially useful due to the difficulty in running constant-strain relaxation tests on stiff materials and

the fact that constant-stress creep tests are much easier to carry out [3]; in many cases, constant-stress creep tests can be performed with a simple deadweight system. Concerning relaxation modulus tests, the difficulty involved in the sudden application of a constant strain level was highlighted by Kim [4]. Moreover, it is necessary to adjust the load level during the test to guarantee that the strain is kept constant. Therefore, a method of interconversion becomes an important tool as it allows for more efficient utilization of resources in a rheology laboratory.

In the context of temperature and frequency dependence studies, the interconversion procedure can also be an important tool to help predict the behavior of polymer-based materials [5].

Different methods have been proposed to solve the interconversion expression of linear viscoelasticity. In this context, reference is made to an extensive theoretical treatment of the subject given in [6,7]. Other studies, such as [8–10], have focused on numerical approaches using Prony series or power laws to characterize the creep and relaxation moduli of polymeric materials.

When studying the mechanical behavior of viscoelastic materials, it is usually assumed that the strains and the stresses are deterministic functions. However, Wang et al. [11] highlighted the importance of considering the uncertainty in the propagation of the frequency response for the robust design of viscoelastic damping structures. According to De Lima et al. [12], among the various methods devised for uncertainty modeling, the stochastic finite element method has received major attention, as it is well adapted for application to complex engineering systems. Despite their potential importance, the experimental quantification of uncertainties and the corresponding stochastic modeling are not addressed in the present study.

In the first part of this paper, a general theoretical background of the viscoelastic behavior of polymeric composites is provided, and a brief review of interconversion methods is presented and discussed. In the second part, based on the works of Crevecoeur [13,14] and the study conducted in [15], this paper proposes a new interconversion procedure, which involves the combination of Laplace transform theory with an approximated Gamma function to convert the measured creep compliance to the relaxation modulus. The main goal of this paper is to demonstrate (i) the mathematical procedure to interconversion from creep to relaxation functions and (ii) the good fitting for creep and relaxation data provided by the proposed methodology.

2. Theoretical Background

2.1. Constitutive Relations

The creep and relaxation properties of polymeric and polymer-based materials allow for prediction of their response when subjected to a step function of stress or strain as a function of time. To predict the response of a material to any history of stress or strain as a function of time, the constitutive integrals of linear viscoelasticity must be used. The creep function is defined as a strain variation as a function of time under constant stress. In the linear range, the Boltzmann superposition principle is valid and expressed as

$$\varepsilon(t) = \int_0^t D(t-\tau)\frac{\partial \sigma(\tau)}{\partial \tau}d\tau \tag{1}$$

where $\varepsilon(t)$ is the strain, t is the time, σ is the stress, and D is the creep compliance function.

If the roles of stress and strain are interchanged and the above arguments are repeated, a complementary relationship is obtained:

$$\sigma(t) = \int_0^t E(t-\tau)\frac{\partial \varepsilon(\tau)}{\partial \tau}d\tau \tag{2a}$$

where E is the relaxation modulus function.

Thus, if the response of a material to a step function of stress or strain has been determined experimentally, the response to any load history can be found for analysis or design.

It must be noted that the relaxation and creep functions are not arbitrary functions, and the restrictions on the form of these functions have been derived based on physical principles [16].

2.2. The Relation between Creep and Relaxation in the Time Domain

A simple relationship between the creep function $D(t)$ and the relaxation function $E(t)$ is convenient to simplify the viscoelastic material characterization. Both functions appear in the Boltzmann superposition integrals (1) and (2), described above.

The two integral expressions may be manipulated with the aid of integral transforms, such as the Laplace transform

$$\overline{f}(s) = \int_0^\infty f(t)e^{-st}dt, \quad t > 0 \tag{2b}$$

where s is the transform variable, e^{-st} is the transformed kernel function, and $\overline{f}$ is the rational function of s.

By integration of (1) and (2) and using the convolution theorem, the following relations are obtained:

$$\tilde{\sigma}(s) = s\overline{E}(s)\overline{\varepsilon}(s) \tag{3}$$

$$\tilde{\varepsilon}(s) = s\overline{D}(s)\overline{\sigma}(s) \tag{4}$$

where $\overline{\sigma}$ is the stress operator in the Laplace domain, $\overline{\varepsilon}$ is the strain operator in the Laplace domain, and $\overline{E}$ and $\overline{D}$ are the rational functions of s.

By appropriate mathematical operations, (3) and (4) are manipulated, yielding

$$\overline{E}(s)\overline{D}(s) = \frac{1}{s^2} \tag{5}$$

The relation (5) between the Laplace-transformed relaxation and creep functions is useful in directly evaluating one transformed function when the other function is known at a particular value of the transform parameter [3].

Applying the inverse of the Laplace transform to (5) and using the convolution theorem and the Laplace operator relation $\overline{f}(t) = 1/s^2$ yields

$$\int_0^t E(t-\tau)D(\tau)d\tau = t \tag{6}$$

or

$$\int_0^t D(t-\tau)E(\tau)d\tau = t \tag{7}$$

Further, differentiating (6) and setting the time to zero ($t = 0$), the initial condition between $D(t)$ and $E(t)$ yields

$$D(0)E(0) = 1 \tag{8}$$

The convolution integrals relating the creep compliance and the relaxation modulus (Expressions (6) and (7)) are the Volterra expressions of the first kind.

3. Interconversion Methods: A Brief Review

Several approximate methods of interconversion between transient relaxation and creep functions are available in the literature. Most of them are based on power laws or exponential functions. In this section, some of these methods are presented and discussed.

3.1. Power-Law-Based Interrelationship by Leaderman (1958)

For many linear viscoelastic materials, the relaxation modulus and the creep compliance function are approximately represented by simple power laws over their transition zones. The simplest form of a power law is the pure power-law (PPL), which is described by the following time loading description for the relaxation modulus [17]:

$$E(t) = E_1 t^{-n} \tag{9}$$

and the following time loading description for the creep compliance:

$$D(t) = D_1 t^{n} \tag{10}$$

where E_1, D_1, and n are material constants.

From (9) and (10), by Laplace transform operations, the following relation occurs:

$$E(t)D(t) = \frac{\sin(n\pi)}{n\pi} \tag{11}$$

The main advantage of the power-law-based approach is its simplicity. As is well known, the power-law functions are graphically represented by straight lines on log–log scales, and the exponent n is identified as *the material regression coefficient* representing the creep or relaxation rate.

3.2. Log–Log Slope-Based Interrelationship by Park and Kim (1999)

Park and Kim [5] introduced an approximate interconversion method that uses the local log–log slope of the source function and is based on the concept of equivalent time determined by rescaling the physical time. The rescaling factor, α, which can be interpreted as a shift factor on a logarithmic time axis, is defined as the local slope of the source function on log–log scales.

From (9) and (10), one may obtain the following expressions relating $D(t)$ and $E(t)$:

$$D(t) = \frac{1}{E(\alpha t)} \tag{12}$$

$$E(t) = \frac{1}{D\left(\frac{t}{\alpha}\right)} \tag{13}$$

The rescaling factor, α, is then given by

$$\alpha = \left(\frac{\sin(n\pi)}{n\pi}\right)^{\frac{1}{n}} \tag{14}$$

This method produces good results when the source functions are characterized by broadband and smooth behavior on doubly logarithmic scales [3].

3.3. Exponential-Based Interrelationship by Schapery and Park (1999)

The use of the Dirichlet series, also known as the Prony series, is a popular method to represent the relaxation function, mainly due to its ability to describe a wide range of viscoelastic responses, associated with the relative simplicity of its exponential basis functions and rugged computational efficiency. In the Dirichlet model approach, the generalized Maxwell model is used as an analogy to represent the creep and relaxation functions.

The generalized Maxwell model (or Wiechert model) consists of a spring and n Maxwell elements connected in parallel. The relaxation modulus derived from this model is given by

$$E(t) = E_0 + \sum_{i=1}^{m} E_i e^{-(t/\tau_i)} \tag{15}$$

where E_0 is the equilibrium modulus, E_i is the relaxation strength, and τ_i is the delay time.

The analytical description of the creep compliance function of the generalized Maxwell model is expressed by the sum of exponential terms

$$D(t) = D_0 + \sum_{i=1}^{m} D_i\left[1 - e^{-(t/\tau_i)}\right] \tag{16}$$

where D_0 is the glassy compliance and D_i is the retardation strength.

In this scheme, because both the source and the target functions are represented in the Prony series, the complete target function can be determined by solving a system of linear algebraic expressions given by [3]

$$[\mathrm{A}]\{\mathrm{E}\} = [\mathrm{B}] \tag{17}$$

where

$$[\mathbf{A}] = \sum_{k=1}^{p}\sum_{i=1}^{m}\left[D_1\left(e^{-t_k/\rho_i} - 1\right) + \sum_{j=1}^{n}\frac{D_j\tau_j}{\rho_i - \tau_j}\left(e^{-t_k/\rho_i} - e^{-t_k/\tau_j}\right)\right] \tag{18}$$

and

$$[\mathbf{B}] = 1 - \sum_{k=1}^{p} E_1\left[D_1 + \sum_{j=1}^{n} D_j\left(1 - e^{-t_k/\tau_j}\right)\right] \tag{19}$$

The main inconvenience of the Dirichlet series adjustment is the potential problem of numerical instability resulting from the generation of negative dependent terms.

4. The Convolution Theorem

It is well known that the convolution theorem can be used to solve integrals and integral–differential expressions. The basic mathematical definition of convolution is the integral over all space of one function at x multiplied by another function at u-x, concerning to x, where x can represent anything, including time, frequency, or even a three-dimensional space, depending on the application [18].

> *"The convolution theorem for s-transforms states that for any (real or) complex causal signals x and y, the convolution in the time domain is equivalent to a multiplication in the s domain."*

Given the functions of time t, $f(t)$ and $g(t)$, the convolution (*) of $f(t)$ and $g(t)$ is a function of t defined by

$$(f * g)(t) = \int_{-\infty}^{\infty} f(t-\tau)g(\tau)d\tau \tag{20}$$

Applying the s-Laplace transform to the second member of (20) and changing the order of the integrals yields

$$\overline{f}\{(f * g)(t)\} = \int_{0}^{\infty}\int_{0}^{t} f(t-\tau)g(\tau)e^{-st}d\tau dt \tag{21}$$

Finally, changing variables in the inner integral (substituting $v = t - \tau$, $dv = dt$ (τ a constant)) (21) yields

$$\overline{f}\{(f * g)(t)\} = F(s)G(s) \tag{22}$$

5. Exponential-Power-Law (EPL) Interconversion

It has been shown in [19] that the creep curve of polymers and polymer-based materials can be well described by the following expression:

$$\varepsilon(t) = k \cdot t^{\beta} \cdot e^{\frac{t}{t_i}} \tag{23}$$

where $\varepsilon(t)$ is the calculated strain, β is a constant related to strain hardening ($\beta < 1$ and $\alpha \ll \beta$), k is a constant related to the main stress influence, and t_i is the instability time.

Indeed, the advantages of (23) in providing a good fitting to a creep curve are summarized as follows: (i) it is a very simple approximation, as only three parameters have to be determined to fit the given creep data (k, t_i, and β); (ii) it provides a good quality of extrapolations because it does not involve addition or subtraction operations; (iii) it combines the three stages of creep; and (iv) it is generally applicable.

As previously shown by the authors [15], the main advantage of using the exponential-power-law (EPL) method as given by expression (23) is its ability to cover the full path of the creep behavior and its capacity to estimate the respective transition points between stages.

Conversion between the creep compliance, fitted with (23), and the relaxation modulus may be required to estimate the fatigue resistance of composite structures; to that end, the relaxation behavior and the corresponding transition points should be known.

Laplace Transform of EPL

Using the Laplace transform properties summarized in Table 1, each term of the EPL expression (21) can be transformed as

$$\overline{f}\left\{e^{\frac{t}{t_i}}\right\} = \frac{1}{s - \frac{1}{t_i}} \tag{24}$$

$$\overline{f}\left\{t^{\beta}\right\} = \frac{\beta!}{s^{\beta+1}} \tag{25}$$

Table 1. Laplace transform properties.

$f(t)$	$\hat{f}(t)$
$e^{\alpha t}$	$\frac{1}{s-\alpha}$
$t^n,\ n > -1$	$\frac{n!}{s^{n+1}}$

After mathematical manipulations, the EPL expression (21), in $\mathcal{L}$ domain, is transformed into

$$\overline{\varepsilon}(s) = k \cdot \frac{\beta!}{s^{\beta+2} + t_i s^{\beta+1}} \tag{26}$$

From (22), the creep compliance can be written as

$$\overline{D}(s) = D_0 \cdot \frac{\beta!}{s^{\beta+2} + t_i s^{\beta+1}} \tag{27}$$

where D_0 is the compliance in the glassy state, given by $D_0 = {}^{k}/_{\sigma}$.

From the relationship given by (5), the relaxation modulus is defined in the Laplace domain as

$$\overline{E}(s) = {D_0}^{-1} \cdot \frac{s^{\beta+2} + t_i s^{\beta+1}}{s^2 \beta!} \tag{28}$$

After necessary simplifications, it follows that

$$\overline{E}(s) = \frac{\sigma}{k} \cdot \frac{s^{\beta} + t_i s^{\beta-1}}{\beta!} \tag{29}$$

Applying the inverse of the Laplace transform to (29), one finds

$$E(t) = \frac{\sigma}{k\, t^{\beta}} \left[\frac{t^{-1}}{\beta\Gamma(\beta)\Gamma(-\beta)} - \frac{t_i}{\beta\Gamma(\beta)\Gamma(1-\beta)} \right] \tag{30}$$

Here, the operator Γ is the Euler Gamma function.

The first definition of the Γ-function resulted from the idea of extending the positive integer factorial $n! = n(n-1)(n-2)\ldots$ to real numbers [20].

The Γ-function is an extension of the factorial function with an argument shifted by one, to real numbers and the complex numbers, as follows:

$$\Gamma(z) = (z-1)! = \int_0^{\infty} t^{z-1} e^{-t} dt, \quad \Re(z) > 0 \tag{31}$$

The Γ-function defined above can be integrated by parts to show the recurrence or functional relation, yielding

$$z! = \Gamma(z+1) = z\Gamma(z) \tag{32}$$

The Γ-function does not have a closed-form solution and needs to be approximated.

The Stirling approximation is the most well-known and cited approximation of the Γ-function [20] and is defined as

$$z! = \Gamma(z+1) \sim \left(\frac{z}{e}\right)^{z} \cdot (2\pi z)^{\frac{1}{2}} \tag{33}$$

Here, the signal "~" means that the two quantities are asymptotic, i.e., their ratio tends to one as z tends to infinity. Despite its effectiveness, the Stirling formula is not the most accurate, especially for values in the range $0 < z < 1$.

Burnside's asymptotic formula for factorial z provides a more efficient estimation of the Γ-function compared to (28). Furthermore, Gosper's formula [21] provides a slightly more accurate estimation of the Γ-function than Stirling's formula.

An important property of the Γ-function is Euler's reflection formula, where, for all non-integer z, one finds

$$\Gamma(z)\Gamma(1-z) = -z\Gamma(-z)\Gamma(z) = (-z)!\Gamma(z) \backsimeq \frac{\pi}{\sin \pi z} \tag{34}$$

As shown in [22], a Γ-function of negative values may be written as follows:

$$\Gamma(-z) = \frac{\Gamma(-z+1)}{-z} = \frac{\Gamma(1-z)}{-z} \tag{35}$$

Applying the numerical approximation discussed above, the relaxation modulus of the EPL creep function given by (25) becomes

$$E(t) = \frac{\sigma}{k\, t^{\beta}} \cdot \frac{\sin(\pi\beta)}{\pi} \cdot \left(\frac{t_i}{\beta} + \frac{1}{t}\right) \tag{36}$$

Based on the creep test data provided in [23] for specimen T28-S15 (a glass-fiber-reinforced polymer (GFRP) laminate tested in three-point bending), Figure 1 presents a graphical representation of the time variation of the expression (25) and the approximation (31)—it can be seen that these functions present a perfect match.

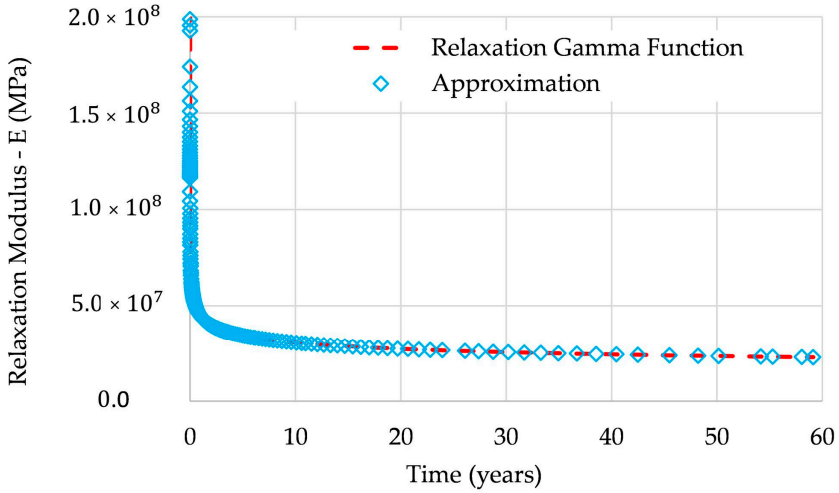


Figure 1. Exponential-power-law (EPL) Γ-function and approximation are given by (31).

6. Application

This section presents the application of the method described above to the creep and stress relaxation tests presented by Garrido et al. [23], Sorvari et al. [24], and Hernández-Jiménez et al. [25].

6.1. Creep Compliance and Relaxation Modulus Fitted from Garrido et al. (2015)

6.1.1. Creep Compliance Fitting

The GFRP laminates used in [23] were manufactured by vacuum infusion, using E-glass fiber rovings and mats embedded in orthophthalic polyester resin. The fiber layup followed an $[0/0/30/-30/90/0]_S$ arrangement, resulting in a laminate with a nominal thickness of 7 mm, a nominal fiber volume fraction of 45%, and a fiber weight of 9000 g/m^2. The glass transition temperature of the material was measured as $T_g = 69.3$ °C. Further mechanical properties can be found in the referenced paper.

The flexural creep behavior was measured and considered to be representative of the overall bending creep behavior by providing a combination of the compressive and tensile creep responses of the laminate. The creep experiments were carried out at 20, 24, and 28 °C, for stress levels corresponding to 15%, 25%, and 35% of the laminate's flexural strength, with test durations ranging between 1000 and 2200 h. The specimens were labeled as "$T_i - S_j$", i.e., specimens tested at temperature i and stress level j.

As the main goal of this paper is to verify the fitting accuracy of the EPL expression and its interconversion method, only data from the 28 °C experiment are used.

The first step is to fit the creep curve to three levels of stress. This procedure is necessary to quantify the influence of stress on the material creep behavior. From the data spectra, the EPL expression coefficients are fitted and shown in Table 2.

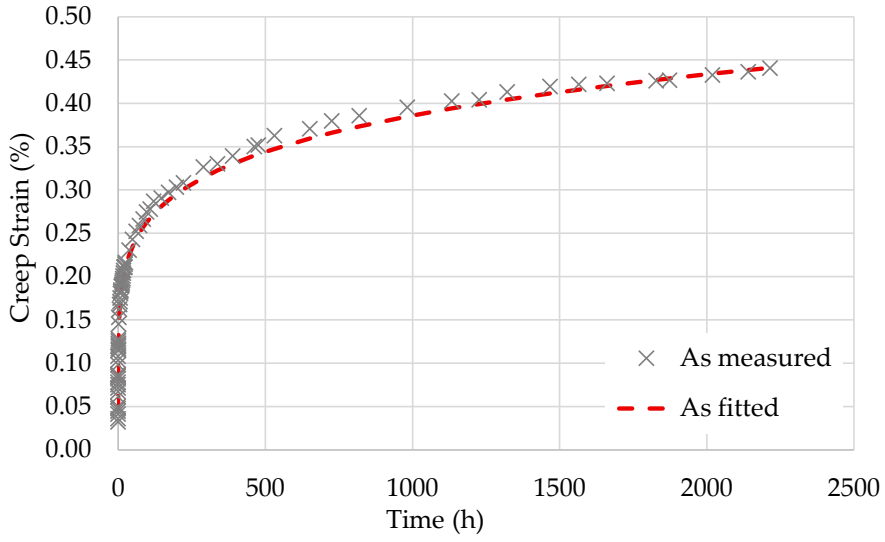
Table 2. EPL coefficients.

Specimen	Stress (MPa)	k	β	t_i (h)
T28-S15	64.30	0.124	0.164	398,500
T28-S25	99.20	0.305	0.127	365,000
T28-S35	142.30	0.329	0.153	344,922

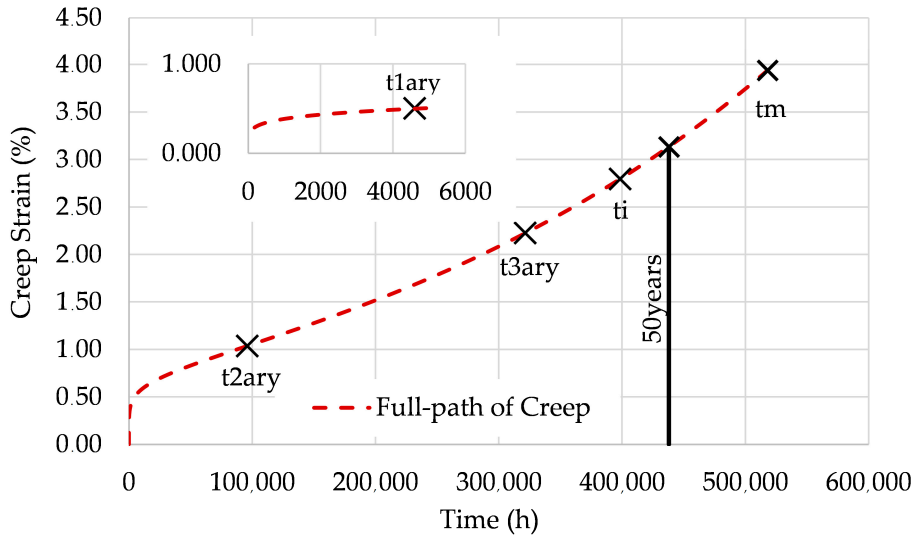
Figures 2–4 show the fitting of the full path of creep from the EPL expression to the three specimens tested at 28 °C: T28-S15, T28-S25, and T28-S35.

As described in [15], the points represented in these figures are as follows:

- t_{1ary} is the transition point between transient and steady creep;
- t_{2ary} is the inflection point of the creep curve;
- t_{3ary} is the second transition point (flow time);
- t_i is the instability time;
- t_m is the maximum possible lifetime.

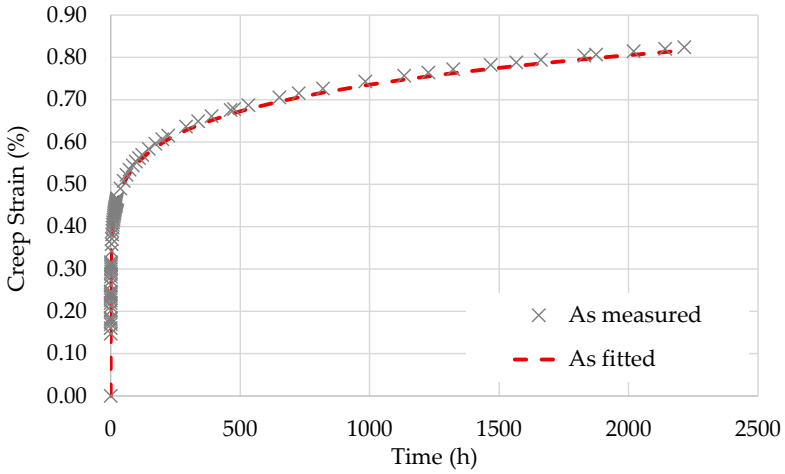


(**a**)

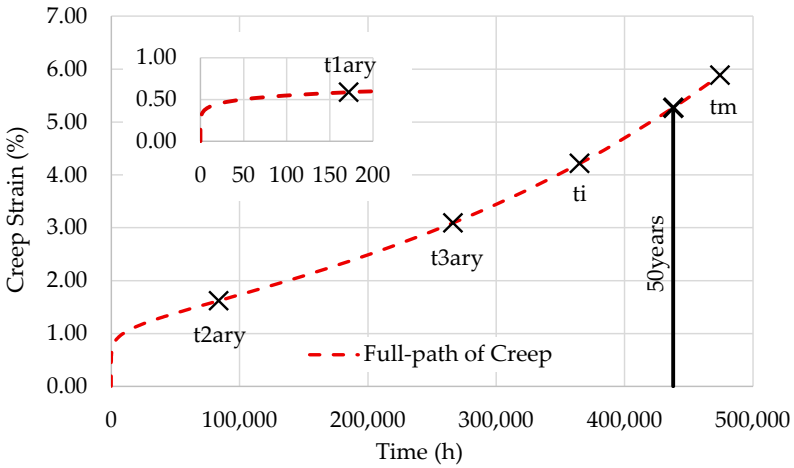


(**b**)

Figure 2. T28-S15: (**a**) data fitting; (**b**) full path of creep and transition points.

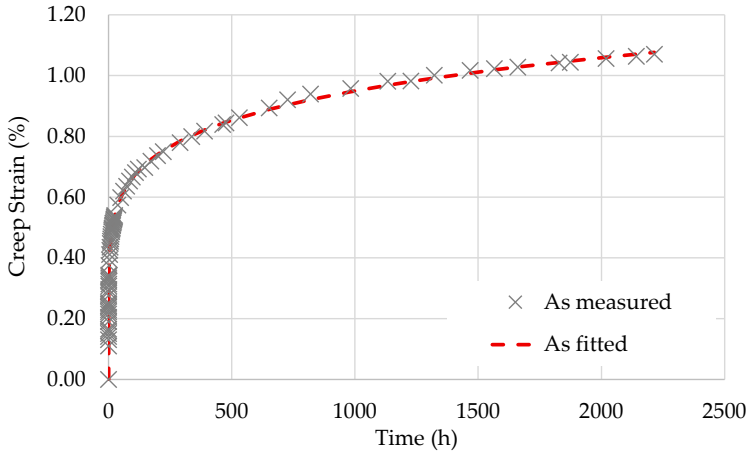


(**a**)



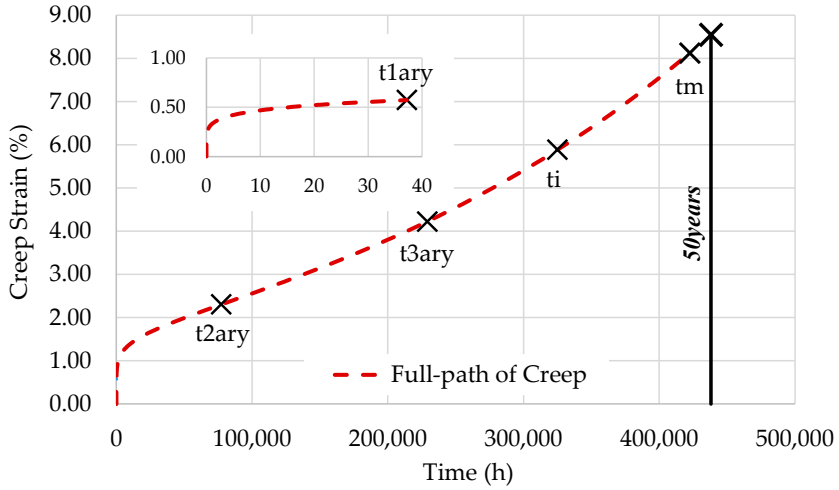
(**b**)

Figure 3. T28-S25: (**a**) data fitting; (**b**) full path of creep and transition points.



(**a**)

Figure 4. *Cont.*



(**b**)

Figure 4. T28-S35: (**a**) data fitting; (**b**) full path of creep and transition points.

Based on D_0, the compliance in the glassy state is given by $D_0 = {}^{k}/_{\sigma}$. Table 3 summarizes the values of D_0 and the parameters used to obtain the creep compliance for each stress level.

Table 3. Parameters to obtain the creep compliance by EPL expression.

Specimen	Stress	D_0	β	t_i
	(MPa)	(1/MPa)		(h)
T28-S15	64.30	0.00193	0.164	398,500
T28-S25	99.20	0.00307	0.127	365,000
T28-S35	142.30	0.00231	0.153	344,922

6.1.2. Relaxation Modulus Prediction

Since the creep tests were conducted under constant stress, the relaxation modulus can be expressed in terms of the EPL constants using the EPL relaxation expression (31), leading to the parameters summarized in Table 4.

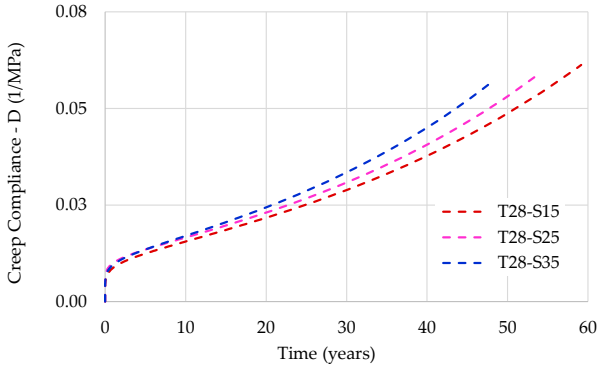
Table 4. Parameters to obtain the creep compliance by EPL expression.

Specimen	Stress	E_0	β	t_i
	(MPa)	(MPa)		(h)
T28-S15	64.30	518.55	0.164	398,500
T28-S25	99.20	325.25	0.127	365,000
T28-S35	142.30	432.52	0.153	344,922

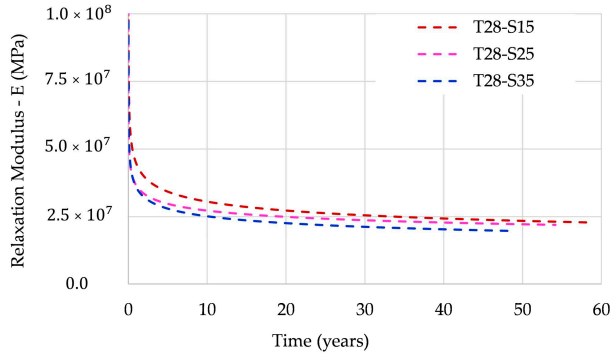
Figure 5 shows the full path of the creep compliance and the relaxation modulus by EPL expressions.

As shown in Figure 5, both the creep compliance and the relaxation modulus present stress dependence. According to [26], this dependence becomes more critical as the temperature approaches the glass transition temperature.

As reported above, the creep compliance and the relaxation modulus are not each other´s reciprocals but they are instead related. Figure 6 shows the relationship between these viscoelastic properties.



(**a**)



(**b**)

Figure 5. Full path of: (**a**) creep compliance; (**b**) relaxation modulus.

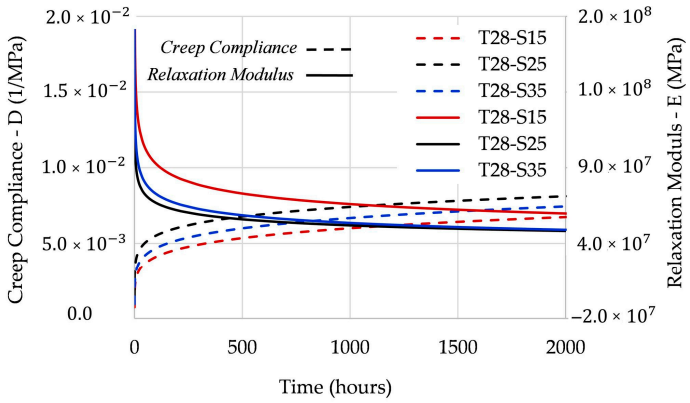


Figure 6. Relationship between the viscoelastic properties.

6.2. Relaxation Modulus Fitted from Sorvari et al. (2006)

Sorvari et al. [24] presented numerical procedures to evaluate the creep compliance from relaxation tests with nonideal loading and noise in simulated experimental data. From several ramp tests, the relaxation modulus was determined under the step strain assumption. The interconversion methods were numerically tested using synthetic data. The following procedure was applied to simulate the determination of creep conformity from the relaxation modulus: (i) the virtual relaxation test was made, from which the stress was determined; (ii) the relaxation modulus was computed; and (iii) the creep compliance was determined from a convenient method (for more details, see [24]). According to the authors, the procedure described above was carried out in different simulation cases with varying material parameters and noise.

The relaxation modulus was chosen to be

$$G(t) = G_0 + G_1 e^{-t/\lambda} \tag{37}$$

where G_0 is the initial shear modulus, G_1 is the constant shear modulus, and λ is the relaxation time.

From the given simulation, the coefficients of (32) were $G_0 = 0.4$ MPa, $G_1 = 0.5$ MPa, and $\lambda = 1$ to 100 s. In this paper, the relaxation modulus for $\lambda = 2$ s and $\lambda = 4$ s is fitted. The average relative error was 1.53% for $\lambda = 2$ s and 1.78% for $\lambda = 4$ s. In both cases, the r-Pearson coefficient was higher than 0.95.

The relaxation modulus is expressed in terms of the EPL constants using the EPL relaxation expression (31), leading to the parameters summarized in Table 5.

Table 5. Parameters of the relaxation modulus by EPL expression.

Relaxation Time-λ [s]	k	β	t_i [s]
2	7	0.980	100
4	5	0.982	97

Figures 7 and 8 show the full path of the relaxation modulus obtained from the EPL expressions.

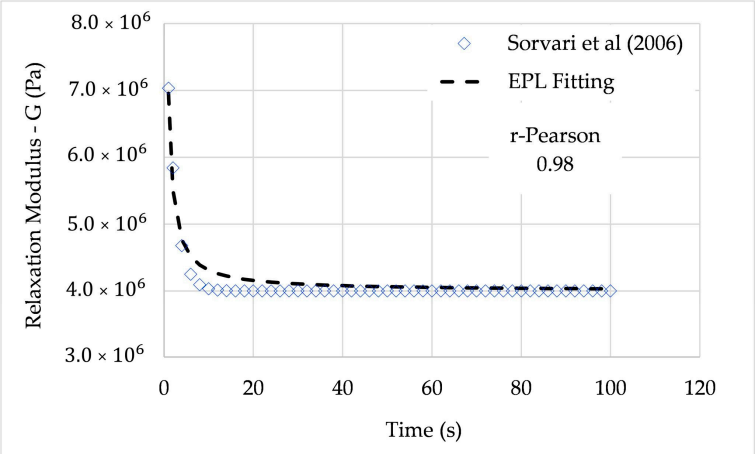


Figure 7. Relaxation modulus from Sorvari et al. (2006) and EPL fitted curve ($\lambda = 2\ s$).

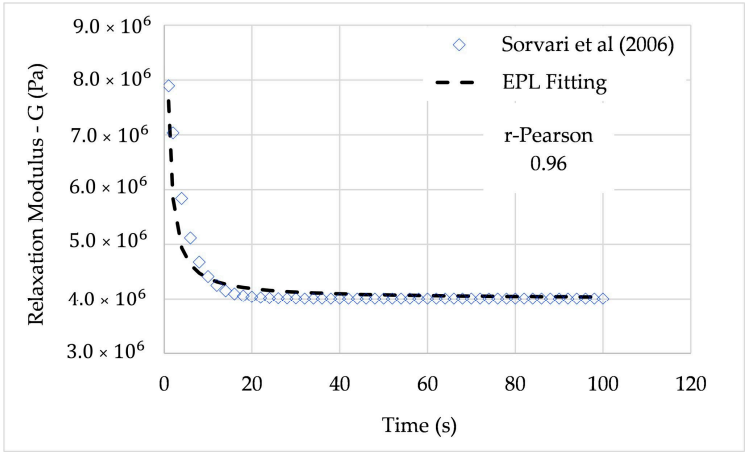


Figure 8. Relaxation modulus from Sorvari et al. (2006) and EPL fitted curve ($\lambda = 4\ s$).

6.3. Relaxation Modulus Fitted from Hernández-Jiménez et al. (2002)

Hernández-Jiménez et al. [25] presented a study of stress relaxation in samples of methylmethacrylate (PMMA) and polytetrafluorethylene (PTFE) polymers; in this study, it was pointed out that there is not only one time of relaxation as predicted by the classic Maxwell model, but rather two distributions of relaxation time.

Two different types of commercial-grade polymer samples from Dupont were used. Standard test samples of dimensions 100 mm × 25 mm × 3 mm for PTFE and 100 mm × 25 mm × 4 mm for PMMA were used and deformed under tension at a crosshead speed of 3 mm/min. In the stress relaxation test, when the deformation was 5%, the testing machine crosshead was stopped and kept in a constant position, and the values of the applied load, $F(t)$, were registered over time. From $F(t)$, the respective stress, $\sigma(t)$, was obtained by dividing it by the normal cross-section of the sample. Finally, the time relaxation modulus function was obtained by dividing the calculated stress by the constant strain of the sample, $\varepsilon_0 = 0.05$.

The relaxation modulus is expressed in terms of the EPL constants using the EPL relaxation expression (31), leading to the parameters summarized in Table 6.

Table 6. Parameters of the relaxation modulus by EPL expression.

k	β	t_i (s)
0.0515	0.045	6600

Figure 9 shows the relaxation modulus fitted by the EPL expressions. The average relative error was 1.85%, and the r-Pearson coefficient was 0.95.

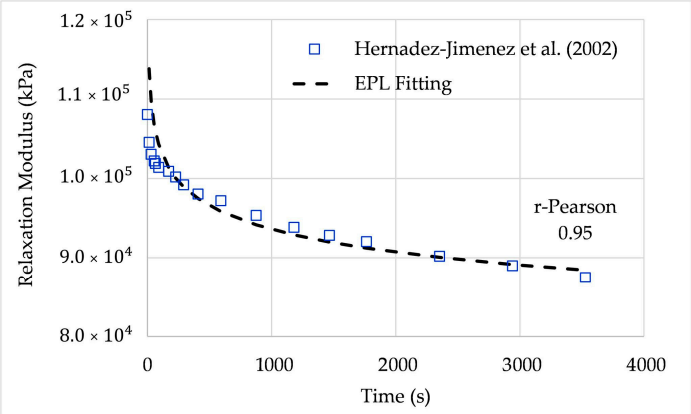


Figure 9. Relaxation modulus from Hernández-Jiménez et al. (2002) and EPL fitted curve for PMMA.

7. Accuracy and Validation

To perform an accuracy test and further validate the EPL fitting and its interconversion, sampled points from the relaxation curves identified in [27] were used, corresponding to cylindrical asphalt mixture specimens at three aging conditions (three replicates for each experimental combination). Direct tension relaxation modulus tests were conducted at 21 °C using the trapezoidal loading pattern at a low level of strain.

The standard sigmoid (SS) and generalized logistic sigmoid (GLS) fitting expressions are

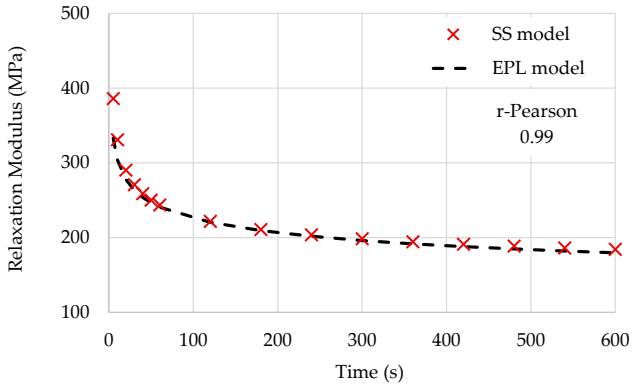
$$E(t) = 18.99 + \frac{623.61}{1 + e^{2.53 + 1.017\ (\log t)}} \tag{38}$$

$$E(t) = 21,32 + \frac{649.63}{\left[1 + 0.67e^{2.02+0.83\ (\log t)}\right]^{1.50}} \quad (39)$$

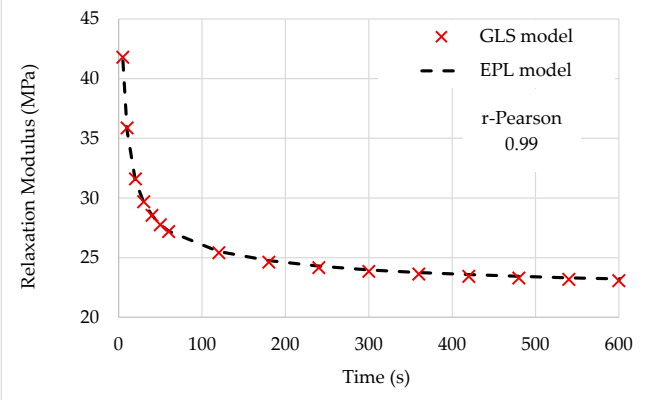
It must be noted that these functions may not provide exact representations of experimental data. However, for a given set of constants, they are exact and thus provide a means for checking the accuracy of the approximate interrelationships deduced in this paper, which is evidenced by the good matching between the experimental and fitting curves.

Figure 10 shows the evaluation of the relaxation modulus fitted by the approximation given by the EPL model to the data expressed by the SS and GLS expressions. The EPL coefficients are summarized in Table 7.

The results illustrated in Figure 10 show a close match between Sigmoid and EPL models, meaning that the proposed model yields a high predictive accuracy. Furthermore, the EPL models show their ability and easiness to fit and simulate the creep and relaxation behavior of polymeric materials.



(**a**)



(**b**)

Figure 10. Relaxation modulus: (**a**) standard sigmoid (SS) x EPL models; (**b**) generalized logistic sigmoid (GLS) x EPL models.

Table 7. Parameters to obtain relaxation modulus by EPL expression.

Method	k	β	t_i [h]
SS	0.910	0.140	3.70×10^2
GLS	12.500	0.495	8.70×10^2

8. Conclusions

This paper first presented a brief review of some methods of interconversion between linear viscoelastic properties of polymeric composites in the time domain. Their theoretical background was presented, and the relation between creep and relaxation and the constitutive integrals of linear viscoelasticity was summarized. It was shown that most of the classical methods of interconversion are based on the power-law and exponential methods of fitting. Despite their ease of application, these methods are not efficient in representing the full-path curve of the creep behavior of polymers and polymer composites, namely their three creep stages.

In the second part of the paper, a new approximate interconversion scheme that uses a convenient Laplace transform and an approximated Gamma function to convert the measured creep compliance to a relaxation modulus was presented. Data available in the literature were used to assess the consistency of the viscoelastic functions via the new interconversions presented in this work. The exponential-power-law (EPL) method of creep fitting (based on [13,14] and described in [15]) was converted to the EPL relaxation modulus expression, and the creep data provided in [23] were successfully fitted. To validate the EPL interconversion, the relaxation models identified in [27] were used as a reference. The results obtained show that the EPL fitting method proposed herein is very simple to implement and quick to apply, due to the small number of coefficients that need to be determined. In addition, the method is stable and accurate, as attested by the achieved Pearson correlation coefficient, greater than 0.97 for all test data considered.

Author Contributions: E.C. and J.R.C. are the supervisor and co-supervisor of this research work, respectively. Conceptualization, V.D., E.C. and J.R.C.; methodology, V.D.; software, V.D.; validation, V.D.; formal analysis, V.D., E.C. and J.R.C.; investigation, V.D.; resources, E.C.; data curation, V.D.; writing—original draft preparation, V.D.; writing—review and editing, V.D., E.C. and J.R.C.; visualization, V.D., E.C. and J.R.C.; supervision, E.C. and J.R.C.; project administration, E.C.; funding acquisition, E.C. All authors have read and agreed to the published version of the manuscript.

Funding: Research supported by Fundação para a Ciência e a Tecnologia (Base Funding-UIDB/04708/2020) of the CONSTRUCT-Instituto de I&D em Estruturas e Construções; national funds through the FCT/MCTES (PIDDAC).

Conflicts of Interest: The authors declare no conflict of interest.

References

1. Pang, M.; Li, Z.; Lou, T. Numerical Study of Using FRP and Steel Rebars in Simply Supported Prestressed Concrete Beams with External FRP Tendons. *Polymers* **2020**, *12*, 2773. [CrossRef] [PubMed]
2. Katsourinis, S.; Kontou, E. Comparing interconversion methods between linear viscoelastic material functions. *Mech. Time Depend. Mater.* **2018**, *22*, 401–419. [CrossRef]
3. Park, S.W.; Schapery, R.A. Methods of interconversion between linear viscoelastic material functions. Part I—A numerical method based on Prony series. *Int. J. Solids Struct.* **1999**, *36*, 1653–1675. [CrossRef]
4. Kim, Y.R. *Modeling of Asphalt Concrete*; McGRaw-Hill Book Company, Inc.: Raleigh, NC, USA, 2009; ISBN 0071596518.
5. Naresh, K.; Khan, K.A.; Umer, R.; Vasudevan, A. Temperature-Frequency–Dependent Viscoelastic Properties of Neat Epoxy and Fiber Reinforced Polymer Composites: Experimental Characterization and Theoretical Predictions. *Polymers* **2020**, *12*, 1700. [CrossRef] [PubMed]
6. Ferry, J.D. *Viscoelastic Properties of Polymers*, 3rd ed.; John Wiley & Sons, Inc.: Madison, WI, USA, 1980; Volume 63, ISBN 1109301219.
7. Tschoegl, N.W. *The Phenomenological Theory of Linear Viscoelastic Behavior*; Springer: Pasadena, CA, USA, 1989; ISBN 9783642736049.
8. Park, S.W.; Kim, Y.R. Interconversion between Relaxation Modulus and Creep Compliance for Viscoelastic Solids. *J. Mater. Civ. Eng.* **1999**, *11*, 76–82. [CrossRef]
9. Schapery, R.A.; Park, S.W. Methods of interconversion between linear viscoelastic material functions. Part II—An approximate analytical method. *Int. J. Solids Struct.* **1999**, *36*, 1677–1699. [CrossRef]
10. Loy, R.J.; de Hoog, F.R.; Anderssen, R.S. Interconversion of Prony series for relaxation and creep. *J. Rheol.* **2015**, *59*, 1261–1270. [CrossRef]

11. Wang, T.; Xu, C.; Guo, N.; Hamdaoui, M.; Daya, E.I.M. Uncertainty propagation of frequency response of viscoelastic damping structures using a modified high-dimensional adaptive sparse grid collocation method. *Mech. Adv. Mater. Struct.* **2020**, 1–19. [CrossRef]
12. De Lima, A.M.G.; Rade, D.A.; Bouhaddi, N. Stochastic modeling of surface viscoelastic treatments combined with model condensation procedures. *Shock Vib.* **2010**, *17*, 429–444. [CrossRef]
13. Crevecoeur, G.U. Quelques réflexions autour de la courbe de fluage—Une nouvelle perspective. *J. Des Ingénieurs* **1992**, *50*, 44–47.
14. Crevecoeur, G.U. A Model for the Integrity Assessment of Ageing Repairable Systems. *IEEE Trans. Reliab.* **1993**, *42*, 148–155. [CrossRef]
15. Dacol, V.; Caetano, E. Modelling the three-stage of creep. In Proceedings of the RILEM Spring Convention 2020, Guimarães, Portugal, 10–14 March 2020.
16. Lakes, R.S. *Viscoelastic Solids*, 1st ed.; CRC Press LLC: Madison, WI, USA, 1999; ISBN 9783540773405.
17. Leaderman, H. Viscoelasticity phenomena in amorphous high polymeric systems. In *Rheology*; Eirich, F.R., Ed.; Elsevier: New York, NY, USA, 1958; Volume 2.
18. Arfken, G.B.; Weber, H.J. *Mathematical Methods for Physics*, 6th ed.; Elsevier Academic Press: San Diego, CA, USA, 2005; ISBN 9781536134117.
19. Crevecoeur, G.U. Four Parameters Databank for Full Creep Curve Characterization. In Proceedings of the American Society of Mechanical Engineers–ASME Pressure Vessels and Piping Conference, Pittsburgh, PA, USA, 9–23 June 1988; Volume: PVP-Vol. 138; NDE-Vol. 4, pp. 203–210.
20. Amenyou, F.K. Properties and Computation of the Inverse of the Gamma Function, The University of Western Ontario. Master's Thesis, The University of Western Ontario, London, ON, Canada, 8 May 2018. Available online: https://ir.lib.uwo.ca/etd/5365 (accessed on 15 December 2020).
21. Mortici, C. On gospers formula for the gamma function. *J. Math. Inequalities* **2011**, *5*, 611–614. [CrossRef]
22. Buck, R.C. *Advanced Calculus*; University of Wisconsin: Madison, WI, USA, 1976; ISBN 0070087288.
23. Garrido, M.; Correia, J.R.; Keller, T. Effect of service temperature on the flexural creep of vacuum infused GFRP laminates used in sandwich floor panels. *Compos. Part B Eng.* **2016**, *90*, 160–171. [CrossRef]
24. Sorvari, J.; Malinen, M. Numerical interconversion between linear viscoelastic material functions with regularization. *Int. J. Solids Struct.* **2007**, *44*, 1291–1303. [CrossRef]
25. Hernández-Jiménez, A.; Hernández-Santiago, J.; Macias-García, A. Relaxation modulus in PMMA and PTFE fitting by fractional Maxwell model. *Polym. Test.* **2002**, *21*, 325–331. [CrossRef]
26. Al-Haik, M.S.; Hussaini, M.Y.; Garmestani, H. Prediction of nonlinear viscoelastic behavior of polymeric composites using an artificial neural network. *Int. J. Plast.* **2006**, *22*, 1367–1392. [CrossRef]
27. Forough, S.A.; Nejad, F.M.; Khodaii, A. Comparing various fitting models to construct the tensile relaxation modulus master curve of asphalt mixes. *Int. J. Pavement Eng.* **2016**, *17*, 314–330. [CrossRef]

Publisher's Note: MDPI stays neutral with regard to jurisdictional claims in published maps and institutional affiliations.



© 2020 by the authors. Licensee MDPI, Basel, Switzerland. This article is an open access article distributed under the terms and conditions of the Creative Commons Attribution (CC BY) license (http://creativecommons.org/licenses/by/4.0/).

Paper 3

Dacol, V.; Caetano, E.; Correia, J.R.

A New Viscoelasticity Dynamic Fitting Method Applied for Polymeric and Polymer-Based Composite Materials

Materials 2020, 13, 5213. *https://doi.org/10.3390/ma13225213*

Published: 18 November 2020.

Impact Factor: 3.920 (2020).

materials

MDPI

Article

A New Viscoelasticity Dynamic Fitting Method Applied for Polymeric and Polymer-Based Composite Materials

Vitor Dacol [1,*], Elsa Caetano [1] and João R. Correia [2]

[1] CONSTRUCT (ViBEST), Faculty of Engineering (FEUP), University of Porto, 4200-465 Porto, Portugal; ecaetano@fe.up.pt

[2] CERIS, DECivil, IST, University of Lisbon, 1049-001 Lisbon, Portugal; joao.ramoa.correia@tecnico.ulisboa.pt

* Correspondence: vitor.dacol@fe.up.pt; Tel.: +351-913-098-842

Received: 25 October 2020; Accepted: 16 November 2020; Published: 18 November 2020



Abstract: The accurate analysis of the behaviour of a polymeric composite structure, including the determination of its deformation over time and also the evaluation of its dynamic behaviour under service conditions, demands the characterisation of the viscoelastic properties of the constituent materials. Linear viscoelastic materials should be experimentally characterised under (i) constant static load and/or (ii) harmonic load. In the first load case, the viscoelastic behaviour is characterised through the creep compliance or the relaxation modulus. In the second load case, the viscoelastic behaviour is characterised by the complex modulus, E^*, and the loss factor, η. In the present paper, a powerful and simple implementing technique is proposed for the processing and analysis of dynamic mechanical data. The idea is to obtain the dynamic moduli expressions from the Exponential-Power Law Method (EPL) of the creep compliance and the relaxation modulus functions, by applying the Carson and Laplace transform functions and their relationship to the Fourier transform, and the Theorem of Moivre. Reciprocally, once the complex moduli have been obtained from a dynamic test, it becomes advantageous to use mathematical interconversion techniques to obtain the time-domain function of the relaxation modulus, $E(t)$, and the creep compliance, $D(t)$. This paper demonstrates the advantages of the EPL method, namely its simplicity and straightforwardness in performing the desirable interconversion between quasi-static and dynamic behaviour of polymeric and polymer-composite materials. The EPL approximate interconversion scheme to convert the measured creep compliance to relaxation modulus is derived to obtain the complex moduli. Finally, the EPL Method is successfully assessed using experimental data from the literature.

Keywords: viscoelasticity; creep and relaxation; interconversion; dynamic behaviour; dynamic mechanical analysis; storage modulus; loss factor

1. Introduction

Polymeric and polymer-based composite materials present viscoelastic behaviour, which is associated with the ability to simultaneously store and dissipate energy when subjected to a mechanical load. This coupled system (elasticity and viscosity) provides an increased rate of damping.

Understanding the response of a polymer or polymer-composite material to dynamic excitation, which is very relevant for many structural applications, involves characterising the physical factors affecting deformation and recovery cycles.

One of the relevant mechanical properties of a polymer is that the modulus, i.e., the ratio of stress to strain, has a complex nature: the real or in-phase part represents the part of the response in phase with the excitation; the imaginary part is associated with the lagging part of the response and expresses the damping capacity of the material.

Furthermore, the interrelationships between linear viscoelastic material functions enable the conversion of certain material functions into other functions that can be more easily obtained over a wide-enough range of time or frequency [1]. An interconversion procedure between time and frequency domain functions can therefore be used in analyses that require the relaxation or compliance time spectrum, $E(t)$ or $D(t)$, instead of the readily available dynamic moduli, $E^*(\omega)$ or $D^*(\omega)$ [2].

A variety of methods exist which are applicable to the interconversion of static (creep) and dynamic (relaxation) functions on the basis of appropriate experimental data of various polymers. Reference [3] presents a method based on the convolution formula of creep compliance to obtain the dynamic modulus using a numerical integration method to solve these integrals. Unfortunately, this method needs to use numerical integration methods to solve complicated integrals and requires complex computing programs. References [4] and [5] present a numerical method of interconversion between linear viscoelastic material functions based on a Prony series representation. Here, the effects of different choices of relaxation and retardation times on the accuracy of the method are discussed. Prony series representation requires the adaptation of many variables; another inherent disadvantage of this approach is the possibility of generating negative coefficients of the Prony series or oscillations, namely when the source data exhibit significant variability. The problem of negative Prony series coefficients is addressed in [6], where the difficulty of the direct fitting of a Prony series function to experimental data without appropriate pre-smoothing is discussed. In Ref. [7], a power-law function is used to express the creep compliance, which is converted into complex compliance.

Despite certain advantages of each of the described methods, all are inefficient to express the complete viscoelastic curve of a polymer or a polymer-based composite, i.e., of covering all stages of their viscoelastic behaviour, whether in creep or relaxation. The EPL function, in turn, is efficient in adjusting experimental creep and relaxation data, and is able to predict viscoelastic behaviour for long periods [1].

When studying the mechanical behaviour of viscoelastic materials, it is usually assumed that the strains and the stresses are deterministic functions. However, Wang et al. [8] highlight the importance of considering the uncertainty propagation of the frequency response for the robust design of viscoelastic damping structures. According to De Lima et al. [9], among the various methods devised for uncertainty modelling, the stochastic finite element method has received major attention, as it is well adapted for applications to complex engineering systems.

In this paper, an interconversion procedure is proposed to convert the measured complex moduli to a relaxation viscoelastic function, and the measured relaxation modulus to complex moduli. Despite the potential importance, the experimental quantification of uncertainties and the corresponding stochastic modelling are not addressed.

The procedure proposed combines (i) Carson and Laplace transform functions, (ii) the Theorem of Moivre, and (iii) Gamma-function approximation. The proposed interconversion function is easy to implement and leads to optimal curve fitting results in both the time- and frequency-domain, without the requirement of rheological models to represent the polymeric system.

2. Theoretical Background

2.1. The Hysteresis Basics

The hysteresis cycle can be analytically characterised by assuming that the response to a harmonic excitation will be harmonically similar. In turn, when polymer and polymer-based composite materials are subjected to harmonic stress cycles, they have harmonic deformation cycles with the same frequency but with a difference of phase with respect to the corresponding stress cycles. Reference [10] quotes that, within limits, the plots of measured stress versus measured strain are elliptical in shape and retain that shape as amplitude increases. Furthermore, the slope of the major axis of the ellipse is a measure of the stiffness of the sample, and the ratio between minor and major axis lengths is a measure of the damping. It should be noted that all types of internal damping, and particularly those inherent to the movement of polymer chains, are related to hysteresis cycles.

From the relationship between strain and stress during a hysteresis cycle of a viscoelastic material, the following relation is obtained

$$\sigma(t) = \frac{\sigma_0}{\varepsilon_o}\cos(\delta)\varepsilon(t) + \frac{\sigma_0}{\varepsilon_o}\sin(\delta)\frac{d\varepsilon(t)}{dt} \quad (1)$$

where $\sigma(t)$ is the applied stress; σ_0 is the amplitude of stress during the hysteresis cycle; ε_0 is the amplitude of the strain during the hysteresis cycle δ is the angle between excitation and response $\varepsilon(t)$ is the strain at time t-$_{th}$.

The first term of Expression (1) represents the storage modulus, E', and the second term represents the damping capacity of the viscoelastic material.

Expression (1) can be written as

$$\sigma(t) = E'\varepsilon(t) + \frac{E'}{\omega}\dot{\varepsilon}\tan(\delta) \quad (2)$$

where $\dot{\varepsilon}$ is the strain rate; E' is the storage modulus; ω is the angular frequency; $\tan(\delta)$ is the so-called "tan-delta", representing the loss factor η ($\eta = \tan(\delta)$).

2.2. A Brief Review of the Complex Moduli

The effect of polymeric material on the damping of a given structure is influenced by the stiffness of the material as well as its damping. In fact, the viscous part of the viscoelastic behaviour of polymers becomes evident under dynamic loading.

By imposing a harmonic excitation of type $\varepsilon(t) = \varepsilon_0 \cdot e^{i(\omega t)}$ on a viscoelastic material, the stress response in the frequency domain, derived from Expression (2), assumes the following form

$$\sigma(\omega) = E'(\omega)\varepsilon(\omega) + iE'(\omega)\eta(\omega)\varepsilon(\omega) \quad (3)$$

where i is the imaginary part of a complex function given by $\sqrt{-1}$.

In Expression (3), the product given by $E'(\omega)\eta(\omega)$ is named the loss modulus, $E''(\omega)$, and represents the imaginary part of the complex modulus, $E^*(\omega)$, which is given by

$$E^*(\omega) = E'(\omega) + iE''(\omega) \quad (4)$$

From the complex modulus, the dynamic modulus amplitude, $|E^*|$, is determined as

$$|E^*| = \sqrt{(E')^2 + (E'')^2} \quad (5)$$

The storage and the loss moduli represent the storage and the dissipation of energy, respectively. In this respect, as the stress and the internal damping of a viscoelastic material depend on the frequency of the imposed load, the relationship between the dissipated energy, H, and the loss modulus, E'', may be described as

$$H = \int_0^{2\pi/\omega} \varepsilon(\omega)[E'(\omega) + iE''(\omega)]\frac{\partial\varepsilon}{\partial t}dt = \varepsilon_0^2\omega\pi E'' \quad (6)$$

2.3. Relationship Between Time and Frequency Domain Moduli

Considering the relationships defined in the previous section, it can be concluded that the knowledge of the relaxation modulus or the creep compliance is sufficient to describe the behaviour of materials with linear viscoelastic behaviour [7]. Consequently, the complex modulus, E^*, and therefore its components (E', E'', $|E^*|$ and η), can be defined from the frequency characterisation of the strain

and stress. Moreover, the relaxation modulus (or creep compliance) can be obtained from the complex relaxation modulus (or complex compliance).

The relationship between the time and the frequency domain moduli is related to the operational functions given as

$$E^*(\omega) = \widetilde{E}(s)\Big|_{s=i\omega} \tag{7}$$

where $\widetilde{E}$ is the Carson Transform of a function, given by $\widetilde{E}(s) = s\overline{E}(s)$; and $\overline{E}$ is the rational functions of s in Laplace domain.

Moreover, the storage and the loss modulus can be readily deduced from the relaxation modulus via Fourier transform [11]:

$$E'(\omega) = \omega \int_0^\infty E(t)\sin(\omega t)dt \tag{8}$$

$$E''(\omega) = \omega \int_0^\infty E(t)\cos(\omega t)dt \tag{9}$$

Consequently, the relaxation modulus (or creep compliance) can be deduced from the complex modulus by the Fourier transform:

$$E(t) = \frac{2}{\pi}\int_0^\infty \frac{E'(\omega)}{\omega}\sin(\omega t)d\omega \tag{10}$$

$$E(t) = \frac{2}{\pi}\int_0^\infty \frac{E''(\omega)}{\omega}\cos(\omega t)d\omega \tag{11}$$

However, the Fourier transform of the creep compliance, $D(t)$, is not convergent because it is an increasing function of time.

Given the above-defined relation (Expression (7)), the following procedure can be followed to derive the complex modulus:

(i) From a given creep test data, to determine the creep compliance;
(ii) To apply the interconversion method to obtain the relaxation modulus from creep compliance;
(iii) To apply the interconversion method to obtain the complex modulus from the relaxation modulus function;
(iv) According to the required frequency, to calculate the viscoelastic parameters of the frequency (E', E'', η).

The steps (i) and (ii) involve the concept of the Exponential-Power Law (EPL) method, which is derived from Ref. [12] and presented in Ref. [1]. A brief description of the method is presented in the next section.

3. Exponential-Power Law

In Ref. [13], the similarity between creep behaviour and mechanical system ageing is shown, where the failure rate of mechanical repairable systems that deteriorate over time due to ageing can usually be visualised by a bathtub curve, as shown by the creep rate curve.

In Ref. [12] a differential equation is proposed to synthesise the behaviour of the creep rate expressed by the bathtub curve. Once integrated, this equation yields

$$\varepsilon(t) = k{\cdot}t^{\beta}{\cdot}e^{\frac{t}{t_i}} \tag{12}$$

where $\varepsilon(t)$ is the strain; β is a constant related to strain hardening ($\beta < 1$ and $1/t_i \ll \beta$); k is a constant related to the main stress influence; and t_i is the instability time.

The instability time is the period of time (after the material is loaded) after which there is a risk that the system starts to fail and occurs in tertiary creep stage.

The conversion between the creep compliance, fitted with *Expression (12)), and the relaxation modulus may be required to estimate the fatigue resistance of composite structures. Thus, a numerical interconversion between the creep compliance and the relaxation modulus was conducted using a convenient Laplace transform and an approximated Gamma-function, and a simple but efficient expression to represent the relaxation modulus may be given as

$$E(t) = \frac{\sigma_0}{k\, t^{\beta}} \cdot \frac{\sin(\pi\beta)}{\pi} \cdot \left(\frac{t_i}{\beta} + \frac{1}{t} \right) \tag{13}$$

As mentioned in Ref. [14], relaxation behaviour emphasises short-term processes, while the creep behaviour weights long-lasting processes. Therefore, interconversion between these two groups of responses is frequently desired. Furthermore, to evaluate the viscoelastic damping of polymeric and polymer-based composite materials, it is useful to interconvert the real and imaginary parts of a complex response function within the frequency domain.

The hierarchical structure of the interconversion between viscoelastic properties is displayed in Figure 1.

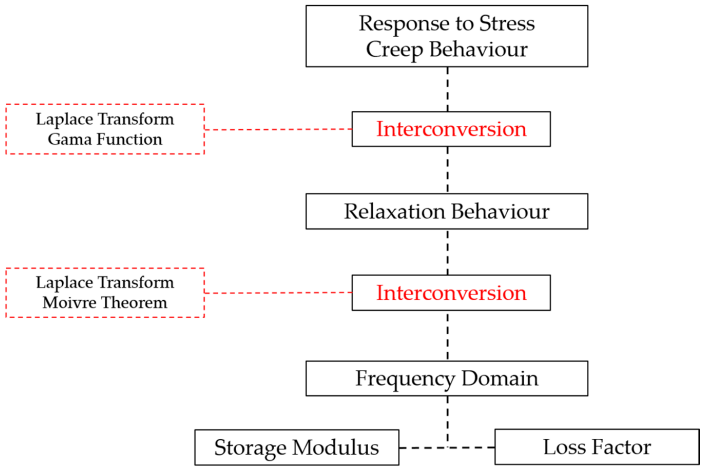


Figure 1. Hierarchy of interconversion relations (adapted from Ref. [14]).

4. Complex Moduli Obtained from EPL Method

A numerical interconversion between the relaxation modulus and the complex modulus is presented below. Laplace and Carson's transformation and Moivre's theorem are used to achieve the frequency domain from the time domain.

Using the Laplace transform properties summarised in Table 1, each term of the EPL function (Expression (13)) can be transformed as

$$\overline{f}\left\{ e^{\frac{t}{t_i}} \right\} = \frac{1}{s + t_i} \tag{14}$$

$$\overline{f}\left\{ t^{\beta} \right\} = \frac{\beta!}{s^{\beta+1}} \tag{15}$$

Table 1. Laplace transform properties.

$f(t)$	$\hat{f}(t)$
$e^{\alpha t}$	$\frac{1}{s-\alpha}$
$t^n,\ n > -1$	$\frac{n!}{s^{n+1}}$

After mathematical manipulations, the EPL function of relaxation modulus (Expression (13)), in $\mathcal{L}$-domain, is transformed into

$$\overline{E}(s) = \frac{\sigma_0}{k} \cdot \frac{\sin(\pi\beta)}{\pi} \cdot s^{\beta} \left[\frac{t_i \Gamma(1-\beta) + s\Gamma(1-\beta)}{\beta s} \right] \tag{16}$$

where $\overline{E}$ is the rational function of s and Γ is the Gamma function operator.

Applying Gamma function properties, $\gamma = -\beta! = \Gamma(\beta - 1)$, and rearranging Expression (16) as $E_\omega = (\sigma_0 \sin(\pi\beta)/k\pi) \cdot \gamma$, yields

$$\overline{E}(s) = \frac{E_\omega}{\beta} \cdot \left(s^{\beta} t_i + s^{\beta+1} \right) \tag{17}$$

Introducing Expression (7) into Expression (17) and after a mathematical manipulation, the complex modulus can be written as

$$E^*(\omega) = \widetilde{E}(s)\Big|_{s=i\omega} = \frac{E_\omega}{\beta} \cdot \left[(i\omega)^{\beta} t_i + (i\omega)^{\beta+1} \right] \tag{18}$$

The following known relationship between the two operational functions is obtained

$$E^*(\omega) D^*(\omega) = 1 \tag{19}$$

From the Theorem of Moivre, Expression (19) can be replaced as

$$E^*(\omega) = E_\omega \cdot \frac{\left[e^{iz} \omega^{\beta} t_i + i e^{iz} \omega^{\beta+1} \right]}{\beta} \tag{20}$$

where $z = \frac{\pi\beta}{2}$.

Applying the Euler identity and separating even and odd terms, Expression (20) yields

$$E^*(\omega) = E_\omega \frac{\omega^{\beta}}{\beta} \left[(t_i \cos z - \omega \sin z) + i(t_i \sin z + \omega \cos z) \right] \tag{21}$$

From Expression (21), the real and imaginary parts of the complex modulus are, respectively,

$$\mathfrak{R}_e = \frac{\omega^{\beta}}{\beta} [t_i \cos z - \omega \sin z] \tag{22}$$

$$\mathfrak{I}_m = \frac{\omega^{\beta}}{\beta} [t_i \sin z + \omega \cos z] \tag{23}$$

The storage, $E'(\omega)$, and loss modulus, $E''(\omega)$, parts of the dynamic modulus, are, respectively,

$$E'(\omega) = E_\omega \cdot \mathfrak{R}_e = E_\omega \cdot \frac{\omega^{\beta}}{\beta} [t_i \cos z - \omega \sin z] \tag{24}$$

$$E''(\omega) = E_\omega \cdot \mathfrak{I}_m = E_\omega \cdot \frac{\omega^{\beta}}{\beta} [t_i \sin z + \omega \cos z] \tag{25}$$

Furthermore, within linear viscoelasticity and from the relationship between the creep compliance and the relaxation modulus, it is possible to rewrite the dynamic modulus as a function of the creep compliance, $D(t)$, and strain, $\varepsilon(t)$, rewriting the factor E_ω, in Expressions (24) and (25), as follows

$$E_\omega = \frac{\varepsilon(t) \cdot \sin(\pi\beta)}{D(t) \cdot k \cdot \pi} \tag{26}$$

Once the creep strain is fitted, it is possible to directly estimate the dynamic behaviour of the polymeric or polymer-based composite material.

5. Application of EPL Method

This section presents the application and assessment of the method described above to the spectrum data collected from the literature, namely the studies by Kehrer et al. [15], Berthelot et al. [16], and Ledi et al. [17].

5.1. Dynamic Modulus Fitted from Kehrer et al. (2018)

Kehrer et al. [15] investigated the dynamic behaviour of a pure polymer (polypropylene—PP). The authors performed dynamic mechanical analysis (DMA) on the pure polymer and also on composite samples (PP reinforced with 30 wt.% of short glass fibres) to experimentally characterise their temperature- and frequency-dependent material behaviour.

The resulting experimental data not only give general information on the material behaviour of the composite subjected to a temperature and frequency load, but also provide input and validation data for the developed material modelling methods.

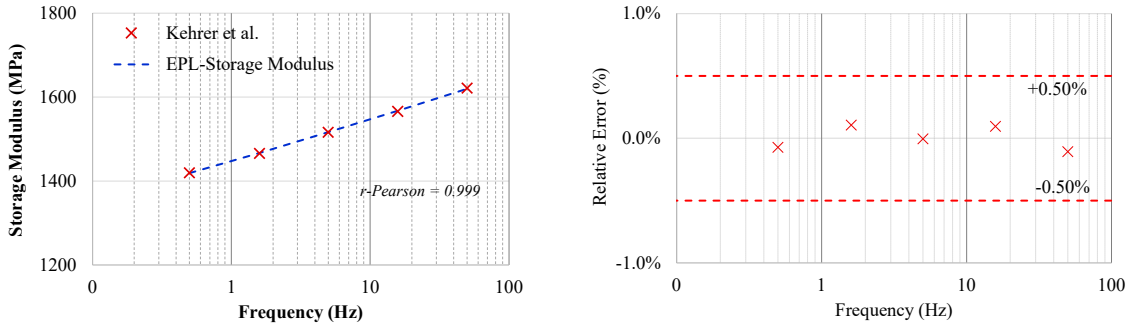
The DMA tests were conducted in tension mode with different frequencies (0.5 to 50 Hz) and temperature (−50 to 120 °C) loads. In the present study, the test data obtained for the pure PP at 30 °C are used. In preliminary works by Ref. [18], it is shown that for loads corresponding to a strain in the material of $\varepsilon \geq 0.60\%$, a nonlinear material behaviour is initiated. To remain below this value and keep the material within the linear range, the applied static preload and the superimposed dynamic load corresponded to maximum strains of 0.1% and 0.05%, respectively. The contact force was fixed at 5 N.

From the data spectra, the EPL equation fitting was conducted, leading to a maximum difference of ±0.50% between the test data and the fitted curve. The EPL coefficients are shown in Table 2.

Table 2. Parameters of the Exponential-Power Law (EPL) equation for Dynamic Moduli.

σ_o(MPa)	k	β	t_i(s)
3.00	58.08	0.0289	26,178

Figure 2 shows the evaluation of the storage modulus, $E'(\omega)$, fitted by the EPL equation to the data obtained in the DMA test for the pure PP polymer. The narrow margin of relative error shown in Figure 2b shows that the data adjustment performed by the EPL method presents a very good match to the data points.



(**a**) (**b**)

Figure 2. Storage Modulus for polypropylene (PP): (**a**) EPL fitting and (**b**) Relative Error in %.

From the obtained results, one may note that:

(i) As expected, the calculated instability time, t_i (26,178 s), is relatively low, reflecting the typical short lifetime for a pure thermoplastic PP;

(ii) The fitting provided by EPL is accurate and may represent the dynamic behaviour of the pure PP thermoplastic polymer;

(iii) The fitted curve of the storage modulus exhibits an r-Pearson factor greater than 99%.

The evaluation of the loss factor and the phase angle range is shown in Figure 3. An increase in the phase angle values is shown, which is logical, because the test temperature of 30 °C is higher than the glass transition temperature, T_g, of PP, which is in the range of −20 °C to 0 °C; however, the test temperature is significantly lower than the softening point of PP, which does not melt below 160 °C.

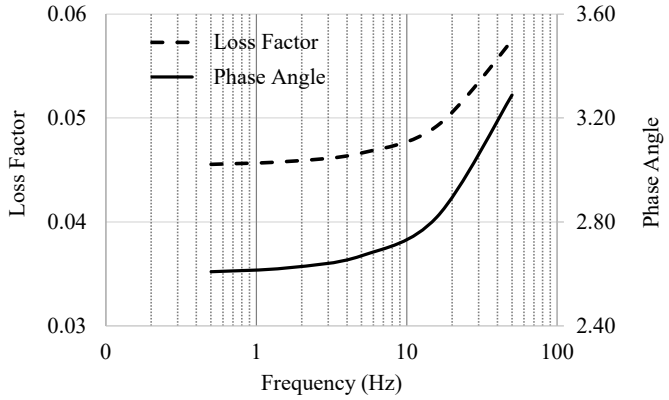


Figure 3. Loss Factor and Phase Angle of pure PP from EPL frequency-domain fitting.

Comparing the loss factor estimated by the EPL method to the measured loss factor at a temperature of 30 °C and a frequency of 5.0 Hz, the EPL gives $\eta = 0.047$, while the measurements show $\eta = 0.050$.

5.2. Dynamic Modulus Fitted from Berthelot et al. (2008)

Berthelot et al. [16] performed a series of analyses of damping of (i) composite laminates, (ii) composite laminates with interleaved viscoelastic layers, and (iii) sandwich specimens. The composite laminates are constituted of unidirectional E-glass fibre unidirectional mats and silk weave layers (both with 300 g/m^2) in an epoxy matrix, for a given fibre orientation of 0°, 15°, 30°, 45°, 60°, 75° and 90° with respect to the longitudinal axes of the specimen. The laminate materials with viscoelastic layers are the unidirectional glass fibre composites considered previously in which a single or two viscoelastic layers constituted of Neoprene-based layers (nominal thickness of 0.2 mm) were interleaved. The sandwich specimens were constructed with the [0/90]s cross-ply laminates as skins, enclosing 15 mm thick PVC closed-cell foams with three different densities (60, 80 and 200 kg/m^3).

The composite laminates were fabricated by hand lay-up in plates of different dimensions; these were cured at room temperature with pressure, using a vacuum moulding process, and then post-cured in an oven. The plates were fabricated with eight layers in such a way to obtain the same plate thickness (nominal value of 2.4 mm) with the same fibre volume fraction (nominal value of 0.40).

The experimental investigation of the damping of the different materials involved using beam test specimens and an impulse technique. Each test specimen was supported horizontally as a cantilever beam in a clamping block. An impulse hammer was used to induce the excitation of the flexural vibrations of the beam, and the beam response was detected using a laser vibrometer.

The evaluation of damping was performed on beams of different lengths (160 mm, 180 mm and 200 mm) to result in a variation of the values of the peak frequencies. Beams had a nominal width of 20 mm and a nominal thickness of 2.5 mm. The results were reported for the first three bending modes.

The following two assumptions were made about this investigation:

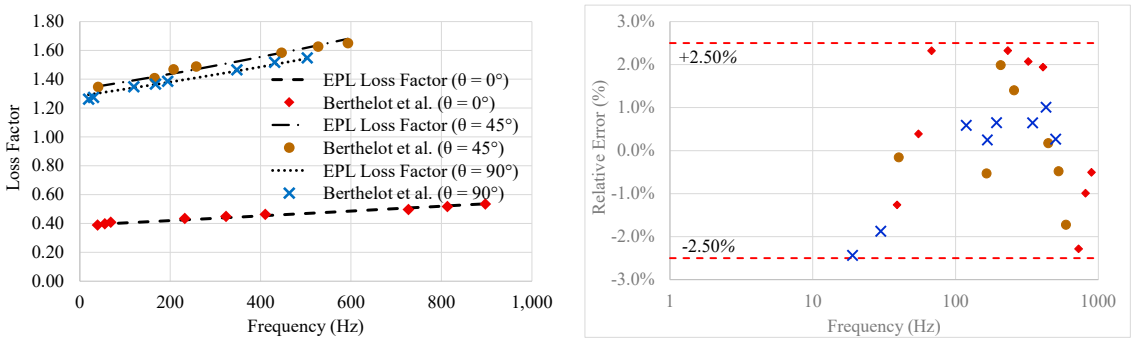
1. The test temperature, not reported in the paper, is assumed to be around 25 °C;
2. The loss factor is β and t_i dependenton the EPL method, therefore the coefficient k is assumed to be the unit for all samples and fibre orientation.

From the loss factor measured for 0°, 45°, and 90° of fibre orientation, the EPL equation fitting was conducted applying the least-squares method to determine the best fit curve to test data. The average relative error to the three adjustments was 4.43%. The EPL coefficients are shown in Table 3.

Table 3. Parameters of EPL equation for Loss Factor.

θ°	k	β	t_i(s)
0°	1	0.235	45,707
45°	1	0.589	34,443
90°	1	0.579	36,275

From Table 3, for given fibre orientation from the longitudinal axis of the specimen, it is observed that the value of β and t_i coefficients are fibre orientation dependent. Figure 4 shows the evaluation of the loss factor, η, fitted by the EPL equation, regarding the data of the impulse technique test for unidirectional glass fibre composites. It is observed that the damping for specimens where the fibre orientation is transverse to their longitudinal axis (45° and 90°) is greater than for specimens where the fibre orientation is parallel to its the longitudinal axis.



(**a**) (**b**)

Figure 4. (**a**) Loss Factor as a function of the frequency for different fibre orientations for unidirectional glass fibre composites and (**b**) Dispersion of the Relative Error in %.

5.3. Dynamic Modulus Fitted from Ledi et al. (2018)

Ledi et al. [17] present an identification method of the viscoelastic material properties (shear modulus and loss factor) of a symmetric three-layered viscoelastic sandwich beam. The authors performed experimental vibration tests to determine resonant frequencies and loss factors for different bending modes.

The viscoelastic sandwich beam tested by the authors was composed of three layers, bonded together: two aluminium elastic face sheets and one viscoelastic core layer, made of polyurethane dielectric resin (made of polyol and isocyanate). Two types of sandwich beams (beam 1 and beam 2) distinguished by their respective core and faces thicknesses were considered. The geometrical and material properties of the sandwich beams are reported in Table 4.

Table 4. Material properties and dimensions for beam 1 and beam 2.

Elastic Layers	
Material	Aluminium
Young's Modulus	$E_f = 6.9 \times 10^{10}$ Pa
Poisson's ratio	$v_f = 0.3$
Density	$\rho_f = 2766$ kg/m^3
Thickness	$h_{f,1} = 1$ mm and $h_{f,2} = 0.5$ mm
Viscoelastic Layer	
Material	Polyurethane dielectric resin
Poisson's ratio	$v_f = 0.3$
Density	$\rho_f = 1550$ kg/m^3
Thickness	$h_{c,1} = 1$ mm and $h_{c,2} = 2$ mm
Whole Beam	
Length	L = 500 mm
Width	b = 30 mm
Thickness	h = 3 mm

The experimental setup to measure sandwich beam frequency response curves comprised of an eloetrodynamic shaker, a laser vibrometer and a sandwich beam sample. The shaker generated vibrations that were controlled and measured by a controller device. The frequency excitation produced by the shaker ranged from 4 Hz and 1500 Hz. The vibration amplitude of the shaker was controlled by an accelerometer. The amplitude of the shaker was chosen to minimise nonlinear vibrations (typically 0.02 mm of displacement between 5 Hz and 157.5 Hz, and a 1 g acceleration between 157.5 Hz and 1500 Hz). A laser vibrometer was used to measure the amplitude of the beam's vibration; this equipment was pointed at the free extremity (tip) of the beam (cantilever), whose boundary condition was clamped-free. The test apparatus used in the experiments allowed adjustments of the clamping length—four lengths (from 318 to 475 mm) were tested.

For a linear, homogeneous and isotropic material, the EPL function of storage modulus Expression (24) may provide the definition of the storage shear modulus, $G'(\omega)$, whose relationship may be established by the complex Poisson's ratio, $v^*(\omega)$, as

$$E'(\omega) = 2G'(\omega) \cdot [1 + v^*(\omega)] \tag{27}$$

Given the reduced dependence on the frequency of Poisson's ratio, its value can be considered a real and constant quantity [19].

From the shear modulus measured, the EPL function of the *shear storage modulus* was fitted and the obtained coefficients are presented in Table 5.

Table 5. Parameters of the EPL equation for the in-Plane Shear Storage Modulus.

k	β	t_i(s)
0.68	0.98	2469.136

The evaluation of the in-plane shear storage modulus for both beams is shown in Figure 5, where it can be noted that the fitting is very close to the data points, providing a good description of the behaviour of the identified shear modulus quantities over a wide range of frequencies. It should be noted that because the adjusted curve refers to the spectrum of two distinct data tests, the evaluation of the relative error through the dispersion plot was not used in this adjustment; as an alternative, the r-Pearson coefficient was used to evaluate the quality of the fitting: values of 0.962 and 0.981 were obtained for beams 1 and 2, respectively.

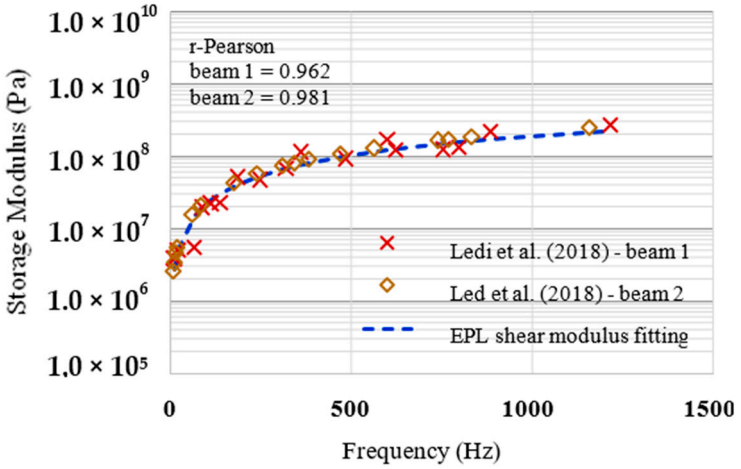


Figure 5. In-plane Shear Storage Modulus for sandwich beams.

6. Conclusions

This paper presents a new approximate interconversion scheme to convert the measured dynamic moduli into creep compliance modulus and relaxation modulus. The proposed method uses a convenient Laplace and Carson transform and its relationship to the Fourier Domain, coupled with the application of the Moivre and Euler Theorem.

The EPL creep fitting method described in Ref. [1] has been converted to the EPL dynamic modulus equation and the data provided in the literature have been successfully fitted. In particular, the test data concerning three different polymeric or polymer-based composites were used to validate the numerical approach: a pure polymer thermoplastic resin specimen, an E-glass-epoxy composite laminate, and an elastic-viscoelastic sandwich beam.

The results obtained show the accuracy of the EPL Method in fitting the data from creep, relaxation, and dynamic tests. Moreover, the method can show the three stages of creep (long-time behaviour). In addition, it is shown that fitting based on the EPL method is easy to implement since only three terms need to be found in any data spectrum, and no pre-smoothing procedure is required to ensure a good fit. Furthermore, the stability of this method is demonstrated by the achieved Pearson correlation coefficients, which was higher than 0.96 for the different examples.

Author Contributions: Conceptualization, V.D., E.C. and J.R.C.; methodology, V.D.; software, V.D.; validation, V.D.; formal analysis, V.D., E.C., J.R.C.; investigation, V.D.; resources, E.C.; data curation, V.D.; writing—original draft preparation, V.D.; writing—review and editing, V.D., E.C., J.R.C.; visualization, V.D., E.C., J.R.C.; supervision, E.C., J.R.C.; project administration, E.C.; funding acquisition, E.C.. All authors have read and agreed to the published version of the manuscript.

Funding: This research was funded by Research supported by Fundação para a Ciência e a Tecnologia (Base Funding—UIDB/04708/2020 of the CONSTRUCT - Instituto de I&D em Estruturas e Construções—national funds through the FCT/MCTES (PIDDAC).

Acknowledgments: Elsa Caetano and João Ramoa are the supervisor and co-supervisor of this research work, respectively.

Conflicts of Interest: The authors declare no conflict of interest.

References

1. Dacol, V.; Caetano, E. Modelling the three-stage of creep. In Proceedings of the 3rd RILEM Spring Convention 2020, Guimarães, Portugal, 10–14 March 2020.
2. Baumgaertel, M.; Winter, H.H. Determination of discrete relaxation and retardation time spectra from dynamic mechanical data. *Rheol. Acta.* **1989**, *28*, 511–519. [CrossRef]
3. Christensen, R.M. *Theory of Viscoelasticuty: An Introduction*, 2nd ed.; Academic Press: Cambridge, MA, USA, 1982.

4. Park, S.W.; Schapery, R.A. Methods of interconversion between linear viscoelastic material functions. Part I—A numerical method based on Prony series. *Int. J. Solids Struct.* **1999**, *36*, 1653–1675. [CrossRef]
5. Schapery, R.A.; Park, S.W. Methods of interconversion between linear viscoelastic material functions. Part II—An approximate analytical method. *Int. J. Solids Struct.* **1999**, *36*, 1677–1699. [CrossRef]
6. Park, S.W.; Kim, Y.R. Fitting prony-series viscoelastic models with power-law presmoothing. *J. Mater. Civ. Eng.* **2001**, *13*, 26–32. [CrossRef]
7. Findley, W.N.; Lai, J.S.; Onaram, K.; Christensen, R.M. Creep and Relaxation of Nonlinear Viscoelastic Materials—With an Introduction to Linear Viscoelasticity. *J. Appl. Mech.* **1977**, *44*, 364. [CrossRef]
8. Wang, T.; Xu, C.; Guo, N.; Hamdaoui, M.; Daya, E.I.M. Uncertainty propagation of frequency response of viscoelastic damping structures using a modified high-dimensional adaptive sparse grid collocation method. *Mech. Adv. Mater. Struct.* **2020**, in press. [CrossRef]
9. De Lima, A.M.G.; Rade, D.A.; Bouhaddi, N. Stochastic modeling of surface viscoelastic treatments combined with model condensation procedures. *Shock Vib.* **2010**, *17*, 429–444. [CrossRef]
10. Jones, D.I.G. *Handbook of Viscoelastic Vibration Damping*; Wiley: Hoboken, NJ, USA, 2001.
11. Mead, D.W. Numerical interconversion of linear viscoelastic material functions. *J. Rheol.* **1994**, *38*, 1769–1795. [CrossRef]
12. Crevecoeur, G.U. Quelques réflexions autour de la courbe de fluage—Une nouvelle perspective. *J. Ingénieurs.* **1992**, *50*, 44–47. (In French)
13. Crevecoeur, G.U. A Model for the Integrity Assessment of Ageing Repairable Systems. *IEEE Trans. Reliab.* **1993**, *42*, 148–155. [CrossRef]
14. Tschoegl, N.W. *The Phenomenological Theory of Linear Viscoelastic Behavior*; Springer: Berlin/Heidelberg, Germany, 1989.
15. Kehrer, L.; Wicht, D.; Wood, J.T.; Böhlke, T. Dynamic mechanical analysis of pure and fiber-reinforced thermoset- and thermoplastic-based polymers and free volume-based viscoelastic modelling. *GAMM Mitteilungen.* **2018**, *41*, 1–16. [CrossRef]
16. Berthelot, J.-M.; Assarar, M.; Sefrani, Y.; El Mahi, A. Damping analysis of composite materials and structures. *Compos. Struct.* **2008**, *85*, 189–204. [CrossRef]
17. Ledi, K.S.; Hamdaoui, M.; Robin, G.; Daya, E.M. An identification method for frequency dependent material properties of viscoelastic sandwich structures. *J. Sound Vib.* **2018**, *428*, 13–25. [CrossRef]
18. Brylka, B. Charakterisierung und Modellierung der Steifigkeit von langfaserverstärktem Polypropylen. Ph.D. Thesis, Karlsruhe Institute of Technology, Karlsruhe, Germany, February 2017.
19. Maurício, M.C. Dynamic Analysis of Structures with Viscoelastic Damping Treatments: Complex Modulus Identification and Transient Response. Master's Thesis, University of Porto, Porto, Portugal, 2017.

Publisher's Note: MDPI stays neutral with regard to jurisdictional claims in published maps and institutional affiliations.



© 2020 by the authors. Licensee MDPI, Basel, Switzerland. This article is an open access article distributed under the terms and conditions of the Creative Commons Attribution (CC BY) license (http://creativecommons.org/licenses/by/4.0/).

Paper 4

Dacol, V.; Caetano, E.; Correia, J.R.

Comparative Study of Damping on Pultruded GFRP and Steel Beams

Polymers 2021, 13, 2201. https://doi.org/10.3390/polym13132201

Published: 2 July 2021.

Impact Factor: 4.493 (2020).

polymers

MDPI

Article

Comparative Study of Damping on Pultruded GFRP and Steel Beams

Vitor Dacol [1,*], Elsa Caetano [1] and João Ramoa Correia [2]

[1] CONSTRUCT (ViBEST), Faculty of Engineering (FEUP), Universidade do Porto, 4200-465 Porto, Portugal; ecaetano@fe.up.pt
[2] CERIS, DECivil, IST, Universidade de Lisboa, 1049-001 Lisbon, Portugal; joao.ramoa.correia@tecnico.ulisboa.pt
* Correspondence: vitor.dacol@fe.up.pt; Tel.: +351-913-098-842

Abstract: The use of glass fibre reinforced polymer (GFRP) composites in civil engineering structures has seen considerable growth in recent years due to their high strength, low self-weight, and corrosion resistance, namely when compared to traditional materials, such as steel and reinforced concrete. To enable the structural use of GFRP composite materials in civil engineering applications, especially in footbridges, it is necessary to gather knowledge on their structural behaviour, particularly under dynamic loads, and to evaluate the ability of current design tools to predict their response. In fact, excessive vibration has a major influence on the in-service performance (comfort) of slender structures as well on their service life. The use of composite materials that combine high damping capacity with relatively high stiffness and low mass can provide functional and economic benefits, especially for footbridges. This paper aims to investigate the dynamic behaviour of GFRP free-supported beams to evaluate their modal characteristics (frequency, damping, and modal shape). To assess the benefits of using a structure made of pultruded GFRP rather than a conventional material—steel, a comparative analysis between the dynamic characteristics of GFRP and steel beams is performed. To specifically address material damping and to minimize the interference of the boundary conditions, the beams are tested in a free condition, resting on a low-density foam base. The results show that the damping capacity of GFRP is much higher than that of steel, as the measured damping factor of GFRP is five times higher than that of steel for the same boundary conditions and similar geometry. Furthermore, the fact that the frequencies of the tested specimens resemble for the two different materials highlights the perceived damping qualities of the polymer-based composite material. Finally, an energy method for evaluating the influence of the scale factor on material damping is applied, which made it possible to infer that the damping varies as a function of frequency but is not explicitly affected by the length of the specimens.

Keywords: composites; GFRP; steel; viscoelasticity; natural frequency; damping; dynamic behaviour; footbridge vibrations

Citation: Dacol, V.; Caetano, E.; Correia, J.R. Comparative Study of Damping on Pultruded GFRP and Steel Beams. *Polymers* **2021**, *13*, 2201. https://doi.org/10.3390/polym13132201

Academic Editor: Shazed Aziz

Received: 13 June 2021
Accepted: 29 June 2021
Published: 2 July 2021

Publisher's Note: MDPI stays neutral with regard to jurisdictional claims in published maps and institutional affiliations.

Copyright: © 2021 by the authors. Licensee MDPI, Basel, Switzerland. This article is an open access article distributed under the terms and conditions of the Creative Commons Attribution (CC BY) license (http://creativecommons.org/licenses/by/4.0/).

1. Introduction

Pultruded glass fibre reinforced polymer (GFRP) profiles are being increasingly considered for civil engineering structural applications, as a replacement of conventional materials, such as reinforced concrete and especially steel. This is mostly due to their lightweight, high strength, and non-corrodibility. Among the various applications of GFRP profiles are building structures and bridges, both vehicular and especially pedestrian. In all these applications, one of the main design requirements is the comfort of users and, for that purpose, the dynamic properties of fibre-polymer composite materials are of paramount importance. In the specific case of pedestrian bridges, design is very often governed by vibration criteria.

To allow for a comprehensive design of pedestrian bridges made of pultruded GFRP profiles, it is necessary to obtain an in-depth understanding of their dynamic properties, namely compared to steel, which is the main alternative material it aims at replacing. The high damping capacity of polymer-based materials is widely known and used in the mechanical, automotive, and aerospace industries. In fact, the vibrations produced in structures and mechanical components are the main sources of problems in high precision instruments, machines, automobiles or aircrafts, and the use of polymeric composites as passive damping elements allows mitigating vibrations in such structures [1,2]. The frequency-dependent stiffness behaviour of a viscoelastic material directly affects the modal characteristics of the structural system, resulting in complex vibration modes and differences in the relative phase of vibration [3].

In what concerns the use of material damping as the sole damping source of a structural system, Vasques et al. [4] pointed out that the viscoelastic damping has been used mainly as distributed surface mounted or embedded damping treatments, utilizing passive viscoelastic materials alone. In the same manner, Nashif et al. [5] introduced fundamentals of both vibrations and shock damping, focusing only on passive treatments for vibration attenuation without the effective use of the structure itself as a damping agent. Finegan and Gibson [6] summarised the research done on the damping of polymer-based composites in two levels: (a) At the macromechanical level, the research efforts aimed to study the properties of the laminate layers, the inertial effects and the contact surfaces; (b) at the micromechanical level, the focus has been on the effects of the orientation and ratio of the reinforcing fibres, the fibre/matrix interface and the properties of the fibres and the matrix. In the same study, the authors state that material damping can contribute to passive vibration control using the inherent ability of polymeric materials to dissipate energy. This ability was explored by Adams and Bacon [7] who examined the effect of fibre orientation and lamination geometry on the flexural and torsional damping and dynamic moduli of fibre reinforced polymer (FRP) composites.

As mentioned above, polymer-based composites are now finding increasing interest in civil engineering to be used as structural members (pultruded profiles, laminated shells and plates, and sandwich panels). Nevertheless, most of the research carried out in this area has focused on the evaluation of the static behaviour of composite structures, and less often on the dynamic behaviour of specific structures [8,9]; comprehensive information about the dynamic characteristics of polymer-based composites is not yet available, namely with respect to the material damping that is necessary to conduct dynamic analysis (in the time domain) under pedestrian loads, which are sometimes necessary to assess/design in a comprehensive way the comfort of users. This lack of information is well reflected in available design standards for composite structures, which provide very limited guidance in this respect (ASCE LFRD Standard [10]; Prospect for New Guidance of FRP Structures [11]; Italian Code [12]). In fact, none of the above-mentioned design guidelines give detailed information on material damping to be used in the dynamic analysis and design of fibre-polymer composite structures.

In this respect, Boscato et al. [13] stated that structures composed of pultruded FRP profiles have been extensively addressed in their static aspects, but the same attention has not yet been given to their dynamic behaviour. Regarding the dynamic behaviour of FRP materials, some studies have been conducted in the last two decades, such as that of Boscato et al. [14], who presented a modal identification of an all-FRP two dimensional frame in free vibration. The results show that the GFRP structural system presents a better dynamic performance compared to systems comprising steel and aluminium members. Stankiewicz et al. [15] presented dynamic in situ tests of a cable-stayed all-GFRP footbridge under human excitation. They found out that the analysed footbridge fulfilled the vibration comfort criteria elaborated by the technical guide Sétra [16].

In this paper, the identification of modal characteristics of free-supported beams is carried out to determine the internal damping of two types of materials: (i) Steel and (ii) a

polymer-based composite. With this purpose, forced vibration tests using hammer excitation are conducted on two sets of similar free-supported beams, considering the lengths of 250, 500, and 1000 mm. A free-supported beam scenario, in which the beams are placed on a low-density polyurethane foam, is considered to avoid damping added by external sources and to minimise the interference from boundary conditions. In this way, it is possible to extract only the material damping ratio. These types of support conditions are common (and well-established) in biomechanical (body in free fall), naval (submarines), and aerospace (aircraft in flight) engineering. The different lengths aimed at verifying the relevance of the structure scale. The application of identification algorithms to the collected data enables the identification of modal properties, namely damping ratios, which are further correlated with damping factors extracted using an energy-based method analytically deduced in this research.

The remainder of this paper is organized as follows: In Section 2, a brief review of the free-supported beam theory is presented first, and the technique employed to identify modal properties is discussed next. The experimental programme is described in Section 3 and the results obtained are presented in Section 4. In Section 5, a comparison is made between modal parameters identified in the tests and the ones analytically calculated. In Section 6, damping estimates obtained for the two materials, GFRP and steel, are compared. Section 7 summarises the main findings of this study.

2. Theoretical Background

2.1. Identification of Modal Properties

The identification of modal properties from an existing structure is a so-called inverse problem, which is formulated from the non-homogenous dynamic equilibrium equation, by the relation between a response and an excitation, expressed either in the time or the frequency domain [17]. In the present case, a frequency-based approach is used and frequency response functions (FRF), $H(i\omega)$, are constructed from the ratio between spectral density functions of the applied modal force and the resulting modal response. From the FRF, the modal parameters are extracted, namely the natural frequencies, damping ratios, and mode shape components.

Figure 1 shows a typical input-output graphic of an experiment using an impact hammer excitation, depicting the typical response of a structural system to an imposed force.

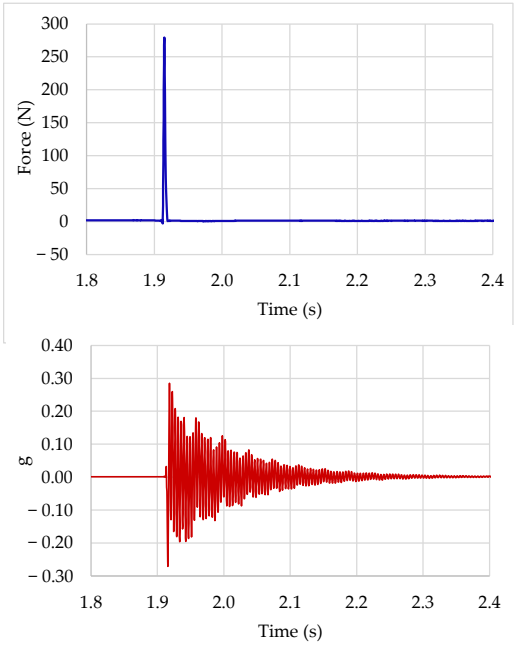


Figure 1. Input-output graphic from an impact experiment.

In a system with separated natural frequencies, modal decoupling enables the transformation of the *N*-coupled dynamic equilibrium equations into *N*-decoupled single-degree-of-freedom (SDOF) equations, *N* being the number of vibration modes to identify. In the frequency domain, the general SDOF dynamic equilibrium equation is given by [18]

$$X(\omega)(-\omega^2 + 2i\xi_n\omega\omega_n + {\omega_n}^2) = \frac{Y(\omega)}{m_n} \quad (1)$$

where m_n, ω_n, and ξ_n are the modal mass, the circular frequency, and the damping ratio, respectively, i is the complex number $(i^2 = -1)$, and $X(\omega)$ and $Y(\omega)$ are the Fourier transforms of the response and excitation, respectively. The FRF is defined as

$$H(\omega) = \frac{X(\omega)}{Y(\omega)} \quad (2)$$

Equation (1) can then be expressed as

$$H(\omega) = \frac{1/m_n}{{\omega_n}^2 - \omega^2 + i2\omega\omega_n\xi_n} \quad (3)$$

Since the FRF is a complex function of frequency, the corresponding real and imaginary parts can be plotted, as shown in Figure 2. Accordingly, it can be observed that the imaginary part of the FRF presents peaks close to the resonance frequencies, while the real part inverts its signal in the vicinity of those frequencies.

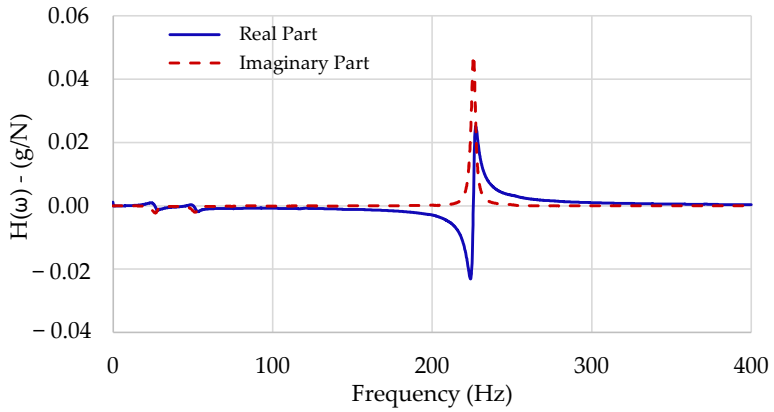


Figure 2. FRF in terms of real and imaginary parts.

These properties can be used to extract the relevant modal parameters. According to Rao [19], when using a single-degree-of-freedom approach, the graph of $H(i\omega)$ is divided into several frequency ranges, each one centred at one peak, whose abscissa approximately coincides with a resonance frequency for a lowly damped system.

To calculate the damping ratio ξ_n, the well-known half-power bandwidth method is commonly used [18]. This method consists of estimating $\omega_{1,n}$ and $\omega_{2,n}$ frequencies, around ω_n, for which the respective FRF amplitude is equal to the peak divided by $\sqrt{2}$. Thereby, the modal damping ratio can be found by

$$\xi_n = \frac{\omega_{2,n} - \omega_{1,n}}{2\omega_n} \quad (4)$$

Figure 3 shows the amplitude of the FRF in terms of logarithmic coordinates and exemplifies the application of the half-power bandwidth method.

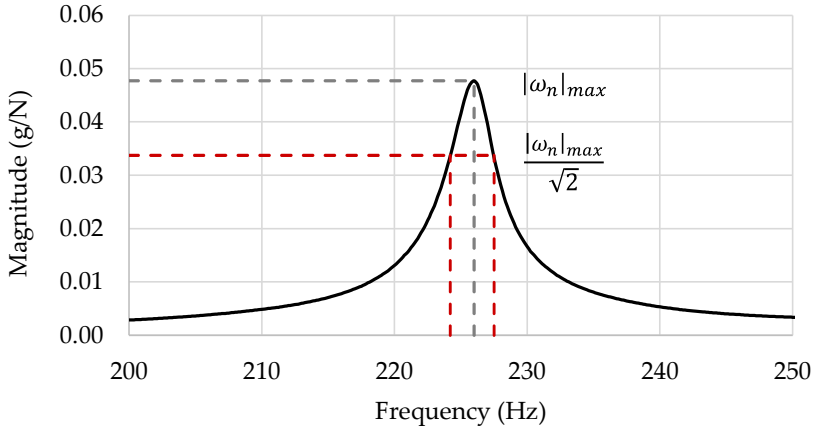


Figure 3. The logarithmic spectra of Fourier in amplitude.

The magnitude of the FRF is given by

$$\overline{H_{ij}}(\omega_n) = \sqrt{\left[H_{r,n}(\omega_n)\right]^2 + \left[H_{i,n}(\omega_n)\right]^2} \quad (5)$$

where $H_{r,n}$ and $H_{i,n}$ are the corresponding real and imaginary part, respectively.

Based on the ω_n and ξ_n values, it is possible to estimate the amplitudes values, $\phi_{i,n}$ and $\phi_{j,n}$, at two measurement points, i and j, of the configuration relative to the mode n. As described by Caetano [18], for a given FRF, the values of $\phi_{i,n}$ and $\phi_{j,n}$, associated with a particular mode n, can be determined at the resonance for each mode. If $\omega \cong \omega_n$, then the amplitude of the FRF relating the response measured at point i with the force applied at point j is given by

$$\overline{H_{ij}}(\omega_n) = \frac{\phi_{i,n} \cdot \phi_{j,n}}{2\xi_n {\omega_n}^2} \quad (6)$$

The amplitudes of the modal components are then given by

$$\phi_{i,n} \cdot \phi_{j,n} = \overline{H_{ij}}(\omega_n) \cdot 2\xi_n {\omega_n}^2 \quad (7)$$

The determination of the quantities $\phi_{i,n}$ and $\phi_{j,n}$ can follow a sequence. For example, if $i = j$, it follows that

$$\phi_{i,n} = \sqrt{\overline{H_{ij}}(\omega_n) \cdot 2\xi_n {\omega_n}^2} \quad (8)$$

Then, at another point j

$$\phi_{j,n} = \frac{\overline{H_{ij}}(\omega_n) \cdot 2\xi_n {\omega_n}^2}{\phi_{i,n}} \quad (9)$$

In summary, the FRF can be used to characterize the dynamic behaviour of a structure and contains information on the modal components of the system, namely the resonance frequencies, the damping ratios, and the mode shapes.

2.2. Energy-Based Evaluation of Equivalent Material Damping Ratio

As earlier related, the knowledge of the damping properties of a structure is necessary to effectively characterise its resonant response. In a structural system as a single-length beam, the energy dissipated per cycle of vibration can be attributed both to material damping and to damping in the supports [20].

Focusing specifically on material damping, the application of the energy method constitutes an alternative for determination of an equivalent damping ratio corresponding to each vibration mode n of the structure. This is achieved considering that the damping

factor is given from the ratio between the dissipated energy, $W_{diss,n}$, and the total energy at resonance, $\mathrm{W}_{total,n}$, over a vibration cycle [21]

$$\xi_n = \frac{W_{diss,n}}{4\pi\ \mathrm{W}_{total,n}} \tag{10}$$

For a single degree of freedom (SDOF) system, at resonance, the total energy may be calculated as the amplitude of either the maximum kinetic and potential energy [22]. If the kinematic energy is considered

$$\mathrm{W}_{total,n} = \left|\frac{1}{2}\rho A \int_0^L \left(\frac{\partial y}{\partial t}\right)^2 dx\right|_t \tag{11}$$

where y describes the transverse deflection of the beam at some position x, ρ is the volumetric mass, A is the cross-sectional area of the beam, the assumed constant along the length L, and $\partial/\partial t$ represents the partial derivative with respect to time.
In a harmonic vibration cycle, the maximum value of Equation (11) is given by

$$\mathrm{W}_{total,n} = \frac{1}{2}(L\rho A)\ {\omega_n}^2 {Y_n}^2 \tag{12}$$

where Y_n is the displacement amplitude; k is the elastic stiffness; and $L\rho A$ is the total mass.

Equations (12) and (13) shows that the energy of a harmonic oscillator is proportional to the square of the amplitude of the oscillation.

On another hand, the free vibrations of any real physical system decay with time. Every such system inevitably has dissipative features through which the mechanical energy of the vibration is depleted. In this sense, French [23] and King [24] showed that it is possible to express the damping ratio in terms of an exponential decay of the total mechanical energy, $\mathrm{W}_{total,n}$.

In such conditions, the oscillations are well described over several cycles by a simple harmonic motion of constant amplitude Y, such that

$$Y(t) = Y_0 e^{-ht/2} \tag{13}$$

where Y_0 is the initial value of the amplitude and h is the hysteretic damping coefficient.

Hence, from Equation (13), one may define the decay of the total energy as

$$W(t) = \mathrm{W}_{total,n}\ e^{-ht} \tag{14}$$

Since the dissipated energy may be computed as $\mathrm{W}_{total,n} - W(t)$, when $t = 2\pi/\omega_n$, and replacing h by a constant given by λ, the damping ratio can be related to the energy decay as

$$\xi_n = \frac{1 - e^{-\left(2\pi\lambda/\omega_n\right)}}{4\pi} \tag{15}$$

3. Experimental Programme

3.1. Overview

In this research, the identification of modal characteristics of free-supported beams is carried out to determine the structural damping of two types of materials, namely: (i) Steel and (ii) pultruded GFRP.

The experiments are conducted for different beam lengths, namely, 250, 500, and 1000 mm. The range of lengths chosen makes it possible to assess the scale effects on the modal properties of the beams, namely on their natural frequencies and damping ratios.

3.2. Characteristics of the Material and Specimens

3.2.1. GFRP Specimens

The specimens of the pultruded GFRP composite used in the experimental programme were extracted from the web of an I-section pultruded profile (200 × 100 × 10 mm, web height × flange width × wall thickness) (Alto-Perfis Pultrudidos Lda, Maia, Portugal). This profile is made of E-glass fibres, combining alternating layers of unidirectional roving and mats embedded in an isophthalic polyester matrix (68% inorganic content by weight). The cross-section and dimensions of GFRP specimens are shown in Figure 4 and their mass and density are shown in Table 1.

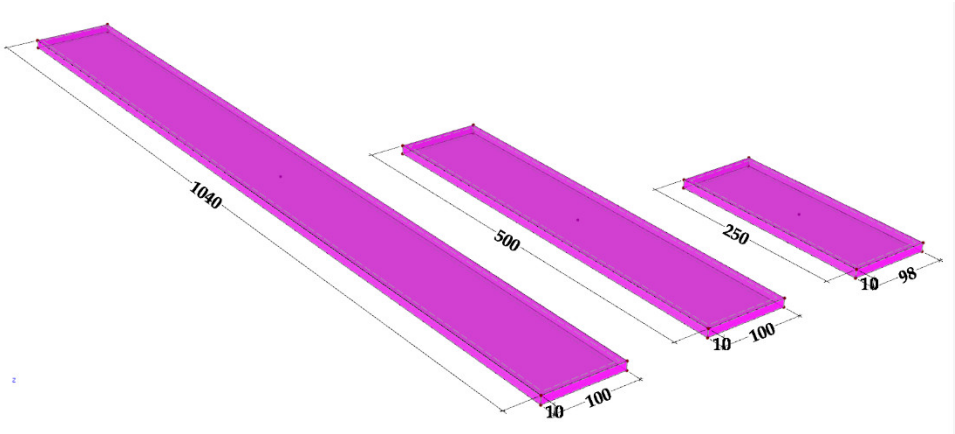


Figure 4. Geometry of GFRP specimens (dimensions in mm).

Table 1. Mass and density of GFRP specimens.

Specimen	Mass	Volumetric Mass (ρ)
(l × w × t)	(kg)	(kg/m^3)
1040 × 100 × 10 mm	2.0088	1931.54
500 × 100 × 10 mm	0.9904	1980.80
250 × 98 × 10 mm	0.4891	1996.33

The dimensions of the composite specimens present some differences compared to the steel ones, which resulted from the cutting process. However, the relative differences are small and exact (measured) geometric values were considered in the calculations. Given the very low porosity of the pultruded material, the apparent density of the specimens was considered, by determining the weight/volume ratio.

The material characterisation tests [25] of GFRP were performed on small-scale coupons extracted from the web plate: (i) Tensile tests (according to ISO 527 [26]), (ii) compression tests (ASTM D695-02 [27]), (iii) in-plane shear tests (ISO 527-5 [28]), and (iv) interlaminar shear tests (ASTM D2344 [29]).

The elastic and strength properties of the GFRP laminates are listed in Tables 2 and 3, respectively, where E is the elastic modulus, G is the shear modulus, υ is the Poisson ratio, σ is the axial strength, and τ is the in-plane shear strength. The subscripts L and T correspond to the in-plane longitudinal (pultrusion) and transverse directions, while subscripts t and c correspond to tensile and compressive loading, respectively.

Table 2. Elastic properties of GFRP.

$E_{L,t}$	$E_{L,c}$	$E_{T,c}$	G_{LT}	υ
(GPa)	(GPa)	(GPa)	(GPa)	
32.7	33.4	10.8	3.65	0.266

Table 3. Strength properties of GFRP.

$\sigma_{L,t}$	$\sigma_{L,c}$	$\sigma_{T,c}$	τ_{LT}
(MPa)	(MPa)	(MPa)	(MPa)
365	468	110	30.6

3.2.2. Steel Specimens

The steel specimens used in the experimental programme were produced with DIN 45WCrV7 steel grade, equivalent to ASTM 681A S1 or S355, a cold work alloy tool steel category. The cross-section and dimensions of steel specimens are shown in Figure 5 and their mass and density are listed in Table 4.

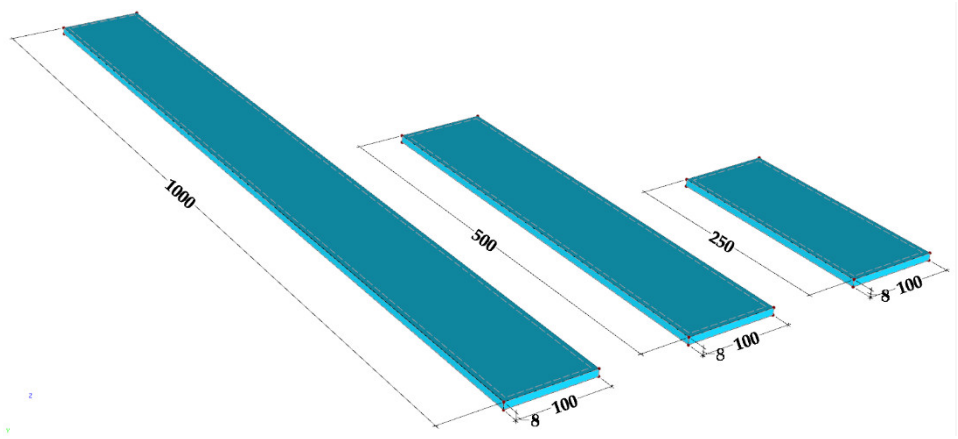


Figure 5. Geometry of steel specimens (dimensions in mm).

Table 4. Mass and density of steel specimens.

Specimen	Mass	Volumetric Mass (ρ)
(l × w × t)	(kg)	(kg/m^3)
1000 × 100 × 8 mm	6.1611	7701.38
500 × 100 × 8 mm	3.0802	7700.50
250 × 100 × 8 mm	1.5417	7865.82

The elastic and strength properties of steel are listed in Table 5, namely the modulus of elasticity E, the minimum yield stress f_y, the ultimate tensile stress f_u, the shear modulus G, and the Poisson ratio υ (properties stated in the supplier catalogue).

Table 5. Elastic and strength properties of A681 Steel.

E	f_y	f_u	G	υ
(GPa)	(MPa)	(MPa)	(GPa)	
210	335	510	80	0.300

3.3. Test Setup, Instrumentation, and Procedure

The modal identification tests were performed to extract the modal data from the specimens, namely, the vibration frequencies, damping ratios, and modal shapes of the beams. For this purpose, input-output tests were conducted based on the excitation by an impact hammer and the measurement of both the applied excitation and the structural acceleration. From the collected time series relating the acceleration at a certain number of points with the force applied at another point, frequency response functions were constructed, and modal identification techniques (described above) were applied.

Figure 6 shows the experimental setup. The test specimens were supported by a (1) low-density foam to simulate a free-supported condition. Impacts were applied with an (2) impulse hammer on the beam and the respective response was measured in terms of vertical accelerations with (3) a high sensitivity and low mass piezoelectric accelerometer (model 393A03, PCB Group, Inc., New York, NY, USA) connected to (4) an amplifier (model SignalCalc Ace, Data Physics, Santa Clara, CA, USA). The data were acquired and processed using a (5) Fourier analyser (model 480E09, PCB Group, Inc., New York, NY, USA).

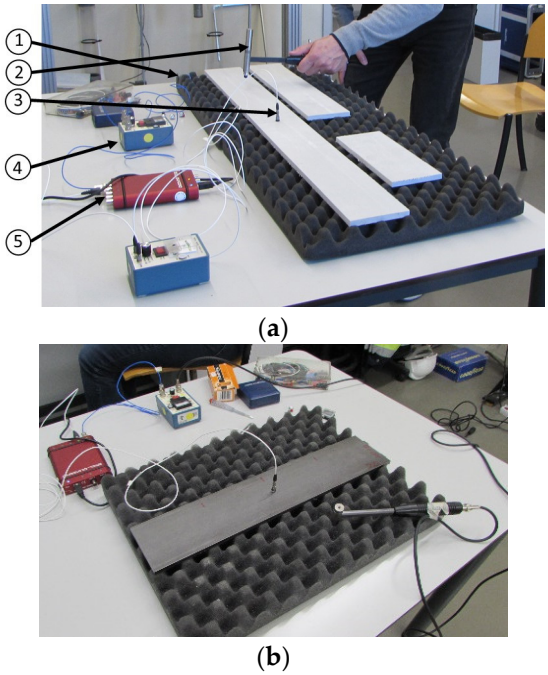
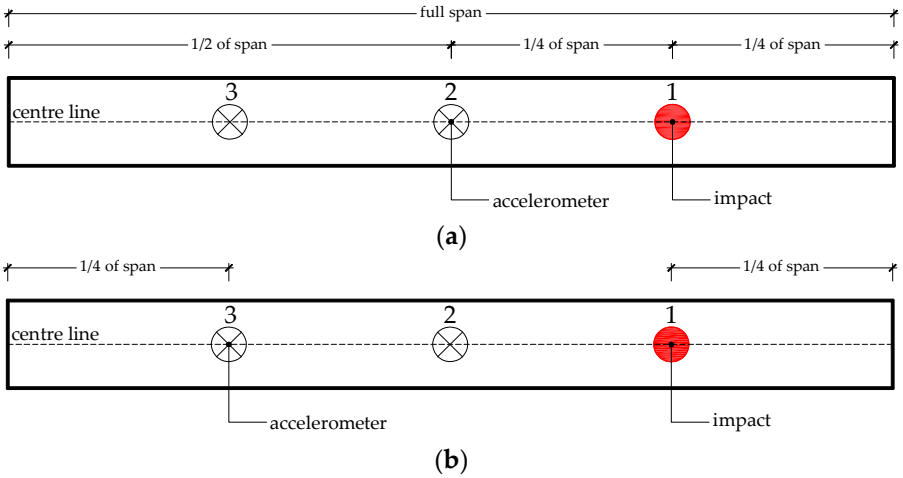


Figure 6. Experimental setup: (**a**) GFRP and (**b**) steel specimens.

The frequency range that can be induced by hammer excitation depends on the mass of the hammer and the hardness of the tip applied to its head. The chosen tip that allowed excitation in the frequency range of 0 to 800 Hz was a rubber- and steel-head for respectively the GFRP and steel specimens.

For each test conducted on, a given specimen (made of steel or GFRP), four different FRFs were constructed relating the accelerations measured at points 1, 2, and 3, with the impact applied at point 1, 2, and 3 (see Figure 7 and Table 6).



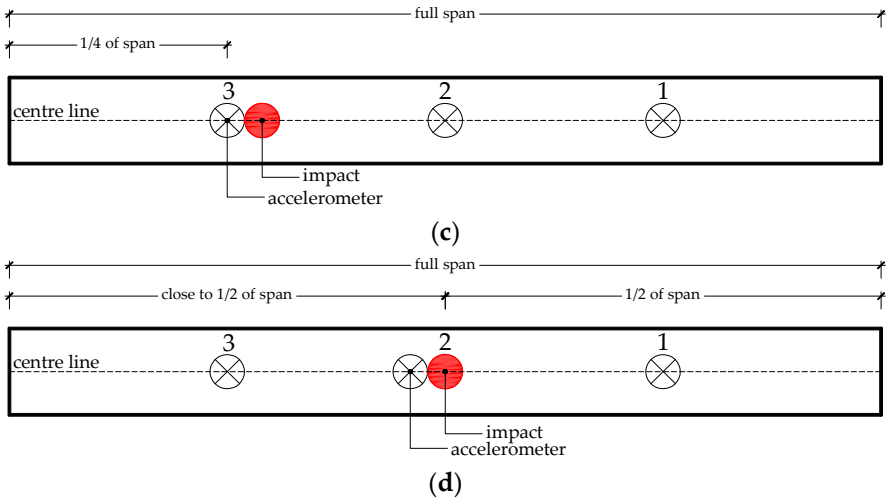


Figure 7. Modal identification test setups: (**a**) Setup 1, (**b**) setup 2, (**c**) setup 3, and (**d**) setup 4.

Table 6. Measurement setting.

Setup	Chanel 1	Chanel 2
	Impact Load Point	**Accelerometer Point**
1	1	2
2	1	3
3	3	3
4	2	2

The modal identification test setups described in Figure 7 were repeated for the three beam lengths. Figure 8 shows one of the modal identification tests being performed.

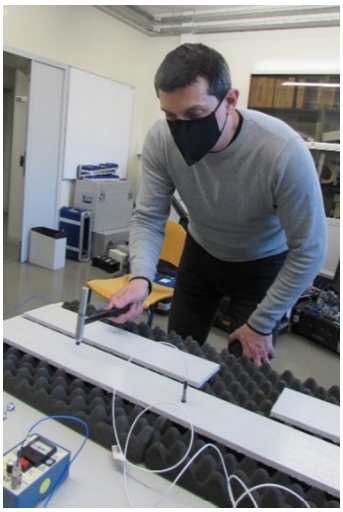


Figure 8. Experimental tests: Example of impact being applied.

In this campaign, 19 tests were conducted and the 14 most relevant results are presented. Figure 9 shows the tested beams arranged in pairs, namely (1) 1000, (2) 500, and (3) 250 mm-length.

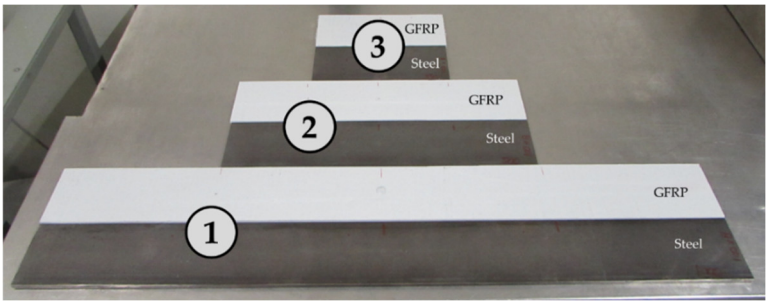


Figure 9. Experimental couples.

The series of experiments were classified following the setup number, as described above, the beam material (C—for composite; S—for steel) and the length (in mm). Table 7 describes the complete set of experiments performed for each series and the beam nomenclature adopted.

Table 7. Test description.

Test	Setup	Impact Load Point	Accelerometer Point	Beam Nomenclature
1	1	1	2	C-1000
2	2	1	3	C-1000
3	3	3	3	C-1000
4	1	1	2	S-1000
5	2	1	3	S-1000
6	3	3	3	S-1000
7	1	1	2	C-500
8	4	2	2	C-500
9	1	1	2	S-500
10	4	2	2	S-500
11	1	1	2	S-250
12	4	2	2	S-250
13	1	1	2	C-250
14	4	2	2	C-250

4. Experimental Results

This section describes the experimental results of the tests carried out on each pair of beams, made of either GFRP or steel. First, results are presented for each of the test lengths. Next, the identified frequencies are summarized. Finally, the mode shapes are described.

4.1. 1000 mm-Length

This subsection presents the results of the modal identification test performed on specimens with 1000 mm of length, namely, for setups 1, 2, and 3 (Table 7). Figure 10 shows the FRF plots and summarises the identified natural frequencies. Figure 11 shows the power spectral density (PSD) of amplitude response plots of the 1000 mm-length tests.

It is first noted that the plots presented in Figure 10 show that the resonance frequencies for both materials are very close. This is confirmed by the values of the resonance frequencies listed in Table 8.

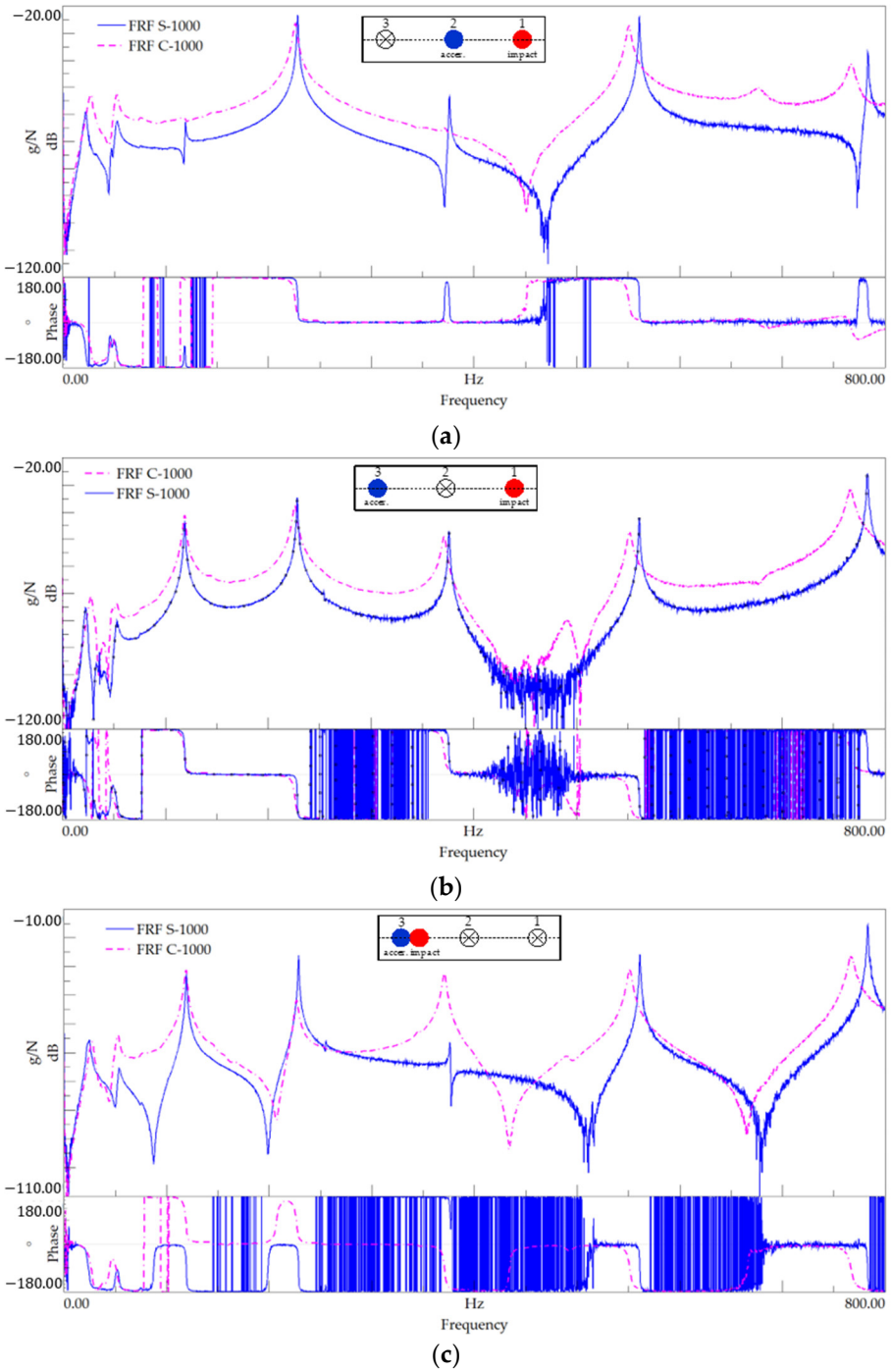


Figure 10. Modal identification for 1000 mm-length specimens—FRF plot for (**a**) setup 1, (**b**) setup 2, and (**c**) setup 3.

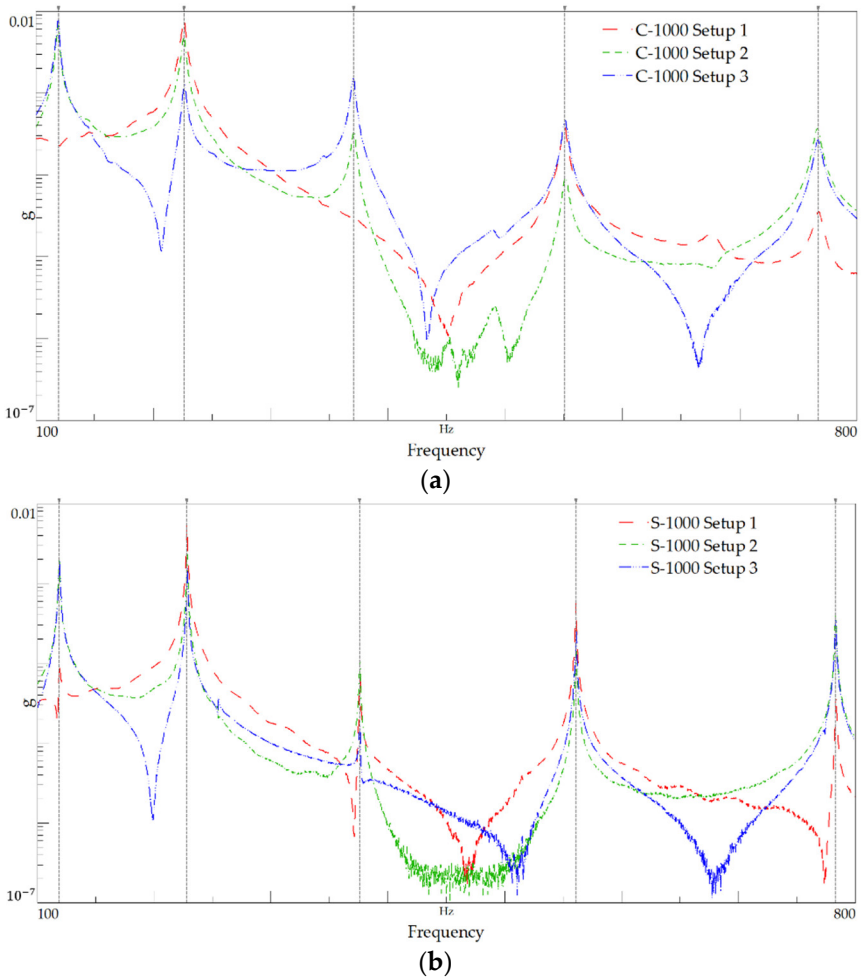


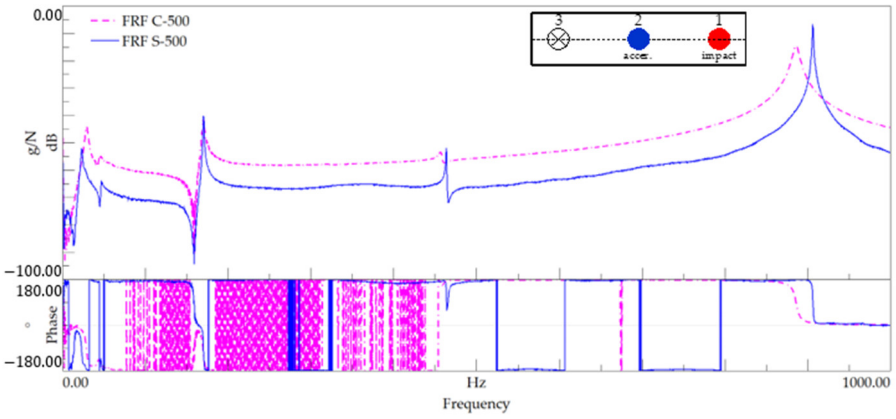
Figure 11. Power spectral density plot for the 1000 mm-length: (**a**) C-1000 and (**b**) S-1000.

Table 8. Identified natural frequencies for the 1000 mm-length.

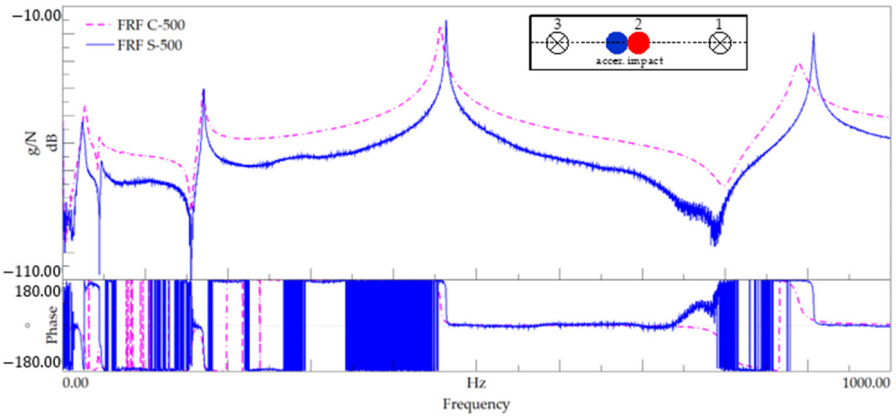
Mode	C-1000	S-1000
No.	Resonance Freq. (Hz)	Resonance Freq. (Hz)
0	27.333 ± 0.312	23.000 ± 1.080
1	52.500 ± 0.204	53.127 ± 0.625
2	118.875 ± 0.125	119.083 ± 0.285
3	226.250 ± 0.205	228.417 ± 0.192
4	370.875 ± 0.375	376.083 ± 0.176
5	551.000 ± 0.204	561.083 ± 0.118
6	766.667 ± 0.514	783.334 ± 0.204

4.2. 500 mm-Length

Figure 12 presents the FRF plots for setups 1 and 4, corresponding to modal identification tests performed on specimens with 500 mm-length, and Table 9 summarises the identified natural frequencies. Figure 13 shows the PSD of amplitude response plots of the 500 mm-length tests.



(**a**)



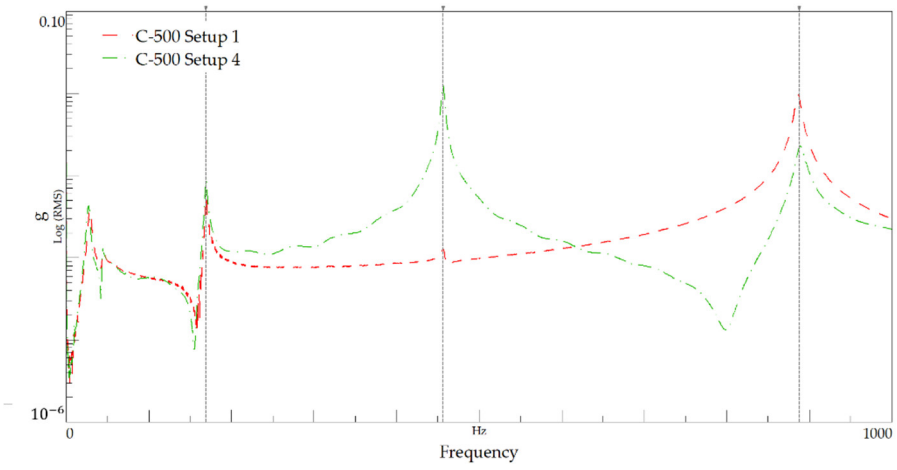
(**b**)

Figure 12. Modal identification for the 500 mm-length—FRF plot for (**a**) setup 1 and (**b**) setup 4.

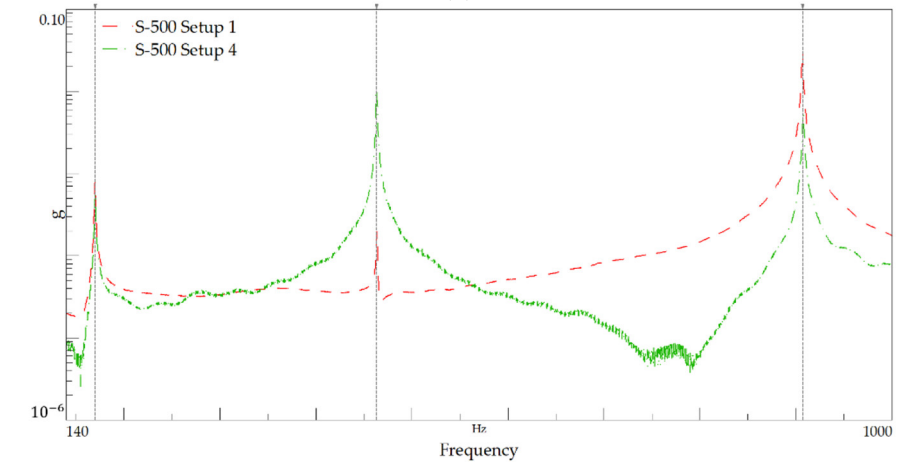
Table 9. Identified natural frequencies for the 500 mm-length.

Mode No.	C-500 Resonance Freq. (Hz)	S-500 Resonance Freq. (Hz)
0	27.656 ± 1.094	23.125 ± 0.313
1	44.219 ± 0.156	46.563 ± 0.001
2	169.219 ± 0.156	170.156 ± 0.156
3	456.406 ± 0.156	463.281 ± 0.156
4	887.504 ± 1.559	907.031 ± 0.469

As in the previous series, it can be noted that the curves shown in Figure 12 and the values given in Table 9 show that the peak frequencies for both materials are close.



(**a**)

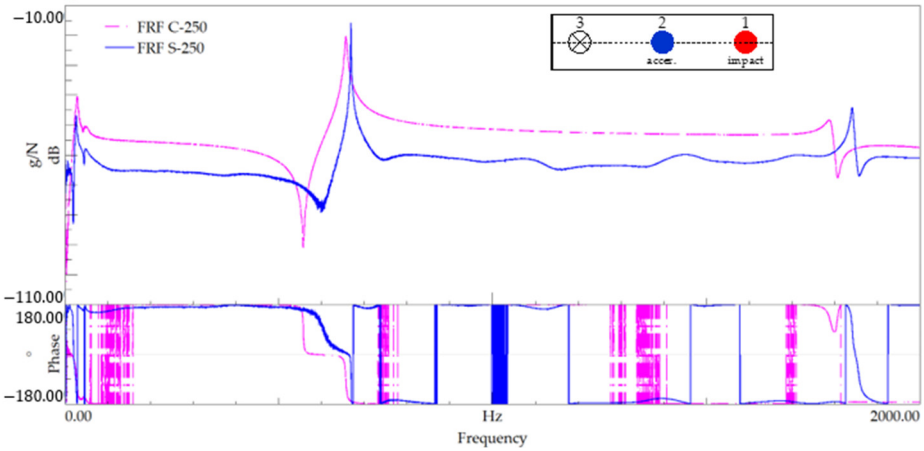


(**b**)

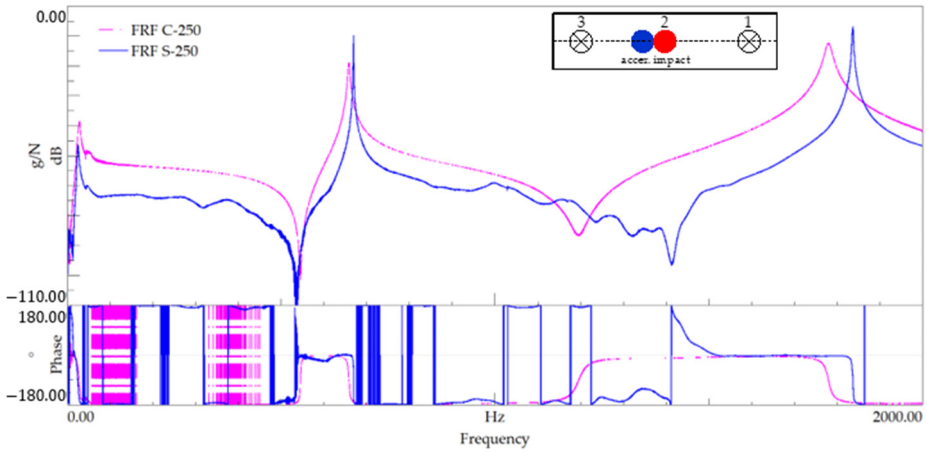
Figure 13. Power spectral density plot for the 500 mm-length: (**a**) C-500 and (**b**) S-500.

4.3. 250 mm-Length

Figure 14 shows the FRF plots for setups 1 and 3, referring to modal identification tests performed on specimens with the 250 mm-length, and Table 10 summarises the identified natural frequencies. Figure 15 shows the PSD of amplitude response plots of the 250 mm-length tests.



(**a**)

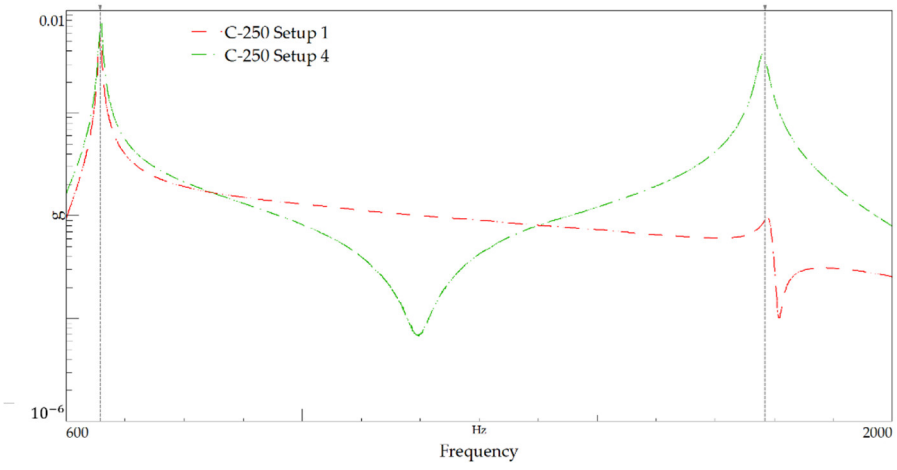


(**b**)

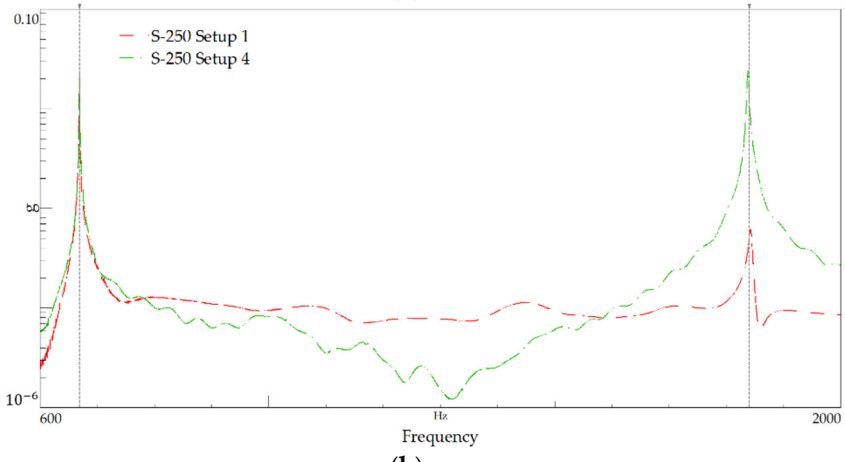
Figure 14. Modal identification for the 250 mm-length—FRF plot for (**a**) series 1 and (**b**) series 4.

Table 10. Identified natural frequencies for the 250 mm-length.

Mode No.	C-250 Resonance Freq. (Hz)	S-250 Resonance Freq. (Hz)
0	27.817 ± 0.004	24.375 ± 0.625
1	657.501 ± 0.624	668.594 ± 0.156
2	1784.362 ± 4.674	1840.000 ± 2.188



(**a**)



(**b**)

Figure 15. Power spectral density plot for the 250 mm-length: (**a**) C-250 and (**b**) S-250.

As mentioned in the previous tests, even for the small length beams, the peak frequencies are very close for both materials, as depicted by the FRF plots in Figure 16 and the values listed in Table 10.

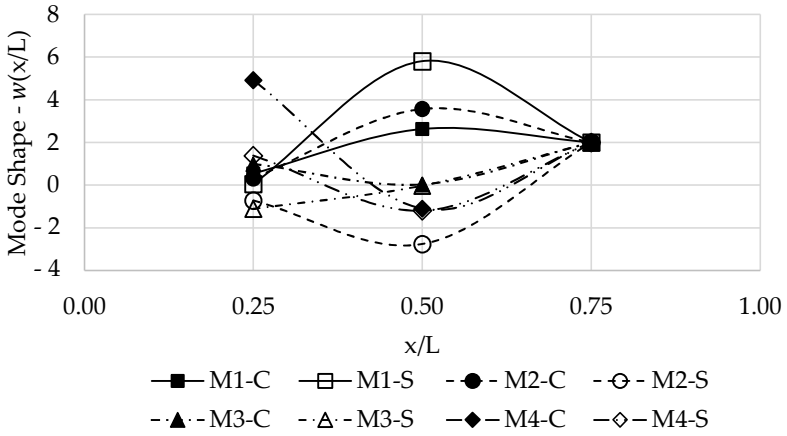


Figure 16. Modal identification: First four mode shapes with impact excitation. The prefix "M*i*" indicates the mode number, the suffix "-C" and "-S" indicates the material, composite (GFRP) and steel, respectively.

4.4. Summary of Identified Frequencies

Table 11 summarises the identified frequencies for the different materials-lengths and modes. The frequencies associated with the mode identified as "0" correspond to the rigid-body mode and are discarded. From the values shown in Table 11, it is possible to verify the existence of similarity in the vibratory behaviour of beams with the same length, but different constituent materials. To confirm this hypothesis, Table 12 shows the ratio between the identified frequencies for GFRP and steel beams with the same length, for the same vibration mode.

Table 11. Summary of identified frequencies (*in Hz*).

Specimen	Mode						
	0	**1**	**2**	**3**	**4**	**5**	**6**
C-1000	27.33	52.50	118.88	226.25	370.88	551.00	766.67
S-1000	27.00	53.13	119.08	228.42	376.08	561.08	783.33
C-500	44.22	169.22	456.41	887.50			
S-500	46.56	170.16	463.28	907.03			
C-250	27.82	657.50	1784.36				
S-250	24.38	668.59	1840.00				

Table 12. Ratio of identified frequencies for different setups.

Specimen	Mode					
	1	**2**	**3**	**4**	**5**	**6**
C-1000/S-1000	0.99	1.00	0.99	0.99	0.98	0.98
C-500/S-500	0.99	0.99	0.98			
C-250/S-250	0.98	0.97				

The values listed in Table 12 show that the relative difference between the values of the identified frequencies for both materials remains within the range of 0 to 0.03, which

reflects the resemblance of modal characteristics of specimens with the same length, regardless of the material. It is important to note that, for the same length, while the bending stiffness ratio is about three times (the estimated bending stiffness of the steel specimens being greater than that of the composite ones), the stiffness-to-mass ratio (composite/steel) of those specimens is less than 8% on average, as already mentioned. This is ascribed to the much lower density of GFRP compared to steel.

4.5. Mode Shapes

To obtain the solution of the vibration modes, the Euler-Bernoulli theory [30] was applied and the modal displacement amplitudes of the beams were calculated. The first four mode shapes are presented in Figure 16, in which the prefix "M*i*" indicates the mode number, and the suffix "-C" and "-S" indicates the material, composite (GFRP) and steel, respectively. It is noted that it was not the purpose of the tests to define in a refined way the modal shapes, as a small number of points were used in the measurements.

5. Comparison of Identified and Calculated Modal Parameters

This section presents a comparison between the modal parameters obtained from the analytical formulae and the experimental results. For this purpose, the Euler-Bernoulli theory [30] and the values of the corresponding wavenumber are used.

Table 13 summarizes the elastic properties of the beams in which the "Ratio EI/m" column emphasizes the relationship between the bending stiffness and the mass of the specimen. It is possible to verify that the relationship "stiffness × mass" for specimens of the same geometry is similar, with a relative difference of only 8% between both (with the calculated ratio for the GFRP composite being higher than that for steel). Table 14 shows the analytical values of natural frequencies, f_n, given by Equation (9).

Table 13. Elastic properties set for the direct problem.

Specimen	Length	Cross-Section	Young's Modulus	Moment of Inertia	Mass	Ratio
	L	*(w x t)*	*E*	*I*	*m*	*EI/m*
	(mm)	(mm)	(GPa)	(mm^4)	(kg)	
C-1000	1040	100 × 10	37.7	8333.33	2.0088	156
S-1000	1000	100 × 8	210.0	4266.67	6.1611	145
C-500	500	100 × 10	37.7	8333.33	0.9904	317
S-500	500	100 × 8	210.0	4266.67	3.0802	291
C-250	250	98 × 10	37.7	8166.67	0.4891	630
S-250	250	100 × 8	210.0	4266.67	1.5417	581

Table 14. Natural frequencies obtained from analytical modelling (in Hz).

Specimen	Mode					
	1	2	3	4	5	6
C-1000	41.987	115.738	226.893	375.065	560.282	782.543
S-1000	42.941	118.369	232.051	383.592	573.020	800.334
C-500	179.378	494.463	969.345	1602.376	2393.674	3343.230
S-500	171.775	473.504	928.257	1534.456	2292.212	3201.519
C-250	714.717	1970.145	3862.272	6384.532	9537.389	13,320.816
S-250	686.743	1893.032	3711.100	6134.637	9164.089	12,799.430

According to the Euler-Bernoulli theory, the natural frequency is inversely proportional to the square of specimen length. In this sense, as the EI/m ratios are similar between specimens with the same geometry, it is expected that the natural frequencies of the specimen C-1000 mm are lower than those of the specimen S-1000, since the length of

the latter is 3.85% smaller than that of the former, it did not occur with the other specimens.

A comparison between the analytical and experimental values of natural frequencies is made to assess the accuracy of the analytical modelling and the test approach, and further, to validate the accuracy of the proposed model in simulating the free-supported beam boundary conditions.

Table 15 summarises the ratios between the experimental and numerical values of the natural frequencies for the different materials-lengths and for each mode.

Table 15. Ratios between experimental and analytical frequencies.

Specimen	Mode					
	1	**2**	**3**	**4**	**5**	**6**
C-1000	1.25	1.03	1.00	0.99	0.98	0.98
S-1000	1.24	1.01	0.98	0.98	0.98	0.98
C-500	0.94	0.92	0.92			
S-500	0.99	0.98	0.98			
C-250	0.92	0.91				
S-250	0.97	0.97				

In what concerns the accuracy aspect mentioned above, a value of ±0.10 was defined as an acceptable threshold. In this sense, the first mode of specimens C-1000 and S-1000 should be discarded from the analysis. Except for the first mode of the 1000 mm-length specimens, the good agreement between the experimental frequencies and those estimated with the analytical models shows that the hypothesis of the free-supported condition was achieved with the use of low-density foam as beams supports. It was not possible to unequivocally identify a clear cause for the differences between experimental and analytical results.

6. Damping Analysis

In this section, the damping ratios extracted for each pair of specimens with an identical length is analysed and compared. The procedure described in Section 2 is applied to calculate the damping ratios.

From the power spectrum of amplitude response plots, the half-power bandwidth method is used and the damping ratio is calculated. The values obtained are shown in Table 16.

Table 16. Damping ratio – ξ_n.

Mode	**C-1000**	**S-1000**	**Ratio**
	(%)		**(C/S)**
1	-	-	-
2	1.01	0.42	2.4
3	0.70	0.16	4.4
4	0.46	0.14	3.3
5	0.36	0.08	4.5
6	0.34	0.06	5.7
Mode	**C-500**	**S-500**	**Ratio**
	(%)		**(C/S)**
1	0.75	0.33	2.3
2	0.37	0.12	3.1
3	0.40	0.09	4.4
Mode	**C-250**	**S-250**	**Ratio**
	(%)		**(C/S)**
1	0.37	0.09	4.1
2	0.46	0.16	2.9

The values given in Table 17 show that for a given mode, the damping ratio, ξ_n, of the GFRP composite is higher than that of the corresponding steel-based specimen. It must be noted that for the same structure, at the same frequency, different response amplitudes will generate different levels of damping [31]. In this sense, it is important to assess the damping ratio concerning the ratio of the response amplitudes of the structure.

To confirm the conclusion on the enhanced damping ability of the GFRP composite with respect to steel, the evaluation of the relative response amplitudes associated with each mode component for the two different materials is performed using the power spectrum amplitude response. Table 17 summarises the amplitude response for each identified mode and the ratio between the measured amplitudes (GFRP/steel) as well as the ratio between the measured damping (GFRP/steel).

Table 17. Amplitudes of acceleration and the respective damping ratios.

Mode	**C-1000**		**S-1000**		**Ratios**	
	Amplitude	**Damping**	**Amplitude**	**Damping**	**Amplitude**	**Damping**
	(g/N)	**%**	**(g/N)**	**%**	**(C/S)**	**(C/S)**
1	-	-	-	-	-	-
2	0.0276	1.01	0.0236	0.42	1.2	2.4
3	0.0083	0.70	0.0493	0.16	0.2	4.4
4	0.0113	0.46	0.0015	0.14	7.8	3.3
5	0.0283	0.36	0.0516	0.08	0.6	4.5
6	0.0480	0.34	0.1700	0.06	0.3	5.7
Mode	**C-500**		**S-500**		**Ratios**	
	Amplitude	**Damping**	**Amplitude**	**Damping**	**Amplitude**	**Damping**
	(g/N)	**%**	**(g/N)**	**%**	**(C/S)**	**(C/S)**
1	0.0088	0.75	0.0097	0.33	0.9	2.3
2	0.1413	0.37	0.1723	0.12	0.8	3.1
3	0.1881	0.40	0.4178	0.09	0.5	4.5
Mode	**C-250**		**S-250**		**Ratios**	
	Amplitude	**Damping**	**Amplitude**	**Damping**	**Amplitude**	**Damping**
	(g/N)	**%**	**(g/N)**	**%**	**(C/S)**	**(C/S)**
1	0.0865	0.37	0.0844	0.09	1.0	4.1
2	0.0036	0.46	0.0051	0.16	0.7	2.9

Table 17 shows that the response amplitude for the various identified modes has an average ratio of 1.4 between the GFRP composite and steel specimens, while the average ratio of damping between those two materials is 4.0. These two figures highlight the fact that the difference in measured amplitudes does not have a direct impact on the damping values. It should be noted that at certain modes the response amplitude for steel was higher than in the GFRP composite.

A consideration to be made refers to the scaling effect, which relates the length of the specimens to the damping variation, within the same frequency range, and which is directly related to the choice of specimen lengths adopted in this research. Furthermore, the natural frequencies of a full-scale system can be related to those of a reduced model, relating the two sets of frequencies by a scaling law taking into account the physical parameters of the model and the full-scale system [32]. In this sense, the damping ratio as a function of the length (scale) was evaluated to identify whether the scale influences material damping. Figure 17 shows the variation of the damping ratio with the frequency for all tested specimens. The damping ratio decreases as the frequency increases, up to a frequency of approximately 700 Hz. At high frequencies (above 800 Hz), the damping ratio starts to increase.

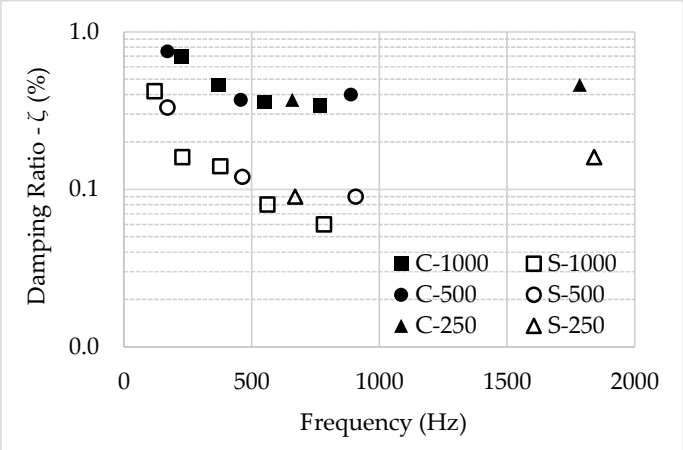


Figure 17. Damping ratio vs. frequency for different materials and lengths.

It may be noted that the material damping varies as a function of frequency but is not explicitly affected by the length of the specimens. As far as only material damping is concerned, the damping ratio is similar for specimens with different lengths, at the same frequency range. This is corroborated by a curve fitting in power law terms that exhibits a very-strong correlation between the damping ratio values and frequency for different lengths, as depicted in Figure 18.

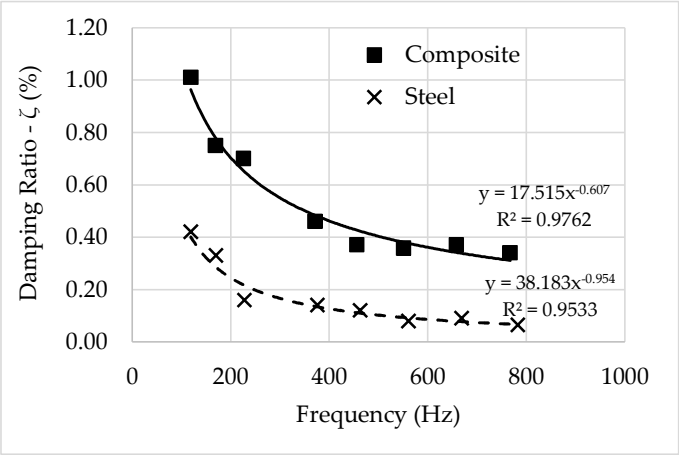


Figure 18. Damping ratio vs. frequency: Curve fitting.

The curve fittings depicted in Figure 18 can be compared to those obtained based on the energy method. From Equation (15), one may evaluate the damping ratio as a function of a constant λ, in terms of exponential decay. In this sense, the results obtained for the GFRP composite, depicted in Figure 19, show that the damping ratios estimated based on the energy ratio are similar to the ones calculated from the curve fitting described above.

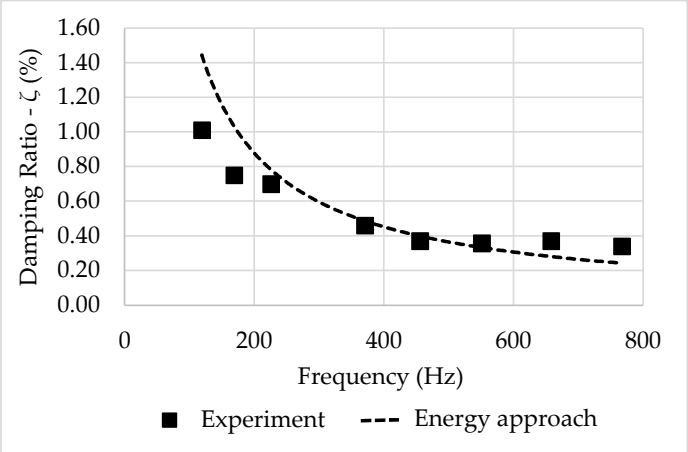


Figure 19. Damping ratio: Curve fitting from the energy method.

7. Conclusions

This paper presents a modal analysis of the dynamic characteristics of free-supported beams, made of pultruded GFRP and steel, to identify and compare their resonance frequencies, damping ratios, and vibration modes.

For the modal identification process, an experimental campaign was conducted by applying the input-output method with the hammer impact and measuring the responses in terms of acceleration of specimens with various lengths. This approach allowed evaluating the damping variation as a function of resonance frequencies as well as achieving a wide range of frequencies, from 27 to 1800 Hz.

The comparison between the identified frequencies and the results obtained from the analytical model showed that the use of low-density foam as support enable a free-support beam condition, also allowing the retrieval of the material damping ratios from the test specimens. The same comparison showed a resemblance between the identified frequency for specimens with similar lengths but made of different materials. Furthermore, the order of magnitude of the relative differences between the frequencies identified for the same mode in the two different materials, did not exceed 3%.

The half-power bandwidth method was applied to the PSD plots and values of material damping ratios could be identified. For similar lengths, the values of the damping ratios of the two materials presented significant differences, with the GFRP composite presenting higher values, between two and six times higher than steel. This better damping behaviour of GFRP was confirmed through the evaluation and comparison of the measured acceleration amplitudes: The ratio of acceleration amplitudes between GFRP and steel was relatively small compared to the corresponding ratio of damping ratios. It is noteworthy that, for certain modes, the response amplitude of steel was higher than that of the GFRP. These results reflect the better performance of the polymer-based composite material in terms of energy dissipation and vibration attenuation.

Finally, an evaluation of the importance of the beam length was assessed to identify its influence on the material damping ratios. It was observed that the material damping ratio varies as a function of frequency but is not explicitly affected by the length of the specimens.

For the materials and geometries used in this study, it was shown that longer specimens exhibited modal characteristics that resemble those of the shorter specimens. Despite the limitations of this study, this points to the feasibility of estimating the material damping of full-scale structures based on small-scale tests at the material level.

Author Contributions: E.C. and J.R.C. are the supervisor and co-supervisor of this research work, respectively. Conceptualization, V.D., E.C., and J.R.C.; methodology, V.D.; software, V.D.; validation, V.D.; formal analysis, V.D., E.C., and J.R.C.; investigation, V.D.; resources, E.C.; data curation, V.D.; writing—original draft preparation, V.D.; writing—review and editing, V.D., E.C., and J.R.C.;

visualization, V.D., E.C., and J.R.C.; supervision, E.C. and J.R.C.; project administration, E.C.; funding acquisition, E.C. All authors have read and agreed to the published version of the manuscript.

Funding: This research was funded by the research supported by Fundação para a Ciência e a Tecnologia (Base Funding—UIDB/04708/2020 of the CONSTRUCT—Instituto de I&D em Estruturas e Construções—national funds through the FCT/MCTES (PIDDAC)).

Institutional Review Board Statement: Not applicable.

Informed Consent Statement: Not applicable.

Data Availability Statement: The data presented in this study are available upon request from the corresponding author.

Conflicts of Interest: The authors declare no conflict of interest.

Nomenclature

Symbol	Description
m_n	modal mass of nth order mode (kg)
ω_n	circular frequency of nth order mode (rad/s)
ξ_n	damping ratio of nth order mode (%)
i	complex number $(i^2 = -1)$
$X(\omega)$	Fourier transform of the response
$Y(\omega)$	Fourier transforms of the excitation
$H(\omega)$	frequency response function (FRF)
$H_{r,n}$	real part of FRF at the circular frequency ω_n
$H_{i,n}$	imaginary part of FRF at ω_n
ϕ_n	amplitude of vibration related to mode n
$W_{diss,n}$	dissipated energy at resonance in mode n
$W_{total,n}$	total energy at resonance in mode n
ρ	volumetric mass (kg/m3)
A	cross-sectional area (m2)
L	length of beam (m)
Y_n	modal displacement amplitude at nth order mode (m)
k	elastic stiffness (kN/m)
E	elastic modulus (GPa)
G	shear modulus (GPa)
υ	Poisson ratio
σ	axial stress (MPa)
τ	in-plane shear stress (MPa)
f_y	minimum yield stress (MPa)
f_u	tensile stress (MPa)
I	second moment of area of A (mm4)

References

1. Kulkarni, P.; Bhattacharjee, A.; Nanda, B.K. Study of damping in composite beams. *Mater. Today Proc.* **2018**, *5*, 7061–7067.
2. Berthelot, J.-M.; Assarar, M.; Sefrani, Y.; Mahi, A. El Damping analysis of composite materials and structures. *Compos. Struct.* **2008**, *85*, 189–204.

3. Wang, Y.; Inman, D.J. Finite element analysis and experimental study on dynamic properties of a composite beam with viscoelastic damping. *J. Sound Vib.* **2013**, *332*, 6177–6191.
4. Vasques, C.; Moreira, R.; Rodrigues, J. Viscoelastic Damping Technologies-Part I: Modeling and Finite Element Implementation. *J. Adv. Res. Mech. Eng.* **2010**, *1*, 76–95.
5. Nashif, A.D.; Jones, D.I.G.; Henderson, J.P. *Vibration Damping*; Wiley & Sons Ltd.: Manchester, UK, 1985; ISBN 978-0-471-86772-2.
6. Finegan, I.C.; Gibson, R.F. Recent research on enhancement of damping in polymer composites. *Compos. Struct.* **1999**, *44*, 89–98.
7. Adams, R.D.; Bacon, D.G.C. Effect of fiber orientation and laminate geometry on the dynamic properties of CFRP. *J. Compos. Mater.* **1973**, *7*, 402–428.
8. Mendes, P.J.D.; Barros, J.A.O.; Sena-Cruz, J.M.; Taheri, M. Development of a pedestrian bridge with GFRP profiles and fiber reinforced self-compacting concrete deck. *Compos. Struct.* **2011**, *93*, 2969–2982.
9. Sonnenschein, R.; Gajdosova, K.; Holly, I. FRP Composites and their Using in the Construction of Bridges. *Procedia Eng.* **2016**, *161*, 477–482.
10. American Society of Civil Engineers (ASCE) *Pre-Standard for Load & Resistance Factor Design (LRFD) of Pultruded Fiber Reinforced Polymer (FRP) Structures*; American Society of Civil Engineers (ASCE): Reston, VA, USA, 2010.
11. Ascione, L.; Caron, J.F.; Correia, J.C.; De Corte, W.; Godonou, P.; Knippers, J.; Moussiaux, E.; Mottram, T.; Oppe, M.; Silvestre, N.; et al. *Prospect for New Guidance in the Design of FRP Structures: Updated Report*; European Composites Industry Association (EuCIA): Berkhamsted, UK, 2018. Available online: www.eucia.eu (accessed on 13 June 2021).
12. Italian National Research Council-CNR-DT 205/2007 *Guide for the Design and Construction of Structures Made of FRP Pultruded Elements*; Advisory Committee on Technical Recommendations for Construction (CNR): Rome, Italy, 2008.
13. Boscato, G.; Dal Cin, A.; Russo, S. Dynamic Identification of All-FRP Pultruded Structures. *Int. J. Eng. Technol.* **2015**, *7*, 81–85.
14. Boscato, G.; Russo, S. Free Vibrations of Pultruded FRP Elements: Mechanical Characterization, Analysis, and Applications. *J. Compos. Constr.* **2009**, *13*, 565–574.
15. Stankiewicz, B.; Górski, P.; Tatara, M. All-GFRP Footbridge under Human-Induced Excitation. *MATEC Web Conf.* **2019**, *262*, 10013.
16. *Setra Guide Méthodologique Passerelles Piétonnes (Technical Guide Footbridges: Assessment of Vibrational Behaviour of Footbridges under Pedestrian Loading)*; Service D'études Techniques des Routes et Autoroutes: Paris, France, 2006.
17. Silva, J.M.M.; Maia, N.M.M. (Eds.) *Modal Analysis and Testing*; Kluwer Academic Publishers: Sesimbra, Portugal, 1999; ISBN 9780792358947.
18. Caetano, E.D.S. Identificação Experimental de Parâmetros Dinâmicos em Sistemas Estruturais. Master's Thesis, University of Porto, Portugal, 1992.
19. Rao, S.S. *Mechanical Vibrations*, 6th ed.; Pearson Education Limited: Harlow, UK, 2017; Volume 6.
20. MacBain, J.C.; Genin, J. Energy dissipation of a vibrating Timoshenko beam considering support and material damping. *Int. J. Mech. Sci.* **1975**, *17*, 255–265.
21. Krifa, M.; Bouhaddi, N.; Cogan, S. Estimation of modal damping for structures with localized dissipation. *Conf. Proc. Soc. Exp. Mech. Ser.* **2015**, *6*, 179–191.
22. Marsh, E.R.; Slocum, A.H. An integrated approach to structural damping. *Precis. Eng.* **1996**, *18*, 103–109.
23. French, A.P. *Vibrations and Waves*; CRC Press LLC: Washington, DC, USA, 2001; ISBN 0748744479.
24. King, G.C. *Vibrations and Waves*; Wiley & Sons Ltd.: Manchester, UK, 2009; ISBN 9788578110796.
25. Nunes, F.F. Structural Behaviour of Frp Pultruded Beams and Columns. Ph.D. Thesis, IST—Civil Engineering, University of Lisboa, Lisboa, Portugal, 2016.
26. International Organization for Standardization. *ISO 527-1 Plastics—Determination of Tensile Properties-Part 1: General Principles*; Vernier: Geneva, Switzerland, 1997.
27. *ASTM D 695-02 Standard Test Method for Compressive Properties of Rigid Plastics*; American Society for Testing and Materials: West Conshohocken, PA, USA, 2002.
28. International Organization for Standardization. *ISO/DIS 527-5 Plastics—Determination of Tensile Properties—Part 5: Test Conditions for Unidirectional Fibre-Reinforced Plastic Composites*; Vernier: Geneva, Switzerland, 2009.
29. *ASTM D2344 D2344M Standard Test Method for Short-Beam Strength of Polymer Matrix Composite Materials and Their Laminates*; American Society for Testing and Materials: West Conshohocken, PA, USA, 2006.
30. Bauchau, O.A.; Craig, J.I. *Structural Analysis. Solid Mechanics and Its Applications*; Springer: Dordrecht, The Netherlands, 2009; p. 958, ISBN 9781856175500.
31. Alsehnawi, R.; Nakajima, A.; Takeshima, R.; Sadeq, A.H. Vibration Amplitude-Dependent Natural Frequency and Damping Ratio of Repaired Pier Model. In Proceedings of the EWSHM-7th European Workshop on Structural Health Monitoring, Nantes, France, 8–11 July 2014.
32. Kristiansen, U.R.; Soedel, W.; Hamilton, J.F. An investigation of scaling laws for vibrating beams and plates with special attention to the effects of shear and rotatory inertia. *J. Sound Vib.* **1972**, *20*, 113–122.

Paper 5

Dacol, V.; Caetano, E.; Correia, J.R.

Modal Identification and Damping Analysis of a Full-Scale GFRP-SFRSCC Hybrid Footbridge

Submitted to Engineering Structures, January 2022.

Impact Factor: 4,471 (2021).

Modal Identification and Damping Analysis of a Full-Scale GFRP-SFRSCC Hybrid Footbridge

Vitor Dacol [a,], Elsa Caetano [a] and João R. Correia [b]*

[a] *CONSTRUCT (ViBEST), Faculty of Engineering (FEUP), University of Porto, Porto, Portugal*

[b] *CERIS, DECivil, Instituto Superior Técnico (IST), University of Lisbon, Lisbon, Portugal*

Abstract

Excessive vibration influences the in-service performance of slender structures, as footbridges, in which the dynamic response is essential as pedestrian comfort criteria typically govern design. In this sense, the use of composite materials that combine high damping capacity with relatively high stiffness and low mass can provide functional benefits. This paper presents a study about the dynamic behaviour of an 11 m long hybrid footbridge, made of two I-shaped pultruded glass fibre reinforced polymer (GFRP) main girders and a thin steel fibre reinforced self-compacting concrete (SFRSCC) deck, in operation since 2015. The main goal was (i) to assess the benefits

[*] Corresponding author. Tel.: +351-913 098 842 (V. Dacol)

Email address: vitor.dacol@fe.up.pt (V. Dacol)

https://paginas.fe.up.pt/vibest/ (ViBEST)

of using a structure made of pultruded GFRP instead of a conventional material (steel), and (ii) to improve the knowledge of the dynamic properties of composite footbridges. Based on experimental techniques of output-only and input-output identification, the resonant frequencies, damping ratios and mode shapes of the footbridge were identified. A finite element (FE) model of the footbridge was developed and, after calibration with test data, a study on the damping characteristics of the GFRP-SFRSCC hybrid footbridge was conducted; in addition, its structural performance under human loads, especially its vibration mitigation capacity, was compared with that of an equivalent structural system made of steel profiles. The identified modal components were also compared to experimental results collected from the literature for conventional-based material footbridge. The important impact of higher harmonics of the pedestrian load in the dynamic response of short-span footbridges was also evaluated and demonstrated. Overall, the results obtained show that polymer-based components can contribute to limit vibrations in footbridges or even act as self-dampers; in this respect, it is shown that GFRP performs better than steel.

Keywords: Composites, GFRP, Steel, Viscoelasticity, Natural Frequency, Damping, Dynamic Behaviour, Footbridge vibrations.

---

1. Introduction

Pultruded glass fibre reinforced polymer (GFRP) profiles are being increasingly considered for civil engineering structural applications, as a replacement of

conventional materials, such as reinforced concrete and steel. This is mainly due to their lightness, high strength and non-corrodibility. Among the various structural applications of GFRP profiles are buildings and bridges, both vehicular and pedestrian. In these applications, one of the leading design requirements is users' comfort and, for that purpose, the dynamic properties are of paramount importance. In the specific case of pedestrian bridges, design is very often governed by vibration criteria, and the main aspects included in standards and guidelines in this respect are [1][2]: (i) the need to verify the criticality of the structure's frequencies; (ii) the need to check the possibility of occurrence of lock-in related to lateral vibrations; and (iii) the need to verify limit acceleration values under specific pedestrian actions and comfort criteria. In fact, excessive vibration has a significant influence on the in-service performance of slender structures and their service life.

Compared to structures made of conventional materials, the lower stiffness of GFRP structures, associated to their increased slenderness, leads to lower natural frequencies, thus involving a higher risk of resonance. In contrast, their lower mass counteracts this effect, but increases the vibration response due to reduced mass inertia [3]. In this sense, hybrid structures – combining composite and conventional materials – may be designed to fully exploit the properties of each material used in the different bridge components, maximising their advantages, and overcoming their limitations.

Understanding the dynamic behaviour of structural materials enables engineers to design structures that perform in service as intended, besides being safe and durable.

To allow for a comprehensive design of pedestrian bridges made of pultruded GFRP profiles, it is thus necessary to understand their dynamic properties, namely compared to steel, which is the primary alternative material it aims at replacing. The high damping

capacity of polymer-based materials is well-known and widely used in the mechanical, automotive, and aerospace industries. In fact, the vibrations produced in structures and mechanical components are the main sources of problems in high precision instruments, machines, automobiles or aircrafts, and the use of polymeric composites as passive damping elements allows mitigating those vibrations due to their viscoelasticity [4][5]. In these applications, the frequency-dependent stiffness behaviour of composites directly affects the modal characteristics of the structural system in which they are applied, resulting in complex vibration modes and differences in the relative phase of vibration [6]. In this context, the use of polymer-based composite materials in footbridges can also be considered in order to mitigate the harmful effects of excessive vibration in terms of in-service performance and comfort criteria [7].

Most of the previous work on composite footbridge structures focused on evaluating their static behaviour. In this respect, Wei *et al.* [8] pointed out that although there are guidelines and pre-standards for structural design of composite structures, they mainly focus on the effects of static actions. Comprehensive information about the dynamic characteristics of polymer-based composites is not yet available, namely concerning the material damping, which is necessary to conduct dynamic analyses (in the time domain) under pedestrian loads and fully assess the comfort of users under dynamic actions. This lack of information is well reflected in available design standards for composite structures, which provide very minimal guidance in this respect (e.g. American ASCE LFRD Standard [9]; European Prospect for New Guidance of FRP Structures [10]; Italian Code [11]).

Regarding the dynamic behaviour of FRP materials, some studies have been conducted in the last two decades, such as those of Boscato *et al.* [12], who presented

a modal identification of an all-FRP two-dimensional frame in free vibration, showing that the GFRP structural system presents better dynamic performance compared to steel and aluminium counterparts. Stankiewicz *et al.* [13] described dynamic in-situ tests of a cable-stayed all-GFRP footbridge under human excitation. They found out that the analysed footbridge fulfilled the vibration comfort criteria of the technical guide Sétra [2]. It is also worth referring the research from Živanović *et al.* [14], in which two FRP footbridges with main spans of 15.6 m and 63.0 m were used as case studies: their vibration behaviour was critically evaluated against steel and concrete structures of comparable span lengths, indicating that the design guidelines for FRP structures need to limit the vibration response, and not the natural frequency; they also highlight the possible need to recommend efficient vibration suppression measures for such extremely light structures.

Most of the research related to the dynamic behaviour of FRP-based footbridges was either limited to the dynamic characterisation of the structure or aimed at evaluating the range of critical frequencies in the structure, without evaluating the potential benefits of viscoelastic damping in controlling vibrations under critical pedestrian actions. As showed in Dacol *et al.* [15], viscoelastic materials in general, and polymer-based composites in particular, due to their dynamic behaviour (closely linked to their molecular structure), can generate high levels of internal damping, in addition to the external damping (connections, supports, etc.) of the structure. Another aspect that did not receive enough attention so far is the consideration of the influence of high harmonics of the action of human walking on the dynamic response of composite footbridges, which may be especially relevant due to their typical short spans.

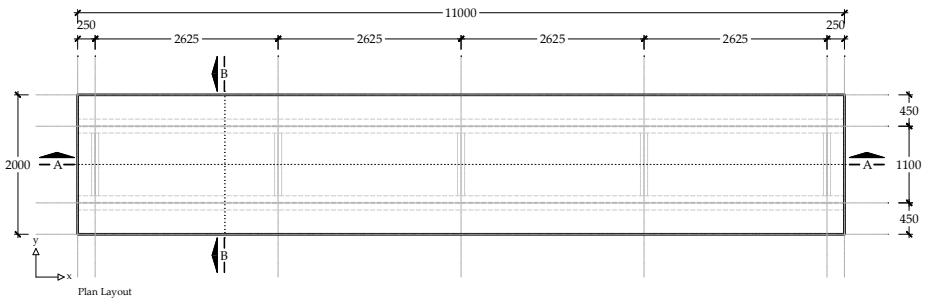
Taking into account the above-mentioned research needs, this paper presents an experimental and numerical study about the modal characteristics and damping of the São Silvestre footbridge (located in Ovar, northern Portugal), a hybrid structure made with two I-shaped pultruded GFRP main girders and a deck of steel fibre reinforced self-compacting concrete (SFRSCC). The main goal is to evaluate the dynamic characteristics of this hybrid footbridge structure and its capacity to dissipate energy, namely in comparison with conventional structures. Based on experimental techniques of output-only (ambient vibration) and input-output (hammer and body-jumping loads) identification, the excitation forces and the vibration response of the footbridge are measured in the time domain and transformed in the frequency domain using the Fast Fourier Transform (FFT) method. From the frequency response functions (FRF) and power spectral density (PSD) functions, the resonant frequencies, damping ratios and mode shapes of the footbridge are extracted using the Enhanced Frequency Domain Decomposition (EFDD) and the Operational PolyMAX methods [16]. A finite element (FE) model of the footbridge is then developed. After calibration with experimental data, a numerical analysis is performed comprising the application of pedestrian loads along the deck; the calculated response in terms of accelerations is then compared with comfort limits. Following the same methodology, another FE model is developed, in which steel profiles replace the GFRP girders, allowing to compare the responses of GFRP- and steel-based solutions for the same pedestrian loads. The research presented in this paper also aimed at assessing the impact of higher harmonics of pedestrian action on the dynamic response, which as mentioned above is particularly important in short span footbridges.

The remainder of this paper is organised as follows: a brief description of the São Silvestre footbridge is provided in section 2. The experimental programme is presented in section 3, and the test results are described in Section 4. In section 5, the numerical models of the footbridge are first described and then the results of numerical simulations for both GFRP- and steel-based models are presented and compared. Finally, section 6 summarises the main findings of this study.

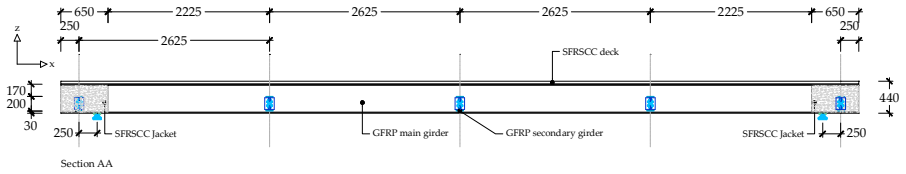
2. Description of São Silvestre Footbridge

2.1. GFRP–concrete hybrid structural systems

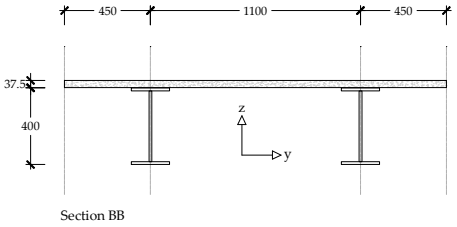
The full-scale GFRP-SFRSCC hybrid footbridge studied in this paper, described in detail in [17], comprises two I-shaped (400 × 200 (× 15) mm^3) pultruded GFRP profiles acting as main girders and a thin 37.5 mm thick SFRSCC deck with a width of 2000 mm positioned on top of the GFRP profiles. The structure presents a total length of 11,000 mm and is simply supported, forming a span of 10,000 mm (L), as shown in **Fig. 1**. Five I-shaped pultruded GFRP profiles (200 × 100 (× 10 mm^3) are used as secondary girders.



(a)



(b)



(c)

Fig. 1. Geometry of the footbridge: (a) Plan view, (b) Section AA, (c) Section BB

(dimensions in mm)

To ensure full interaction with minimum slip between the main girders and the deck, a 2 mm thick epoxy adhesive layer (S&P Resin 220) is used between these elements.

The secondary girders are positioned close to the supports and at three additional sections symmetrically distributed along the footbridge length. These girders contribute to prevent lateral-torsional buckling and minimis the effects of initial lateral imperfections. The connection between the main girders and secondary beams is made with M10 mm stainless steel bolts and GFRP pultruded angle section profiles (160 × 60 × 8 mm^3), as shown in **Fig. 2**.

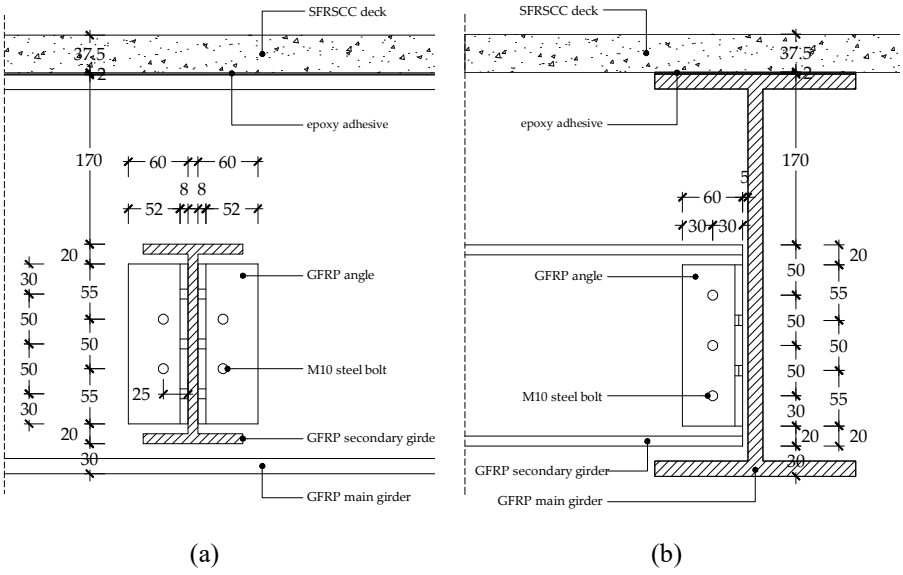


Fig. 2. Connections between main and secondary girders: (a) Section AA; (b) Section BB

(dimensions in mm)

(a) (b)

Fig. *3* shows the São Silvestre footbridge installed *in* Ovar, Portugal, opened to pedestrians in November 2015. To ensure simply supported boundary conditions, the GFRP beam supports were designed to allow free-rotation about the x and y axes (pinned) and free-translation (sliding) in the longitudinal axis x (*cf.* **Fig. 1** for axes definition). These supports were materialized by top metal plates over pinned bars. It

is noted that the sliding in the longitudinal direction was not entirely free due to friction between the GFRP beams and the top metal plate. Furthermore, at the support areas, SFRSCC jackets were cast in-between flanges of the main girders in a length of 650 mm. These jackets aimed at preventing premature web crippling failure of the GFRP webs under concentrated loads.



(a) (b)

Fig. 3. (a) São Silvestre footbridge; and (b) support detail.

2.2. Material properties

The GFRP profiles, comprising the main and secondary girders, are made of E-glass fibre rovings and mats embedded in an isophthalic polyester resin matrix, and were produced by ALTO Perfis Pultrudidos, Lda. The main mechanical properties of the GFRP profiles were derived from coupon tests performed by Gonilha *et al.* [17] in: (i) tension (EN ISO 527 [18]), (ii) compression (ASTM D695 [19]), and (iii) shear (10° off-axis tension tests according to [20]).

Table 1 summarises the density (ρ) and the average in-plane mechanical properties of the GFRP section walls (main girders), namely the elastic modulus (E) in the longitudinal (L) and transverse (T) directions, the shear modulus (G_{LT}), the longitudinal tensile strength ($f_{tu,L}$) and the in-plane shear strength ($\tau_{u,LT}$).

CiviTest Company developed the SFRSCC, and its compressive strength and flexural properties were assessed according to the test standards NP EN 12390-3 [21] and RILEM TC 162-TDF [22].

Table 2 summarises the average mechanical properties of SFRSCC.

Table 1.

Mechanical properties of the GFRP

Section wall	$\mathbf{E_{L,t}}$ (GPa)	$\mathbf{E_{T,t}}$ (GPa)	$\mathbf{G_{LT}}$ (GPa)	$\boldsymbol{f_{tu,L}}$ (MPa)	$\boldsymbol{\tau_{u,LT}}$ (MPa)	$\boldsymbol{\rho}$ (kN/m^3)
Webs	24.0	7.73	3.49	278.9	20.4	18.0
Flanges	35.7	3.57	-	336.9	-	

Table 2.

Mechanical properties of the SFRSCC

$\mathbf{E_{c,28}}$ (GPa)	$\boldsymbol{f_{cm}}$ (MPa)	$\boldsymbol{f_{ct,L}}$ (MPa)
37.8	76.0	6.21

The epoxy adhesive used to bond the main girders and the deck presents average values of elasticity modulus of $E_a = 8.8$ GPa and tensile strength of $f_{a,u} = 17.3$ MPa.

3. Experimental Programme

The footbridge's modal identification tests were carried out to identify natural frequencies, vibration modes, and associated modal damping ratios. The experimental programme included two types of tests: (i) ambient vibrations tests and (ii) forced vibration tests based on the excitation of the footbridge by an adequate impact hammer. In these tests, acceleration was measured at 18 different positions along both

longitudinal edges of the deck, as depicted in **Fig. 4** (1D to 9D and 1U to 9U). The ambient temperature was 13 °C.

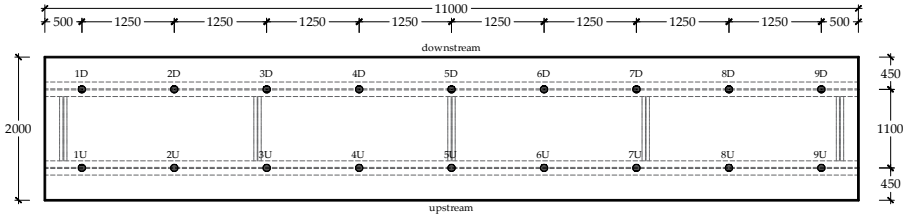


Fig. 4. Position of measurement points (dimensions in mm).

3.1. Ambient Vibration Tests

The ambient vibration tests were performed by measuring vertical and horizontal accelerations for periods of 14 min at nine different positions along both edges of the deck. The tests were performed using four triaxial GeoSIG seismographs including 24-bit converters with a 96 dB dynamic range. The ambient response was recorded according to eight setups (*cf.* **Fig. 5**), using two fixed reference stations located at points 4D and 4U, and 16 other measurement stations, scanning the bridge deck, as depicted in **Fig. 5**.

It should be mentioned that the tests were conducted with the footbridge in service and subject to pedestrian traffic. **Fig. 6** shows an image of the bridge during the ambient vibration test when a group of 18 pedestrians passed.

The sampling frequency was 50 Hz and the recorders operated independently but were programmed and synchronised by a laptop.

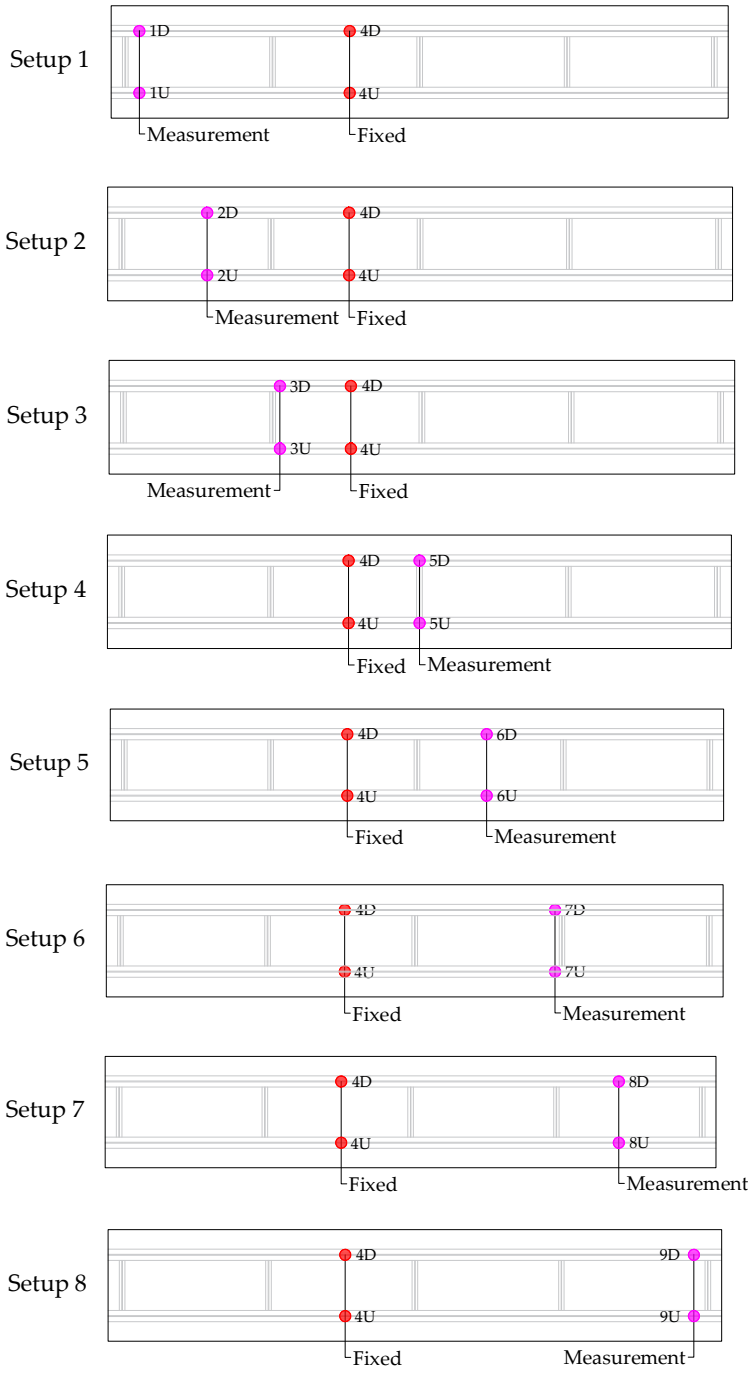


Fig. 5. Modal identification - ambient vibration: acceleration measuring positions.



Fig. 6. Example of ambient vibration test: 18 pedestrians crossing the footbridge (Setup 6).

For each set of time records, collected with a duration of 14 min, estimates of power spectral density (PSD) functions and frequency response functions (FRF) relating the response at each section to the reference station were obtained.

3.2. Forced Vibration Tests

A forced vibration test was conducted as a complement to the ambient vibration tests in view of the limited frequency range of natural excitation. In this case, the loads were applied using an impact hammer (from PCB, model 086D50) with a rubber tip containing a built-in load cell. The acceleration was measured with two high sensitivity piezoelectric accelerometers at four different positions (*cf.* **Fig. 8**) along the longitudinal edges of the deck, as depicted in **Fig. 7**. Data were sampled at a rate of 500 Hz with a Fourier Analyser and stored in a laptop. Frequency response functions were constructed from the power spectrum of the measured acceleration and force (power spectral density – PSD) with a resolution of 0.1563 Hz.

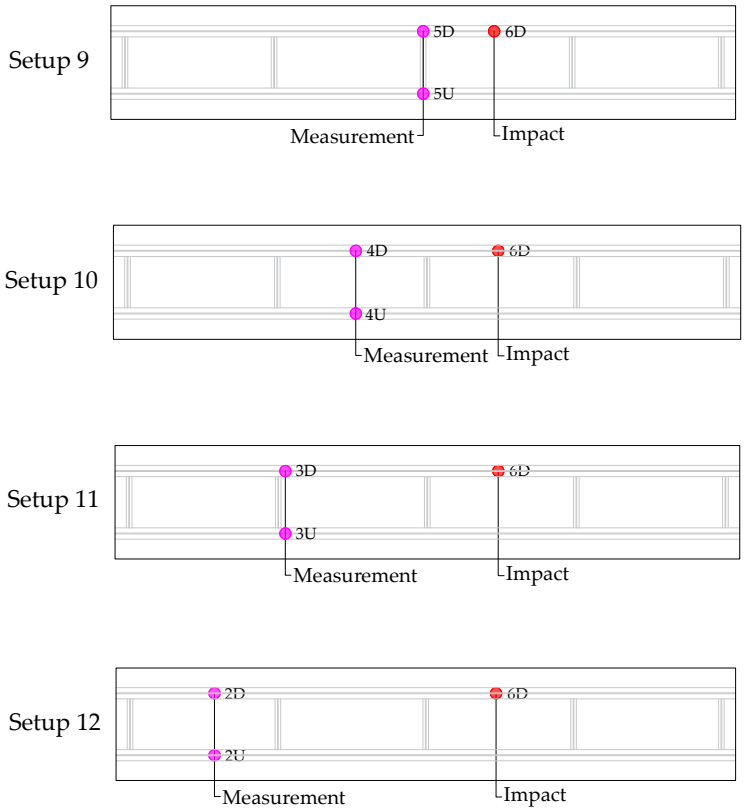


Fig. 7. Forced vibration tests: Impact at 6D, acceleration measured at different points.



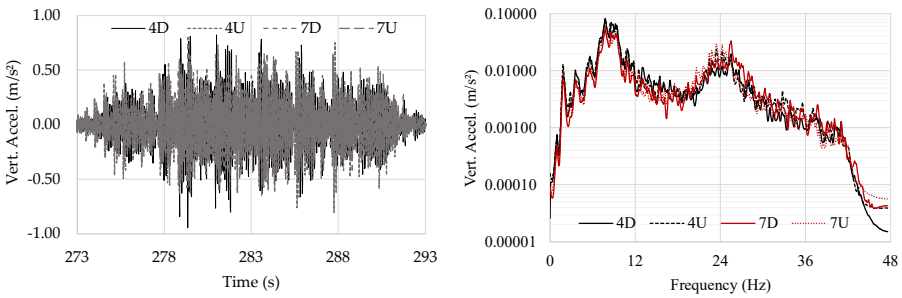
Fig. 8. Experimental tests: impact being applied.

4. Experimental Results

This section describes the experimental results of the tests carried out on the São Silvestre footbridge, including the identified frequencies, mode shapes and extracted damping ratios.

4.1. Ambient Vibration Tests

The time records collected during the ambient vibration tests were used to extract modal parameters. In addition, the amplitude of pedestrian induced accelerations was assessed, as their traffic was not interrupted during the test. Maximum vertical acceleration occurred for Setup 6, in which the deck was excited by a group of 18 pedestrians. The measured absolute vertical acceleration had maximum values of 0.887 m/s^2, 0.936 m/s^2, 0.696 m/s^2, and 0.798 m/s^2, at points 4D, 4U, 7D and 7U, respectively. **Fig. 9** shows the time history and the spectrum amplitude of the records collected in Setup 6 during the 18 pedestrians crossing.

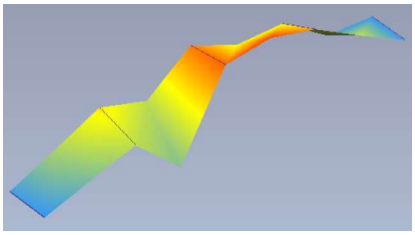


(a) (b)

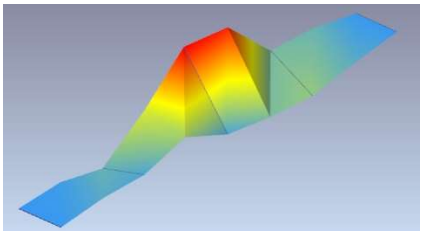
Fig. 9. Vertical acceleration: (a) time history, and (b) spectrum amplitude of Setup 6 (time lapse of 18 pedestrians).

From the measured time required for the group of 18 pedestrians to cross the footbridge length (11 m), the average frequency was calculated as $1.93\,\mathrm{Hz}$. The spectrum depicted in **Fig. 9b** shows several harmonics related to the walking of the pedestrian group. In this respect, Bachmann *et al.* [23] point out that the feet are always in contact with the floor during the walking activity, and the load function will have components of the 2nd, 3rd, and 4th harmonics. Furthermore, it should be noted that in footbridges with natural frequencies higher than the frequency of the footstep, the excitation of the 1st vibration mode may occur due to the higher-order harmonics [24].

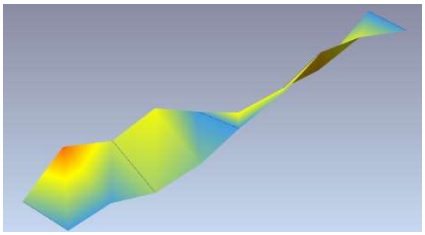
The estimation of spectral densities was performed using 1024 frequency lines and a frequency line spacing of 0.049 Hz. This was achieved by setting 66% overlapping and using a Hanning window. Based on the Enhanced Frequency Domain Decomposition (EFDD) method, the dynamic parameters were identified and are summarised in **Table 3**. A total of four mode shapes were identified, the first three mode shapes being depicted in **Fig. 10**. It should be stressed that the identified modes evidence some scatter, which is likely due to the presence of noise in the measurements, as the ambient excitation has a small frequency content in the range of the footbridge frequencies [25]. It is noted that it was not the purpose of the tests to identify the modal shapes in a refined way, as only nine points were used in the measurements (*cf.* **Fig. 5**).



Mode 1



Mode 2



Mode 3

Fig. 10. EFDD Modal identification: the first 3 mode shapes with ambient excitation.

Table 3.

Modal parameters identified with the EFDD method.

Mode	Frequency	Damping	Mode Shape
	Mean (Hz)	Mean (%)	
1	8.39	2.47	bending, symmetric
2	9.96	-	torsion, symmetric
3	24.64	1.47	torsion, asymmetric

The fundamental frequency of the footbridge is compared to the one calculated using the relationship suggested by Bachmann [26] given by $f_1 = 33.6 \times L^{-0.73}$, where f_1 is the first resonance frequency, and L is the span. In the case of the São Silvestre footbridge, this would lead to a fundamental frequency $f_1 = 6.25$ Hz, 26% lower than the first frequency identified in the ambient vibration tests. Gonilha [27] reported the first fundamental frequency of the São Silvestre prototype as 6.60 Hz (although these tests were carried out in a 10.5 m span), very close (9% relative difference) to the value suggested by Bachmann [26]. Section 5 discusses aspects concerned with the support conditions (assessed using the numerical model) that may also justify this difference.

4.2. Forced Vibration Tests

The forced vibration tests were based on the load applied by an impact hammer and the measurement of both the excitation and the structure response, by applying conventional input-output modal identification techniques.

Fig. 11 shows an example of the time records of force and acceleration collected simultaneously for Setup 9.

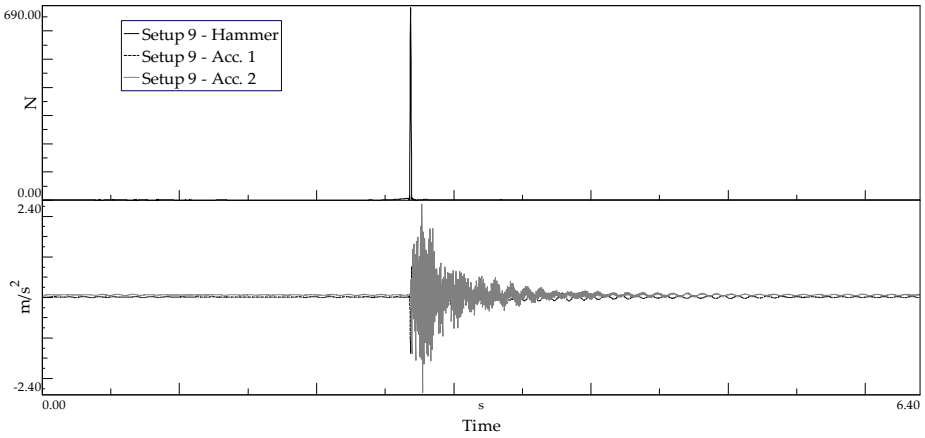


Fig. 11. Modal identification test: time-domain recording values (Setup 9).

The time history signals acquired by each accelerometer were stored. To separate the bending response from the torsion response, the half-sum and half-difference of the vertical acceleration recorded simultaneously in the opposite edges of the deck were calculated. The Fast Fourier Transform (FFT) was applied directly to the processed data, enabling the direct identification of the frequencies for which the FFT presents peak values. The auto-power and the cross-spectrum, calculated by multiplying a frequency spectrum by its complex conjugate, were calculated and averaged. **Fig. 12** shows the average normalised power spectral density (ANPSD) plot for Setup 9 and the peak frequency poles. Frequency response functions were also calculated relating the

output averaged cross-spectrum with the input spectrum. These functions were then used to identify modal parameters using the PolyMAX algorithm [16].

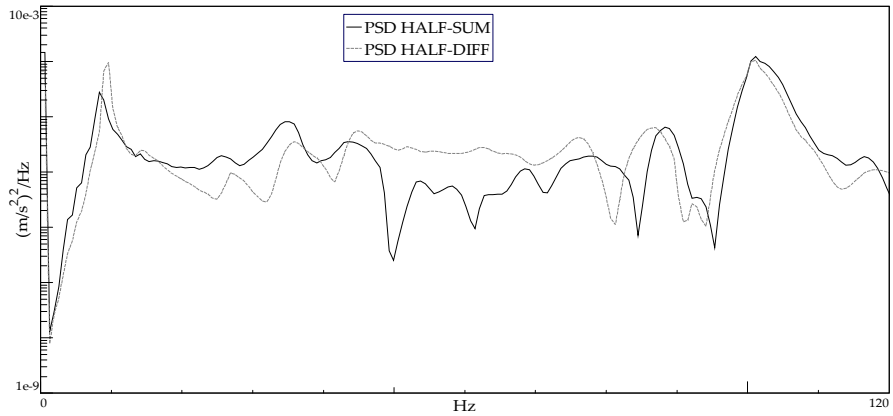


Fig. 12. Modal identification test: ANPSD plot for Setup 9.

Fig. 13 shows the PolyMAX stabilisation diagram applied to the sum of the imaginary parts of FRFs. The stabilisation diagram tolerances were adjusted to 0.1%, 0.1%, and 0.2%, for vector, frequency, and damping ratio, respectively. The tolerance values have been adjusted to reduce the variability between frequencies, vectors, and damping ratios for the related mode. A total of 17 stabilised poles were found, the first 6 being summarised in **Table 4**. **Fig. 14** shows the first four mode shapes, which exhibit better quality compared to those identified from the ambient vibration test. The fact that the impact excitation has a frequency content in a wide range below 130 Hz explains the lower noise level when the structure frequency is relatively high.

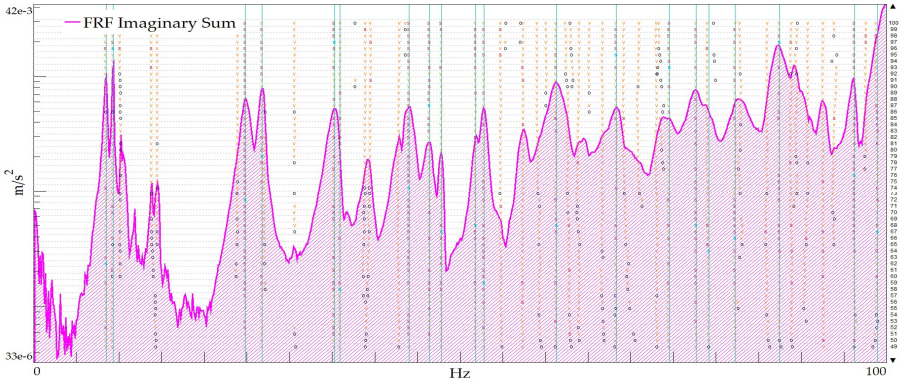
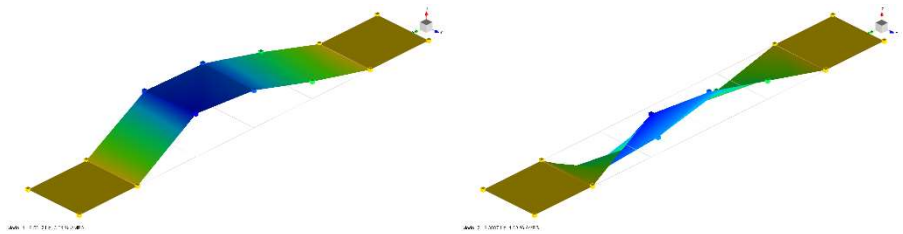


Fig. 13. Stabilisation diagram: the PolyMAX method applied to the sum of the imaginary parts of FRFs.

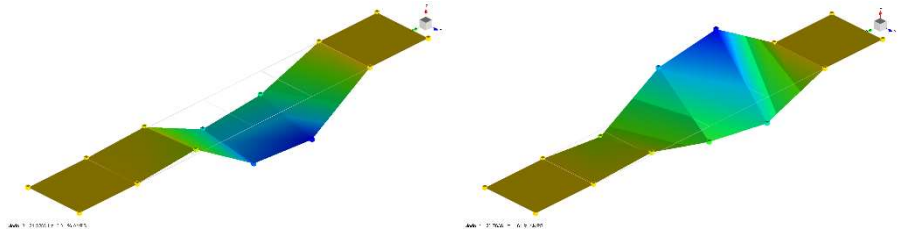
Table 4.

Modal parameters identified with POLYMAX.

Mode	Frequency (Hz)	Damping (%)	Mode shape
1	8.62	4.17	1st Bending, symmetric
2	9.24	3.40	1st Torsion, symmetric
3	24.86	3.04	2nd Bending, anti-symmetric
4	26.81	1.41	2nd Torsion, anti-symmetric



Mode 1 Mode 2



Mode 3 Mode 4

Fig. 14. PolyMAX Modal identification: the first 4 mode shapes with forced excitation

The application of the PolyMAX method to the data collected with forced excitation enabled the separation of very closely spaced bending and torsion modes, whose interaction was already evident in the plot of **Fig. 12**. On the contrary, the very small level of vibration generally present during the ambient vibration tests, and the limited frequency content associated with natural excitation prevented the separation of the torsion and bending second order modes, and only one mode with mixed characteristics had been identified in the ambient vibration test.

4.3. Summary of Identified Modal Parameters

The results obtained in the preceding sections are summarised in **Table 5**. The analysis of this table shows a good correlation between the ambient and the forced vibration test results. However, it is noted that the higher-order frequency modes could not be identified from the ambient vibration test due to the insufficient frequency content of natural excitation. Also, the second-order modes (modes 3 and 4) could not be well separated in their bending and torsion contributions from the ambient vibration test. Regarding damping estimation, relative differences between both types of tests were significant. In this case, given the higher confidence in the forced vibration test,

the result of the latter will be used next. It is noted that different amplitudes of the response could be responsible for the damping variation found.

Table 5.

Summary of experimental measurements.

Mode	Identified Frequency		Extracted Damping Ratio	
	Ambient	Hammer-impact	Ambient	Hammer-impact
	(Hz)		(%)	
1	8.10	8.62	2.23	4.17
2	9.43	9.24	1.25	3.40
3	24.61	24.86	0.96	3.04
4	25.46	26.81	1.15	1.41
5	-	35.32	-	1.92
6	-	43.98	-	1.66

The results summarised in **Table 5** show that the experiments with the forced-vibration load given by the hammer impact provides a wider frequency range. In fact, according to Cunha and Caetano [28], the forced vibration test with this device has the advantage of offering a wide-band input that can stimulate different vibration modes, compared to the ambient and human-jumping impulsive force.

It should be highlighted that the vibration modes identified in this experimental campaign present significant differences with those identified by Gonilha [27] from laboratory tests, namely regarding the characteristics of the first two modes. The first natural frequency experimentally identified in [16] was 6.56 Hz, which is 29% lower than the frequency of the first mode obtained herein. This difference is partly explained by the fact that the free span of the prototype tested in [27] is 10.50 m, while that of the

installed footbridge is 10.0 m. Further reasons, concerned with the support conditions are discussed ahead.

Concerning the damping ratios, it is worth comparing the results obtained herein for the GFRP-based hybrid footbridge with the research of Faisca [29], which focused on a hybrid footbridge prototype made of steel beams (I-profiles) for the stringers and transversals members, and a reinforced concrete deck (2.20 m wide and 100 mm thick slab), which was tested under human-induced loads to assess its modal components (frequency, mode shape and damping ratio). The structure rests on four supports, two at each end, resulting in a maximum free span of 11.5 m. Vega *et al.* [30] used that footbridge prototype to evaluate the responses of the structure when subjected to pedestrian actions. Concerning the 1st bending and 1st torsional mode shapes measured in a jumping test, the estimated damping ratios were $\xi_1 = 0.6\ \%$ and $\xi_2 = 0.7\ \%$, respectively. As presented above, the São Silvestre footbridge presented damping ratios of $\xi_1 = 4{,}17\ \%$ and $\xi_2 = 3.40\ \%$ for its two first modes, concerning the impact load test, which corresponds to a damping ratio five times higher, on average, than that of the steel-based hybrid structure; these results are in agreement with the comparative damping study conducted by Dacol *et al.* [15].

4.4. Energy-based fitting of Damping

The application of the energy method constitutes an alternative for the determination of an equivalent damping ratio corresponding to each vibration mode of the structure. In this context, an evaluation of the measured damping ratio was performed. Based on the study conducted by Dacol *et al.* [15], the energy-based damping fitting was performed concerning the measured damping ratios for the hammer-impact test.

Despite the fact that the energy dissipation curve only represents the damping "trend" as a function of natural frequency, it may indicate possible deviations in the experimental characterisation of the damping. In the present study, as shown in **Fig. 15**, the calculated damping ratios show good agreement with the energy dissipation process since the r-Pearson coefficient reveals a strong correlation, with a value of 0.88.

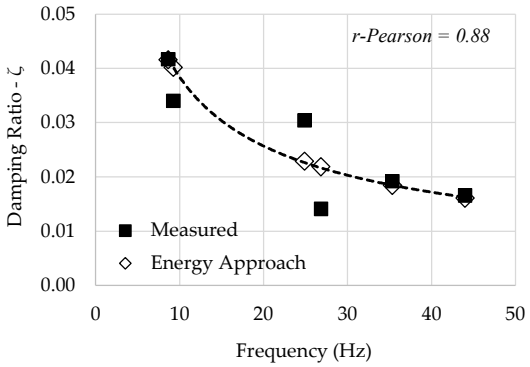


Fig. 15. Energy-based fitting of damping ratio variation.

5. Numerical Study

For the numerical study, a FE model was developed, tuned using the experimental data described above, and then used for the numerical simulation of the footbridge response. To assess the relative performance of the GFRP-based hybrid structure with that of a more conventional alternative, an additional FE model was developed where the GFRP profiles were replaced by commercial steel profiles. The same load simulations were considered in both FE models, and the results obtained were compared.

5.1. Model Development and Calibration

The FE model was developed using software RFEM (student version), from Dlubal Software GmbH. The FE model included 8-node solid brick elements to simulate most structural components, namely: (i) the SFRSCC deck; (ii) the 2 mm thick epoxy adhesive layer; (iii) the GFRP main girders; (iv) the GFRP secondary girders, (v) the steel support plates, (vi) the GFRP angle sections, and (vii) the M10 steel bolts. A sensitivity study of the mesh was carried out to obtain sufficiently accurate results without compromising the speed of the computational effort. In this sense, the target length of the finite elements was set to 100 mm. The interfaces between the various materials were considered perfectly bonded. **Fig. 16** shows a view of the 3-dimensional numerical model of the footbridge.

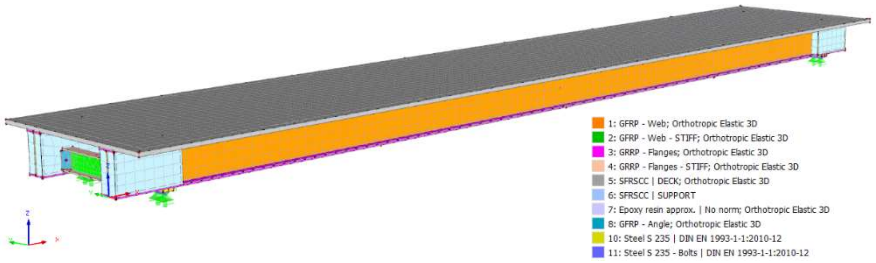


Fig. 16. The perspective of the 3D finite element model

The material properties considered are those obtained from experimental testing as indicated in

Table 1 and

Table 2.

The numerical model was calibrated based on experimental results through a tuning process in which the linearity of stiffness and the influence of support conditions were evaluated. For the calibration process, in terms of accuracy, a value of ±5% was deemed

as an acceptable threshold for the relative differences between experimental and tuned natural frequencies.

Concerning stiffness, the ratio between frequencies of consecutive modes was compared ($f_2/f_1 = f_3/f_2 = f_4/f_3 = \cdots$), to identify any potential non-linearity in the global stiffness of the system. In this sense, it was observed that the ratio between frequencies remained constant, with slight variations (below 10%), denoting that stiffness may be assumed as continuous within the identified frequency range.

Several iterations were performed with a modification of the support characteristics, namely in the longitudinal translational degree of freedom (x-axis). As shown in



Fig. 17, the support conditions idealised in the laboratory model (enabling sliding in the longitudinal (x) direction, ensured by metal spheres in-between the support plates) differed from the actual support conditions in situ, that constrained sliding in the longitudinal direction. This restriction to free sliding was caused by the friction between the GFRP girders and the top metal plate of the support (both bottom plates were anchored to the abutments); moreover, lateral (y) deflections and rotations may have

also been partially restricted[†]. In this context, the tuned model (*see* **Table 7**) was achieved setting up a translational spring coefficient as follows: (i) free rotation about the axes x, y and z (**Fig. 17**) $\varphi_x = \varphi_y = \varphi_z = free$, (ii) longitudinal spring $k_x = 1.8 \times 10^5$ kN/m^2, and (iii) fixed transverse displacements in y and z directions, $u_y = u_z = 0$.



Fig. 17. Support detail of laboratory model [16].

5.2. Static Simulation

A static numerical simulation was performed using the FE model of the São Silvestre footbridge to assess its flexural behaviour, namely the vertical deflections and the axial strains for predefined load configurations. Regarding the load configuration, Eurocode 1, part 2 [31] recommends that for the design of pedestrian bridges a uniformly distributed live load q_{fk}, calculated according to Equation (1), should be

[†] It is worth mentioning that the free rotation of the metal rollers may have also been partly prevented by the debris accumulated over the bottom metal plates of the supports.

applied only in the unfavourable parts of the influence surface, longitudinally and transversally, where q_{fk} is expressed in kN/m^2, and L is the loaded length in m according to

$$2.5 \leq q_{fk} = 2.0 + \frac{120}{L + 30} \leq 5.0 \quad (1)$$

From Equation (1), for a loaded length of $11.0\ m$, a uniformly distributed load about $5.0\ kN/m^2$ applied across the deck surface is obtained.

To establish combinations of actions for serviceability limit states (SLS) and ultimate limit states (ULS) verifications, the variable and accidental actions and the combination factors presented in the Eurocode 0 (2017), Annex A2 [32] are used and result in the following Equations

$$q_{SLS} = 1.0 * g_{sw} + 0.3 * q_{fk} \quad (2)$$

$$q_{ULS} = 1.5 * g_{sw} + 1.5 * q_{fk} \quad (3)$$

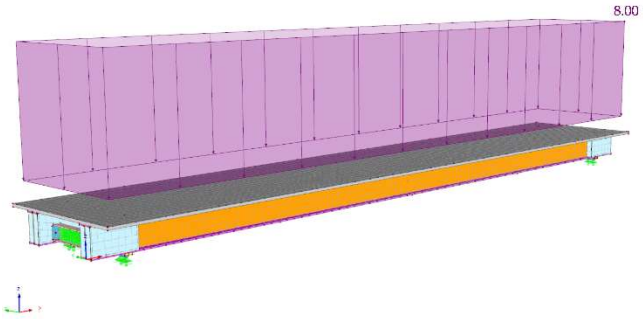
where g_{sw} is the self-weight of the structure (including other permanent loads, as the surface coating and handrails) in kN/m^2.

As described in Gonilha [27], the laboratory load tests were performed on the full-scale footbridge prototype, in which the deck was loaded with water reservoirs, which had an average weight of 10.6 kN and plan dimensions of 1.0×1.2 m^2, corresponding to a uniformly distributed load of 8.80 kN/m^2. The distribution of the reservoirs over the deck of the footbridge prototype is shown in **Fig. 18Error! Reference source not found.**.

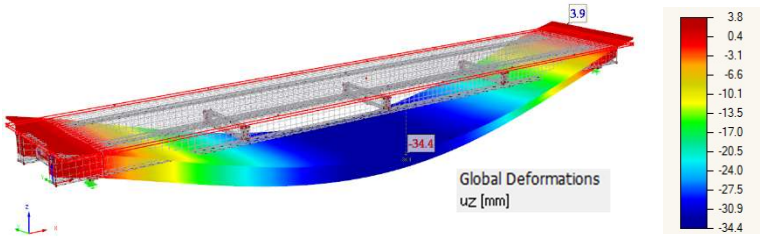


Fig. 18. Static test of the experimental model (*courtesy of* [27])

Using as a reference the midspan displacement measured by Gonilha [27] in the laboratory load tests of the footbridge prototype, the same load was applied in the model simulating the structure in the present configuration, and a linear elastic analysis was performed. **Fig. 19** shows the deformed shape obtained using the numerical model.



(a)



(b)

Fig. 19. Model of GFRP-SFRSCC footbridge prototype - **S**tatic simulation.

The SLS requirements for footbridges defined in Eurocode 0 (2017) do not include any deformation limits but only vibration limits to guarantee pedestrian comfort. The total mid-span deflection calculated with the FE model is $\delta_{md} = 34.4$ mm $(L/305)$.

To compare the dynamic performance of the GFRP-based hybrid footbridge with that of an equivalent steel-based hybrid structure, a similar numerical model was developed in which the GFRP profiles were replaced by I-shaped steel profiles acting as main girders. In this model, the choice of the commercial steel section was made targeting a global stiffness equivalent to that of the GFRP-based model. The equivalent stiffness was calculated by dividing a concentrated unit force applied at mid-span by the resulting displacement. Three steel sections were initially evaluated – IPE 200, IPE A 300, and IPE 330 – and their equivalent stiffness was calculated, yielding $k_{IPE200} = 0.9$ kN/mm, $k_{IPE\,A\,300} = 2.7$ kN/mm, and $k_{IPE330} = 3.6$ kN/mm. The equivalent stiffness of the GFRP model is $k_{GFRP} = 2.5$ kN/mm, and therefore the IPE A 300 profile was used in the main girders for dynamic comparison between models $(k_{IPE\,A\,300}/k_{GFRP} = 1.08)$. As secondary girders, IPE 120 profiles were used. The same SFRSCC-slab was considered as well as the same loads.

The calculated maximum mid-span deflection of the steel-based model for the 8.80 kN/m^2 load applied in the laboratory was $\delta_{md} = 33{,}1$ mm $(L/317)$, 3.8% lower than that calculated for the GFRP model. The maximum axial strain of the SFRSCC slab was $\varepsilon_c = 0.300$ ‰, 8% higher than in the GFRP model ($\varepsilon_c = 0.278$ ‰). **Table 6Error! Reference source not found.** summarises the predictions of static response

for both models in terms of mid-span deflections, axial strains on the SFRSCC slab and maximum stresses in the webs and bottom flanges of the main girders.

Table 6.

Predicted static response of GFRP- and steel-based hybrid systems for a load of $8.80\ kN/m^2$.

Material	System mass (kg)	δ_{md} (mm)	ε_{slab} (‰)	σ_{web} (MPa)	σ_{flange} (MPa)
GFRP	3,007	34.4	0.278	26.2	40.5
Steel	3,126	33.1	0.300	60.7	162.0
Relative Diff.	+ 3.9	- 3.8%	+ 8%	+ 132%	+ 400%

5.3. Dynamic Analysis

The tuned numerical model of the São Silvestre footbridge was used to perform a dynamic analysis to assess its natural frequencies and mode shapes. Fourteen eigenvalues and vibration modes were calculated, and the first four were used for dynamic pedestrian simulation. For this purpose, a consistent mass matrix was used. The Subspace Iteration method was used to solve the eigenvalue problem. The dynamic analysis was performed under two mass conditions: (i) empty footbridge, and (ii) footbridge subject to a uniformly distributed load corresponding to a density of 0.82 pedestrians/m^2, representing the Setup 6 of the ambient vibration tests, in which the footbridge was simultaneously crossed by 18 pedestrians. The mass of the pedestrians was defined as 70 kg for this purpose. The same dynamic analysis was

performed in the numerical model of the steel-based footbridge (IPE A 300), for which the four first modes were considered.

The natural frequencies obtained with the FE model and their comparison to the experimental estimates are summarised in **Table 7**, including both situations of the empty footbridge and the inclusion of mass relating to 44% of the total mass of the 18 pedestrians. **Fig. 20** shows the mode shape configurations calculated for the model of the empty GFRP-based footbridge.

Table 7 and **Fig. 20** allow concluding that the GFRP-based FE model represents well the identified modal parameters, namely frequencies and mode shapes. The highest relative differences between the numerical model and the actual structure correspond to the 3rd vibration mode.

It is relevant to note that for the case of the loaded footbridge (**Table 7** (ii)), the increase in mass of the structural system (44%) caused reductions in the calculated natural frequency of 15% and 16%, on average, for GFRP- and steel-based hybrid systems, respectively.

Table 7.

Frequencies obtained for the first 4 mode shapes from experimental tests and numerical models[a].

Mode	**Frequency**				
	Identified (GFRP) (Hz)	FE model (Hz)			
		GFRP		Steel	
		Empty	Loaded	Empty	Loaded

1	8.62	8.60	7.76	8.43	7.62
2	9.24	9.48	8.20	9.33	8.17
3	24.86	22.11	18.64	25.75	20.19
4	26.81	25.85	19.91	29.73	23.41

[a] *(i) empty footbridge, and (ii) loaded footbridge.*

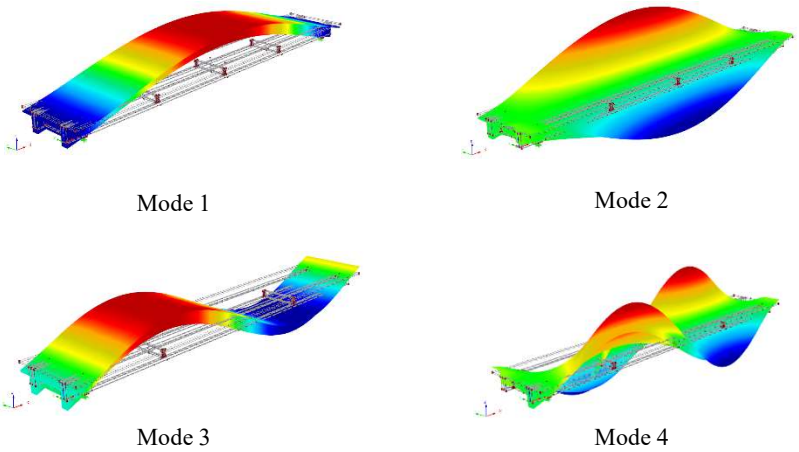


Fig. 20. Numerical model: first 4 mode shapes.

The ratio between the calculated frequencies for the GFRP- and steel-based hybrid models is close to 1, reflecting the resemblance of the modal characteristics of both models. Furthermore, it can be observed that all identified and calculated frequencies are outside the resonance risk range. In this study, only the vertical vibration modes are investigated.

5.4. Pedestrian Load Simulation and Performance Analysis

In this section, the response under dynamic pedestrian actions of the São Silvestre footbridge is numerically analysed for both GFRP- and steel-based hybrid models. The

response is compared with threshold values defined in standards, namely in terms of maximum vertical accelerations. For the GFRP-based hybrid footbridge, even though the calculated frequencies are outside the resonance risk range, a numerical analysis is conducted because the dynamic behaviour of GFRP-based footbridges has not been sufficiently studied in the past. As mentioned, short-span footbridges are particularly susceptible to the actions of higher harmonics of the pedestrian force, in which the amplification of acceleration responses may occur due to the 2nd, 3rd and even 4th harmonic [23, 33]; this specific behaviour is discussed in section 5.4.2.

The actions induced by a person when walking on a footbridge are periodic and depend on several parameters: stride frequency, stride length, walking speed and foot-floor contact time. Summarily, there are two types of time-domain models: (i) the deterministic, in which the random variation among human population is disregarded, and a uniform walking force model for each pedestrian is adopted, and (ii) the probabilistic type, which address the distinct gait parameters that influence human-induced forces such as body weight, step and frequency [34]. The use of deterministic models to characterise human loads has been questioned by different authors, as Santos [35]. Therefore, in this research, a probabilistic approach was used to define pedestrian group action.

5.4.1. Effects of a single pedestrian walking

In this paper, the experimental curves derived from testing by Gonilha [7] are used to construct deterministic load-time functions to model the pedestrian loads, namely (i) slow walk; (ii) normal walk; and (iii) fast walk, as depicted in **Fig. 21**.

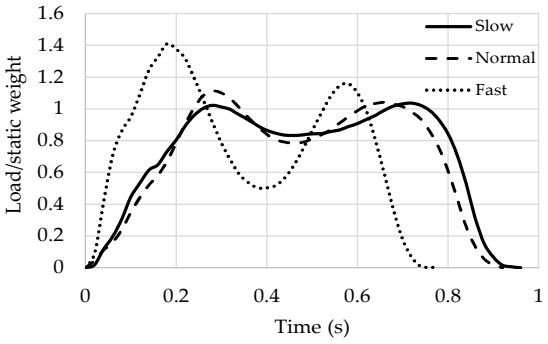
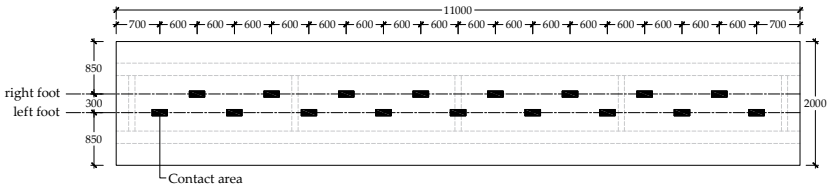
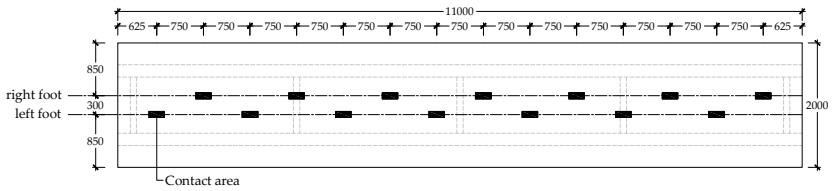


Fig. 21. Load-time curves (slow, normal and fast walk), as defined in [7].

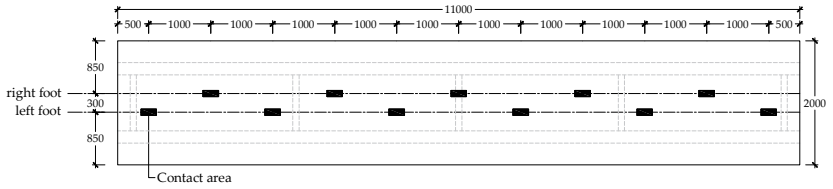
In the numerical model, the simulation of the pedestrian walking load on the footbridge was made by defining a rectangular area with dimensions of 100×250 mm (width × length) associated with each foot. A load of 800 N was applied to this area according to the motion characteristics presented by Wheeler [36]. Transversely, the two feet were 300 mm distant, while longitudinally, they were separated by a length *L*, according to the footstep speed (slow, normal or fast). The load cases were then combined in time history analyses with the respective load-time function depicted in **Fig. 21**. **Fig. 22** shows the numerical simulation setup for (a) slow, (b) normal, and (c) fast walk.



(a)



(b)

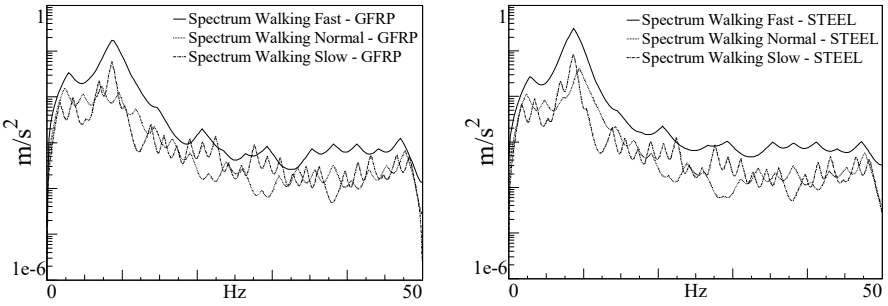


(c)

Fig. 22. Dynamic tests: motion positioning: (a) slow, (b) normal, and (c) fast walk

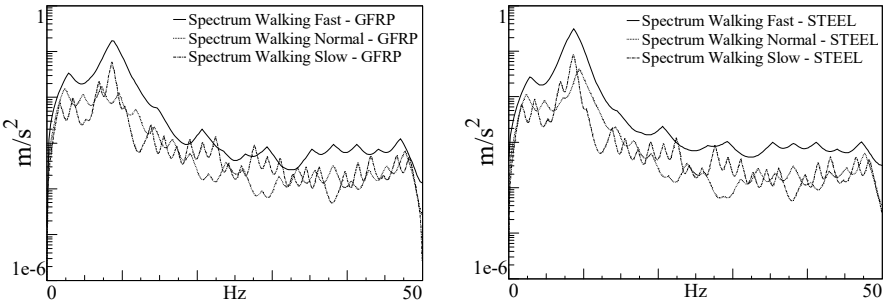
(dimensions in mm).

The values of the extracted damping ratio summarised in **Table 5.** (related to the hammer-impact test) were used for the modal analysis of the GFRP-based model considering a single pedestrian walking and four modes. Based on the studies of Dacol *et al.* [15], in which values of GFRP material damping ratio are up to 5 times higher than those of steel, and the damping ratios described in Vega *et al.* [30], the damping ratio of the steel-based model were set as 0.8%, 0.7%, 0.6%, and 0.3% for the first four modes of vibration, respectively. The weight of the pedestrian was not added to the self-weight of the footbridge structure (due to its limited relevance). The maximum vertical acceleration at midspan obtained for each load function is summarised in **Table 8.**



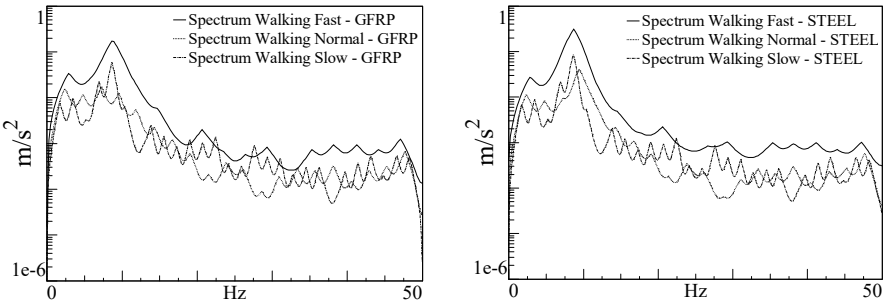
(c) (d)

Fig. 23a and



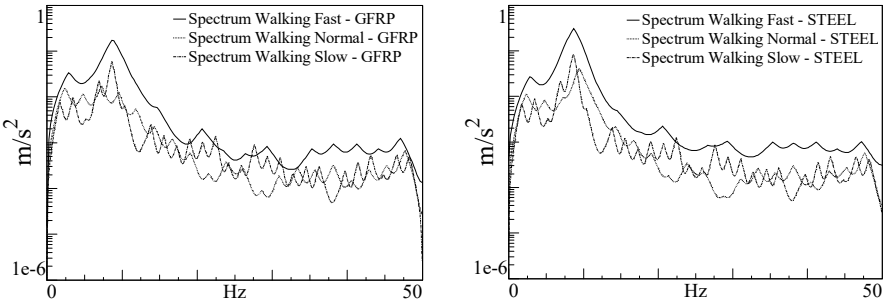
(c) (d)

Fig. 23b depict the calculated vertical accelerations and



(c) (d)

Fig. 23c and



(c) (d)

Fig. 23d depict the acceleration spectrum for GFRP- and steel-based models, respectively.

Table 8.

Single pedestrian simulation: numerical model response: maximum vertical acceleration.

Load Function	**Vertical Acceleration**		
	GFRP-based	**Steel-based**	**Rel. Diff. to GFRP**
	(m/s^2)		(%)
Slow walk	0.157	0.207	+32
Normal walk	0.129	0.180	+39
Fast walk	0.527	0.669	+27

For the GFRP-based model, the maximum time-domain amplitude slightly exceeded the comfort level 1 (0.527 m/s^2) by +3.8% for the fast walk; for the steel-based model, this figure was +27%. The maximum vertical accelerations occur at the midspan of the deck during the fast walk. These values were compared to the limits recommended by Hivoss [1], which suggests that the footbridge can be classified as **CL**

2 (medium degree of comfort) for the single pedestrian load case. The GFRP-hybrid footbridge model showed good performance under dynamic loads, presenting a maximum acceleration amplitude under slow and fast walk 24% lower (on average) than the steel counterpart.

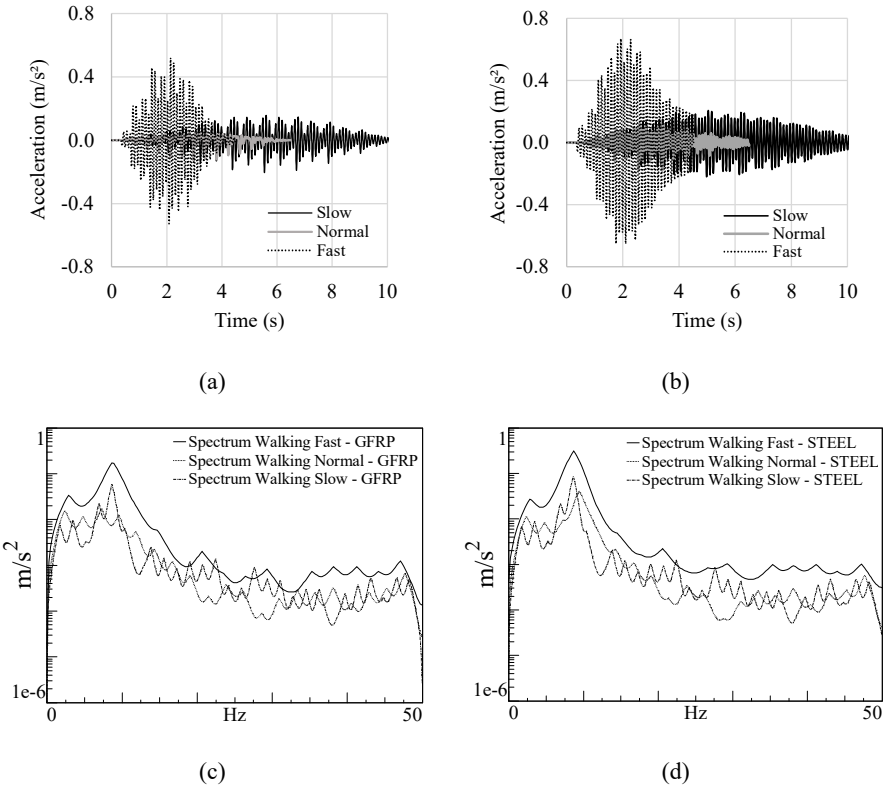


Fig. 23. Time- and frequency-domain responses for a single pedestrian load case:

(a) GFRP time-domain, (b) Steel time-domain, (c) GFRP freq.-domain, (d) Steel freq.-domain

5.4.2. Effects of pedestrian group loads

The load cases defined hereafter have been established to represent the effects of a non-synchronised number of pedestrians acting on the deck of the footbridge. For

modal analysis, the measured damping ratio summarised in **Table 5.** concerning the hammer-impact test are used and the first four modes are considered. The response was evaluated by applying a stochastic load to simulate the walking of 18 pedestrians on the deck, and the results were compared to those from the measurements summarized in section 4.3. The representation of such stochastic load is given by the application of 18 harmonic point-loads randomly distributed on the surface of the deck (**Fig. 24**), defined as follows [23]

$$p(t) = \sum_{i=1}^{n} G\alpha_i \cdot \sin\left[\left(2i\pi f_{p,\delta}\right)t - \varphi_i + f_{a,\delta}\right] \quad (4)$$

where $p(t)$ is the harmonic action (in N), G is the force component due to an isolated pedestrian assumed to weigh 700 N; α_i is the Fourier coefficient of the *i-th* harmonic; $f_{p,\delta}$ is the step frequency for each individual person ($\delta = 1, 2, \ldots 18$); t is the time given in seconds; i is the harmonic order number; n is the total number of considered harmonics; and φ_i is the phase angle of different harmonics, assumed as $\varphi_1 = 0$, and $\varphi_2 = \varphi_3 = \varphi_4 = \pi/2$ [23], and $f_{a,\delta}$ is the individual load phase. The Fourier coefficients α_1, α_2, α_3 and α_4 are 0.4, 0.1, 0.1 and 0.04, respectively. To avoid high response amplitudes at the start of the time series, a time window was applied by multiplying the load function by a sinusoid function given by $\sin(2\,\pi/50\,t)$.

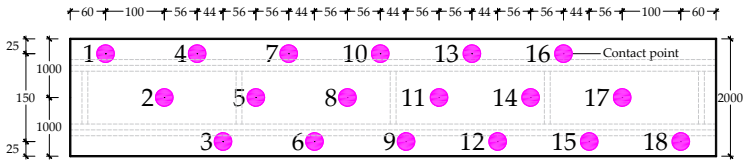
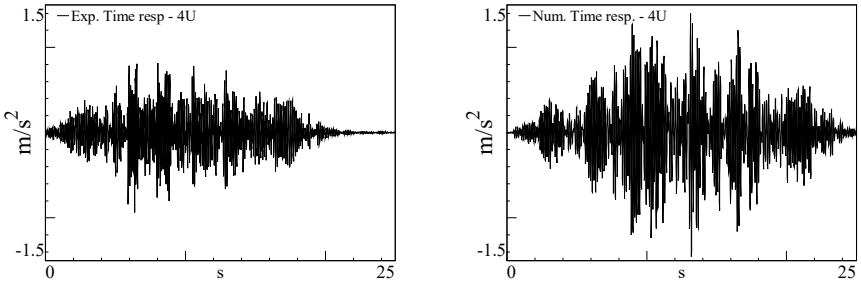


Fig. 24. 18 harmonic point-loads on deck surface.

Five series for each loading point were built: the frequency distribution for each pedestrian was randomly defined in an interval of $\pm$ 0.25 Hz about the step frequency extracted from the experimental measurements ($f_p = 1.93\ Hz$), and the phase ($f_{a,\delta}$) was also randomly defined in the interval between 0 and 2π. This random loading was applied in four different scenarios: including 1, 2, 3 and 4 active harmonics, totalizing 20 numerical simulations performed for both the GFRP- and the steel-based models. The 44% mass increase due to the pedestrians was incorporated within the mass of the structure. The step size of time domain integration defined for this study was 10 ms, and the crowd simulations were run for a period of 25 s.

For the time history analysis, the maximum response was extracted, and the average of the maxima for the five simulated sets of loads was calculated. For each of the five series of the time-domain records, the FFT was applied, and the average of each set of 5 complex series was calculated. **Fig. 25** depicts the measured and calculated time

response at point 4U concerning the action of 18 pedestrians. It can be observed that the stochastic load model was able to simulate the non-synchronized action of the 18 pedestrians. Moreover, as the numerical simulations were performed with the application of sinusoidal action at fixed points (*cf.* **Fig. 24**), the calculated response amplitudes are expected to be larger than those measured during the random walk of the pedestrian group.



(a) (b)

Fig. 25. Time-domain responses (a) measured, and (b) calculated at point 4U.

The averaged maximum vertical acceleration at the measurement points 4D, 4U, 7D and 7U is summarised in **Table 9** for the GFRP- and steel-based models. The analysis of **Table 9** highlights the relevance of the consideration of more than one harmonic to assess the response. Moreover, despite the very low amplitude of the 4th harmonic (only

10% of the first), it can be observed that its inclusion in the dynamic response is essential to reproduce the response effectively measured on the GFRP-based structure.

Table 9.

Maximum vertical accelerations caused by a group of 18 pedestrians: numerical response (maximum averaged accelerations for varying number of active harmonics) and experiments (only for GFRP-based structure).

			GFRP-based model		**Experiment**
Node	1 harmonic	2 harmonics	3 harmonics	4 harmonics	
			(m/s^2)		
4D	0.074 ± 0.014	0.137 ± 0.009	0.532 ± 0.122	1.260 ± 0.188	0.887
4U	0.085 ± 0.012	0.151 ± 0.019	0.506 ± 0.050	1.279 ± 0.207	0.936
7D	0.054 ± 0.009	0.106 ± 0.009	0.405 ± 0.088	0.925 ± 0.126	0.696
7U	0.063 ± 0.013	0.113 ± 0.015	0.377 ± 0.046	0.933 ± 0.141	0.798
			Steel-based model		
Node	1 harmonic	2 harmonics	3 harmonics	4 harmonics	
			(m/s^2)		
4D	0.068 ± 0.012	0.125 ± 0.011	0.474 ± 0.104	2.250 ± 0.349	-
4U	0.079 ± 0.012	0.134 ± 0.018	0.460 ± 0.038	2.534 ± 0.310	-
7D	0.052 ± 0.009	0.094 ± 0.004	0.362 ± 0.077	1.701 ± 0.260	-
7U	0.060 ± 0.011	0.104 ± 0.014	0.351 ± 0.033	1.921 ± 0.242	-

The **Fig. 26** shows the relative influence of the first four harmonics on the dynamic response of the GFRP-based numerical model in terms of maximum vertical accelerations in four different measurement points. The maximum calculated acceleration concerning four harmonics presents a difference of 12% on average to the experimentally measured acceleration values. In comparison, the consideration of only

three harmonics results in 55% lower accelerations than the experimental ones, on average.

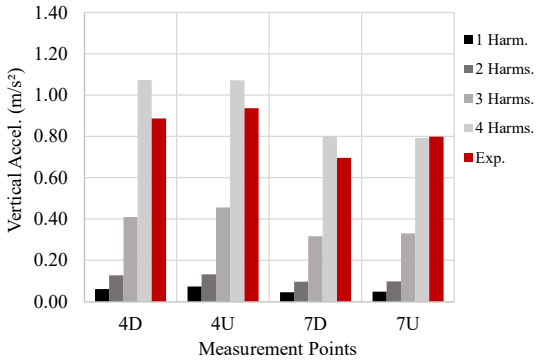


Fig. 26. GFRP numerical model: the modal response according to the number of harmonics

This important aspect can be observed in the frequency content of the response shown in **Fig. 27**. Accordingly, the average response spectrum obtained under the consideration of one, two, three and four harmonics shows how the response spectrum gradually approaches the measured spectrum for a particular location 4 U.

Considering the standard deviation of the acceleration (*cf.* **Table 9**), the dynamic responses of the GFRP- and steel-based models are similar where the driving frequencies are away from the resonance zone, *i.e.*, for the action of the first three harmonics. The dynamic response peaks when the 4th harmonic is included. In this scenario, the response of the GFRP-based model doubles while the response of the steel model increases up to five times (**Fig. 28**a), This means that the response amplitude of the GFRP-based model is about 48% smaller than that of the steel-based model close to resonance. Furthermore, the evaluation of the Dynamic Magnification Factor - DMF curve, shown in **Fig. 28b**, confirms an improved behaviour of the GFRP-based structure

under dynamic loads acting in the vicinity of the resonance frequency range, compared to the steel-based model.

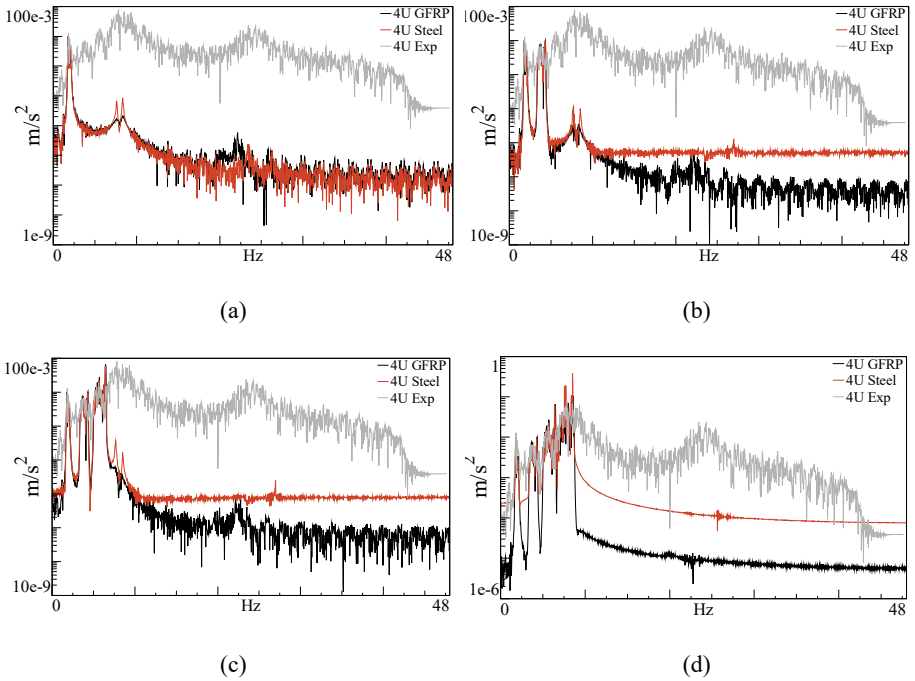


Fig. 27. Average spectrum amplitude at point 4U: (a) 1 Harm., (b) 2 Harm., (c) 3 Harm., and (d) 4 Harm.

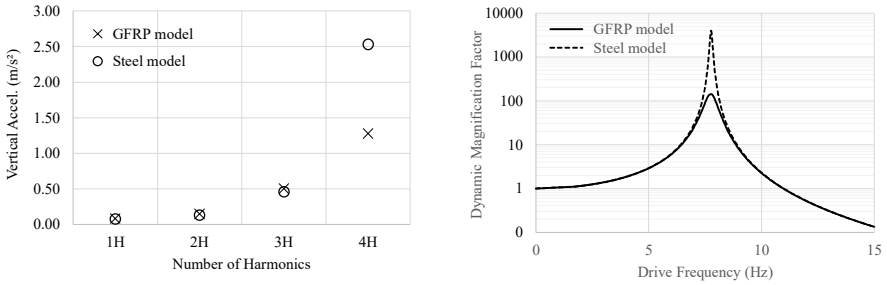


Fig. 28. Vert. Acceleration of point 4U: (a) amplitude response *vs.* harmonic, and (b) dynamic magnification factor curve.

6. Conclusions

This paper presents an experimental and numerical study about the dynamic behavior of a hybrid footbridge made of pultruded GFRP profiles and an SRRSCC deck, installed in northern Portugal and in operation since 2015. The study comprised: (i) the identification of the resonant frequencies, damping ratios and mode shapes of the footbridge, using the Enhanced Frequency Domain Decomposition (EFDD) and the Operational PolyMAX methods; and (ii) the assessment of the dynamic behaviour under ambient and forced-pedestrian loads. One of the main goals was to evaluate the damping performance of polymer-based composite materials, namely GFRP, to dissipate energy and to mitigate the vibrations of slender structures, as footbridges.

The experimental program based on output-only and input-output methods allowed the extraction of the modal components of the footbridge, and the results were compared with an alternative steel-based footbridge design reported in the literature: the results obtained showed the superior (5 times) damping capacity of the GFRP-based hybrid footbridge compared to the conventional steel-based hybrid system, under comparable geometry and boundary conditions.

The identified frequencies and the measured accelerations of the GFRP-based hybrid footbridge were compared with the current guidelines. The identified natural frequency for the first mode of vibration was 8.62 Hz, which is relatively high compared to typical footbridge frequencies, but expectable for a short-span footbridge; the maximum vertical acceleration was 0.936 m/s^2, activated from a pedestrian density

of 0.82 (person/m^2). In this respect, according to Hivoss [1], the São Silvestre footbridge was classified in the comfort category 2.

Numerical (FE) analyses of the dynamic response under a single pedestrian load were performed. Three pedestrian velocities were considered, and, in general, the footbridge's response under dynamic loads was within limits suggested by guidelines. The calibrated FE model was used to compare the dynamic response of the GFRP-based hybrid footbridge with an alternative structural system in which the GFRP profiles were replaced by commercial steel ones - the ratio between the equivalent stiffness of those solutions was 1.08 (k_{steel}/k_{GFRP}).

When subject to the same load cases, the GFRP-based model showed better responses, in terms of maximum vertical acceleration, with 24% lower amplitudes for a single pedestrian moving, on average.

Concerning the crowded simulations (0.82 pedestrian/m^2), a probabilistic approach was followed to represent the effects of a non-synchronised number of pedestrians acting on the footbridge deck. The results indicated the importance of considering high harmonic loads in the modal analysis of short-span footbridges. It was also concluded that pedestrians acting in a group cannot achieve perfect synchronisation of their movement, and when dynamic loads with driving frequency are acting in the vicinity of a structural frequency, the GFRP-based model presents a response amplitude around 48% smaller than that of steel one. This observation is well explained with the DMF curve, which attests the better capacity of the polymer-based composite material to mitigate vibrations close to resonances when compared to steel. This ability can guarantee better comfort performance of composite-based structures subjected to

pedestrian loads compared to steel-based structural systems – this is a relevant finding of the present study.

The overall results presented herein confirm the potential of using polymer-based composite materials, such as GFRP, in the construction of footbridges, which are characterised by their susceptibility to excessive vibrations.

Author Contributions: Dra. Elsa Caetano and Dr. João Ramôa Correia are the supervisor and co-supervisor of this research work, respectively. The following statements should be used "Conceptualization, V.D., E.C. and J.C.; methodology, V.D.; software, V.D.; validation, V.D..; formal analysis, V.D., E.C., J.C.; investigation, V.D.; resources, E.C.; data curation, V.D.; writing—original draft preparation, V.D.; writing—review and editing, V.D., E.C., J.C.; visualisation, V.D., E.C., J.C.; supervision, E.C., J.C.; project administration, E.C.; funding acquisition, E.C.. All authors have read and agreed to the published version of the manuscript.

Funding: This research was funded by Research supported by Fundação para a Ciência e a Tecnologia (Base Funding - UIDB/04708/2020 of the CONSTRUCT - Instituto de I&D em Estruturas e Construções - national funds through the FCT/MCTES (PIDDAC).

Acknowledgements: The authors wish to express their utmost thanks to Doctor José A. Gonilha for his useful remarks and for all the information and material kindly provided about the São Silvestre footbridge.

Conflicts of Interest: The authors declare no conflict of interest.

Nomenclature

Symbol	Description	Symbol	Description
m_n	modal mass of nth order mode	q	uniformly distributed live
ω_n	circular frequency of nth order	g_{sw}	self-weight load (kN/m^2)
f	Frequency, in Hz	δ	deflection (mm)
ϕ_n	amplitude of vibration related	ε	strain (‰)
ξ_n	damping ratio of nth order	$p(t)$	uniformly distributed
T	period of oscillation (s)	n	the number of pedestrians
A	cross-sectional area (m^2)	S	area of deck (m^2)
L	length of beam (m)	d	pedestrian density
k	elastic stiffness (kN/m)	t	time (s)
E	Elastic modulus (GPa)	G_i	force component of isolated
G	Shear modulus (GPa)	ψ	reduction coefficient
υ	Poisson ratio	τ	in-plane shear strength (MPa)
ρ	volumetric mass (kg/m^3)	$f_{tu,L}$	longitudinal tensile strength
a	Acceleration, in m/s^2	σ	axial stress (MPa)
φ	rotational degree of freedom		

References

[1] Research Fund for Coal and Steel, "Hivoss - Human induced Vibrations of Steel Structures - Design of Footbridges - Background Document," 2007.

[2] Setra, “Guide méthodologique passerelles piétonnes (Technical guide Footbridges: Assessment of vibrational behaviour of footbridges under pedestrian loading),” Service d’études techniques des routes et autoroutes, Paris - France, 2006.

[3] C. Heinemeyer and M. Feldmann, “European design guide for footbridge vibration,” *Footbridge Vib. Des.*, pp. 13–30, 2008, doi: 10.1201/9781482266511-8.

[4] P. Kulkarni, A. Bhattacharjee, and B. K. Nanda, “Study of damping in composite beams,” *Mater. Today Proc.*, vol. 5, no. 2, pp. 7061–7067, 2018, doi: 10.1016/j.matpr.2017.11.370.

[5] J.-M. Berthelot, M. Assarar, Y. Sefrani, and A. El Mahi, “Damping analysis of composite materials and structures,” *Compos. Struct.*, vol. 85, no. 3, pp. 189–204, 2008, doi: 10.1016/j.compstruct.2007.10.024.

[6] Y. Wang and D. J. Inman, “Finite element analysis and experimental study on dynamic properties of a composite beam with viscoelastic damping,” *J. Sound Vib.*, vol. 332, no. 23, pp. 6177–6191, 2013, doi: 10.1016/j.jsv.2013.06.016.

[7] J. A. Gonilha, J. R. Correia, and F. A. Branco, “Dynamic response under pedestrian load of a GFRP-SFRSCC hybrid footbridge prototype: Experimental tests and numerical simulation,” *Compos. Struct.*, vol. 95, pp. 453–463, 2013, doi:

10.1016/j.compstruct.2012.07.029.

[8] X. Wei, J. Russell, S. Živanović, and J. Toby Mottram, “Measured dynamic properties for FRP footbridges and their critical comparison against structures made of conventional construction materials,” *Compos. Struct.*, vol. 223, no. May, p. 110956, 2019, doi: 10.1016/j.compstruct.2019.110956.

[9] American Society of Civil Engineers (ASCE), “Pre-standard for load & resistance factor design (LRFD) of pultruded fiber reinforced polymer (FRP) structures,” Reston, VA, 2010. [Online]. Available: http://dev1.kreysler.com/information/specifications/specs-resources/LRFD PreStandard - Revised FINAL - Nov 9 2010.pdf.

[10] L. Ascione *et al.*, “Prospect for New Guidance in the Design of FRP Structures: Updated Report,” European Composites Industry Association (EuCIA), available at www.eucia.eu, 2018.

[11] Italian National Research Council - CNR-DT 205/2007, “Guide for the Design and Construction of Structures made of FRP Pultruded Elements,” Rome: Advisory Committee on Technical Recommendations for Construction (CNR), 2008.

[12] G. Boscato and S. Russo, “Free Vibrations of Pultruded FRP Elements: Mechanical Characterization, Analysis, and Applications,” *J. Compos. Constr.*, vol. 13, no. 6, pp.

565–574, 2009, doi: 10.1061/(asce)1090-0268(2009)13:6(565).

[13] B. Stankiewicz, P. Górski, and M. Tatara, “All-GFRP footbridge under human-induced excitation,” *MATEC Web Conf.*, vol. 262, p. 10013, 2019, doi: 10.1051/matecconf/201926210013.

[14] S. Živanović, G. Feltrin, J. T. Mottram, and J. M. W. Brownjohn, “Vibration performance of bridges made of fibre reinforced polymer,” *Conf. Proc. Soc. Exp. Mech. Ser.*, vol. 4, no. January, pp. 155–162, 2014, doi: 10.1007/978-3-319-04546-7_18.

[15] V. Dacol, E. Caetano, and J. R. Correia, “Comparative Study of Damping on Pultruded GFRP and Steel Beams,” *Polymers (Basel).*, vol. 13, no. 2201, 2021, doi: https://doi.org/10.3390/polym13132201.

[16] B. Peeters, H. Van Der Auweraer, P. Guillaume, and J. Leuridan, “The PolyMAX frequency-domain method: A new standard for modal parameter estimation?,” *Shock Vib.*, vol. 11, no. 3–4, pp. 395–409, 2004, doi: 10.1155/2004/523692.

[17] J. A. Gonilha *et al.*, “Static, dynamic and creep behaviour of a full-scale GFRP-SFRSCC hybrid footbridge,” *Compos. Struct.*, vol. 118, no. 1, pp. 496–509, 2014, doi: 10.1016/j.compstruct.2014.08.009.

[18] CEN, “ISO 527-4 Plastics - Determination of Tensile Properties - Part 4: Test Conditions

for Isotropic and Orthotropic Fibre-Reinforced Plastic Composites," 1997.

[19] ASTM, "ASTM D 695-02 Standard Test Method for Compressive Properties of Rigid Plastics," 2002.

[20] J. M. Hodgkinson, *Mechanical Testing of Advanced Fibre Composites*. Boca Raton, California: CRC Press, 2000.

[21] IPQ, "NP EN 12390–3:2011. Testing hardened concrete. Part 3: compressive strength of test specimens.," Caparica, 211AD.

[22] RILEM TC 162-TDF, "RILEM TC 162-TDF. Test and design methods for steel fibre reinforced concrete.," *Mater. Struct.*, vol. 35, no. 253, pp. 579–582, 2002.

[23] H. Bachmann and W. Ammann, *Vibrations in Structures - Induced by Man and Machines*. Zurich: IABSE - AIPC - IVBH, 1987.

[24] "Bulletin Ouvrages métaliques.," *Off. Tech. pour l' Util. l'Acier*, no. 2, 2002.

[25] J. M. M. Silva and N. M. M. Maia, *Modal analysis and testing*. Sesimbra, Portugal: Kluwer Academic Publishers, 1999.

[26] H. Bachmann, *Vibration problems in structures - Practical guidelines*, First. Basel, Birkhäuser, 1997.

[27] J. M. C. de A. Gonilha, "GFRP – concrete hybrid structural systems. Application to the

development of a footbridge prototype," Phd Thesis. UNIVERSIDADE DE LISBOA - INSTITUTO SUPERIOR TÉCNICO, 2014.

[28] A. A. M. F. Cunha and E. D. S. Caetano, "Experimental Modal Analysis of Civil Engineering Structures," *Sound Vib.*, vol. 6, no. 40, pp. 12–20, 2006.

[29] R. G. Faisca, "Caracterização de cargas dinâmicas geradas por atividades humanas.," PhD Thesis. COPPE. Universidade Federal do Rio de Janeiro, 2003.

[30] D. Vega, C. Magluta, and N. Roitman, "Análise de Cargas Humanas e a sua Interação com a Estrutura," in *Proceedings of the XXXVI Iberian Latin American Congress on Computational Methods in Engineering*, 2015, p. 15, doi: 10.20906/cps/cilamce2015-0387.

[31] European Committee for Standardization, "EN 1991-2:2003+AC:2010 (E): Eurocode 1 - Action on structures. Part 2: Traffic load on bridges," 2010.

[32] European Committee for Standardization, "EN 1990 (2002): Eurocode - Basis of structural design," 2011.

[33] I. J. Drygala, J. M. Dulinska, R. Ciura, and K. Lachawiec, "Vibration serviceability of footbridges: Classical vs. innovative material solutions for deck slabs," *Materials (Basel).*, vol. 13, no. 13, 2020, doi: 10.3390/ma13133009.

[34] V. Racic, A. Pavic, and J. M. W. Brownjohn, “Experimental identification and analytical modelling of human walking forces: Literature review,” *J. Sound Vib.*, vol. 326, no. 1–2, pp. 1–49, 2009, doi: 10.1016/j.jsv.2009.04.020.

[35] C. M. dos Santos, “Avaliação do comportamento dinâmico de uma passarela submetida a carregamentos induzidos por pedestres,” Master Thesis, Universidade Federal do Rio de Janeiro, 2011.

[36] J. E. Wheeler, “Prediction and control of pedestrian-induced vibration in footbridges,” *J. Struct. Div.*, pp. 2045–2065, 1982.